Hunting the charged Higgs boson with lepton signatures in the ATLAS experiment

Alexander Madsen

To cite this version:

Alexander Madsen. Hunting the charged Higgs boson with lepton signatures in the ATLAS experiment. High Energy Physics - Experiment [hep-ex]. Université Grenoble Alpes; Uppsala universitet, 2015. English. NNT : 2015GREAY043 . tel-01271042

HAL Id: tel-01271042
https://theses.hal.science/tel-01271042v1

Submitted on 8 Feb 2016

UPPSALA
UNIVERSITET

UNIVERSITÉ
GRENOBLE
ALPES

THÈSE

Pour obtenir le grade de

DOCTEUR DE L'UNIVERSITÉ GRENOBLE ALPES

préparée dans le cadre d'une cotutelle entre l'*Université Grenoble Alpes* et *Uppsala Universitet*

Spécialité : **Physique Subatomique et Astroparticules**

Arrêté ministériel : le 6 janvier 2005 - 7 août 2006

Présentée par

Alexander Kondrup MADSEN

Thèse dirigée par **Johann COLLOT** et **Arnaud FERRARI**
et co-encadrée par **Mattias Ellert**

préparée au sein des **Laboratoire de Physique Subatomique et de Cosmologie de Grenoble et Ångströmlaboratoriet**

dans **les Écoles Doctorales de Physique de Grenoble et Uppsala**

À la recherche d'un boson de Higgs chargé impliquant des signatures leptoniques à l'aide de l'expérience ATLAS

Thèse soutenue publiquement le **22 Mai 2015**,
devant le jury composé de:

Mme Susan GASCON-SHOTKIN
Prof. Université de Lyon, Présidente et Rapporteure
Mme Ritva KINNUNEN
Dr. Helsinki Institute of Physics, Rapporteure
M. Christophe CLÉMENT
Dr. Stockholm University, Membre
M. Oscar STÅL
Dr. Stockholm University, Membre
M. Volker ZIEMANN
Dr. Uppsala University, Membre
M. Johann COLLOT
Prof. Université Joseph Fourier, Directeur de thèse
M. Arnaud FERRARI
Dr. Uppsala University, Directeur de thèse

Abstract

This thesis presents searches for a charged Higgs boson ($H^{\pm}$) in proton-proton collisions with center-of-mass energies of 7 TeV and 8 TeV, using data collected by the ATLAS experiment at the Large Hadron Collider at CERN. Multiple search channels are used with the common characteristic of at least one charged lepton (electron or muon) that effectively reduces the multi-jet background and is used for efficient triggering. Charged Higgs bosons decaying to a tau lepton and a neutrino are searched for using final states with two charged leptons, or one charged lepton and a hadronically decaying tau. A significant background originates from quark- or gluon-initiated jets that may be misidentified as hadronic tau decays. Methods to estimate this background are presented, including a largely data-driven matrix method. Signal processes with a charged Higgs boson mass below or above that of the top quark are considered. With the dataset collected at a center-of-mass energy of 8 TeV, corresponding to an integrated luminosity of 20.3 fb^{-1}, upper limits at 95% confidence level are placed on the branching fraction $\mathscr{B}(t \to bH^{\pm}) \times \mathscr{B}(H^{\pm} \to \tau\nu)$ in the range 1.1–0.3% for charged Higgs boson masses between 80 GeV and 160 GeV, as well as on the top-quark associated $H^{\pm}$ production cross section in the range 0.93–0.03 pb for charged Higgs boson masses between 180 GeV and 1 TeV.

Résumé

Cette thèse présente la recherche d'un boson de Higgs chargé ($H^{\pm}$) qui serait produit dans les collisions proton-proton à des énergies de 7 TeV et 8 TeV, en utilisant les données recueillies par l'expérience ATLAS au LHC (Large Hadron Collider). Plusieurs canaux de recherche sont utilisés, présentant la caractéristique commune de contenir au moins un lepton chargé (électron ou muon) énergétique, ce qui réduit efficacement le bruit de fond contenant des jets, tout en permettant un déclenchement efficace du détecteur. Ici, le boson de Higgs chargé se désintègre en un lepton tau et un neutrino, ce qui conduit à des états finaux avec deux leptons chargés, ou bien un lepton chargé et un tau hadronique. Une source importante de taus mal identifiés provient de quarks et de gluons, par l'intermédiaire des jets hadroniques qu'ils initient. Plusieurs méthodes ont été développées pour estimer ce bruit de fond, l'une d'elles étant basée directement sur les données. Des processus avec des bosons de Higgs chargés dont la masse est soit en dessous soit au-dessus de celle du quark top sont considérés. Avec l'ensemble de données recueillies à une énergie de 8 TeV, correspondant à une luminosité intégrée de 20,3 fb^{-1}, des limites avec un taux de confiance de 95% sont placées sur le rapport de branchement $\mathscr{B}(t \to bH^{+}) \times \mathscr{B}(H^{+} \to \tau\nu)$ entre 1,1 et 0,3% pour des masses du boson de Higgs chargé entre 80 GeV et 160 GeV, et sur la section efficace de production du boson de Higgs chargé en association avec un quark top entre 0,93 et 0,03 pb, pour un boson de Higgs chargé ayant cette fois une masse comprise entre 180 GeV et 1 TeV.

To my parents.

Contents

Introduction

In 2012, a Higgs boson was discovered at the Large Hadron Collider (LHC) at CERN, with properties in agreement with those predicted by the Standard Model of particle physics. The question remains, however, if the discovered particle is indeed the single Higgs boson predicted by the Standard Model or if additional Higgs bosons exist. A straightforward extension of the Standard Model Higgs sector is the Two-Higgs-Doublet Model, in which there are two scalar doublet fields, compared to only one in the Standard Model. This extension also describes the Higgs sector of the Minimal Supersymmetric Standard Model. With two scalar doublet fields, there are five physical Higgs bosons, two of which are fundamentally different to the one predicted by the Standard Model in that they carry electric charge.

This thesis describes several searches for charged Higgs bosons[1] decaying into a tau lepton and a neutrino, i.e. $H^+ \to \tau\nu$. The analyses are conducted using data from proton-proton collisions at center-of-mass energies of 7 TeV and 8 TeV, recorded by the ATLAS experiment at the LHC. Charged Higgs boson masses below and above that of the top quark are considered. The production modes are different in these two cases, but both involve at least one top quark. Event topologies involving the Standard Model decay of a top quark into a bottom quark, at least one neutrino, and an electron or a muon are used, as such events are relatively easy to identify over the large multi-jet background. Both leptonic and hadronic decay modes of the tau lepton arising from the charged Higgs boson are investigated.

The theoretical framework and motivations are described in more detail in Part I, including the Standard Model, its possible extensions in the form of Two-Higgs-Doublet Models and Supersymmetry, as well as the production and decay modes of charged Higgs bosons. Part II discusses the LHC and the ATLAS experiment, and summarizes some important recent experimental results of particular relevance to this thesis. Part III presents three analyses of the 7 TeV dataset, with different strategies aimed at searching for charged Higgs bosons, and finally also an analysis of the 8 TeV dataset, which builds on a combination of lessons learned from the previous efforts. Results are presented in the form of upper limits on charged Higgs boson production in the decay of a top quark or in association with a top quark, and are interpreted in benchmark scenarios of the Minimal Supersymmetric Standard Model.

---

[1] Charge-conjugate states will be implied in the notation used throughout this thesis. The charged Higgs bosons may thus be denoted H^+, with H^- implied when applicable, and the formula $H^+ \to \tau\nu$ should be understood as both $H^+ \to \tau^+\nu$ and $H^- \to \tau^-\bar{\nu}$.

Author's contribution

The work presented here was performed within the ATLAS collaboration, which comprises some 3000 scientists. The complexity of our experiment requires the joint effort of all members in order to operate the detector and the technical infrastructure, to understand the data and to produce physics results. Hence, the results presented in this thesis are really the fruits of the work of many people. The personal contributions of the author are indicated below.

Working within the Physics Analysis Tools and Distributed Analysis groups, the author of this thesis was one of two developers of the analysis software packages described in section 4.6.3. In addition, the author helped monitor the nightly builds of the reconstruction software also described in section 4.6.3. The measurements of the SCT detector presented in section 4.7.1 were mostly performed by the author. The upgrade of the heater pad control system described in section 4.7.2 is entirely the author's own work, but could not have been realized without extensive support from Inner Detector and central DCS experts.

The focus of this thesis is the hunt for charged Higgs bosons in the ATLAS data. For the analyses of the 7 TeV data, described in chapter 6, the author implemented the corresponding event selection procedures. This work entailed processing D3PD data files (see section 4.6.3), applying relevant corrections derived by the ATLAS combined performance groups, and producing final histograms for use in the calculation of exclusion limits, including the variations needed to assess the impact of systematic uncertainties. This same effort was repeated by multiple people to ensure that each member of the analysis team could individually reproduce all results. This was deemed necessary to build confidence in the results obtained with early ATLAS data. The author also contributed to the estimation of the background with jets misidentified as hadronic tau decays. Different strategies were explored, based on template fitting or the determination of scale factors in various control regions. After settling on the use of scale factors measured in $W+$jets events, correlations of the misidentification probability with other variables were investigated and suitable parametrizations derived by the author.

In the analysis of the 8 TeV data (chapter 7), the author performed the event selection in the lepton+tau channel. Two independent implementations of the analysis were written in order to cross-check the results with different toolchains. The data-driven matrix method for the estimation of the background from jets misidentified as hadronic tau decays, which has several advantages over the previously used methods, was developed entirely by the author.

Beyond the scope of this thesis, the author has also participated in a search for charged Higgs bosons decaying to tb, which is being finalized at the time of writing. Among other contributions, an event reconstruction method utilizing boosted decision trees or maximum likelihood functions was developed and found to significantly improve the sensitivity of the analysis.

Part I: Theory

1. The Standard Model of particle physics

The idea that all matter is made of a set of fundamental (indivisible) particles goes back to the early days of natural philosophy. Experimental support for this hypothesis first appeared when it was found that chemical elements are composed of atoms. Later, with the discoveries of the electron and of radioactivity, it was realized that atoms themselves have an internal structure. Soon, it was even found that they in fact consist mostly of empty space, with the bulk of the atomic mass located in a tiny nucleus. And further investigations revealed that the nucleus itself consists of individual *nucleons*. Following this, as experiments were performed at higher and higher energies, a plethora of new particles were discovered. In parallel, an understanding of radiation and forces in terms of particles also emerged. Eventually, it was determined that most of the new particles, including the nucleons, were themselves composite objects – the myriad of subatomic particles could be reduced to a relatively small set of *elementary particles*, which are today the smallest known constituents of the universe.

The theoretical description of the known elementary particles is called the *Standard Model*. It encompasses all observed particles and the interactions that underlie all known microscopic phenomena. Many predictions of the Standard Model, including the existence of previously unobserved particles, have been tested with high experimental accuracy. In this chapter, a very brief review of the Standard Model is given, with emphasis on the role of the recently discovered Higgs boson. Finally, a number of limitations of the Standard Model are highlighted, explaining why, despite its remarkable success, it is not considered a final theory of the universe. In the next chapter, proposed extensions to the Standard Model, which aim at solving some of these problems, will be presented.

1.1 Overview

The Standard Model treats particles as excitations of quantum fields. The so-called matter particles are spin-$\frac{1}{2}$ fermions, which obey the Pauli exclusion principle – meaning that two such particles can not simultaneously occupy the same quantum state. By imposing certain local gauge symmetries on the theory, the three fundamental forces of nature that are relevant at small length scales – electromagnetism, the weak force and the strong force – emerge as interactions with spin-1 gauge bosons. Gauge invariance initially requires both

Table 1.1. *The fermions of the Standard Model, and their observed masses [1]. The light quark masses are indicative only and depend on the calculation scheme.*

	Leptons		Quarks	
	charged	neutrino	up-type	down-type
Electric charge [e]	-1	0	$+2/3$	$-1/3$
Weakly interacting	yes	yes	yes	yes
Strongly interacting	no	no	yes	yes
1st generation particle	e (electron)	ν_e	u (up)	d (down)
Mass [GeV]	5.1×10^{-4}	$<2\times10^{-9}$	≈ 0.002	≈ 0.005
2nd generation particle	μ (muon)	ν_μ	c (charm)	s (strange)
Mass [GeV]	0.105	$<1.9\times10^{-4}$	≈ 1.3	≈ 0.095
3rd generation particle	τ (tau)	ν_τ	t (top)	b (bottom)
Mass [GeV]	1.78	<0.018	173	≈ 4.2

Table 1.2. *The bosons of the Standard Model and their masses [1]. The photon and the gluons are assumed to be massless. Gravitation is not considered.*

Interaction	Particle	Mass [GeV]	Charge [e]	Spin
Electromagnetic	γ (photon)	0	0	1
Weak	Z	91.2	0	1
Weak	W^+	80.4	$+1$	1
Weak	W^-	80.4	-1	1
Strong	g (gluon) $\times 8$	0	0	1
Higgs	H	125	0	0

fermions and bosons to be massless, but the fields are mixed into effectively massive particles via interactions with a scalar Higgs field, which has a non-zero vacuum expectation value. The physical particles of the Standard Model are summarized in Tables 1.1 and 1.2.

There are two types of fermions: *leptons* and *quarks*. They are divided into three *generations*, each containing two particles of each type and the corresponding *antiparticles* with identical masses but opposite internal quantum numbers. All fermions carry *weak isospin*. Weak isospin is the charge of the weak force, which is mediated by the massive spin-1 W and Z bosons. By emitting or absorbing a W boson, a quark or lepton can be transformed into its counterpart of the same type in the same generation, which has the opposite weak isospin. Quarks may also to some extent be transformed into quarks of other generations, a phenomenon known as Cabibbo-Kobayashi-Maskawa (CKM) mixing. Due to the mass of the mediating particles, the weak force has a limited range. In contrast, the electromagnetic force is mediated by the photon, which also has a spin of 1 but no mass, hence it has an infinite range.

Each generation of leptons consists of one electrically charged and one neutral particle. They are the electron and the electron neutrino, the muon and the muon neutrino, and the tau and the tau neutrino. For each particle, the corresponding antiparticle has the opposite electric charge. As the electric charge of the neutrinos is zero, it is currently unclear whether neutrinos and anti-neutrinos are distinct particles. The tau is the heaviest lepton and has a relatively short lifetime (0.3 ps). Over the time scales studied experimentally in this thesis, the muon (with a lifetime of 2 μs) can be considered as a stable particle together with the electron and the neutrinos.

As for the leptons, there are six flavors of quarks. Each generation consists of one quark with electric charge $+\frac{2}{3}e$ and one with electric charge $-\frac{1}{3}e$, as well as their antiparticles. They are the up and down quarks, the charm and strange quarks, and the top and bottom quarks. Quarks carry exactly one of three different charges of the strong force, called *colors*, and anti-quarks carry exactly one of three corresponding anti-colors. Gluons carry a mixture of color and anti-color charges in eight linearly independent combinations. All three colors mixed together, or one color and its anti-color, give a net color charge of zero.

The strong force does not actually appear very strong over short distances. Quarks in close proximity are said to be asymptotically free of its effects. The gluon, however, is itself charged under the strong force since it also carries a color quantum number, and this self-interaction creates a vacuum polarization effect that amplifies the strength of the gluon field over increasing distances. This leads to the peculiar phenomenon that the interaction between two colored objects becomes stronger the farther apart they are. Quarks are therefore usually found in close proximity to other quarks, with which they form color neutral bound states called hadrons. Hadrons may have an electric charge but no net color charge. Two of the most well known hadrons are the proton and the neutron, both consisting of a mixture of three up and down quarks, which together with the electron make up the atoms of ordinary matter.

An isolated quark will undergo a process called hadronization during which the energy in the surrounding gluon field is transformed into quark-anti-quark pairs, which arrange themselves into hadrons until there is no longer any unconfined color charge. In collider experiments, the hadronization of individual quarks and gluons emitted in a collision gives rise to collimated *jets* of hadrons leaving the interaction point.

Of central interest in this thesis is the top quark, which has the largest mass of all elementary particles, even larger than most atoms. It is so heavy, in fact, that its lifetime is shorter than the time it would take for hadronization to occur. This makes it possible to study top quark decays in relative isolation. Its large mass also gives the top quark a special relationship with the Higgs boson which, due to the nature of the Higgs field, couples more strongly to heavier particles.

The Higgs boson is electrically neutral and is the only known elementary particle without spin. The confirmation of its existence is the most recent triumph of the Standard Model (see section 3.2) – it was the long sought "missing puzzle piece" predicted by the theory.

1.2 The Higgs field

The Higgs field generates the masses of all elementary particles. Historically, it was first introduced [2–5] to explain how the mediating particles of the weak force acquire their masses, which are needed to ensure the short-ranged nature of the force. Descriptions of the weak interaction as a non-Abelian gauge theory seemed to necessitate that the force carriers were massless. The first clue to resolve this inconsistency came from solid state physics and the fact that inside a superconductor, electromagnetism is a short-range force. The breaking of a local gauge symmetry, when a metal becomes superconducting, makes the photon massive. The same idea is applied [6] in the electroweak part of the Standard Model by introducing the complex scalar doublet Higgs field,

$$\Phi(x) = \begin{pmatrix} \phi^+(x) \\ \phi^0(x) \end{pmatrix}, \tag{1.1}$$

which has a Lagrangian density given by

$$\mathscr{L} = (D_\mu \Phi)^\dagger (D^\mu \Phi) - V(\Phi). \tag{1.2}$$

The Higgs field is coupled to the electroweak gauge fields of weak isospin, W^a_μ, and of *weak hypercharge*, B_μ, via the covariant derivative:

$$(D_\mu \Phi) = (\partial_\mu - igW^a_\mu \tau^a/2 - ig'YB_\mu/2)\Phi, \tag{1.3}$$

where $\tau^{1,2,3}$ are the Pauli matrices. The components of equation (1.1) are eigenstates of τ^3, with the eigenvalues $T_3 = \pm\frac{1}{2}$ giving their weak isospin quantum numbers. The hypercharge quantum number Y connects the weak force with electromagnetism via the relation $Y \equiv 2(Q - T_3)$, where Q is the electric charge. The field Φ has hypercharge $Y = 1$.

The purpose of Φ is to break the gauge symmetry of the vacuum, which corresponds to a field configuration with the lowest possible energy. This is accomplished if Φ has a non-zero value in this vacuum state, for which at least two self-interaction terms are needed. Renormalizability and gauge invariance of the Lagrangian then require the minimal form of the potential to be:

$$V(\Phi) = -\mu^2(\Phi^\dagger\Phi) + \lambda(\Phi^\dagger\Phi)^2. \tag{1.4}$$

A well-defined minimum of the potential exists if $\lambda > 0$. If $\mu^2 > 0$, it does not occur at zero but when $\Phi^\dagger\Phi = \mu^2/(2\lambda)$, breaking the invariance under gauge transformations. Note that the gauge symmetry is *spontaneously* broken, meaning that the symmetry of the Lagrangian remains but is not manifest at low energy.

The physical vacuum must correspond to one of the degenerate solutions. Wishing to identify ϕ^+ and ϕ^0 in equation (1.1) as the charged respectively neutral components of the field, the *vacuum expectation value* of Φ that conserves electric charge is

$$\langle\Phi\rangle = \frac{1}{\sqrt{2}}\begin{pmatrix}0\\ v\end{pmatrix}, \tag{1.5}$$

with $v = \sqrt{\mu^2/\lambda}$. Anticipating that the physical fields of the weak interaction will be the linear combinations

$$W_\mu^\pm = (W_\mu^1 \mp W_\mu^2)/\sqrt{2}, \tag{1.6}$$

$$Z_\mu = \cos\theta_W W_\mu^3 - \sin\theta_W B_\mu, \tag{1.7}$$

with $\cos\theta_W = g/\sqrt{g^2+g'^2}$ and $\sin\theta_W = g'/\sqrt{g^2+g'^2}$, and then inserting $\Phi = \langle\Phi\rangle$ in equation (1.3), the kinetic part of the Lagrangian can be written as

$$(D_\mu\langle\Phi\rangle)^\dagger(D^\mu\langle\Phi\rangle) = \frac{v^2}{8}\left(g^2(W_\mu^+)^2 + g^2(W_\mu^-)^2 + \frac{g^2}{\cos^2\theta_W}(Z_\mu)^2\right), \tag{1.8}$$

which confirms that these are massive fields. The remaining orthogonal combination $A_\mu = \cos\theta_W W_\mu^3 + \sin\theta_W B_\mu$ is the photon, which does not acquire a mass term. The relationship between the W and Z boson masses,

$$m_W^2/m_Z^2 = \cos^2\theta_W, \tag{1.9}$$

was a very successful prediction of the Standard Model. Even without the explicit values of these parameters, the vacuum expectation value of the Higgs field is fixed by the Fermi coupling constant G_F, which is precisely determined from muon decay measurements [1]:

$$v = \frac{2m_W}{g} = \sqrt{\frac{1}{\sqrt{2}G_\mathrm{F}}} = 246\ \text{GeV}. \tag{1.10}$$

The second important role of the Higgs field is to generate fermion masses. Quantum mechanics allows two kinds of spin-$\frac{1}{2}$ particles, with left- or right-handed chirality. The distinction is important because they are treated differently in the Standard Model: only the left-handed fermions (and right-handed anti-fermions) interact with W bosons. The left-handed fermions are therefore represented as weak isospin doublets. The fermion fields of the first generation, for example, are:

$$l_L = \begin{pmatrix}\nu_{eL}\\ e_L\end{pmatrix}, \quad q_L = \begin{pmatrix}u_L\\ d_L\end{pmatrix} \tag{1.11}$$

while the right-handed fields e_R, u_R and d_R are singlets. Right-handed neutrinos have never been observed and are not included here. For the other fermions, the left- and right-handed states can be connected with each other via Yukawa couplings with the Higgs field:

$$\mathscr{L}_{Yukawa} = -y_e \bar{l}_L \Phi e_R - y_u \bar{q}_L i\tau^2 \Phi u_R - y_d \bar{q}_L \Phi d_R + h.c + \cdots , \qquad (1.12)$$

where $h.c.$ stands for the Hermitian conjugates of the preceding terms, and similar terms for the second and third fermion generations are implied. For reasons of charge conservation, a transformation of Φ is needed in the u_R term. In some extensions of the Standard Model, the up-type quarks may instead couple to an entirely different Higgs field (as will be discussed in section 2.1).

Inserting the vacuum expectation value $\langle\Phi\rangle$ of the Higgs field and collecting the electron term and its Hermitian conjugate, equation (1.12) becomes:

$$\mathscr{L}_{Yukawa} = -y_e \frac{v}{\sqrt{2}} (\bar{e}_L e_R + \bar{e}_R e_L) + \cdots = -y_e \frac{v}{\sqrt{2}} \bar{e} e + \cdots \qquad (1.13)$$

This is a mass term for a so-called Dirac fermion, which is the physical electron. Masses for the muon, the tau and the quarks arise in the same way. For the latter, terms involving left- and right-handed quarks of different generations can also be added. This is the origin of the CKM mixing: The quark states of definite mass are actually combinations of more than one of the weakly interacting fields.

The fermion masses depend on the vacuum expectation value of the Higgs field, but also on the Yukawa couplings y, which are free parameters. Note that such mass terms could not have been added without the Higgs field, precisely because the weak interaction treats the left- and right-handed components differently. The masses arise from particles switching between left- and right-handed states, which would not conserve weak isospin. Here, one unit of weak isospin is carried away by the omnipresent non-zero ϕ^0.

The Higgs field can be parametrized by expanding around $\langle\Phi\rangle$:

$$\Phi(x) = e^{i\tau^a \pi_a(x)} \frac{1}{\sqrt{2}} \begin{pmatrix} 0 \\ v + h(x) \end{pmatrix}. \qquad (1.14)$$

The excitations $\pi_a(x)$ along the minimum of the potential are the Goldstone bosons that necessarily appear whenever a continuous symmetry is spontaneously broken. However, they are coupled to the electroweak fields via the covariant derivative and it is possible to choose a gauge, called the unitary gauge, in which there is no explicit dependence on $\pi_a(x)$. The three degrees of freedom which are thus eliminated compensate for those seemingly introduced via the longitudinal polarizations of the massive vector bosons. The excitation $h(x)$ in the orthogonal direction remains as a physical particle – the *Higgs boson* [4]. As can be seen by inserting the full expression (1.14) in equations (1.2) and (1.12), h has three- and four-point interactions with the massive vector bosons (but not the photon) and three-point interactions with the fermions, proportional in strength to the masses of these particles. From the expression of the potential (1.4) it can be seen that the Higgs boson also has three- and four-point interactions with itself, and that it has a non-zero mass. This prediction of a massive scalar particle made it possible to experimentally confirm the existence of the Higgs field. Its mass is a free parameter of the theory but has been found to be 125 GeV (see section 3.2).

1.3 Limitations of the Standard Model

It is generally accepted that, despite its many successes, the Standard Model is not and can not be a complete theory of nature. Problems with the Standard Model include:

- It postulates that neutrinos are massless, which is incompatible with the experimental observation of *neutrino oscillations*. If neutrino masses are generated via Yukawa couplings to the Higgs field, the couplings must be curiously small and require the existence of right-handed neutrinos that do not participate in any other interaction.
- Even with massive neutrinos, the Standard Model can only account for a small fraction of the *dark matter* in the universe. It also does not explain the observed amount of *dark energy*.
- It does not include any mechanism that could have caused the rapid *inflation* that appears to have taken place in the very early universe.
- It also does not include *gravitation*.
- The Charge-Parity (CP) symmetry violation allowed via the CKM mixing of quarks can only account for a modest amount of baryogenesis. Unless CP violation in the lepton sector is eventually observed, there is no explanation for the apparent *matter-antimatter asymmetry* in nature.
- The couplings of the strong, weak and electromagnetic forces all notably seem to converge at higher energies, but within the Standard Model there is no point at which they are actually identical. The Standard Model therefore fails to achieve *grand unification* of the forces.
- It has a number of *free parameters* with arbitrary values that can only be determined experimentally. There is for example no explanation for the large variation of masses between the fermion generations, or for the large variation of mixing angles between the mass and weak eigenstates of the quarks.
- There is also no explanation of why there are specifically three generations of fermions, why charges are quantized, or why the strong interaction does not seem to violate the CP symmetry, while the weak force does.
- The effective mass of the Higgs boson is largely influenced by loop corrections, mainly involving virtual top quarks, which should drive it up to some energy scale, possibly even the Planck scale, at which some new physics

could be expected to cut off the effect. In order to preserve the observed (low) Higgs boson mass, there must be a remarkably precise cancellation between these corrections and the bare Higgs mass. This "unnatural" fine-tuning of the Higgs boson mass is called the *hierarchy problem*.

Some of the problems listed above amount to direct contradictions with experimental observations. Others are merely perceived inelegances of the model, but are nevertheless irreconcilable with many physicists' intuitions of a sound theory. This motivates the search for new physics beyond the Standard Model!

2. Beyond the Standard Model

2.1 Two-Higgs-Doublet Models

The Standard Model uses a minimal form of the so-called Brout-Englert-Higgs mechanism to achieve electroweak symmetry breaking. There is no theoretical motivation for this, other than simplicity. Nature, however, have been less economical in other respects (e.g. with the number of fermion generations). Having established the existence of at least one Higgs field, we must now try to find out if also the Higgs sector could in reality have a more complex structure. Arguably the most straightforward extension is to add a second $Y = 1$ complex scalar doublet to the theory, which then contains two fields Φ_1 and Φ_2 with a total of eight degrees of freedom. This is called the Two-Higgs-Doublet Model (2HDM) [7]. Specific motivations for the 2HDM include its appearance in many attempts to solve some of the problems with the Standard Model outlined in the previous chapter. Embedding the Standard Model in a minimally supersymmetric theory (as will be discussed in the next section) requires two Higgs doublets. Additional sources of CP violation in a 2HDM could explain the matter-antimatter asymmetry of the universe. It is also an effective low-energy theory of Peccei-Quinn models [8, 9], which could explain why the strong force is not seen to violate CP symmetry. Extensive reviews of the 2HDM are available in e.g. Ref. [10] and, more recently, Ref. [11]. Here, it will be briefly explored with the aim of demonstrating the appearance of electrically charged Higgs bosons.

One of the most serious potential problems facing any model with an extended Higgs sector is the appearance of tree-level Flavor-Changing Neutral Currents (FCNC), which are hard to reconcile with experimental data. It was pointed out in section 1.2 that the quark states with definite masses appearing via Yukawa interactions with the Standard Model Higgs field are mixtures of the fields that interact with the W boson. Likewise, fields with well-defined mass terms appearing via Yukawa interactions with one of the 2HDM Higgs doublets may in the general case be mixtures of the fields that interact with the other Higgs doublet. The Paschos-Glashow-Weinberg [12, 13] theorem states that a necessary and sufficient condition for avoiding tree-level FCNC is that all fermions of a given charge must couple to a single Higgs doublet. A 2HDM in which all fermions couple to the same Higgs doublet is said to be of Type I. If up-type quarks couple to one of the doublets while down-type quarks and charged leptons couple to the other doublet, the model is said to be of Type II. The cases in which either the charged leptons or the down-type quarks have unique couplings to one of the doublets are respectively called "lepton-specific" and "flipped" 2HDMs. Conformance with the Type I criteria can be achieved by requiring the model to be symmetric under the discrete $\mathbb{Z}_2$ transformation $\Phi_1 \to -\Phi_1$. Type II can similarly be enforced with a symmetry under the simultaneous transformations $\Phi_1 \to -\Phi_1$ and $d_R \to -d_R$, and so on. The generic case, which does not avoid tree-level FCNC, is sometimes referred to as Type III[1]. The different 2HDM categories are summarized in Table 2.1, by convention Φ_2 is always taken to be the doublet that couples to up-type quarks.

Table 2.1. *The different types of Two-Higgs-Doublet Models.*

Model	u,c,t couple to	d,s,b couple to	e,μ,τ couple to
Type I	Φ_2	Φ_2	Φ_2
Type II	Φ_2	Φ_1	Φ_1
Lepton-specific	Φ_2	Φ_2	Φ_1
Flipped	Φ_2	Φ_1	Φ_2
Type III	Φ_1 and Φ_2	Φ_1 and Φ_2	Φ_1 and Φ_2

The most general form of the 2HDM potential contains 14 parameters. However, some simplifying assumptions can be made. It is usually assumed that it conserves CP and that the global $\mathbb{Z}_2$ symmetry is, at most, softly broken. The general form of a potential respecting these criteria is:

$$\begin{aligned} V = {} & m_{11}^2\Phi_1^\dagger\Phi_1 + m_{22}^2\Phi_2^\dagger\Phi_2 - m_{12}^2\left(\Phi_1^\dagger\Phi_2 + \Phi_2^\dagger\Phi_1\right) \\ & + \frac{\lambda_1}{2}\left(\Phi_1^\dagger\Phi_1\right)^2 + \frac{\lambda_2}{2}\left(\Phi_2^\dagger\Phi_2\right)^2 + \lambda_3\Phi_1^\dagger\Phi_1\Phi_2^\dagger\Phi_2 + \lambda_4\Phi_1^\dagger\Phi_2\Phi_2^\dagger\Phi_1 \\ & + \frac{\lambda_5}{2}\left[\left(\Phi_1^\dagger\Phi_2\right)^2 + \left(\Phi_2^\dagger\Phi_1\right)^2\right], \end{aligned} \tag{2.1}$$

where Φ_1 and Φ_2 both have hypercharge 1 and all parameters are real-valued. Minimizing the potential gives the vacuum expectation values:

$$\langle\Phi_1\rangle = \frac{1}{\sqrt{2}}\begin{pmatrix}0\\v_1\end{pmatrix}, \quad \langle\Phi_2\rangle = \frac{1}{\sqrt{2}}\begin{pmatrix}0\\v_2\end{pmatrix}. \tag{2.2}$$

Excitations around these minima can be parametrized as:

$$\Phi_1 = \begin{pmatrix}\phi_1^+\\(v_1+\rho_1+i\eta_1)/\sqrt{2}\end{pmatrix}, \quad \Phi_2 = \begin{pmatrix}\phi_2^+\\(v_2+\rho_2+i\eta_2)/\sqrt{2}\end{pmatrix}, \tag{2.3}$$

---

[1] There are unfortunately some notational inconsistencies in the literature, with "Type III" and "Type IV" having been used to refer to the lepton-specific and flipped models, which are sometimes also called "Type X" and "Type Y", respectively. Here, we use what appears to be the most common names.

consisting of scalar (ρ), charged scalar (ϕ^+) and pseudoscalar (η) components. Mass terms are then given by:

$$\begin{aligned}\mathscr{L}_{\phi\,mass} = & \left[m_{12}^2 - (\lambda_4 + \lambda_5)v_1 v_2\right] (\phi_1^-, \phi_2^-) \begin{pmatrix} \frac{v_2}{v_1} & -1 \\ -1 & \frac{v_1}{v_2} \end{pmatrix} \begin{pmatrix} \phi_1^+ \\ \phi_2^+ \end{pmatrix} \\ & + \left[m_{12}^2/(v_1 v_2) - 2\lambda_5\right] (\eta_1, \eta_2) \begin{pmatrix} v_2^2 & -v_1 v_2 \\ -v_1 v_2 & v_1^2 \end{pmatrix} \begin{pmatrix} \eta_1 \\ \eta_2 \end{pmatrix} \\ & - (\rho_1, \rho_2) \begin{pmatrix} m_{12}^2 \frac{v_2}{v_1} + \lambda_1 v_1^2 & \lambda_{345} v_1 v_2 - m_{12}^2 \\ \lambda_{345} v_1 v_2 - m_{12}^2 & m_{12}^2 \frac{v_1}{v_2} + \lambda_1 v_2^2 \end{pmatrix} \begin{pmatrix} \rho_1 \\ \rho_2 \end{pmatrix},\end{aligned} \tag{2.4}$$

with $\lambda_{345} = \lambda_3 + \lambda_4 + \lambda_5$. The structure of the potential mixes the different fields – to obtain physical states with definite masses, the matrices in equation (2.4) must be diagonalized. The parameter α is defined to be the rotation angle that performs the diagonalization of the mass-squared matrix of the scalars. The parameter β is defined to be the rotation angle that diagonalizes the mass-squared matrices of the charged scalars and of the pseudoscalars. These diagonalizations produce the following linear combinations of the fields:

$$\begin{array}{llll} h = & \rho_1 \sin\alpha - \rho_2 \cos\alpha, & H^+ = & -\phi_1^+ \sin\beta + \phi_2^+ \cos\beta, \\ H = & -\rho_1 \cos\alpha - \rho_2 \sin\alpha, & H^- = & -\phi_1^- \sin\beta + \phi_2^- \cos\beta, \\ A = & \eta_1 \sin\beta - \eta_2 \cos\beta, & G^+ = & \phi_1^+ \cos\beta + \phi_2^+ \sin\beta, \\ G^0 = & \eta_1 \cos\beta + \eta_2 \sin\beta, & G^- = & \phi_1^- \cos\beta + \phi_2^- \sin\beta. \end{array} \tag{2.5}$$

The matrices connecting the charged scalars and the pseudoscalars each have a zero eigenvalue. These correspond to the massless charged and pseudoscalar Goldstone bosons G^0 and $G^\pm$. In a process of electroweak symmetry breaking analogous to the one described in section 1.2, they become the longitudinal components of the W and Z bosons. In contrast to the Standard Model, however, no less than five massive Higgs bosons now remain in the physical spectrum. H and h are both neutral scalars, the former defined to be the heavier of the two. The combination $h\sin(\alpha-\beta) - H\cos(\alpha-\beta)$ has couplings identical to the Standard Model Higgs boson. The so-called *alignment limit* $\cos(\beta-\alpha) = 0$ is therefore a special case in which h behaves according to the Standard Model prediction. There is also a pseudoscalar Higgs boson A, and two charged Higgs bosons $H^\pm$. The scalars and pseudoscalars are only well-defined if the potential indeed conserves CP (which requires v_1 and v_2 to be real-valued), but the charged Higgs bosons are a general feature of any 2HDM. Note also that diagonalization of the matrices in equation (2.4) implies that:

$$\tan\beta = \frac{v_2}{v_1}. \tag{2.6}$$

The Higgs boson masses and the mixing angles can be taken as six free parameters of the model, together with the m_{12} parameter. The vacuum expectation values are then fixed by the relation $v_1^2 + v_2^2 = v^2$, where v is the Standard Model predicted value, and by the choice of $\tan\beta$.

2.2 Supersymmetry

Standard Model processes are symmetric under the following ten space-time transformations: translations, rotations and Lorentz boosts in any of the three spatial dimensions, and translation through time. In addition to these space-time symmetries, which constitute the *Poincaré group*, the Standard Model also exhibits the *internal symmetries* of weak hypercharge, weak isospin, and color transformations that give rise to the interactions discussed in chapter 1. Since symmetry principles have been so important for the successful construction of the Standard Model, and indeed in physics in general, it would be prudent to ask whether a more complete theory could include any type of symmetry other than the internal symmetries and the Poincaré group. It turns out that there is only one other possibility: symmetry under transformations that change particle spin, i.e. turning bosons into fermions and vice versa [14]. Such a symmetry is called a Supersymmetry (SUSY), and the new particles created by SUSY transformations of the Standard Model particles are called their superpartners.

SUSY is attractive not only for being the single non-internal symmetry not yet observed in nature, it also offers elegant remedies to several of the previously discussed shortcomings of the Standard Model. It could directly eliminate the hierarchy problem: as loops with bosons and fermions have opposite signs, any Standard Model loop contributions to the Higgs boson mass could be directly canceled by the superpartners. And if couplings that change baryon number and lepton number are forbidden – so-called R-parity conservation – then the Lightest Supersymmetric Particle (LSP) can not decay and would therefore be a dark matter candidate. Grand unification is also achievable with SUSY. For these reasons, SUSY models are among the theoretically most studied extensions to the Standard Model.

An obvious problem immediate presents itself, however, in the fact that the superpartners are supposed to have the same properties as the corresponding Standard Model particles (including mass) except for spin – and no such particles have been observed. If SUSY is realized in nature, it must therefore be a broken symmetry. The superpartners of the Standard Model particles could then, in general, have any mass. A viable solution to the hierarchy problem and the observationally favored mass of the LSP both mandate, however, that they should start showing up around the TeV scale – i.e. at energies accessible at the LHC.

2.2.1 The Minimal Supersymmetric Standard Model

The Minimal Supersymmetric Standard Model (MSSM) embeds the Standard Model in an R-parity conserving, softly broken, supersymmetric theory with a minimum number of new fields. For each chiral state of the Standard Model fermions, the MSSM adds a spin-0 *sfermion*; namely the *squarks* $\tilde{q}_{L,R}$, *sleptons* $\tilde{\ell}_{L,R}$, and *sneutrinos* $\tilde{\nu}$. The left- and right-handed sfermions of each type interact with each other with a strength proportional to the mass of the corresponding fermion. This may cause the superpartners of the heaviest fermions (the *stops*, the *sbottoms* and the *staus*) to mix into new mass states. For each Standard Model gauge boson, the MSSM adds a corresponding spin-$\frac{1}{2}$ *gaugino*: the *Bino* $\tilde{B}$, three *Winos* $\tilde{W}$, and eight *gluinos* $\tilde{g}$. For each Higgs field, there is a corresponding spin-$\frac{1}{2}$ *Higgsino* $\tilde{H}$. SUSY actually requires that there are at least two Higgs fields, for two reasons. First, the charge conjugation operator employed to give mass to the up-type quarks in equation (1.12) is not allowed in a supersymmetric Lagrangian, which must be analytic. A separate Higgs field is therefore needed to give mass to the up-type quarks in a SUSY theory. Second, renormalizability requires [15, 16] the sum of fermionic hypercharges to be zero. There must therefore be an even number of Higgs fields, so that there can be an even number of Higgsinos with opposite hypercharges to make this possible. As the MSSM is the minimal supersymmetric extension to the Standard Model, it is constructed with exactly two Higgs fields, one of which couples only to the up-type quarks. The MSSM is therefore a Type II 2HDM[2]. As such it has the five massive Higgs bosons discussed in the previous session, and four Higgsinos corresponding to the charged and neutral components of the two Higgs fields. The Higgsinos mix with the Bino and Winos, creating four *charginos* $\tilde{\chi}^{\pm}_{1,2}$ and four *neutralinos* $\tilde{\chi}_{1,2,3,4}$. A neutralino is the most likely LSP candidate.

2.2.2 The MSSM Higgs sector

Although the MSSM introduces the minimum number of new particles, there is a large freedom of choice as to the exact mechanism of supersymmetry breaking[3] and, in total, the MSSM introduces no less than 105 free parameters. In the Higgs sector, however, certain relations that are not present in the generic Type II 2HDM offer considerable simplifications. At tree-level, the

---

[2] This is true at tree-level. When radiative corrections are taken into account, the MSSM effectively becomes a Type III 2HDM. The approximate Type II behavior of the MSSM is assumed throughout this thesis.

[3] The breaking of local supersymmetry also produces a new massless particle, which in this case is a fermion: the *Goldstino*. It can be pointed out that for a complete theory, the hypothetical mediator of gravity, the graviton, should also be included. Its superpartner, the *gravitino*, mixes with the Goldstino and becomes massive.

Higgs and vector boson masses can now be related via:

$$m_{H,h}^2 = \frac{1}{2}\left[m_A^2 + m_Z^2 \pm \sqrt{(m_A^2 + m_Z^2)^2 - 4m_A^2 m_Z^2 \cos^2 2\beta}\right] \tag{2.7}$$

$$m_{H^\pm}^2 = m_A^2 + m_W^2 \tag{2.8}$$

The inadequacy of the tree-level prediction is immediately apparent, however, as it requires $m_h < m_Z$, which is not compatible with experimental results. But with higher order corrections taken into account, in particular from stop loops, the mass of h can become much larger. With stop masses at the TeV scale as indicated above, h can be compatible with the experimentally observed Higgs boson. Another important constraint is the following relation between the mixing angles of the charged and neutral scalars:

$$\tan 2\alpha = \frac{m_A^2 + m_Z^2}{m_A^2 - m_Z^2} \tan 2\beta. \tag{2.9}$$

Given equations (2.7)–(2.9), the Higgs sector of the MSSM can at tree-level be fully specified by just two parameters. In the context of charged Higgs boson searches, the free parameters can be conveniently chosen to be the charged Higgs boson mass $m_{H^\pm}$ and $\tan\beta$ (which gives its couplings). Furthermore, a number of benchmark scenarios have been defined that keep the low number of parameters even when taking higher order corrections into account. The m_h^{max} scenario [17, 18] is constructed to yield the highest possible h mass for a given $\tan\beta$. Searches for CP-even neutral Higgs bosons therefore give conservative exclusion limits on $\tan\beta$. Due to the ubiquity of search interpretations in m_h^{max}, it is still commonly used (also in charged Higgs boson searches). Now that a Higgs boson has been discovered, however, new benchmark scenarios have been proposed. These include the so-called $m_h^{\text{mod}-}$ and $m_h^{\text{mod}+}$ scenarios[4], in which h can be interpreted as the LHC signal in a large part of the parameter space [19].

2.3 The charged Higgs boson

A key feature of all 2HDMs, including the MSSM, is the existence of charged scalars that are the orthogonal states to the longitudinal components of the $W^\pm$ bosons. The couplings of the charged Higgs bosons to vector bosons in any CP-conserving 2HDM are summarized in Table 2.2. Couplings of the form HH^+H^- and hH^+H^- are also allowed but are model-dependent. The

---

[4] The difference between $m_h^{\text{mod}-}$ and $m_h^{\text{mod}+}$ is the sign of the quantity X_t/M_{SUSY}, where X_t is a parameter that controls the amount of mixing between the stops and M_{SUSY} is the overall SUSY mass scale. In both cases, the absolute value of this quantity is lowered with respect to the m_h^{max} scenario. This reduces the contributions from stop loops and therefore gives a lower Higgs boson mass for a given $\tan\beta$.

Table 2.2. *The couplings of the charged Higgs bosons to vector bosons.*

Couplings	Allowed?
ZH^+H^- $\quad$ γH^+H^-	yes
$ZH^\pm W^\mp$ $\quad$ $\gamma H^\pm W^\mp$	no
$H^\pm W^\mp h$ $\quad$ $H^\pm W^\mp Zh$ $\quad$ $H^\pm W^\mp \gamma h$	proportional to $\cos(\beta-\alpha)$
$H^\pm W^\mp H$ $\quad$ $H^\pm W^\mp ZH$ $\quad$ $H^\pm W^\mp \gamma H$	proportional to $\sin(\beta-\alpha)$
$H^\pm W^\mp A$ $\quad$ $H^\pm W^\mp ZA$ $\quad$ $H^\pm W^\mp \gamma A$	yes

Table 2.3. *The couplings of the charged Higgs bosons to fermions. P_L and P_R are projection operators for left- and right-handed fermions, u and d are any up-type and down-type quarks and V_{ud} is the strength of their CKM mixing.*

Model	$H^+\bar{u}d$	$H^+\ell_R\bar{\nu}_\ell$
Type I	$V_{ud}\,(m_u\cot\beta P_L + m_d\cot\beta P_R)$	$m_\ell\cot\beta$
Type II	$V_{ud}\,(m_u\cot\beta P_L + m_d\tan\beta P_R)$	$m_\ell\tan\beta$
Lepton-specific	$V_{ud}\,(m_u\cot\beta P_L + m_d\cot\beta P_R)$	$m_\ell\tan\beta$
Flipped	$V_{ud}\,(m_u\cot\beta P_L + m_d\tan\beta P_R)$	$m_\ell\cot\beta$

couplings to fermions depend differently on α and β in the different types of 2HDMs and are summarized in Table 2.3. In a Type I 2HDM, all couplings to fermions are suppressed if $\tan\beta \gg 1$, yielding a "fermiophobic" charged Higgs boson. Conversely, the charged Higgs boson in a lepton-specific model is "quarkphobic" in this case. In the Type II and flipped models, charged Higgs boson couplings to quarks are maximized for intermediate values of $\tan\beta$, with lepton couplings increasing respectively decreasing with larger $\tan\beta$. For a detailed discussion, see e.g. Ref. [11]. A comprehensive review of Higgs bosons in the MSSM in particular can be found in Ref. [20]. In the MSSM, the charged Higgs boson can also decay to SUSY particles, which is not considered here. We now proceed to summarize some important H^+ phenomenology, focusing on the Type II 2HDM which is the most widely studied model.

2.3.1 Decay modes

Figure 2.1 shows the branching fractions for charged Higgs boson decays into Standard Model particles, for $\tan\beta = 10$ and $\tan\beta = 50$ in the three MSSM benchmark scenarios introduced in the previous section [21]. The decays of the charged Higgs boson to SUSY particles (charginos and neutralinos) were taken into account in the calculation of these branching fractions but are not shown in the plots. Their effects are visible at the kinks in the lines of the other channels, in particular for $\tan\beta = 10$.

The charged Higgs boson decays predominantly via $H^+ \to tb$ when this is kinematically allowed. Note that, as indicated in Table 2.3, the decays to quarks are suppressed according to the CKM mixing of the daughters. Decays into quarks of different generations are therefore disfavored and the dominant mode when tb is kinematically forbidden is not cb, but $\tau\nu$. The preferred decay mode into light quarks is instead cs. For the leptonic decay modes, the relative branching fractions are directly proportional to the mass-squared of the charged lepton. Decays into $\mu\nu$ are therefore suppressed by a factor 1000 with respect to the $\tau\nu$ mode (and $e\nu$ is suppressed by over a million). Depending on $\tan\beta$, the branching fraction into $\tau\nu$ can still be sizable for higher masses. Decays into SUSY particles can also compete with tb when they become kinematically allowed.

2.3.2 Production at colliders

In e^+e^- collisions, charged Higgs bosons could be produced through a Drell-Yan process $e^+e^- \to Z/\gamma^* \to H^+H^-$. The LEP collaborations searched for H^+ decays to cs, $\tau\nu$, and WA. A combination of the search channels excludes charged Higgs bosons with a mass below 80 GeV for Type II 2HDMs and 72.5 GeV for Type I 2HDMs [22]. At hadron colliders, it is convenient to distinguish between searches for *light* charged Higgs bosons ($m_{H^+} \lesssim m_t$), and *heavy* charged Higgs bosons ($m_{H^+} \gtrsim m_t$).

Light charged Higgs boson production at hadron colliders

Light charged Higgs bosons would be readily produced in the decays of top quarks via $t \to bH^+$. Top quarks are abundantly produced at both the Tevatron and at the LHC in the form of $t\bar{t}$ pairs. Charged Higgs boson production can thus proceed at tree-level as shown in Figure 2.2. D0 has set an upper limit on $\mathscr{B}(t \to bH^+)$ around 0.2 assuming $\mathscr{B}(H^+ \to \tau\nu) + \mathscr{B}(H^+ \to cs) = 1$, with a somewhat stronger limit if instead $\mathscr{B}(H^+ \to \tau\nu) = 1$, while CDF excluded $\mathscr{B}(t \to bH^+)$ above 0.1 if $\mathscr{B}(H^+ \to cs) = 1$ [23, 24].

Figure 2.3 shows the cross section for $pp \to t\bar{t} \to b\bar{b}W^{\mp}H^{\pm}$ at 7 TeV in the m_h^{max} scenario, and its dependence on m_{H^+} and $\tan\beta$ [25]. At the LHC, no combined search has yet been performed, but the limits from the Tevatron on individual H^+ branching fractions have been significantly improved, as will be shown in section 3.2.2.

Heavy charged Higgs boson production at hadron colliders

With the full 8 TeV LHC dataset available, focus has shifted towards searches for heavy charged Higgs bosons. If $m_{H^+} > m_t$, any Standard Model particle mediating the H^+ production is necessarily off-shell. The main production mode of a heavy charged Higgs boson is then in association with a top quark: $pp \to tH^+(b)$. There are two ways of calculating this process. In a Five-Flavor

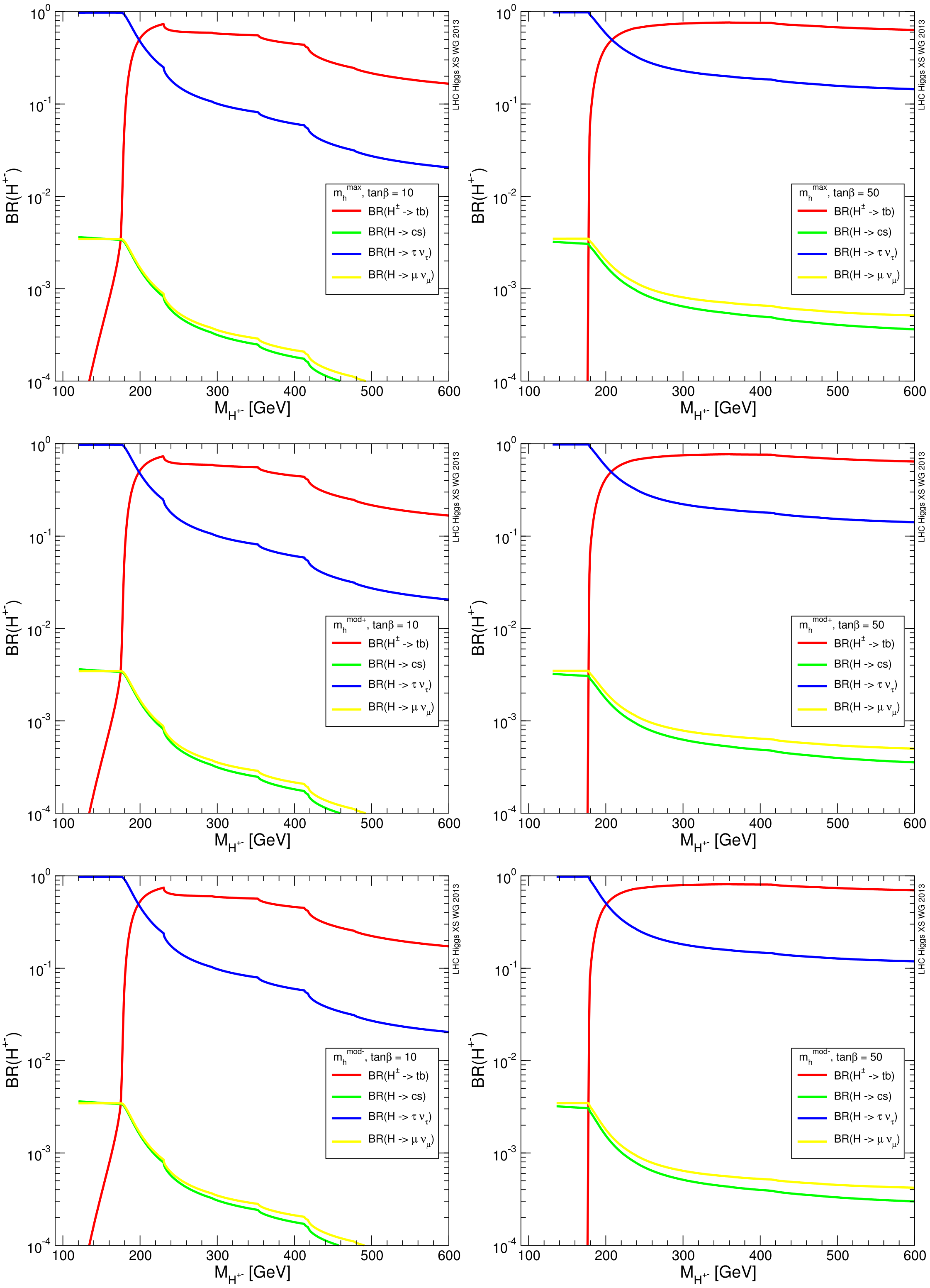

Figure 2.1. Branching fractions of the charged Higgs boson in the MSSM m_h^{max} (top row), $m_h^{\text{mod}+}$ (middle row), and $m_h^{\text{mod}-}$ (bottom row) scenarios with $\tan\beta = 10$ (left column) and $\tan\beta = 50$ (right column) [21].

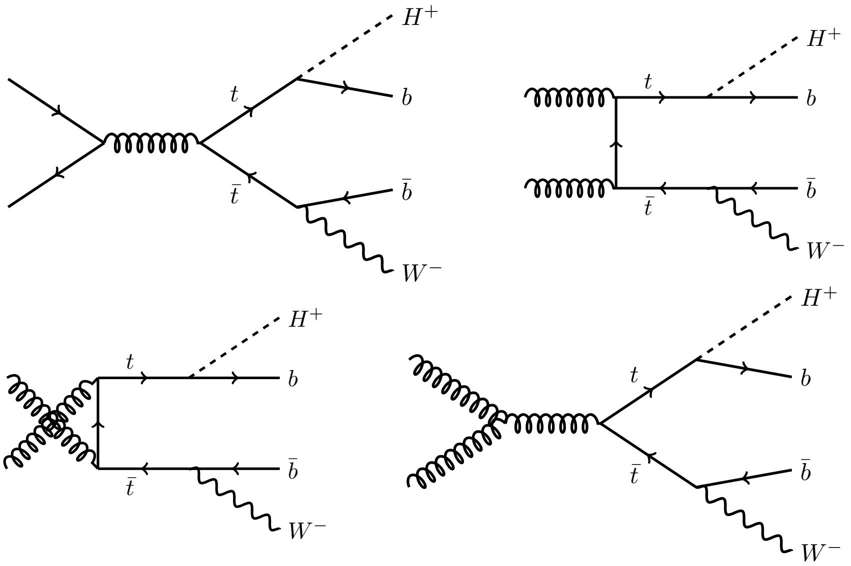

Figure 2.2. Light charged Higgs boson production in the decay of top quarks. Top quark pair production proceeds mainly via $q\bar{q}$ fusion at the Tevatron and gluon-gluon fusion at the LHC.

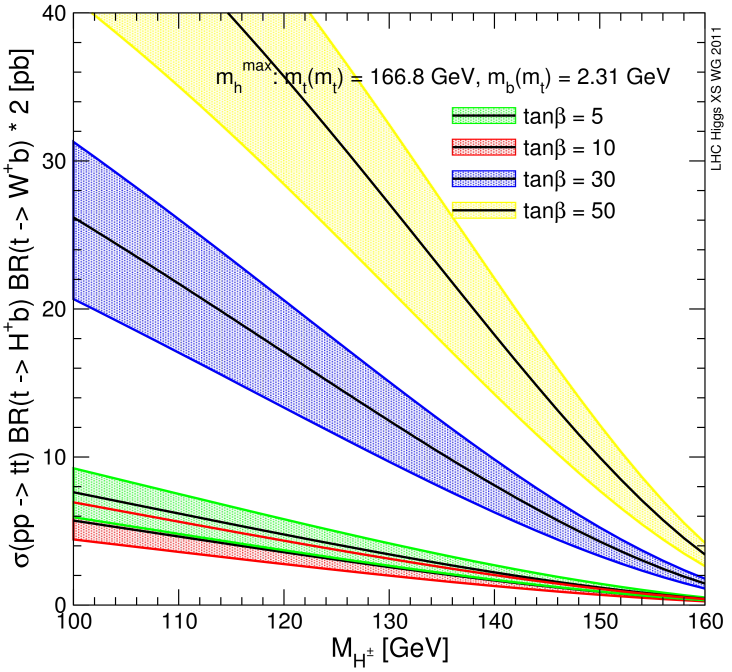

Figure 2.3. Cross section for the process $pp \to t\bar{t} \to b\bar{b}W^{\mp}H^{\pm}$ at 7 TeV in the m_h^{max} scenario, including scale and PDF uncertainties, as well as uncertainties due to missing electroweak, QCD, and SUSY corrections [25]. Note that both H^+ and H^- production is taken into account.

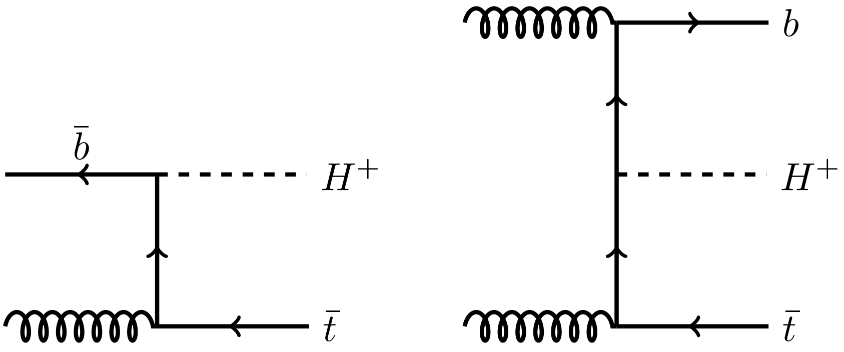

Figure 2.4. Tree-level diagrams for the production of a heavy charged Higgs boson in the 5FS (left) and 4FS (right).

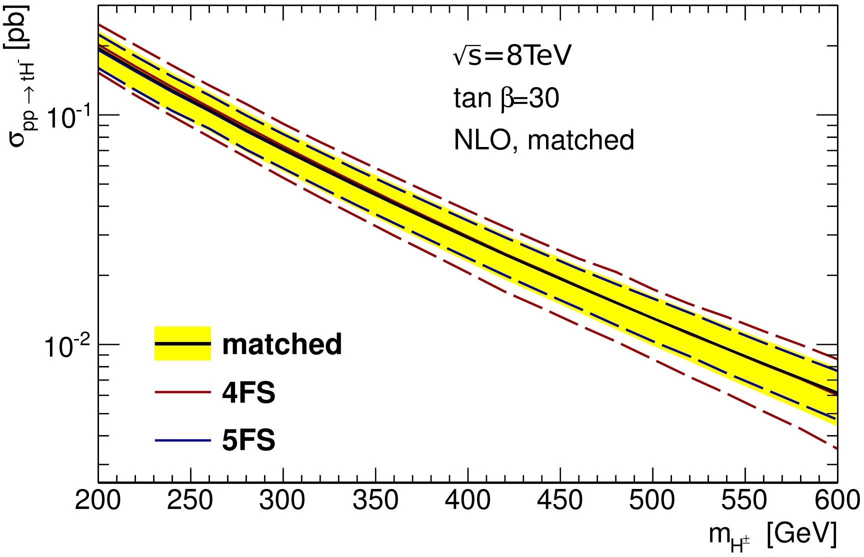

Figure 2.5. Cross section for the process $pp \to tH^{\pm} + X$ at 8 TeV in a Type II 2HDM, with Santander matching [27].

Scheme (5FS) calculation, the b quark is considered massless and is treated as a constituent of the proton. It may therefore appear in the initial state, and charged Higgs boson production can proceed via $gb \to tH^+$. If the process takes place at such an energy scale that the b quark mass can not be ignored, a Four-Flavor Scheme (4FS) should be used, in which there are only four massless quarks in the proton and the b quark must itself be produced in the hard process: $gg \to tH^+b$. This treatment gives a better description of the kinematics and is needed if the b quark receives a large p_T, but is computationally more challenging due to the higher particle multiplicity. A 5FS calculation is also less convergent in a perturbation series due to potentially large logarithms involving the ratio of the hard scale and the b quark mass appearing in the splitting of gluons into collinear bb pairs, which are not summed to all orders. The 4FS and 5FS tree-level processes are shown in Figure 2.4. It must be stressed that they are not independent, but are different approximations of the same underlying process, valid in the limits $m_{H^\pm}/m_b \to 1$ and $m_{H^\pm}/m_b \to \infty$, respectively. In the intermediate region, so-called Santander matching [26] can be used to interpolate between the 4FS and 5FS predictions. Figure 2.5 shows the 4FS, 5FS, and matched cross sections at 8 TeV in a Type II 2HDM [27].

At the Tevatron, the D0 experiment performed a search for a heavy charged Higgs boson with a mass in the range 180–300 GeV and decaying to tb, but with limited sensitivity to a Type II 2HDM [28].

2.3.3 Effects on B-physics observables

Decays of B-mesons are sensitive to the presence of charged Higgs bosons. A succinct review of the experimental situation is given in Ref. [29]. An important example is the decay $b \to s\gamma$ shown in Figure 2.6, for which the contribution of additional diagrams involving a charged Higgs boson may significantly enhance the branching fraction. Measurements of the decays of the $\bar{B}$-meson, with the quark content $\bar{d}b$, excludes charged Higgs bosons with a mass below 360 GeV in a Type II 2HDM [30].

Tauonic decay modes of B-mesons, as illustrated in Figure 2.7, can be another strong test for the presence of charged Higgs bosons thanks to the high mass of the tau lepton. BABAR has measured the ratios

$$\mathscr{R}(D) = \frac{\mathscr{B}(B \to D\tau\nu)}{\mathscr{B}(B \to D\ell\nu)} = 0.440 \pm 0.058(\mathrm{stat}) \pm 0.042(\mathrm{syst}), \tag{2.10}$$

$$\mathscr{R}(D^*) = \frac{\mathscr{B}(B \to D^*\tau\nu)}{\mathscr{B}(B \to D^*\ell\nu)} = 0.332 \pm 0.024(\mathrm{stat}) \pm 0.018(\mathrm{syst}), \tag{2.11}$$

where ℓ is either an electron or a muon [31]. These results have a combined deviation of 3.4σ from the Standard Model values of

$$\mathscr{R}_{SM}(D) = 0.297 \pm 0.017, \qquad \mathscr{R}_{SM}(D^*) = 0.252 \pm 0.003. \tag{2.12}$$

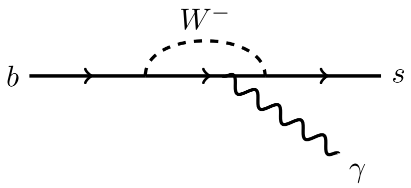

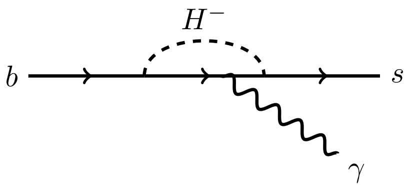

Figure 2.6. Examples of contributions to the $b \to s\gamma$ decay from a W boson (left) and a charged Higgs boson (right).

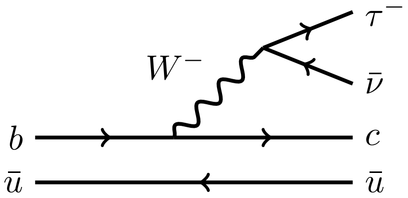

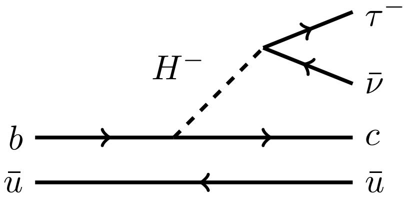

Figure 2.7. $B \to D^{(*)}\tau\nu$ decay, mediated by a W boson (left) or a charged Higgs boson (right).

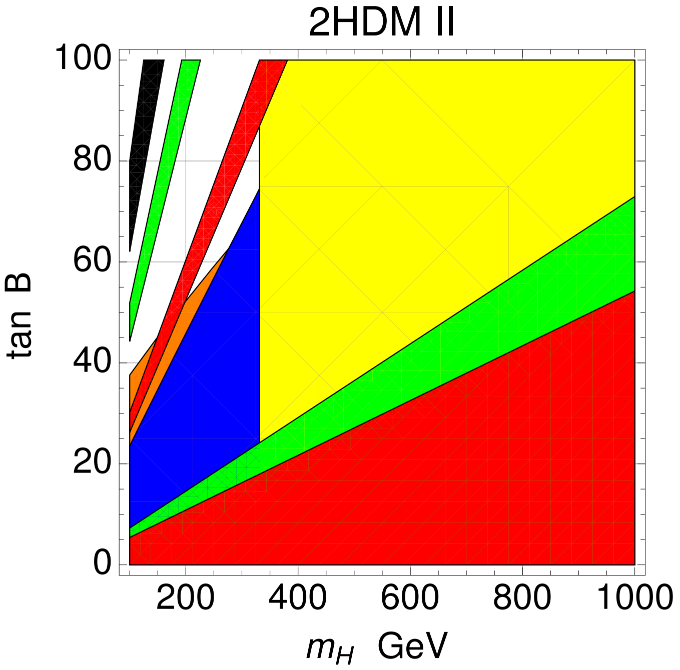

Figure 2.8. Allowed regions (superimposed) in the $\tan\beta$, $m_H = m_A = m_{H^\pm}$ parameter space of the Type II 2HDM, using constraints from $b \to s\gamma$ (yellow), $B \to D\tau\nu$ (green), $B \to \tau\nu$ (red), $B_s \to \mu^+\mu^-$ (orange), $K \to \mu\nu/\pi \to \mu\nu$ (blue) and $B \to D^*\tau\nu$ (black). The regions shown include theoretical uncertainties added linearly to the 2σ experimental errors [33].

This evidence for new physics is also supported by a 1.6σ deviation of the branching fraction $\mathscr{B}(B \rightarrow \tau\nu)$ [32]. Figure 2.8 shows the impact of a number of flavor-physics results on the Type II 2HDM. The measurement of $\mathscr{R}(D^{(*)})$ is incompatible with the constraints from all other measurements and can therefore not be explained within this model [33]. This conclusion holds also for the MSSM. However, a generic Type III model could possibly accommodate all constraints.

Part II: Experiment

3. The Large Hadron Collider

The Large Hadron Collider (LHC) [34], built and operated by the European Organization for Nuclear Research (CERN), is the world's largest and most powerful particle collider. It is designed to accelerate two beams of up to 2808 bunches of 1.15×10^{11} protons with a 25 ns separation and to deliver collisions with a center-of-mass energy of up to 14 TeV at a target luminosity of 10^{34} $\text{cm}^{-2}\text{s}^{-1}$. The analyses presented in this thesis use data collected during 2011 and 2012, when the LHC operated with several key parameters below their design values and delivered proton-proton collisions with center-of-mass energies of 7 TeV, respectively 8 TeV. These datasets nevertheless present an opportunity to study physics processes at energies never probed before in a laboratory setting. In addition to proton-proton collisions, the LHC also performs heavy ion collisions, which are not discussed in this thesis.

The high bunch intensity required to meet the target luminosity excluded the use of an anti-proton beam for the LHC. Counter-rotating beams of same-charge particles, however, require two separate magnet systems. Due to the limited space in the LHC tunnel, which previously housed the Large Electron-Positron Collider (LEP), the machine uses a design with two sets of superconducting magnets and beamlines sharing the same cryostat. The magnets are based on niobium-titanium coils, cooled to 1.9 K using superfluid helium and generating magnetic fields of up to 8.3 T. Over 1600 main magnets are used to control the beams. Although a hadron accelerator does not suffer prohibitively large energy losses from synchrotron radiation and could ideally be made nearly circular, the LHC follows the layout of the LEP tunnel with eight straight sections and eight arcs for a total circumference close to 27 km.

The LHC is linked to the rest of the accelerator complex at CERN, which provides it with 450 GeV protons. After their injection into the LHC, particles are accelerated using 400 MHz superconducting cavities located in one of the eight straight sections. Two other straight sections contain sets of beam cleaning collimators and a fourth is dedicated to the dumping system used to safely extract the beams at the end of a run. The remaining four straight sections each have an interaction point where the beams cross. This is where the main LHC experiments are placed. These are the general-purpose experiments ATLAS (which will be described in chapter 4) and CMS, and two more specialized experiments: LHCb with the purpose to study B-physics, and the dedicated heavy ion experiment ALICE. In LHCb and ALICE, the beams cross with reduced overlap, as the experiments are designed for lower luminosities, while ATLAS and CMS make full use of the maximum possible luminosity provided by the LHC.

The LHC computing grid

The LHC experiments produce data at a truly massive scale – in total about 30 petabytes per year. The Worldwide LHC Computing Grid (WLCG) connects more than 170 computing centers in 40 countries to provide the resources needed for storing and analyzing the LHC data. A tiered architecture is used by the WLCG: Tier 0, at CERN, safe-keeps a first copy of the raw data and performs a first-pass reconstruction. Thirteen large Tier 1 centers with sufficient storage capacity perform reprocessing of the data and also provide storage of raw, reconstructed, and simulated data. Around 160 Tier 2 sites located in universities and other scientific institutes provide additional storage, produce simulated events, and run end-user analysis jobs.

3.1 Experimental challenges

Detectors at hadron colliders face challenges that are not present, or much less severe, at e.g. an e^+e^- collider. The unprecedented collision energies and luminosity provided by the LHC also come at a cost to the experiments.

Hadrons are composite objects and energies such as those provided by the LHC are enough to resolve their internal structure, i.e. collisions can be seen as taking place between individual partons (quarks and gluons). Each parton carries an unknown fraction of the total hadron momentum. The 7, 8 or 14 TeV center-of-mass energies mentioned throughout this thesis should therefore be seen as upper bounds on the energy available in a collision, while the actual center-of-mass energy in an individual interaction between two partons is unknown and varying from event to event. In particular, the longitudinal momentum is unknown, while the initial transverse momentum can be neglected. When analyzing hadron collisions, one is therefore mainly concerned with transverse variables. Accurate simulations of proton-proton collisions require the use of experimentally determined Parton Distribution Functions (PDFs), which give the probability for a certain type of parton to have a certain fraction of the longitudinal momentum of the proton.

Physics processes in hadron collisions tend to be dominated by the strong interaction, which mostly produces hadronic jets. Very high luminosities are therefore needed in order to collect a sizable amount of “interesting” events involving more elusive electroweak processes, Higgs boson production, or new physics. Hadron collisions also tend to produce events with high particle multiplicities. This not only makes the reconstruction process more complex, but high collision rates and large event sizes also make it implausible to read out and record the detector data in every event. High-luminosity experiments therefore need a *trigger* system to make real-time decisions of which events to save. Furthermore, detectors need to be designed to cope with a high-radiation environment.

The instantaneous luminosity increases quadratically with the number of protons in each bunch and with the inverse of the bunch diameter, but only linearly with the number of bunches. At some point, the luminosity is therefore most efficiently increased by having as tightly squeezed bunches and as many protons per bunch as possible. This corresponds to increasing the mean number of individual proton-proton collisions taking place in every bunch crossing. As the LHC experiments mainly search for very rare processes, at most one of the collisions in each bunch crossing, called the *primary interaction*, is likely to be of interest. The other collisions are referred to as *pile-up* and bring a number of problems. The interaction region has a longitudinal extension of a few centimeters and it is typically possible to associate tracks, and often even photons and jets, with individual collision points. However, the increased ambient activity in the calorimeters makes it more challenging to determine the correct *jet energy scale* and also affects the measurement of missing transverse energy (see section 5.2.6). More particles in each event also means more data to read out, process and store.

Considerations for charged Higgs boson searches
Charged Higgs bosons can be produced at the LHC in the decays of top quarks, in particular in $t\bar{t}$ pairs, or in association with top quarks. They may subsequently decay predominantly into $\tau\nu$ or tb. The Standard Model decay of the top quark occurs almost exclusively via Wb. Events involving charged Higgs bosons would therefore have high jet multiplicities and require good jet reconstruction. Furthermore, the tagging of b-jets and hadronic tau decays require good tracking in the inner detector volume. The very large background of multi-jet events can be reduced by selecting events in which a top quark decays leptonically, i.e. with an electron or a muon in the final state. The lepton can also be used for triggering, which is more straightforward than triggering on jets. This is the strategy followed in the analyses presented in this thesis. Electron reconstruction can be performed with a combination of tracking and calorimeter information, while muon reconstruction requires a dedicated tracking system since muons are not absorbed in calorimeters and an inner tracking system is typically not sufficient. To detect the presence of neutrinos produced in association with electrons, muons, or tau leptons, a good reconstruction of missing transverse energy is also required.

3.2 Run 1 summary

The first long near-continuous run of the LHC spanned over three years and resulted in several major scientific achievements, including the discovery of the Higgs boson, observations of the $\Xi_b'^-$ and Ξ_b^{*-} resonances and of the rare $B_s^0 \to \mu^+\mu^-$ decay, new measurements of Standard Model processes, and many searches for new physics.

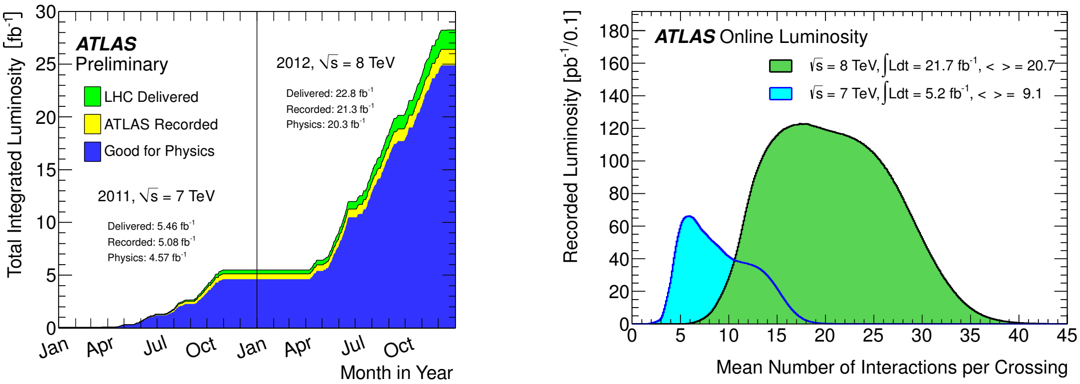

Figure 3.1. Cumulative luminosity versus time (left) and mean number of interactions per bunch crossing (right) delivered to ATLAS during proton-proton collision data-taking at 7 and 8 TeV center-of-mass energies in 2011 and 2012 [35]. Also shown in the left plot are the fractions recorded (reflecting inefficiencies in the data acquisition and the “warm start” of the detector after stable beams have been established) and certified to be of good quality (meaning that all sub-detectors were fully operational).

Collisions between 3.5 TeV proton beams first took place in March 2010, with much of the rest of that year dedicated to commissioning, reducing β^* and slowly increasing the number of protons in each beam[1]. The year 2010 ended with beams of a few hundred proton bunches with 150 ns separation, each bunch consisting of 1.2×10^{11} protons – already slightly more than the design value. A total integrated luminosity of 40 pb^{-1} was well received by ATLAS and CMS, but was soon superseded by the much larger datasets collected over the following two years.

Figure 3.1 shows the integrated luminosity delivered to ATLAS in 2011 and 2012. These are the datasets analyzed in this thesis. The beam energy remained at 3.5 TeV in 2011, while the effort to increase the luminosity continued with a switch to a 50 ns bunch spacing. The number of bunches was then methodically increased up to the maximum of 1380 for this separation. This was followed by reduced emittances[2] and β^* of the beams, as well as a somewhat increased bunch intensity. By the end of the year, ATLAS and CMS had each received around 5.6 fb^{-1} of proton-proton collisions. In 2012, the beam energy was increased to 4 TeV. After β^* was further reduced to 0.6 m – close to its design value of 0.55 m – and with 200 days dedicated to proton-proton physics, about 23 fb^{-1} of data was delivered to ATLAS and CMS.

Overall, a high operational efficiency of this new accelerator was quickly established, with more than a third of the time being spent with stable beams and integrated luminosities of 1 fb^{-1} per week routinely delivered in 2012.

---

[1] β^* is the value of the *beta function* of the beams at the interaction point. The transverse beam size is equal to $\sqrt{\varepsilon\beta^*}$ where ε is the *emittance*, a measure of the spread of transverse particle coordinates in the position-and-momentum phase space.

[2] See footnote 1.

The use of the 50 ns bunch spacing, as compared to the design value of 25 ns, was somewhat compensated for by the higher bunch intensity and lower than expected emittance. This made it possible to eventually reach an instantaneous luminosity of 7.7×10^{33} cm^{-2}s^{-1}, close to the target of 1×10^{34} cm^{-2}s^{-1}. The cost to the experiments was the high pile-up (as shown in Figure 3.1) with the mean number of interactions per bunch crossing eventually reaching 37, almost twice the design value.

In addition to the proton physics program, the LHC also produced lead-lead collisions with an energy of 2.76 TeV per nucleon, with a total of 177 μb^{-1} accumulated in 2010 and 2011. Before the start of the first Long Shutdown (LS1) in early 2013, the LHC also successfully delivered proton-lead collisions.

During LS1 (2013–2015), the collider is being prepared for higher energies and luminosities. Upgrades and consolidation works are also undertaken by the experiments, and in the earlier stages of the CERN chain of accelerators.

3.2.1 Discovery of the Higgs boson

The most important result of the LHC Run 1 is the discovery of a Higgs boson [36, 37], achieved independently by the ATLAS and CMS collaborations. The most important channels to study the Standard Model-like Higgs boson are its decay to two photons or two Z bosons that subsequently decay to electrons and/or muons. Both channels offer the possibility to precisely measure all final state particles and to reconstruct the Higgs boson mass with good resolution. As the Higgs boson only couples to massive particles, its decay to two photons proceeds at lowest order via a heavy fermion or boson loop. This decay mode is therefore suppressed due to the additional vertex but is enhanced due to the strong Yukawa coupling between the Higgs boson and the top quark, which is the most important loop contribution. Other important Higgs decay channels at the LHC are $H \to WW \to l\nu l\nu$ (which has a large branching fraction but poor mass resolution due to the presence of neutrinos) and $H \to \tau\tau$. The latter channel offers, despite its lower resolution and large backgrounds, the best direct measurement of Higgs couplings to fermions. The decay into a pair of bottom quarks has the largest branching fraction of all decay modes for a Higgs boson mass below 135 GeV and is also analyzed, but is very difficult to isolate at a hadron collider due to the jet-rich background. Only production modes in association with a vector boson or a $t\bar{t}$ pair are therefore considered.

The mass of the Higgs boson is measured by combining the two high-resolution channels in both of the experiments. The measured values are:

$$\begin{aligned}
\text{ATLAS}: \; m_H &= 125.36 \pm 0.37(\text{stat}) \pm 0.18(\text{syst})\ \text{GeV}\ \ [38], \\
\text{CMS}: \; m_H &= 125.03^{+0.26}_{-0.27}(\text{stat})^{+0.13}_{-0.15}(\text{syst})\ \text{GeV}\ \ [39], \\
\text{combination}: \; m_H &= 125.09 \pm 0.21(\text{stat}) \pm 0.11(\text{syst})\ \text{GeV}\ \ [40].
\end{aligned} \tag{3.1}$$

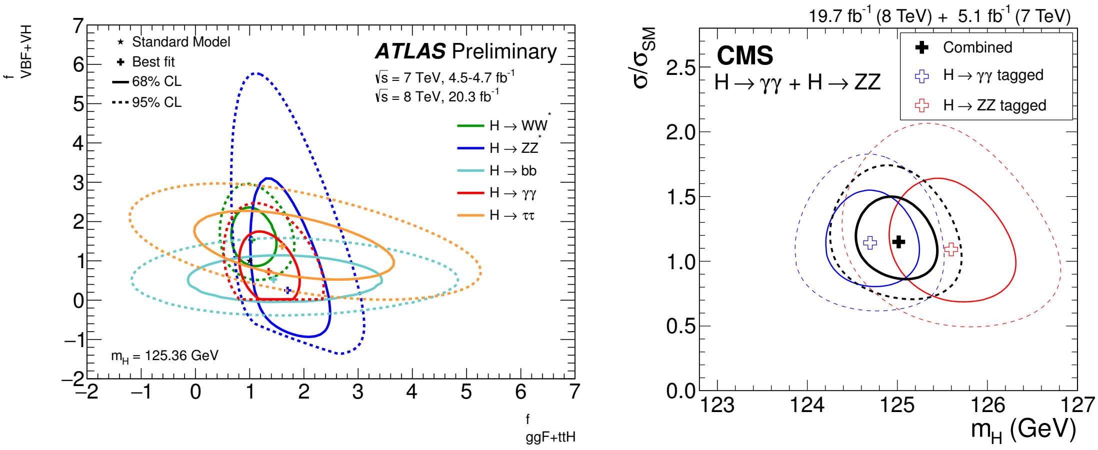

Figure 3.2. Signal strengths and mass of the Higgs boson with best-fit values to the data and 68% (full) and 95% (dashed) confidence level contours indicated. The left plot [44] shows the ATLAS measured signal strength (defined as cross section times branching fractions, relative to the Standard Model expectation) for two groups of production modes (gluon-gluon fusion and $t\bar{t}$ associated production, and vector boson fusion and Higgs-strahlung) in five different search channels. The right plot [39] shows the CMS measured mass and the total signal strength in the two high mass resolution channels (the relative signal strength for the two decay modes is set to the Standard Model expectation).

A mass around 125 GeV is within 1.3σ of the expected value of 94^{+25}_{-22} GeV obtained from a global fit of Standard Model parameters to electroweak precision data [41]. The observed decay modes and angular distributions of the decay products are compatible with the particle having zero spin and positive parity, as expected for the Standard Model Higgs boson, with alternative hypotheses strongly disfavored [42, 43]. The couplings (assessed by measuring different production modes as well as decay channels) are found to agree with the Standard Model predictions [39, 44], as illustrated in Figure 3.2.

3.2.2 SUSY and 2HDM searches

A large number of searches for SUSY particles have been undertaken at the LHC, so far with negative results. Due to the proliferation of SUSY theories, searches target simplified models that focus on a single production mode and one- or two-step decay chains. As an illustration, Figure 3.3 summarizes the current status of SUSY searches in the ATLAS experiment. In particular, gluinos and first- and second-generation squarks should be produced with large cross sections at the LHC and the lower limits on their masses approach or exceed 1 TeV in many important benchmark models.

The most stringent constraints on the MSSM Higgs sector is offered by the search for neutral Higgs bosons in the $\tau\tau$ final state, in particular at large $\tan\beta$. Figure 3.4 shows the ATLAS exclusion limits interpreted in the m_h^{max}, $m_h^{\mathrm{mod}-}$,

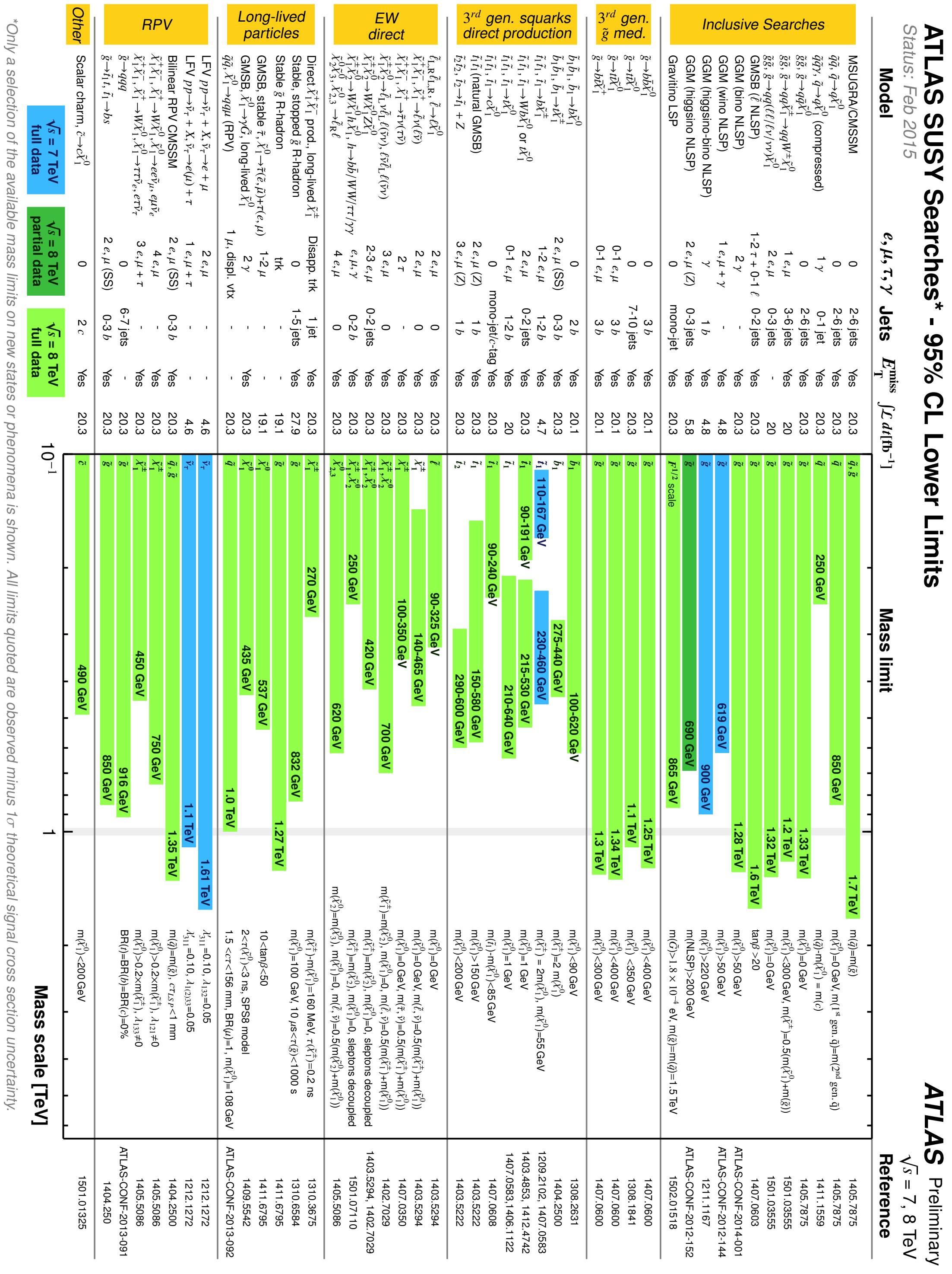

Figure 3.3. A representative selection of ATLAS searches for Supersymmetry.

and $m_h^{\mathrm{mod}+}$ scenarios [45]. Similar results are available from CMS [46]. The overall most sensitive search channel for 2HDMs is $A \to Zh$. ATLAS has searched for decays of h to $\tau\tau$ or bb together with Z decays to electron or muon pairs, as well as h decays to bb together with Z decays to neutrinos [47]. Figure 3.5 shows the excluded parameter space in Type I, Type II, lepton-specific and flipped 2HDMs, with the constraints from $A \to Zh$ indicated in pink and the constraints from $A \to \tau\tau$ indicated in blue. These plots are made assuming that $m_h = 125$ GeV and $\cos(\beta - \alpha) = 0.1$ (recall that small values of this quantity correspond to SM-like couplings of h). Furthermore, it is assumed that $m_A = m_H = m_{H^\pm}$. CMS searches for $A \to Zh$ are reported in Refs. [48, 49].

The single most sensitive channel for charged Higgs boson searches at the LHC is the all-hadronic final state including the hadronic decay of a tau lepton, i.e. $gg \to t\bar{t} \to b\bar{b}(W^- \to q\bar{q})(H^+ \to \tau^+\nu)$ for a light charged Higgs boson and $gg \to b(\bar{t} \to q\bar{q}\bar{b})(H^+ \to \tau^+\nu)$ for a heavy charged Higgs boson. Interpretations of the ATLAS results, which set upper limits on the product of branching fractions $\mathscr{B}(t \to bH^+) \times \mathscr{B}(H^+ \to \tau^+\nu)$ between 0.23% and 1.3% for charged Higgs boson masses in the range 80–160 GeV and upper limits on $\sigma(pp \to \bar{t}H^+ + X) \times \mathscr{B}(H^+ \to \tau^+\nu)$ between 0.76 pb and 4.5 fb for charged Higgs boson masses in the range 180–1000 GeV, are shown in Figure 3.6 for the m_h^{max}, $m_h^{\mathrm{mod}-}$, and $m_h^{\mathrm{mod}+}$ scenarios [50]. Similar results are available from CMS [51]. For the decay $H^+ \to c\bar{s}$, the experiments have placed upper limits on $\mathscr{B}(t \to bH^+) \times \mathscr{B}(H^+ \to c\bar{s})$ between 1% and 7% for charged Higgs boson masses in the range 80–160 GeV [52, 53]. CMS has also searched for heavy charged Higgs bosons decaying to $t\bar{b}$ in the dilepton final state, placing upper limits on $\sigma(pp \to \bar{t}H^+ + X) \times \mathscr{B}(H^+ \to t\bar{b})$ in the range 0.4–4 pb for charged Higgs boson masses in the range 180–600 GeV [54].

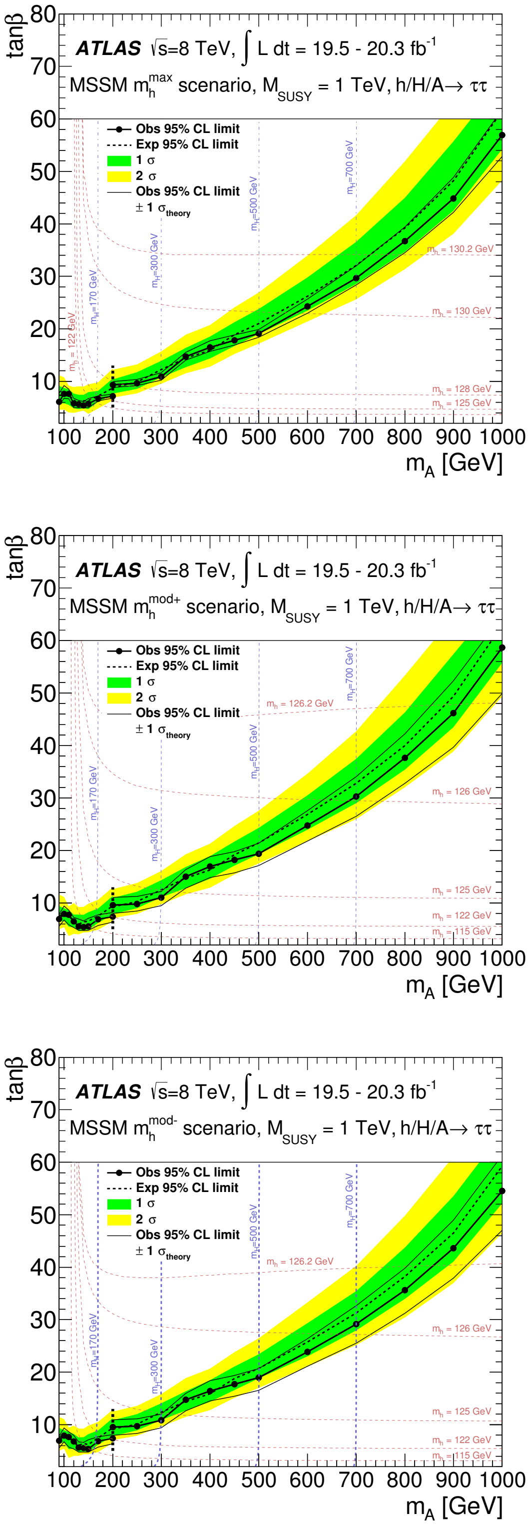

Figure 3.4. 95% confidence level exclusion limits in the $\tan\beta, m_A$ parameter space from a search for neutral Higgs bosons decaying to $\tau\tau$ in ATLAS [45]. Results are shown in the $m_h^{\max}$ (top), $m_h^{\text{mod}+}$ (middle), and $m_h^{\text{mod}-}$ (bottom) scenarios.

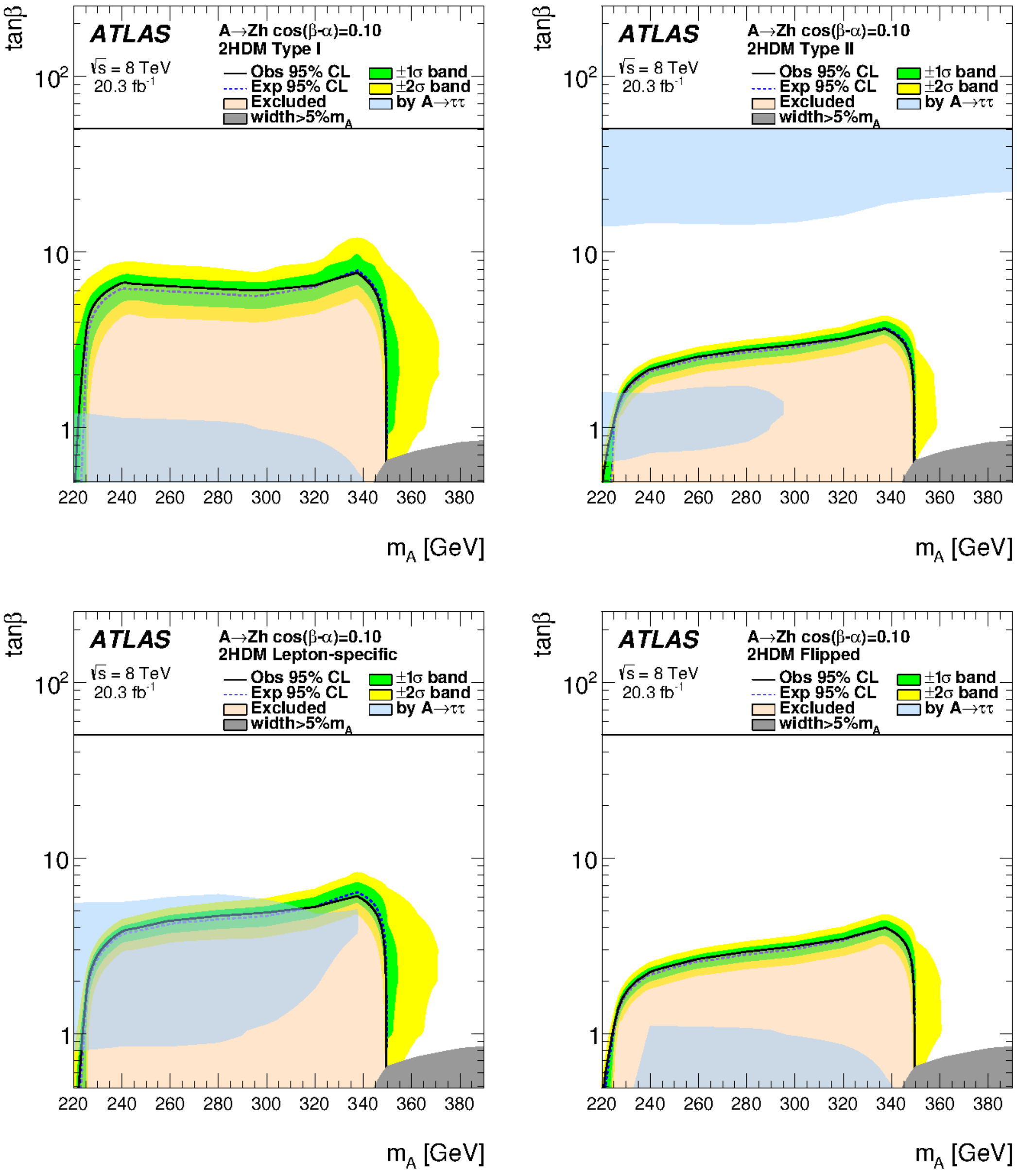

Figure 3.5. 95% confidence level exclusion limits in the $\tan\beta, m_A$ parameter space from searches for $A \to Zh$ (pink) and $A \to \tau\tau$ (blue) in ATLAS [47]. Results are shown for the four types of CP-conserving 2HDMs, with $\cos(\beta - \alpha) = 0.1$.

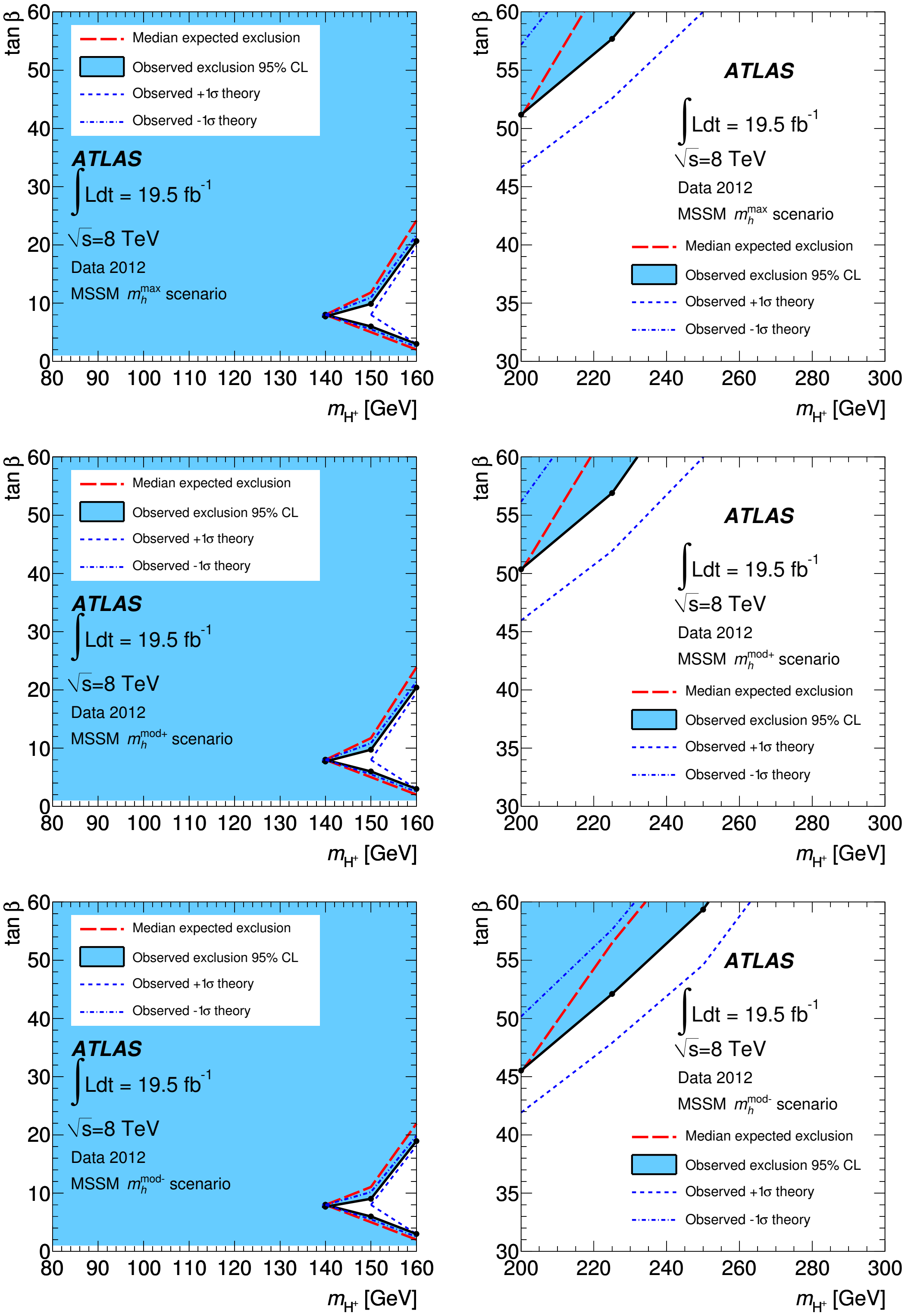

Figure 3.6. 95% confidence level exclusion limits in the $\tan\beta, m_{H^+}$ parameter space from a search for $H^+ \to \tau\nu$ in fully hadronic events in ATLAS [50]. Results are shown in the m_h^{max} (top), $m_h^{\text{mod}+}$ (middle), and $m_h^{\text{mod}-}$ (bottom) scenarios.

4. The ATLAS experiment

The ATLAS experiment [55] is a multi-purpose detector designed to make full use of the rich LHC physics potential, especially in the search for the Standard Model Higgs boson and new physics phenomena at the TeV scale. To cover a wide range of interesting final states, it identifies and measures electrons, photons, muons, $E_{\mathrm{T}}^{\mathrm{miss}}$, and jets, with tagging of hadronic tau decays and *b*-jets. To be sensitive to rare processes, ATLAS takes advantage of the full luminosity offered by the LHC, which means that all of its sub-detectors need to be fast, radiation-hard, and able to handle large amounts of pile-up.

An overview of the ATLAS experiment is shown in Figure 4.1. It is constructed with a forward-backward symmetric geometry consisting of a large barrel cylinder surrounding the beamline around the collision point, and end-cap plugs for near-hermetic coverage. Measuring 44 m in length and 25 m in diameter, and weighing 7000 tons, it is the largest of the LHC experiments.

The design of the detector was largely driven by the choice of magnet system, which consists of a thin superconducting solenoid surrounding the inner detector and three sets of eight superconducting toroids integrated in the muon system. The inner detector consists of semiconductor pixel and strip detectors, and a straw tube transition radiation tracker, providing vertexing, momentum measurement and particle identification capabilities. Outside the inner detector and the solenoid magnet are liquid argon electromagnetic sampling calorimeters, surrounded by hadronic calorimeters using scintillating tiles in the barrel and liquid argon in the end-caps. The outermost and physically largest part is the muon system, consisting of multi-wire chambers, single-wire drift tubes and resistive plate chambers, with different technologies used to provide both precision tracking and fast trigger capabilities.

Coordinate system

A right-handed Cartesian coordinate system with its origin at the center of the detector (the nominal interaction point) is defined in ATLAS such that the z-axis lies along the beam pipe, the y-axis points upwards and the x-axis points towards the center of the LHC ring. Spherical coordinates are often used as well, with ϕ being the azimuthal angle in the x-y plane and θ being the polar angle in the y-z plane.

The *pseudorapidity* η is a function of θ such that

$$\eta = -\ln\tan\left(\frac{\theta}{2}\right). \tag{4.1}$$

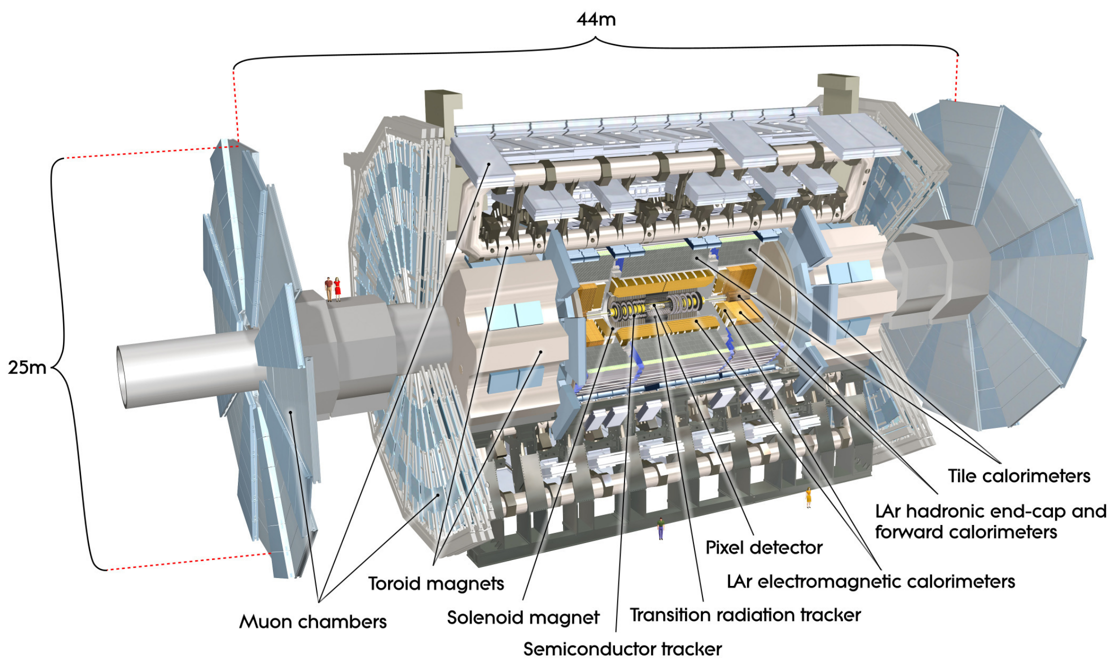

Figure 4.1. The ATLAS detector [55].

In the low-mass limit, the pseudorapidity of a particle is a good approximation of its rapidity,

$$y_r = \frac{1}{2}\ln\left(\frac{E+p_z}{E-p_z}\right), \tag{4.2}$$

which has the convenient property that rapidity differences Δy_r are invariant under Lorentz boosts along the z-axis, i.e. Δy_r between two collision products is independent of the unknown longitudinal momenta of the colliding partons. The angular distance between two directions in the η-ϕ space is defined as

$$\Delta R = \sqrt{(\Delta\phi)^2 + (\Delta\eta)^2}. \tag{4.3}$$

4.1 Inner detector

The purpose of the inner detector is to provide tracking and transverse momentum measurements of charged particles. It uses a combination of precision trackers, which allow accurate vertexing and impact parameter measurements for heavy-flavor and tau lepton tagging, and a larger gaseous tracking volume that also provides electron identification capabilities via detection of transition radiation. The arrangement of these detectors is shown in Figure 4.2, with the highly granular semiconductor pixel and microstrip detectors covering the region $|\eta| < 2.5$ and the transition radiation tracker limited to $|\eta| < 2.0$. The design resolution of the inner detector is $\sigma_{p_\mathrm{T}}/p_\mathrm{T} = 0.05\% p_\mathrm{T} \oplus 1\%$. It is ulti-

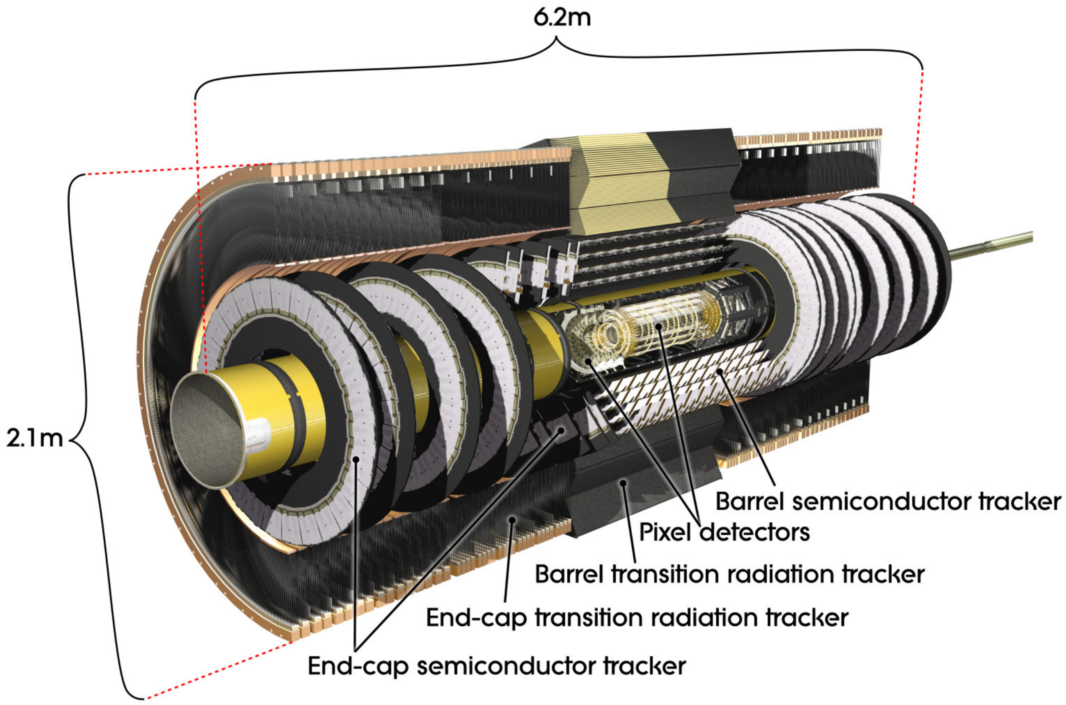

Figure 4.2. The ATLAS inner detector [55].

mately limited mainly by the effects of multiple scattering and degrades with increasing p_T as particles leave tracks with reduced curvature.

Pixel detector
The pixel detector is located closest to the interaction point. It consists of silicon sensors finely segmented into rectangular elements for good spatial resolution in two coordinates, with a total of over 80 million pixel elements. The detector modules are grouped into three cylindrical shells in the barrel region and three vertical discs in each end-cap, so that each track crosses three pixel layers.

Semiconductor tracker
The SemiConductor Tracker (SCT) uses silicon microstrips oriented in the beam direction in the barrel and radially in the end-caps to measure the coordinate in the bending direction of the magnetic field. The detector modules are installed in four cylindrical shells in the barrel region and nine vertical discs in each end-cap, arranged so that a track passes through four modules. Each module consists of two detector layers, with the strips in the second layer rotated relative to the first to also allow reconstruction of the second coordinate. The rotation angle is small (40 mrad) to keep a redundancy in the measurement of the primary coordinate.

Transition radiation tracker

The Transition Radiation Tracker (TRT) consists of densely packed thin straw tubes interleaved with a transition radiation material. The straws are oriented parallel to the beam axis in the barrel region and radially in the end-caps, thereby providing R-ϕ respectively z-ϕ positioning only. The lower intrinsic resolution of the straw tubes compared to the silicon detectors is compensated for by a large number of hits (36 on average) and longer track length in the TRT. This tracking device also provides electron identification thanks to the emission and detection of transition radiation, with an average of 7–10 transition radiation hits expected from electrons with a transverse momentum above 2 GeV.

4.2 Calorimeters

The calorimeters, shown in Figure 4.3, are designed to measure the energy of electrons and photons with a resolution of $\sigma_E/E = 10\%/\sqrt{E} \oplus 0.7\%$, and of hadronic jets with a resolution of $\sigma_E/E = 50\%/\sqrt{E} \oplus 3\%$ (which becomes $\sigma_E/E = 100\%/\sqrt{E} \oplus 10\%$ above $|\eta| = 3.2$). The constant terms account for local non-uniformities in the calorimeter response, the energy-dependent stochastic terms correspond to statistical fluctuations, and the effects of electronic noise are negligibly small. Statistical fluctuations become less detrimental with increasing energy. In contrast to the inner detector, the resolution therefore improves with increasing energy.

The high resolution is ensured by the thickness of the calorimeters, which is more than 22 radiation lengths in the electromagnetic calorimeter and approximately 10 interaction lengths in the hadronic calorimeter, providing good containment[1]. Together with the large η coverage (up to $|\eta| = 4.9$), this also allows for a good $E_{\mathrm{T}}^{\mathrm{miss}}$ measurement. The thickness of the calorimeters is also crucial to prevent punch-through of hadrons into the muon system.

The electromagnetic (EM) calorimeter is a sampling calorimeter using lead absorber plates and liquid argon as the active material. Liquid argon is used due to its radiation tolerance and linear, time-stable, response. To ensure full ϕ coverage, the absorbers and electrodes are folded in a zig-zag accordion shape. The central part of the EM calorimeter consists of two half-barrels, together covering the region $|\eta| < 1.475$. Each end-cap consists of an inner and an outer wheel, together covering the region $1.375 < |\eta| < 3.2$. In the precision-measurement region matched to the inner detector, $|\eta| < 2.5$, the EM calorimeter has three sampling layers, while it has two sampling layers in the region $2.5 < |\eta| < 3.2$. The innermost layer has the highest granularity,

---

[1] The radiation length is the mean distance which an electron travels before having lost a fraction $1 - \frac{1}{e}$ of its initial energy due to bremsstrahlung. The interaction length is the mean distance which a hadron travels before undergoing an inelastic nuclear interaction. These numbers are highly material-dependent.

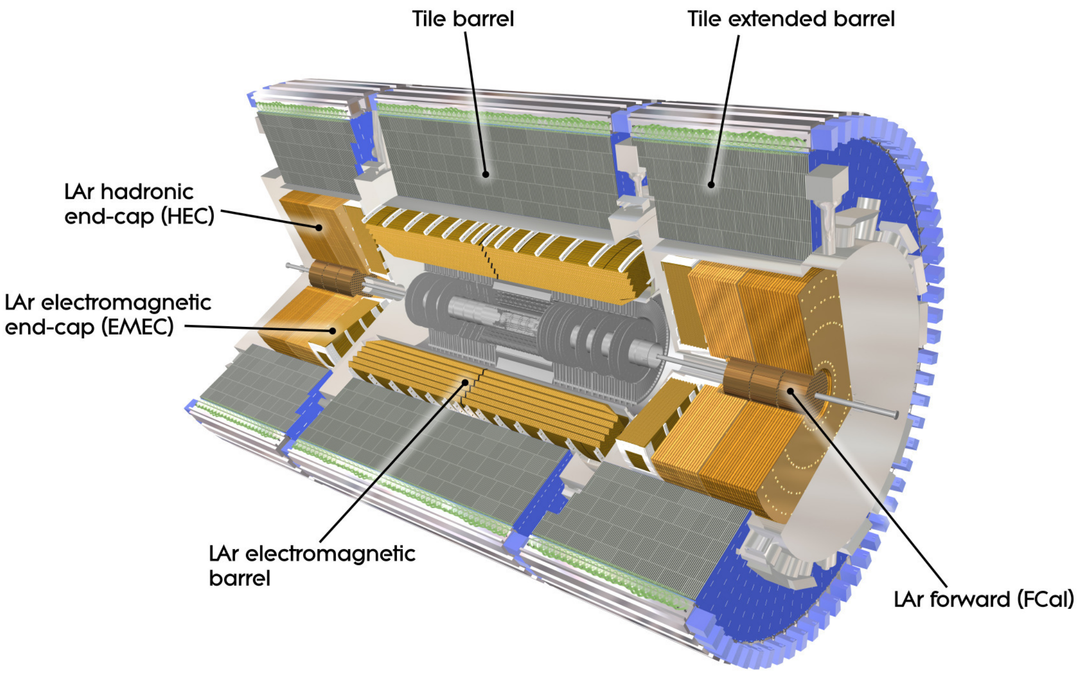

Figure 4.3. The ATLAS calorimeters [55].

with strip cells of size $\Delta\eta \times \Delta\phi = 0.003 \times 0.1$ in the central part. In the region $|\eta| < 1.8$, the calorimeter is also complemented with a thin presampling layer of liquid argon which is used to correct for energy lost in the material upstream of the calorimeter (up to several radiation lengths).

ATLAS has three hadronic calorimeters: the tile calorimeter, the Hadronic End-cap Calorimeter (HEC), and the Forward Calorimeter (FCal). The tile calorimeter consists of a central barrel part and two extended barrels, segmented in depth in three layers, and together covering the region $|\eta| < 1.7$. It uses steel as absorbing material and scintillating tiles as active material. In the HEC and FCal, covering larger rapidities, the liquid argon technology is used, again because of its radiation tolerance. The HEC, covering the region $1.5 < |\eta| < 3.2$, uses copper plates as absorbers and consists of two independent wheels per end-cap, each divided into two segments in depth, for a total of four layers in each end-cap. The FCal, covering the very forward region $3.1 < |\eta| < 4.9$, consists of three modules in each end-cap. Copper is used as absorbing material in the innermost module in each end-cap, while tungsten is used in the other two in order to provide good containment in this relatively small detector. The first module is optimized for electromagnetic measurements, thereby complementing the EM calorimeter. For good coverage and minimum radiation background in the muon spectrometer, both the HEC and the FCal are integrated in the same cryostats as the EM end-cap calorimeters.

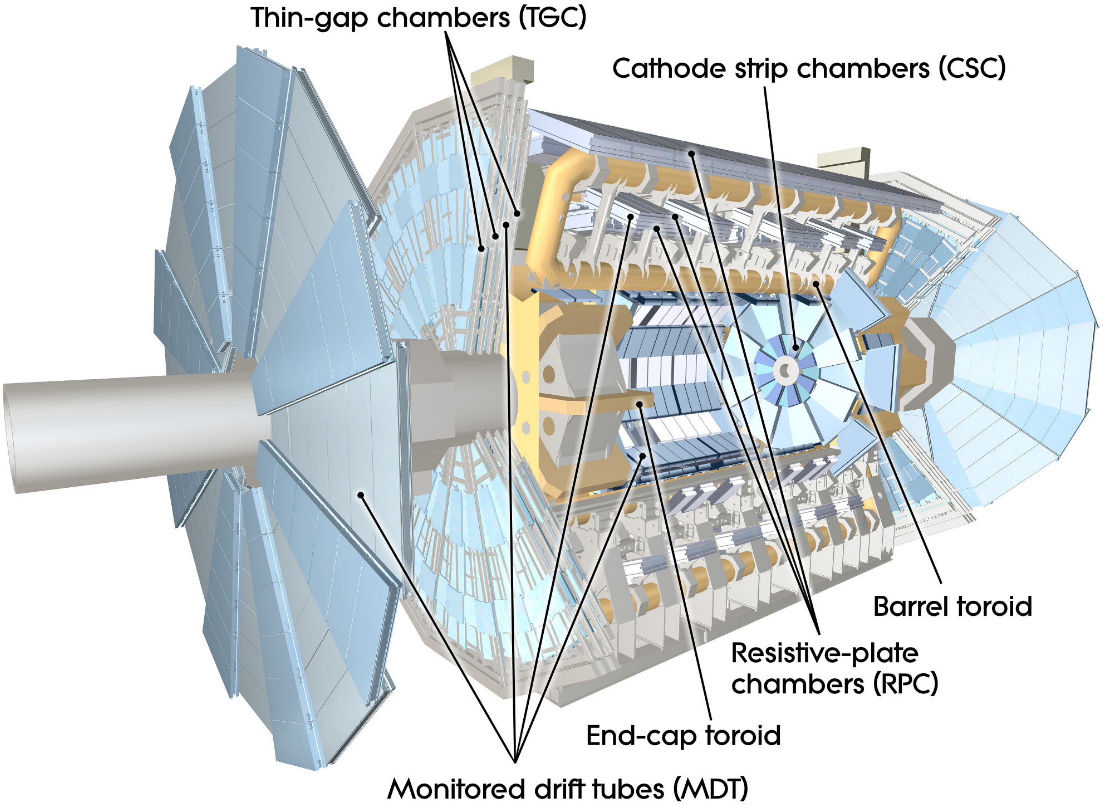

Figure 4.4. The ATLAS muon system [55].

4.3 Muon system

The muon spectrometer is designed to measure the transverse momentum of muons with a resolution of 10% at 1 TeV, independently of the inner detector. The layout of the system is shown in Figure 4.4. It consists of separate trigger and high-precision tracking chambers used to measure the deflection of muon tracks in the field of the toroid magnets. The chambers are installed in three cylindrical shells in the barrel region and three vertical wheels in the end-cap regions.

The precision tracking chambers consist mainly of Monitored Drift Tubes (MDTs) covering the full η range up to $|\eta| = 2.7$. Each MDT chamber consists of three to eight layers of high-pressure (3 bar absolute) drift tubes oriented to measure track coordinates in the bending direction. The use of sensor wires isolated in individual tubes ensures reliable operation.

To handle the high occupancy at large rapidities, Cathode Strip Chambers (CSCs) with high rate capability and time resolution are used in the central parts of the innermost end-cap wheels, covering the region $2.0 < |\eta| < 2.7$. The CSCs are multi-wire chambers with cathodes segmented into orthogonal strips, which allow both coordinates to be measured.

The read-out time of the precision chambers exceeds the minimum 25 ns bunch crossing interval of the LHC. Trigger capabilities are therefore provided by dedicated detectors which consist of Resistive Plate Chambers (RPCs) in the barrel and Thin Gap Chambers (TGCs) in the end-cap regions, together covering the region $|\eta| < 2.4$. TGCs are multi-wire chambers characterized by a wire-cathode distance smaller than the distance between wires. A RPC has no wires, but parallel electrode plates separated by a narrow gas gap, with the signal read out via capacitive coupling to metallic strips located outside the resistive plates. In the TGCs, both the wire and the perpendicular cathode strip signals are read out, and in the RPCs, two orthogonal sets of read-out strips are used. In addition to triggering, these chambers therefore also allow measurement of the second track coordinate not determined by the MDTs.

4.4 Forward detectors

Online monitoring of the luminosity delivered to ATLAS is provided by the Cherenkov detector LUCID (LUminosity measurement using Cherenkov Integrating Detector) located at ±17 m from the interaction point. The absolute luminosity is determined by the ALFA (Absolute Luminosity For ATLAS) detector, which uses Roman pots with scintillating-fiber trackers located at ±240 m from the interaction point. Besides the luminosity detectors, the very forward region is also instrumented by the quartz-tungsten Zero-Degree Calorimeter (ZDC) at ±140 m from the interaction point, used to determine the centrality in heavy-ion collisions.

4.5 Trigger and data acquisition

The trigger system has three levels: L1, L2, and the event filter. The L1 trigger is based on custom-made electronics, while L2 and the event filter, collectively known as the high-level trigger, are implemented in software running on commercial computers. Events are selected according to a “menu” of hundreds of interesting signatures, with most of the bandwidth dedicated to the most generic triggers. The analyses presented in this thesis make use of single electron and single muon triggers, with minimum requirements on transverse momentum and isolation, which together account for about one fourth of all recorded events. Data corresponding to selected events are transferred by the Data Acquisition (DAQ) system to the CERN computing center, written to tape and distributed over the worldwide LHC computing grid.

The L1 trigger uses reduced-granularity information from the muon system trigger chambers and from the calorimeters to search for high-p_{T} muons, electrons/photons, jets, hadronic decays of tau leptons, and $E_{\mathrm{T}}^{\mathrm{miss}}$. It also defines Regions of Interest (RoI), i.e. parts of the detector where interesting features are observed. The L1 decision time is less than 2.5 μs, during which the event data is held in memories within the front-end electronics of each detector. After this time, if the event is accepted, it is read out and buffered by the DAQ system. The bandwidth of this operation limits the L1 trigger rate to 75 kHz.

Data corresponding to the RoI identified by the L1 trigger (on average 2% of the overall data in each event) is passed on to the L2 trigger, which uses this extended information to refine the L1 selection and reduces the acceptance rate to about 5 kHz. The L2 processing time is approximately 40 ms.

The final event selection is performed by the event filter, which uses offline analysis procedures to perform a full event reconstruction and reduces the output rate to approximately 400 Hz. The reconstruction takes about four seconds per event and, at this point, the DAQ capacity is higher than the available processing power. An additional 200 events per second (passing lower priority L2 triggers) are therefore stored in a “delayed stream” for reconstruction between data-taking periods.

4.6 Software

4.6.1 Detector control system

The Detector Control System (DCS) provides a high-level interface for the operation of the ATLAS detectors and associated technical infrastructure. This includes the control and monitoring of equipment such as power supplies, cooling, and environmental sensors. The DCS is responsible for safely transitioning the hardware between well-defined operational states and signaling any problematic conditions. It monitors and records operational data, and also handles communication with other systems such as the ATLAS DAQ and the LHC beam information.

The base of the DCS software is WinCC, an industrial Supervisory Controls And Data Acquisition (SCADA) product which provides, among other things, a scripting facility, user interfaces in the form of alarm screens and fully programmable control panels, and a generic application programming interface for extended functionality. A key feature of WinCC is its high scalability. This is crucial for the ATLAS DCS, which needs to process data from over 200 000 sensors. Different WinCC instances, called “projects”, can be connected via a LAN to form a distributed system allowing information exchange between all connected projects. The ATLAS DCS comprises about 150 projects, each of which is running on a dedicated server, organized in a three-layer architecture as illustrated in the top part of Figure 4.5. The first layer consists of the so-called Local Control Stations (LCS), which are connected to the front-end electronics of a set of related hardware. The second layer consists of Sub-detector Control Stations (SCS), which integrate associated systems to provide stand-alone control of each sub-detector. The third layer consists of Global Control Stations (GCS), providing e.g. human interfaces in the ATLAS control room for the high-level operation of the experiment.

WinCC is oriented around the concept of "data points", which are data structures used to read and write information to and from connected equipment as well as between projects. An alarm mechanism is provided, with configurable levels for each data point, and the options to mask known alarms or require acknowledgement by the operator. Data point values are recorded in an Oracle database for later analysis. Some of this information is also used for physics reconstruction.

For the physical connection between front-end devices and control stations, the industrial Controller Area Network (CAN) fieldbus and the CANopen protocol are used whenever possible. CAN is a high-speed network system which prevents message collisions and provides good error detection and recovery. It is also tolerant to strong magnetic fields, in contrast to e.g. Ethernet. In most cases, the software interface to the SCADA system is composed of device-specific server applications providing access to the equipment via the industry standard OPC protocol, for which WinCC provides a client.

The DCS is modeled as a hierarchical Finite State Machine (FSM), which allows homogeneous control of all connected systems. The lower level FSM elements are managed by each LCS. They correspond to individual or groups of devices, which may be structured into logical units according to purpose or physical location. These are in turn grouped into representations of sub-detectors and sub-detector partitions at the SCS level. A GCS contains the top node of the hierarchy, which allows control of the complete experiment. As an example, part of the FSM tree is illustrated in the lower part of Figure 4.5. Commands are propagated downwards and state changes are propagated upwards in the hierarchy. The *state* is a property of each FSM element, representing its condition and readiness for physics data-taking. Each element automatically assumes the most severe state reported by any of its underlying elements. Similarly, each element also has a *status* property indicating the highest severity of alarms active for the underlying devices, allowing error detection at any level of the hierarchy.

4.6.2 Simulation

Monte Carlo modeling is used to simulate physics processes in ATLAS. In the first step, the interaction of two partons participating in a LHC proton-proton collision is simulated. This is called the *hard process*, and it is simulated by an *event generator* program. Different types of hard processes are typically simulated separately. The *order* of a generator refers to the complexity of the Feynman diagrams describing the type of hard process that the generator implements. A Leading-Order (LO) diagram contains only the minimum number of vertices through which a type of process can take place, while higher-order diagrams can provide a more complete description, including the effects of radiation and loop corrections.

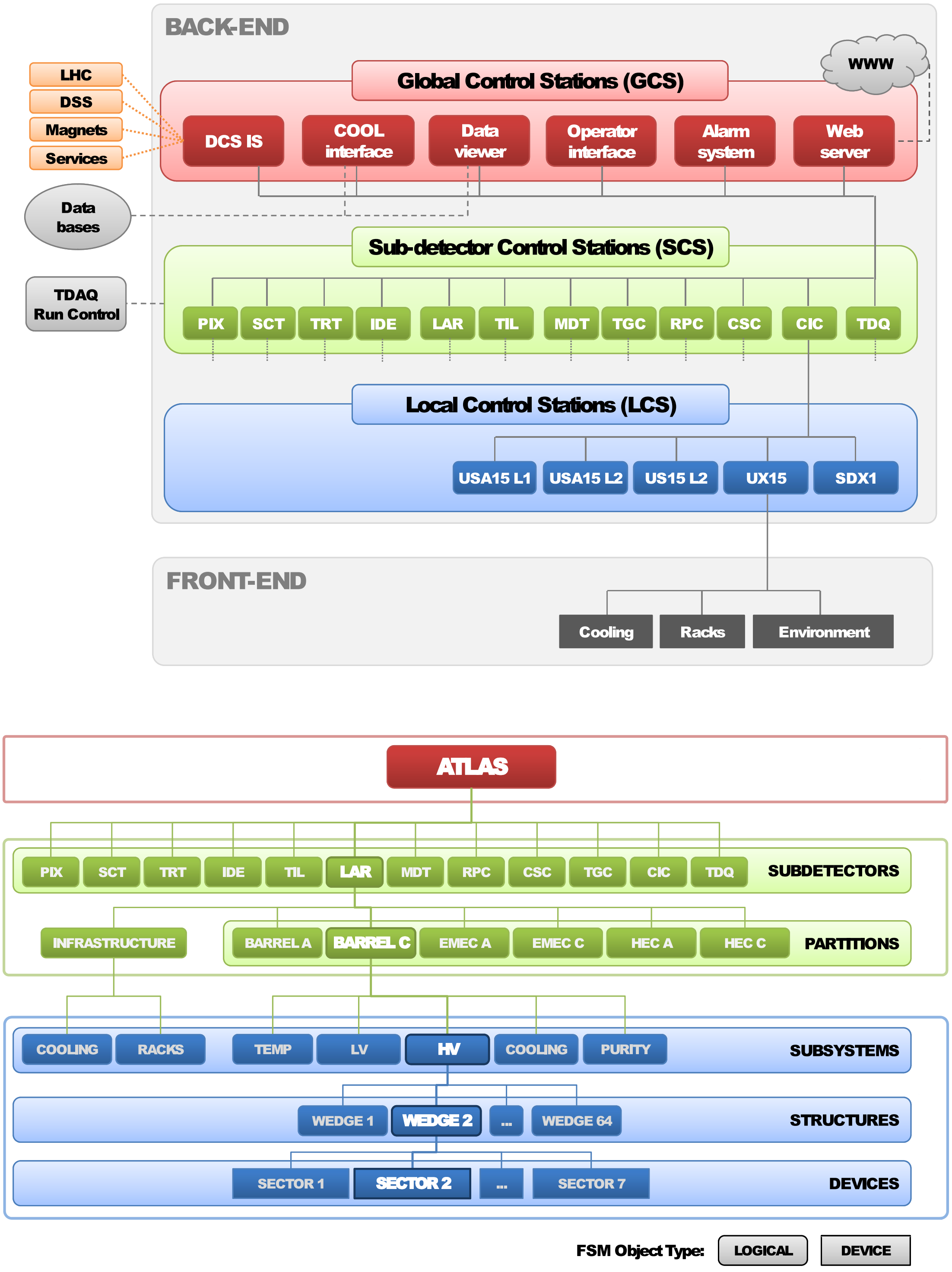

Figure 4.5. The ATLAS DCS architecture (top) and parts of its logical representation as a Finite State Machine (bottom). This figure is reprinted from Ref. [56].

Higher-order corrections involving the strong interaction that are not included in the event generator are subsequently approximated in the *parton shower*. This step gives an effective description of the large amounts of gluon radiation emitted by partons involved in the large momentum transfers of the hard interaction. The gluons themselves emit new partons, which produce even more gluons, and so on, until hadronization occurs. Interactions of remnants of the original protons, called the *underlying event*, and finally the decay of unstable hadrons are also simulated.

A range of available programs are used depending on the process being studied, and different programs may be used for different steps of the simulation. The programs used to simulate the signal and background processes studied in this thesis are listed in section 5.1.

Long-lived particles in the simulated events are propagated through a detailed simulation of the ATLAS detectors, implemented using the GEANT4 toolkit [57]. Interactions with all active detector elements are recorded, and the response of the experiment is approximated in a process called *digitization*, in which the effects of noise and timing constraints of the readout electronics and DAQ system are included. The result is a collection of *hits*, which are then passed to the same reconstruction algorithms as real data from the detectors. The full GEANT4 simulation is very detailed, and consequently rather slow. An alternative simulation using parametrized descriptions of the ATLAS detectors is occasionally used to trade precision for speed.

All simulation tasks, from event generation to detector simulation, are handled by a central ATLAS software framework named ATHENA and take place on the WLCG grid.

4.6.3 Reconstruction and analysis

The ATHENA software also handles reconstruction of physics objects (electrons, muons, jets, etc.). Like simulation tasks, this is also typically done in large coordinated campaigns on the WLCG grid. The reconstruction, in which simulated events and real data are treated on equal footing, proceeds in two steps. The first step is stand-alone reconstruction of primitive objects within the different sub-systems of the experiment. Charged particle tracks are formed from hits in the inner detector, energy clusters are formed from energy depositions in the calorimeters, and muon tracks are formed from hits in the muon system. This information is stored in Event Summary Data (ESD) files.

The second step is the combined reconstruction, during which information from all sub-systems are combined to form high-level objects. Electrons are formed from a track in the inner detector and an electromagnetic cluster. Muons are reconstructed by matching a track in the muon spectrometer to a track in the inner detector or to small energy depositions in the calorimeter. Jets are formed by grouping energy clusters in the calorimeters, and tracking information from the inner detector is added to identify *b*-jets and hadronic tau decays. Tracking information is also used to reconstruct the primary vertex. Multiple algorithms exist for the reconstruction of each type of object. The output of this step is therefore multiple collections of electrons, jets, etc. – all with different definitions. In addition, tracks and energy deposits may at this point be double-counted between different types of objects. An object preselection is later performed in each analysis to ensure a self-consistent event description. The output of the combined reconstruction are Analysis Object Data (AOD) files.

Analysis tasks can also be performed within ATHENA, but are often instead implemented as stand-alone applications based on ROOT [58] and using so-called D3PD (from Derived Physics Data) files as input (this is also the case for the analyses presented in this thesis). D3PD files contain selected subsets of the AOD content, stored as primitive data types. During LS1, ATLAS is transitioning to a new analysis model in which the (somewhat redundant) AOD and D3PD files are replaced by a common, object-oriented, "xAOD" format. This is foreseen to reduce the total storage space needed.

The EventLoop analysis framework

During the preparation of this thesis, the author has been involved in the development and support of a light-weight and extensible ROOT-based analysis framework called EVENTLOOP. The aim of the EVENTLOOP project is to provide users with a truly uniform interface for configuring and running their analysis jobs on different back ends, including one or multiple cores of a local workstation, PROOF-farms [59], various batch systems, and the WLCG grid. EVENTLOOP was partly used to produce the results presented in part III of this thesis, and has been adopted as the officially supported analysis framework by the ATLAS Analysis Software Group.

EVENTLOOP is based on the ROOTCORE build system, which defines a structure for modular software packages. An analysis software consists of a collection of packages, typically including a few core framework components, ATLAS common tools for applying object corrections and evaluating uncertainties, and the user provided code that defines the analysis task. The EVENTLOOP suite of packages includes SAMPLEHANDLER, and EVENTLOOP itself.

SAMPLEHANDLER manages references to the input files, which may be located on a local disk or on remote resources, including the WLCG grid. Collections of input files are defined based on e.g. the simulated physics process or the data-taking period, and can be searched, split or joined based on tags. Arbitrary meta-data based on key-value pairs can also be assigned to each collection, and can be queried by the user's code during execution.

EVENTLOOP is responsible for job management and steering the execution. The analysis code is written as *algorithms*, which are C++ classes that define the logic to be executed for each event, while EVENTLOOP manages input and output *streams* (files or chains of files). Multiple algorithms may be added to a single job, and may produce any number of common or isolated output streams.

EVENTLOOP has a modular architecture with optional packages provided for optimized reading of D3PD and xAOD files, ROOT ntuple management, “white board” services for inter-algorithm communication, or even parsing plain text formulas for setting up simple analyses with no code at all. These may be used as building blocks for a full analysis, or replaced with custom solutions – EVENTLOOP is not tied to any specific input or output format or type of analysis, the only requirement is that the user’s code operates on individual events.

Jobs are configured by ROOT macros. Algorithm classes are instantiated and can be manipulated during the configuration. Their state is then saved to disk using a serialization mechanism provided by ROOT. The saved file is shipped to the place of execution where the state of the algorithm is recovered. This eliminates the need for auxiliary configuration files and command line options. Instead, full and direct interaction with each algorithm is possible in the job macro, including the setting of data members, function calls, and other operations. This can also be performed interactively, if desired.

In the job macro, a *driver* object is instantiated. The driver handles the process of submitting jobs to the desired processing system, as well as retrieving and merging the output upon completion. Advanced drivers may also monitor the job progress and resubmit problematic jobs. For long-running jobs, users may log out from the local workstation and reconnect with running jobs at a later point. On the processing back end, a *worker* object iterates over all input data, feeding events to each algorithm, and manages the output. There are driver-worker pairs for most popular platforms for ROOT-based analysis. The most complex drivers are those interfacing to the ATLAS grid tools due to the massive scale, range of configuration possibilities, and inherent unreliability of such jobs. The grid worker also has special features for reporting errors and job statistics to the ATLAS grid job management system. The following example illustrates a typical EVENTLOOP job steering macro:

```
//Define a job to process some datasets
EL::Job job;
SH::SampleHandler sh;
SH::scanDQ2(sh, "data12_8TeV.periodA.physics_Muons/");
SH::scanDQ2(sh, "mc12_8TeV.117050.PowhegPythia_ttbar/");
SH::scanDQ2(sh, "mc12_8TeV.105986.Herwig_ZZ/");
sh.setMetaString("nc_tree", "physics");
job.sampleHandler(sh);

//Configure a single algorithm to run in the job
MuonAnalysis* alg = new MuonAnalysis;
alg->maxMuonEta = 2.5;
alg->useTightSelection = true;
TGoodRunsListReader* grlTool = new TGoodRunsListReader();
grlTool->SetXMLFile("v61_PHYS_StandardGRL_All_Good.xml");
grlTool->Interpret();
alg->setGoodRunsList(grl->GetMergedGoodRunsList());
job.algsAdd(alg);

//Submit the job to the grid
job.options()->setDouble(EL::Job::optMaxEvents, 500);
EL::GridDriver driver;
driver.submit(job, "muonTestJob");

//Upon completion, retrieve and plot some output
SH::SampleHandler shHistograms;
shHistograms.load("muonTestJob/hist");
TH1* hist = shHistograms.get(
  "data12_8TeV.periodA.physics_Muons/")->readHist("pt");
hist->Draw();
```

4.7 Run 2 preparations

During LS1, a new silicon pixel detector layer was installed in ATLAS, the Insertable B-Layer (IBL). It is now the innermost detector element, mounted around a new, smaller, beam pipe. This additional layer will, thanks to its proximity to the interaction region, offer improved tracking and vertexing. In turn, future searches for charged Higgs bosons should benefit from improved tagging of *b*-jets and hadronic tau decays.

In addition, the muon spectrometer coverage was improved, and a range of technical infrastructure upgrades and other activities were performed during LS1. Some projects that the author of this thesis has been involved in are documented in this section.

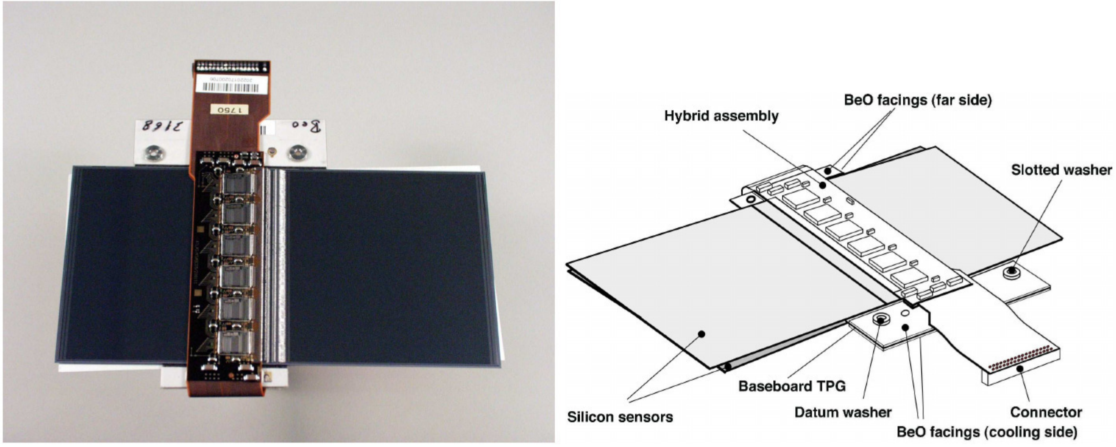

Figure 4.6. Photograph (left) and drawing (right) of a SCT barrel module [55]. The TPG base-board between the sensors extends sideways with beryllia facings where it is attached to its support structure. Aluminium washers allow precision alignment.

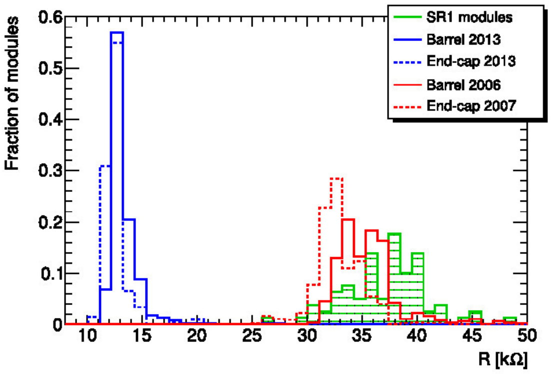

Figure 4.7. Measured resistance of SCT modules under a 10 μA current sourced in the forward direction. "SR1" test modules were measured in 2013 and have not been irradiated.

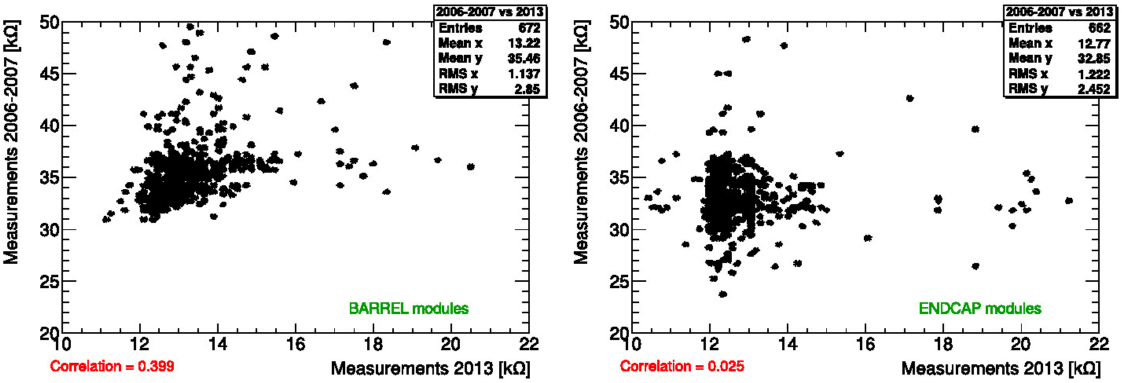

Figure 4.8. Scatter plots of old and new measurements for barrel (left) and end-cap (right) modules.

4.7.1 SCT backplane resistance measurements

During their installation in 2006 and 2007, it was found that some of the 4088 SCT modules exhibited unusually high resistance under forward bias. With a 10 μA current sourced in the forward direction, the typical resistance was around 35 kΩ. However, about 20% of the barrel modules and 5% of the end-cap modules showed a significantly higher resistance. Fortunately, it was also found that sourcing a larger current – or operating the module at higher than normal reverse bias voltage (350 V instead of 150 V) – usually brings back the higher resistances to normal levels. Concerns remained, however, that the problem might get worse in the future. As the leakage current increases with increasing bulk damage, a significant voltage drop may develop if the resistance is too high. A maximum of 400 V can be supplied to the SCT. If that is not enough to fully deplete the sensors, signal loss will occur. It was therefore decided to repeat the measurements during LS1 to see how the resistances had changed over time.

The SCT modules have two layers of sensors with 768 active strips and a mean strip pitch of 80 μm, glued to either side of a 380 μm thick Thermal Pyrolitic Graphite (TPG) base-board, which provides mechanical structure and carries away heat. A Cu/polyimide flexible circuit hybrid reinforced with carbon fibre carries the front-end electronics. Figure 4.6 depicts a barrel module, which consists of two such sensor pairs with a total active length of 126 mm and one hybrid mounted on a common TPG base-board. The end-cap modules use different variations of this design depending on their location in the outer, middle or inner rings. Power is supplied to the sensors via the TPG base-board, which is connected to the aluminized backplanes of the sensors by a silver-loaded epoxy adhesive. The unusually high resistances were tentatively attributed to problems with these connections.

Rack-mounted power supply crates located outside the ATLAS cavern contain Low Voltage (LV) cards supplying power to the front-end electronics and High Voltage (HV) cards providing bias voltage for the sensors. Each HV card supplies eight SCT modules. To measure the module resistance under forward bias, a HV card is replaced with a custom adapter card that allows connection of a sourcemeter and a data acquisition unit directly to the bias circuit. The measurement follows the procedure developed in 2006–2007:

1. A current of 10 μA is applied for 1 s and the resistance is measured.
2. If the resistance is above 40 kΩ, the current is increased to 100 μA for 3 s.
3. The resistance measurement is repeated with 10 μA.
4. If the resistance is above 40 kΩ, the current is increased to 100 μA for 10 s.
5. The resistance measurement is repeated with 10 μA.

This process is automated in a LabVIEW application for consistency and efficiency.

New measurements have been performed on a sample of barrel and end-cap modules in 2013. In total, more than a third of the SCT modules were measured. Contrary to what was originally feared, no increase in resistance has been observed. While the mean resistance measured after installation was 35 kΩ for barrel modules and 32 kΩ for end-cap modules, it has decreased to 13 kΩ for both types of modules in 2013.

It was suggested that the high voltage applied to the circuits over long periods could have affected their conductive properties. However, a small number of end-cap modules have been installed but never powered due to cooling problems and can therefore be used as a control sample in order to test this hypothesis. The mean value of the resistances of these modules is 15 kΩ, close to that of the modules which have been powered during Run 1.

Instead, the differences between the old and new measurements are most likely due to the high radiation doses received during LHC operation. Radiation damage causes changes in the effective doping concentration (including type inversion) and is expected to alter the diode characteristic. This hypothesis was confirmed by performing the same measurements on SCT modules installed in the SR1 test facility at CERN. These modules have only been exposed to natural radiation levels and show a mean resistance of around 37 kΩ. Historical data are unfortunately not available for these modules but this number is compatible with the other measurements made in 2006–2007, suggesting that it has remained constant throughout this time. The nominal resistance of the bias circuit is about 12 kΩ. It appears that the strip diodes of the SCT modules installed in ATLAS are fully turned on at 10 μA after irradiation, while this was not the case before. No variation is observed between the four SCT barrel layers that should have received different radiation doses.

The measurements of the barrel modules, the end-cap modules and the test modules installed in SR1 are summarized in Figure 4.7. Some modules still exhibit a higher than expected resistance at 10 μA. This prompted an investigation of the correlation between outliers in the old and new measurements. As can be seen in Figure 4.8, the modules that exhibit unusually high resistance are in general not the same in 2013 as in 2006–2007.

Even after having first applied a current of 100 μA for 10 s, four of the tested barrel modules and two of the tested end-cap modules showed a resistance higher than 40 kΩ (42–81 kΩ) at 10 μA in 2013. To test if these modules could be “cured” by a larger current, 1 mA was applied before the measurement was again repeated at 10 μA. The resistances had then been reduced to between 12 kΩ and 17 kΩ. This is accounted for in Figures 4.7 and 4.8.

In conclusion, the new measurements most importantly show that the number of outliers has not increased over time and that modules with unusually high resistance still can be returned to average levels by applying a higher current. The backplane resistance therefore does not present an issue for the future performance of the SCT detector.

4.7.2 Heater pads control system upgrade

Electric resistance heating pads are used to maintain specific temperatures at various points within the inner detector. The most critical region is the thermal enclosure separating the SCT (which may be cooled to temperatures as low as -25 °C) from the TRT (which is operated at room temperature). Accidental cooling would not only be detrimental to the operation of the TRT but it could also physically damage the detector. To maintain the temperature difference while placing a minimum amount of material between the detectors, the enclosure is actively heated.

The heater pads consist of thin (5–8 μm) copper tracks with a resistance of 32–65 Ω sandwiched between two polyimide sheets. The heater pads range from 0.04 to 0.64 m^2 in size and provide a power output between 12 and 120 W. There are in total 280 pads with a total heating capacity of 23 kW, installed along the pixel detector support tube, the TRT barrel, the SCT barrel and SCT end-caps, and the inner detector end-plates. They are operated from a 48 V power source. With voltage drop across the cabling, there is nominally 40 V across the pads. The relatively low voltage is chosen out of safety concerns, as some heater pads are operated also during maintenance access to the inner detector in order to keep temperatures above the cavern dew-point. Heater pads are also equipped with 10 kΩ Negative Temperature Coefficient (NTC) thermistors for monitoring the temperature in the vicinity of each heater. Not all installed heater pads are currently used for active heating, but all available NTC thermistors are used to monitor the temperature in various locations. Active heaters use the temperature readings to keep the temperature at the desired level using Proportional-Integral-Derivative (PID) regulation. Some heaters are configured in a master/slave fashion, in which case multiple heaters follow the temperature readings of a single thermistor, effectively linking them together to a larger heating element.

Heater power is controlled by current pulses of varying length. Switching on and off is done over a period of about 1 ms to limit electromagnetic interference with sensitive detector elements. The switching is handled by custom made *switching cards*, each of which contains switching elements controlling 16 channels, together with power handling electronics and an on-board controller in the form of a CERN Embedded Logical Monitoring Board (ELMB). The ELMB features an 8-bit microprocessor running at 4 MHz, multiple I/O channels, and a CAN bus interface. The switching cards are installed in rack-mounted crates in the relatively low radiation environment of the two underground caverns located next to the experiment. In each location, there is also a *controller card*. A number of safety features are in place to prevent damage to the ATLAS detector in the event of a component failure causing a too high power output, one of which is the controller cards. They can prevent current flow through connected heater pads independently of the switching circuits. The current is also limited by fuses in each switching element. Each ELMB continuously reports temperature readings, current output, and other data to the Detector Control System. The DCS is in turn used to start and stop heaters and configure switching parameters such as temperature set points and powering schemes. The PID algorithm and other logic, however, is executed directly on the switching card and can continue operation without an active connection to the DCS.

During LS1, extensive upgrades of the ATLAS DCS infrastructure have been performed, including the heater pad control system. The Windows operating system has been replaced with Linux, the SCADA system has been upgraded from PVSS II to WINCC 3.11 (which is a rebranded successor to the former) and a transition from the use of the OPC Data Access protocol to the modern OPC Unified Architecture (OPC UA) has been performed. The underlying hardware has also been upgraded, with new computers and CAN bus interfaces.

The adaption to the OPC UA standard proved especially non-trivial for the heater pad system, which uses a non-standard ELMB firmware to implement the PID functionality and has a different set of input and output parameters. Customized XML descriptions of the I/O of the switching cards and control cards for use with the OPC UA server was prepared together with an automated procedure to generate full server configurations for the installed system.

Special care was taken to ensure that the WINCC project is always recreatable with minimum manual effort beyond importing control scripts and user interface panels into an empty project. This is to make sure that the project is always in a reproducible state and that a new installation can be immediately prepared in case of a system failure. To this end, a script is used to automatically generate the WINCC datapoint structure (consisting of more than 10 000 elements), the corresponding OPC address mapping, and default configurations to be written to each card upon reset from a plain-text file describing the layout of the installed heater pads. It also sets up OPC UA subscription groups for datapoints that are continuously read from the system. The change to a “subscription” paradigm is a significant improvement introduced with the move to OPC UA, in which the server monitors requested variables and notifies the client only in the case of changes. This makes the system more responsive and reduces the amount of inter-process communication compared to continuous polling by the client.

A test system using a dummy load to simulate connected heater pads, which was originally used during development of the control system, was recommissioned and used to exercise the full migration process before implementing changes in the production system. The test system now consists of:

- Dell PowerEdge R620 server with Scientific Linux CERN 6,
- Systec 8 port CAN bus controller,
- one controller card and one switching card,
- thermistors and resistors to emulate connected heater pads,

- WINCC 3.11 with a similar setup as on the production system (this instance, however, is configured to run stand-alone while the production version is part of a distributed system),
- OPC UA Server,
- UAEXPERT software for interactive communication with the OPC UA server,
- low level tools for frame-by-frame debugging of CAN communication.

After migration of the production system, this setup is used for continuing work on the heater pad control system. During LS1, the software/hardware mapping of heater pads was also verified and corrected, and additional updates were made to the software, including control panel functions and alarm status definitions. Documentation on how to handle hardware failures was also assembled.

Part III: Data analyses

5. Analysis techniques

5.1 Signal and background processes

This thesis presents searches for light and heavy charged Higgs bosons produced, respectively, in top quark decays and in association with a top quark. Final states involving leptons (electrons and muons) and b quarks are used in all analyses. The largest backgrounds thus come from Standard Model processes with top quarks, in particular the process $gg \to t\bar{t} \to b\bar{b}W^+W^-$, and also from vector boson production in association with jets. The modeling of signal events and the main backgrounds is performed with Monte Carlo simulations. Some backgrounds are difficult to simulate correctly and are therefore estimated using data-driven techniques. In particular, this is the case for multi-jet processes. Such events can yield "fake" or non-prompt leptons that are misidentified as electrons or muons from the hard process. This background is always estimated using the matrix method, which will be described in section 5.3. With the event selections considered in the following, backgrounds with misidentified hadronic tau decays arise mainly from $t\bar{t}$ events. The misidentification probability is, however, not expected to be well reproduced by the simulation. In analyses of the data collected in 2011, this background is estimated using simulated events corrected to account for the misidentification probabilities measured in the data. In analyses of the data collected in 2012, this background is instead estimated with the matrix method, which does not directly depend on simulated events.

5.1.1 Data samples

Only events recorded with stable proton beams and all ATLAS detectors fully operational are used for the analyses presented here. The 2011 dataset with $\sqrt{s} = 7$ TeV fulfilling these conditions corresponds to an integrated luminosity of 4.6 fb^{-1} with an uncertainty of 3.9%, while the 2012 dataset with $\sqrt{s} = 8$ TeV corresponds to an integrated luminosity of 20.3 fb^{-1} with an uncertainty of 2.8%. The analysis presented in section 6.1 is performed with only the first 1.03 fb^{-1} of data collected in 2011. Events are only used for analysis if they fulfill basic data quality criteria and also do not contain any jet consistent with having originated from instrumental effects such as calorimeter noise or non-collision backgrounds. Events are also required to have at least five tracks with $p_{\mathrm{T}} > 400$ MeV associated to the primary vertex. The primary vertex is the reconstructed vertex with the highest $\sum p_{\mathrm{T}}^2$ of associated tracks.

In all analyses, events are triggered by unprescaled single-lepton (electron or muon) triggers with the lowest threshold available in each data-taking period. An OR condition with a trigger having a higher p_{T} threshold but relaxed isolation requirements allows for improved efficiency during the data-taking of later periods in 2011 and during 2012.

5.1.2 Simulated events

The main samples of simulated events are summarized in Tables 5.1 and 5.2. The listed cross sections depend on the exact generator settings, which often include filters for "interesting" events containing high-p_{T} leptons, and should not be compared directly between e.g. samples of different center-of-mass energies. Details on each process are given in the sections below.

Signal processes

Three types of signal samples with light charged Higgs bosons have been used: $t\bar{t} \to b\bar{b}H^+W^-$, $t\bar{t} \to b\bar{b}H^-W^+$, and $t\bar{t} \to b\bar{b}H^+H^-$, where the charged Higgs bosons decays into $\tau\nu$. The cross sections of the signal processes depend only on the total cross section for $t\bar{t}$ production and on the branching fraction $\mathscr{B}(H^+ \to \tau\nu)$. These events are simulated with PYTHIA 6 [60], using the CTEQ6L1 PDF set [61]. For the analyses of 7 TeV data, samples are generated with the charged Higgs boson mass m_{H^+} between 90 GeV and 160 GeV, in steps of 10 GeV. For the analyses of 8 TeV data, the mass range is increased to 80 GeV $\leq m_{H^+} \leq$ 160 GeV.

Heavy charged Higgs bosons are only searched for in the analyses of 8 TeV data, where the mass range 180 GeV $\leq m_{H^+} \leq$ 1 TeV is considered. Events are generated with POWHEG [62], using the CT10 PDF set [63], according to the 5FS process $gb \to tH^+$. The parton shower, hadronization, and underlying event are simulated with PYTHIA 8 [64]. The charged Higgs boson decays via $H^+ \to \tau\nu$. Samples are generated with m_{H^+} at 180 GeV, 190 GeV, then in steps of 25 GeV in the range 200–600 GeV, and finally at 750 GeV and 1 TeV. The ratio between the natural width of the charged Higgs boson and its mass is 3.5% for a mass of 600 GeV in the Type II 2HDM with $\tan\beta = 50$, and decreases rapidly with lower values of $\tan\beta$. As this is much smaller than the experimental resolution, events are generated with the narrow-width approximation $\Gamma_{H^+} = 0$ in order to obtain model-independent results.

For charged Higgs bosons close to the mass of the top quark, there is interference between the two production mechanisms. Presently, no event generator approved for use in ATLAS takes this interference into account. This mass region is also more difficult to study experimentally as one of the b quarks is produced nearly at rest. Hence, this region is not included in the analyses.

Table 5.1. *Simulated events used for analysis of 7 TeV data. All processes except Wt production are required to contain at least one lepton $\ell = e, \mu, \tau$ in the decay chain. In the analysis of early data presented in section 6.1,* MC@NLO *is used also for the t-channel production of single top quark events, and the $V+\text{heavyflavor}$ samples are not included. The $W+c(\bar{c})+\text{jets}$ samples are used only in section 6.3.*

Process	Generator	Cross section [pb]
$t\bar{t}$	MC@NLO	90.6
Single top quark (t-channel)	ACERMC	20.9
Single top quark (s-channel)	MC@NLO	1.5
Single top quark (Wt-channel)	MC@NLO	15.7
$W+\text{jets}$	ALPGEN	3.1×10^4
$Wb\bar{b}+\text{jets}$	ALPGEN	1.3×10^2
$Wc\bar{c}+\text{jets}$	ALPGEN	3.6×10^2
$Wc+\text{jets}$	ALPGEN	1.1×10^3
$Z/\gamma^*+\text{jets}$ ($m_{\ell\ell} > 10$ GeV)	ALPGEN	1.5×10^4
$Z/\gamma^* b\bar{b}+\text{jets}$ ($m_{\ell\ell} > 30$ GeV)	ALPGEN	38.7
WW	HERWIG	17.0
ZZ	HERWIG	1.3
WZ	HERWIG	5.5
$t\bar{t} \to b\bar{b}H^\pm W^\mp$, $t\bar{t} \to b\bar{b}H^+H^-$ with $H^+ \to \tau\nu$	PYTHIA	–

Table 5.2. *Simulated events used for analysis of 8 TeV data. All processes except Wt production are required to contain at least one lepton $\ell = e, \mu, \tau$ in the decay chain.*

Process	Generator	Cross section [pb]
$t\bar{t}$	POWHEG	137.3
Single top quark (t-channel)	POWHEG	28.4
Single top quark (s-channel)	POWHEG	1.8
Single top quark (Wt-channel)	POWHEG	22.4
$W+\text{jets}$	ALPGEN	3.6×10^4
$Wb\bar{b}+\text{jets}$	ALPGEN	1.5×10^2
$Wc\bar{c}+\text{jets}$	ALPGEN	4.8×10^2
$Wc+\text{jets}$	ALPGEN	1.7×10^3
$Z/\gamma^*+\text{jets}$ ($m_{\ell\ell} > 10$ GeV)	ALPGEN	5.2×10^3
$Z/\gamma^* b\bar{b}+\text{jets}$ ($m_{\ell\ell} > 30$ GeV)	ALPGEN	60.7
$Z/\gamma^* c\bar{c}+\text{jets}$ ($m_{\ell\ell} > 30$ GeV)	ALPGEN	2.3×10^2
WW	HERWIG	20.9
ZZ	HERWIG	1.5
WZ	HERWIG	7.0
$t\bar{t} \to b\bar{b}H^\pm W^\mp$ with $H^+ \to \tau\nu$	PYTHIA	–
$\bar{t}H^+$ with $H^+ \to \tau\nu$	POWHEG	–

Backgrounds with top quarks

In the analyses using 7 TeV data, the generation of Standard Model $t\bar{t}$ and single top quark events is performed with MC@NLO [65], with the exception that in the analyses described in sections 6.2 and 6.3, ACERMC [66] is used for t-channel single top quark production. The parton shower, hadronization, and underlying event are simulated with HERWIG [67] and JIMMY [68] for events generated with MC@NLO and with PYTHIA 6 for events generated with ACERMC. In the analysis using 8 TeV data, the generation of SM $t\bar{t}$ and single top quark events is performed with POWHEG. The parton shower, hadronization, and underlying event are simulated with PYTHIA 8. The PDF set used is CT10. The nominal simulations of $t\bar{t}$ events are also compared with alternative samples to evaluate the systematic uncertainty associated with the choice of event generator and parton shower programs, as will be detailed in the description of each analysis. The top quark mass is taken to be 172.5 GeV in all samples. Inclusive cross sections are taken from approximate next-to-next-to-leading-order (NNLO) calculations for $t\bar{t}$ production at 7 TeV [69] and 8 TeV [70], and for single top quark production [71–73]. Overlaps in the final states between the Wt and $t\bar{t}$ samples are removed.

In the analyses using 8 TeV data, a reweighting scheme is applied to the $t\bar{t}$ events based on the generator level p_{T} of both the top quark and the $t\bar{t}$ system. The applied weights were derived to improve agreement between simulated events and the measured $t\bar{t}$ differential cross section at 7 TeV [74].

Backgrounds with vector bosons

Single vector boson production is simulated with ALPGEN [75], using the CTEQ6L1 PDF set. In the analyses using 7 TeV data, the parton shower, hadronization, and underlying event are added with POWHEG and JIMMY. In the analyses using 8 TeV data, PYTHIA 8 is used. Inclusive $W+$jets and $Z/\gamma^{*}+$jets samples are formed by adding samples generated with up to five additional partons. The so-called MLM parton-jet matching scheme [76] is used to avoid overlap of parton configurations created by the event generator and the parton shower. In most analyses, dedicated samples containing additional b and c quarks are used in order to have a larger fraction of such events. Overlaps with events in the inclusive sample are removed. The cross sections are normalized to NNLO predictions [77, 78]. Diboson (WW, ZZ, and WZ) events are simulated with HERWIG and normalized to NLO predictions [79].

Pile-up, tuning, and charged leptons

All simulated events described above are overlaid with a variable number of minimum-bias events in order to simulate the effect of multiple pp collisions. PYTHIA 6 is used to generate these events for the 7 TeV samples, while PYTHIA 8 is used for the 8 TeV samples. At an early stage in each analysis, the simulated events are reweighted to match the distribution of the average

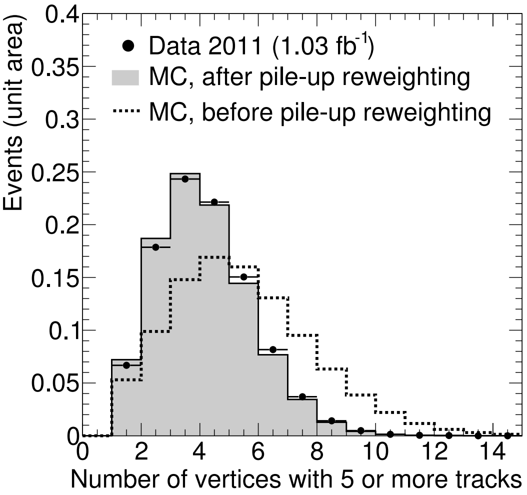

Figure 5.1. Example of pile-up reweighting of a $t\bar{t}$ Monte Carlo (MC) sample to match the distribution of the average number of simultaneous pp collisions in data. The reweighting is validated by comparing the normalized distributions of the number of reconstructed vertices.

number of pp collisions per bunch crossing in the corresponding data sample, as illustrated in Figure 5.1.

Some tools are tuned to describe ATLAS data. The AUET2 tune is used with HERWIG and PYTHIA 6, except when interfaced to ACERMC, in which case the AUET2B tune is used [80, 81]. The Perugia 2011 C tune [82] is used with PYTHIA 8. In all cases, except with PYTHIA 8, TAUOLA [83] is used to model the decays of tau leptons and PHOTOS [84] is used to model photon radiation from charged leptons.

5.2 Particle identification

5.2.1 Electrons

Electrons traverse the inner detector and deposit most of their energy in the electromagnetic calorimeter. Electron candidates are therefore reconstructed by finding a cluster of energy deposits in the calorimeter that matches, both in terms of position and energy, a track in the inner detector. The transverse energy of the electron candidate is defined as $E_\mathrm{T} \equiv E_\mathrm{clus}/\cosh(\eta_\mathrm{track})$, combining the precision information on the track direction with the superior resolution of the calorimeter at high energies. The analyses presented in this thesis require electrons to have E_T larger than 15–25 GeV and to be within $|\eta_\mathrm{clus}| < 2.47$. In the transition region between the barrel and end-cap calorimeters ($1.37 < |\eta_\mathrm{clus}| < 1.52$), the electron identification and energy resolution are degraded by the large amount of material in front of the instrumented layers. Electrons in this region are therefore excluded.

The electron identification is refined by a set of quality requirements on calorimeter and track variables that include information on the shower shape, the number of hits in the inner detector, and the longitudinal impact parameter with respect to the primary vertex. The exact criteria used have evolved over time but typically correspond to an electron efficiency of 70–80% given the above mentioned E_T thresholds. To favor prompt electrons over electrons produced inside jets, tracking- and calorimeter-based isolation requirements are imposed within cones of radius $R = 0.2$ respectively 0.3 around the electron. The thresholds used are E_T- and η-dependent to give a flat efficiency of about 90% for true isolated electrons. The track-based isolation for electrons was a later introduction and is not used in the analysis presented in section 6.1.

5.2.2 Muons

Muons penetrate all ATLAS detectors. All detector systems can therefore contribute to the muon reconstruction and identification. The analyses documented in this thesis use muons reconstructed with a track in both the inner detector and the muon spectrometer, with quality requirements on the number of hits and on the longitudinal impact parameter with respect to the primary vertex. Muons must therefore be in the range $|\eta| < 2.5$ covered by the inner detector. The muon p_T is obtained as a weighted combination of both tracks. It is required to be at least 15 GeV in the analyses using data with $\sqrt{s} = 7$ TeV and at least 25 GeV in the analyses using data with $\sqrt{s} = 8$ TeV. To reduce the contribution of muons produced inside jets, isolation requirements are applied. The analyses of 7 TeV data use fixed thresholds on the transverse momentum of inner detector tracks and calorimeter energy deposits (excluding those originating from the muon itself) within cones of radius $R = 0.2$ respectively 0.3. In the analysis of 8 TeV data, only the track-based isolation is used, but with a p_T-dependent cone size.

5.2.3 Jets

Jets are reconstructed from energy clusters in the calorimeters using the anti-k_t algorithm [85, 86] with a size parameter value $R = 0.4$. Two different jet energy calibration schemes [87] are used in the analyses presented here. The analyses of 7 TeV data use a scheme in which the (non-compensating) calorimeter cells are initially calibrated at the electromagnetic scale appropriate for energy deposits from electrons and photons. The energy of a reconstructed jet is then first corrected for pile-up effects and then restored to the hadronic energy scale based on correction factors derived from simulation. The analysis of 8 TeV data use jets reconstructed with locally calibrated clusters. In this scheme, which aims at reducing energy fluctuations, each cluster is individually classified as either electromagnetic or hadronic based on shape variables. It is then calibrated accordingly, with additional corrections to account for energy lost out of clusters and in dead material. The anti-k_t algorithm is run over the locally calibrated clusters, and the reconstructed jets are corrected for pile-up. Only jets with p_T above 20–25 GeV are considered in the analyses presented here. Furthermore, the use of b-tagging (see below), which relies on tracking information, excludes the use of jets above $|\eta| = 2.5$.

Jet vertex fraction

To select jets originating from the hard-scatter interaction, the Jet Vertex Fraction (JVF) method [88] is used. The JVF quantity is the fraction of the total momentum of all charged particle tracks associated with the jet that originate from the primary vertex (pv):

$$\mathrm{JVF}(\mathrm{jet},\mathrm{pv}) = \frac{\sum\limits_i p_\mathrm{T}(\mathrm{trk}_i^\mathrm{jet},\mathrm{pv})}{\sum\limits_n\sum\limits_j p_\mathrm{T}(\mathrm{trk}_j^\mathrm{jet},\mathrm{vtx}_n)} \tag{5.1}$$

In all analyses, except section 6.1, jets with $p_\mathrm{T} < 50$ GeV and $|\eta| < 2.4$ are required to have JVF > 0.5 (jets that do not have any associated tracks are assigned JVF $= 1$). This selection is shown to be insensitive to pile-up.

***b*-tagging**

Jets that originate from a b quark can be identified by tagging the decay of a B-hadron inside the jet. The large masses (> 5 GeV) and relatively long lifetimes (1.5 ps) of B-hadrons can be exploited for this purpose. The b-tagging methods used in the analyses presented here ultimately rely on three different algorithms. The IP3D algorithm uses impact parameter significances in both the longitudinal and transverse directions for all tracks within a jet. The SV1 algorithm attempts to explicitly reconstruct a secondary vertex. Finally, the JetFitter algorithm seeks to reconstruct the full decay chain from a B-hadron to a charm hadron to its decay products, i.e. the common flight path and the position of additional vertices along it. These methods are combined into highly performant taggers using neural networks. The dilepton analysis in section 6.1 uses a b-tagger which combines information from JetFitter and IP3D, while the other analyses in this thesis use a b-tagger that also includes information from SV1. In both cases, the working point has been chosen such that the tagging efficiency is approximately 70% in $t\bar{t}$ events.

5.2.4 Hadronic tau decays

The tau lepton has a mean lifetime of only 0.3 ps, meaning that it decays very close to the interaction point. In the case of leptonic decays, it is not possible to reliably identify electrons or muons as originating from a tau. However,

Table 5.3. *Common decay modes of tau leptons [1].*

Decay mode	Branching fraction
Leptonic	35.2%
$e\bar{\nu}_e\nu_\tau$	17.8%
$\mu\bar{\nu}_\mu\nu_\tau$	17.4%
1-prong hadronic	50.1%
$\pi^-\nu_\tau$	10.8%
$\pi^-\pi^0\nu_\tau$	25.5%
$\pi^-\pi^0\pi^0\nu_\tau$	9.3%
other	4.5%
3-prong hadronic	14.6%
$\pi^-\pi^-\pi^+\nu_\tau$	9.3%
$\pi^-\pi^-\pi^+\pi^0\nu_\tau$	4.6%
other	0.7%

approximately 65% of tau leptons decay to hadrons, and these decays have rather characteristic signatures. Table 5.3 summarizes the most common tau decay modes. The hadronic decay modes typically contain either one or three charged pions, and are respectively referred to as 1-prong and 3-prong decays.

In order to reconstruct hadronically decaying tau leptons [89, 90], henceforth denoted τ_{had}, all anti-k_t jets constructed with the size parameter $R = 0.4$ are considered as τ_{had} *candidates* if they have $p_{\text{T}} > 10$ GeV and contain either one or three tracks within the central cone of radius $R = 0.2$. This would be consistent with the presence of one or three charged pions among the tau decay products. Identification variables are then calculated and combined into multivariate discriminants used to reject τ_{had} candidates originating from jets and leptons. Variables related to the shower shape are used to discriminate between real τ_{had} candidates and jets, exploiting the fact that quark- or gluon-initiated jets tend to be wider than jets from hadronic tau decays. The significance of a reconstructed secondary vertex is also important, in particular for 3-prong τ_{had} candidates. Variables based on tracking information are relatively robust against pile-up effects. To decrease the pile-up dependence of the calorimeter based variables, only clusters within the central cone ($R = 0.2$) are considered in the 2012 data (correspondingly $R = 0.4$ in 2011). Different sets of variables are combined using either a projective Log-Likelihood function (LLH), which assumes that the inputs are uncorrelated, or Boosted Decision Trees (BDT). In the analyses presented in this thesis, the LLH-based identification is used with the 2011 dataset, while the BDT is used with the 2012 dataset. Based on p_{T}- and η-dependent thresholds on the discriminant output, τ_{had} candidates are accepted with an efficiency of 30% for 1-prong and 35% for 3-prong τ_{had} candidates in the 2011 data. In the 2012 data, these numbers become 40% and 35%, respectively. After rejection of a large fraction of τ_{had} candidates originating from jets, the background from electrons may become important, in particular for 1-prong τ_{had} candidates. Electrons are rejected using a dedicated BDT, with input variables sensitive to the transition radiation emitted by an electron, as well as the shorter and narrower shower in the electromagnetic calorimeter compared to hadronic tau decays. Finally, a cut-based veto is employed to suppress τ_{had} candidates originating from an energetic calorimeter cluster associated with a muon track in cases where the muon was not successfully reconstructed in the muon spectrometer.

The τ_{had} energy is calculated based on calorimeter clusters within the central cone, with a special calibration scheme appropriate for the specific mixture of charged and neutral pions present in hadronic tau decays. Due to the use of tracking information, the τ_{had} reconstruction is limited to the region $|\eta| < 2.5$ covered by the inner tracker.

5.2.5 Removal of overlapping objects

When multiple objects overlap geometrically, the following steps are applied, in this order:

1. a τ_{had} object is removed if found within $\Delta R < 0.2$ of a muon;
2. a τ_{had} object is removed if found within $\Delta R < 0.2$ of an electron;
3. a muon is removed if found within $\Delta R < 0.4$ of a jet;
4. the single closest jet to an electron is removed if it is within $\Delta R < 0.2$;
5. an electron is rejected if found within $\Delta R < 0.4$ of a jet;
6. a τ_{had} object is removed if found within $\Delta R < 0.4$ of a b-tagged jet;
7. a jet is removed if found within $\Delta R < 0.4$ of a τ_{had}.

The procedures involving τ_{had} objects are only applied in analyses using these objects. The removal of a τ_{had} object overlapping with a b-tagged jet is only performed in the most recent analyses presented in section 6.3 and chapter 7, and in the latter case, only 3-prong τ_{had} objects are considered in this step. Finally, in the rare case where an electron and a muon share a track in the inner detector, the whole event is discarded.

5.2.6 Missing transverse energy

Neutrinos do not interact with any detector and hence are effectively invisible. Their presence in an event can be inferred, however, from an apparent violation of momentum conservation in the transverse plane. The vector sum of transverse momenta in an event is first constructed from all energy clusters in the calorimeters, with the appropriate calibration of any associated high level objects, and from muon tracks reconstructed in the muon spectrometer. Energy deposited by muons in the calorimeter is taken into account with different treatments of isolated and non-isolated muons. Energy deposits in calorimeter cells not associated to any object are also included. The analyses presented in this thesis do not use any special treatment of τ_{had} objects for this purpose, they are treated as ordinary jets. The magnitude of the total transverse momentum is equal to that of the *missing transverse momentum* which would be needed in the opposite direction in order to balance the total sum to zero. It is denoted $E_{\text{T}}^{\text{miss}}$ and would correspond to the transverse energy of a single, massless, undetected particle in the event.

5.3 The matrix method

Non-negligible backgrounds arise from events with misidentified leptons or hadronic tau decays. These include "fake" signatures of such objects and, in the case of leptons, real but "non-prompt" leptons originating from hadronic objects. Misidentified electrons arise from the semileptonic decays of b and c quarks, photon conversion, and from jets that deposit a large fraction of their energy in the electromagnetic calorimeter. Misidentified muons arise from semileptonic decays of b and c quarks, in-flight decays of charged hadrons, and from punch-through of energetic particles into the muon system. Misidentified τ_{had} objects are mainly caused by quark- or gluon-initiated jets, or from electrons, and to a lower extent by energy deposits in the calorimeter coming from passing muons.

In event selections requiring a single lepton, the largest such background is from multi-jet events. In event selections requiring two leptons or one lepton and a τ_{had}, backgrounds with misidentified objects consist of $t\bar{t}$ and $W+\text{jets}$ events with one real lepton and one misidentified lepton or τ_{had}, and to a much smaller extent, events with two misidentified objects.

These backgrounds are particularly challenging to simulate accurately, and would in addition require very large samples of simulated events due to their low probability to occur. Hence, they are estimated using data-driven techniques. In the analyses presented here, the so-called *matrix method* is frequently used for this purpose. This method uses object (mis)identification probabilities measured in data, simulated events, or a mixture of both, and can be used to assess the backgrounds of events with one or several misidentified objects, both in terms of overall normalization and in the distributions of any number of kinematic variables. It takes its name from a characteristic equation appearing in its derivation, as will be shown below.

5.3.1 Description of the matrix method

Consider first the case where only one reconstructed object (electron, muon or τ_{had}) has a significant possibility of being misidentified. We define two event selections, differing only in the isolation and/or identification criteria applied to that type of object. The *tight* criteria correspond to the nominal object selection (i.e. as detailed in section 5.2) and supposedly select mainly real objects.

The *loose* criteria select a larger fraction of events with misidentified objects and are obtained by relaxing some of the requirements of the tight selection. By construction, the loose selection is a superset of the tight selection.

A sample of N events passing the loose object selection contains N^{T} events in which the object fulfills the *tight* selection and N^{L} events in which the object fulfills the *loose but not tight* selection. It also contains N_{r} events with a real (r) object and N_{m} events with a misidentifed (m) object: $N_{\mathrm{r}}+N_{\mathrm{m}}=N=N^{\mathrm{L}}+N^{\mathrm{T}}$. We seek to determine the number of events in N^{T} that are also in N_{m}, that is, the amount of events passing the *tight* selection that contain a misidentified object.

If we define p_{r} and p_{m} as the probabilities for a real or misidentified object, respectively, to pass the tight criteria if it has already passed the loose criteria, the following relations can be established:

$$\begin{pmatrix} N^{\mathrm{T}} \\ N^{\mathrm{L}} \end{pmatrix} = \begin{pmatrix} p_{\mathrm{r}} & p_{\mathrm{m}} \\ 1-p_{\mathrm{r}} & 1-p_{\mathrm{m}} \end{pmatrix} \times \begin{pmatrix} N_{\mathrm{r}} \\ N_{\mathrm{m}} \end{pmatrix}. \tag{5.2}$$

The number of events, $N_{\mathrm{m}}^{\mathrm{T}}$, in which the misidentified object passes the tight selection can, after inverting the 2×2 matrix above, be written as:

$$N_{\mathrm{m}}^{\mathrm{T}} = p_{\mathrm{m}}N_{\mathrm{m}} = \frac{p_{\mathrm{m}}p_{\mathrm{r}}}{p_{\mathrm{r}}-p_{\mathrm{m}}}N^{\mathrm{L}} + \frac{p_{\mathrm{m}}(p_{\mathrm{r}}-1)}{p_{\mathrm{r}}-p_{\mathrm{m}}}N^{\mathrm{T}}. \tag{5.3}$$

This equation is, however, only valid if p_{r} and p_{m} are constants. This is typically not the case in a broad selection of events. Instead of directly calculating $N_{\mathrm{m}}^{\mathrm{T}}$ for a whole selection of events, a weight is assigned to each individual event and the total contribution of misidentified objects is obtained by summing over all events. The weights, denoted w^{T} for events that pass the tight selection and w^{L} for events that pass the loose-but-not-tight selection, have the form:

$$w^{\mathrm{L}} = \frac{p_{\mathrm{m}}p_{\mathrm{r}}}{p_{\mathrm{r}}-p_{\mathrm{m}}}, \qquad w^{\mathrm{T}} = \frac{p_{\mathrm{m}}(p_{\mathrm{r}}-1)}{p_{\mathrm{r}}-p_{\mathrm{m}}}, \tag{5.4}$$

where p_{r} and p_{m} are now functions of the properties of the object of interest (for example its p_{T}). Note that the weight is negative for events in the tight sample.

The (mis)identification probabilities must be measured, in the data or in simulated events. If the available control sample is of limited size, a too fine binning of p_{m} and p_{r} may introduce large statistical fluctuations of the measured values. This effectively limits the number of variables that can be used in the parametrization of p_{m} and p_{r}. If p_{m} and p_{r} depend only on largely uncorrelated variables, however, the situation simplifies. With n uncorrelated variables $\boldsymbol{x}$, p_{m} and p_{r} can be constructed by convoluting n one-dimensional parametrizations. If $\langle p_{\mathrm{m}}\rangle$ and $\langle p_{\mathrm{r}}\rangle$ are the average values of p_{m} respectively

p_r over the whole data sample, the final identification and misidentification probabilities in each event are computed as:

$$p_\mathrm{r} = p_\mathrm{r}(x_0) \times \prod_{i=1}^{n-1} \frac{p_\mathrm{r}(x_i)}{\langle p_\mathrm{r} \rangle}, \qquad p_\mathrm{m} = p_\mathrm{m}(x_0) \times \prod_{i=1}^{n-1} \frac{p_\mathrm{m}(x_i)}{\langle p_\mathrm{m} \rangle}. \tag{5.5}$$

This method is used in the matrix method for misidentified leptons.

5.3.2 Two misidentified objects

Having now established the strategy, the matrix method is easily generalized to treat events with a larger number of potentially misidentified objects. Of interest in this thesis are events with two leptons, or one lepton and one τ_had. In this case, we distinguish four classes of events, labeled rr, rm, mr, and mm. They correspond to events with two real objects, events with one real and one misidentified object (in two different combinations), and events with two misidentified objects. For each object, a nominal, tight (T) selection and a loose-but-not-tight (L) selection are defined.

A loose sample of events is again considered, consisting of the four subsets N^TT, N^TL, N^LT, and N^LL. The composition of the loose sample in terms of N_rr events with two real objects, N_rm (N_mr) events where the first (second) object is real and the other one is misidentified, and N_mm events with two misidentified objects, is not directly observable. The two sets of numbers are however related by:

$$\begin{pmatrix} N^\mathrm{TT} \\ N^\mathrm{TL} \\ N^\mathrm{LT} \\ N^\mathrm{LL} \end{pmatrix} = \begin{pmatrix} p_\mathrm{r1}\, p_\mathrm{r2} & p_\mathrm{r1}\, p_\mathrm{m2} & p_\mathrm{m1}\, p_\mathrm{r2} & p_\mathrm{m1}\, p_\mathrm{m2} \\ p_\mathrm{r1}\, \overline{p_\mathrm{r2}} & p_\mathrm{r1}\, \overline{p_\mathrm{m2}} & p_\mathrm{m1}\, \overline{p_\mathrm{r2}} & p_\mathrm{m1}\, \overline{p_\mathrm{m2}} \\ \overline{p_\mathrm{r1}}\, p_\mathrm{r2} & \overline{p_\mathrm{r1}}\, p_\mathrm{m2} & \overline{p_\mathrm{m1}}\, p_\mathrm{r2} & \overline{p_\mathrm{m1}}\, p_\mathrm{m2} \\ \overline{p_\mathrm{r1}}\, \overline{p_\mathrm{r2}} & \overline{p_\mathrm{r1}}\, \overline{p_\mathrm{m2}} & \overline{p_\mathrm{m1}}\, \overline{p_\mathrm{r2}} & \overline{p_\mathrm{m1}}\, \overline{p_\mathrm{m2}} \end{pmatrix} \times \begin{pmatrix} N_\mathrm{rr} \\ N_\mathrm{rm} \\ N_\mathrm{mr} \\ N_\mathrm{mm} \end{pmatrix} \tag{5.6}$$

where the numeric index distinguishes the two objects of interest, and the short-hand notation $\overline{p} \equiv (1-p)$ is introduced to exhibit the regular structure of the matrix.

The number of events with two tight objects, where *at least* one of them is misidentified, can be written as:

$$N^\mathrm{TT}_\mathrm{misid} = N^\mathrm{TT}_\mathrm{rm} + N^\mathrm{TT}_\mathrm{mr} + N^\mathrm{TT}_\mathrm{mm} = p_\mathrm{r1} p_\mathrm{m2} N_\mathrm{rm} + p_\mathrm{m1} p_\mathrm{r2} N_\mathrm{mr} + p_\mathrm{m1} p_\mathrm{m2} N_\mathrm{mm}. \tag{5.7}$$

As before, solving equation (5.6) for N_mm, N_mr and N_rm gives the weights to be applied to events passing the LL, LT, TL, respectively TT selections:

$$\begin{aligned} w^\mathrm{LL} &= \frac{-p_\mathrm{r1} p_\mathrm{r2} p_\mathrm{m1} p_\mathrm{m2}}{(p_\mathrm{r1} - p_\mathrm{m1})(p_\mathrm{r2} - p_\mathrm{m2})}, & w^\mathrm{TT} &= 1 - \frac{p_\mathrm{r1} p_\mathrm{r2} \overline{p_\mathrm{m1}}\, \overline{p_\mathrm{m2}}}{(p_\mathrm{r1} - p_\mathrm{m1})(p_\mathrm{r2} - p_\mathrm{m2})}, \\ w^\mathrm{LT} &= \frac{p_\mathrm{r1} p_\mathrm{r2} p_\mathrm{m1} \overline{p_\mathrm{m2}}}{(p_\mathrm{r1} - p_\mathrm{m1})(p_\mathrm{r2} - p_\mathrm{m2})}, & w^\mathrm{TL} &= \frac{p_\mathrm{r1} p_\mathrm{r2} (1 - p_\mathrm{m1}) p_\mathrm{m2}}{(p_\mathrm{r1} - p_\mathrm{m1})(p_\mathrm{r2} - p_\mathrm{m2})}. \end{aligned} \tag{5.8}$$

Similar weights can be derived for each of the indvidual $N^{\mathrm{TT}}_{\mathrm{rm}}$, $N^{\mathrm{TT}}_{\mathrm{mr}}$, and $N^{\mathrm{TT}}_{\mathrm{mm}}$ contributions, which can reveal the sensitivity of the analysis to different combinations of misidentified objects. The weights in equation (5.8) can also be conveniently expressed as functions of two sets of object-specific weights as constructed in equation (5.4):

$$\begin{aligned} w^{\mathrm{LL}} &= -w_1^{\mathrm{L}} \times w_2^{\mathrm{L}}, & w^{\mathrm{TT}} &= w_1^{\mathrm{T}} + w_2^{\mathrm{T}} - w_1^{\mathrm{T}} \times w_2^{\mathrm{T}}, \\ w^{\mathrm{TL}} &= (1 - w_1^{\mathrm{T}}) \times w_2^{\mathrm{L}}, & w^{\mathrm{LT}} &= w_1^{\mathrm{L}} \times (1 - w_2^{\mathrm{T}}). \end{aligned} \tag{5.9}$$

This form can have practical advantages if one wishes to combine the results of two independently developed methods for different object types.

5.4 Hypothesis testing

All results are interpreted by testing the compatibility of the data with the background-only and signal+background hypotheses using a modified frequentist *profile likelihood* method which incorporates systematic uncertainties as nuisance parameters and fits (profiles) them to the data. This procedure can minimize the impact of systematic uncertainties on the search sensitivity by taking advantage of background-dominated control regions.

5.4.1 Statistical model

Let m and n be the number of events that are expected respectively observed to pass some selection criteria. The expected number of events m depends on some *parameter of interest* μ, describing the strength of the signal process. It is chosen such that $\mu = 0$ corresponds to the background-only hypothesis and larger values of μ correspond to increasing amounts of signal. Uncertainties in the calculation of m are described by its additional dependence on a set of nuisance parameters $\boldsymbol{\theta}$ with unknown values. Each nuisance parameter θ_i is, however, provided with a nominal estimate $\tilde{\theta}_i$ and a Gaussian constraint $\mathrm{p}(\tilde{\theta}_i|\theta_i)$ which gives the estimated probability density of having obtained the estimate $\tilde{\theta}_i$ if the true value is in fact θ_i. A nuisance parameter could for example be the integrated luminosity, in which case $\tilde{\theta}_i$ is the measured luminosity and the standard deviation of $\mathrm{p}(\tilde{\theta}_i|\theta_i)$ is the uncertainty on the measurement. The *likelihood* of the model parameters μ and $\boldsymbol{\theta}$ having certain values given the observed n events is equal to the probability of obtaining the observed n events given those parameter values:

$$\mathscr{L}(\mu, \boldsymbol{\theta}) = \mathrm{Poisson}(n|\, m(\mu, \boldsymbol{\theta})) \prod_i \mathrm{p}(\tilde{\theta}_i|\theta_i). \tag{5.10}$$

This likelihood function describes a simple event counting experiment. Typically, the search sensitivity is improved by examining the distribution of some discriminating variable among the selected events. A likelihood function can then be built from the expected and observed number of events, m_j and n_j, found in each bin j of the distribution of this variable.

Furthermore, an analysis may simultaneously use multiple event selections. We call each event selection a Signal Region (SR) if it is expected to contain a significant amount of events from the signal process, or a Control Region (CR) if it mainly contributes to the sensitivity by constraining the nuisance parameters. The resulting likelihood is then given by:

$$\mathscr{L}(\mu,\boldsymbol{\theta}) = \prod_k \prod_{j_k} \text{Poisson}(n_{j_k} | m_{j_k}(\mu,\boldsymbol{\theta})) \prod_i \text{p}(\tilde{\theta}_i|\theta_i), \tag{5.11}$$

where each region k may use a different discriminating variable with j_k bins, or none (in which case j_k has only one possible value and n_{j_k} corresponds to all events found in that region).

Light charged Higgs boson

In searches for a light charged Higgs boson appearing in the decay of a top quark, the parameter of interest is the branching fraction $B \equiv \mathscr{B}(t \to bH^+)$. Varying this parameter changes not only the expected amount of signal but also the expected amount of background from $t\bar{t} \to b\bar{b}W^+W^-$ events. The cross sections of the possible $t\bar{t}$ decays are:

$$t\bar{t} \to b\bar{b}W^+W^- : \quad \sigma_{bbWW} = \sigma_{t\bar{t}} \times (1-B)^2 \tag{5.12}$$

$$t\bar{t} \to b\bar{b}H^\pm W^\mp : \quad \sigma_{bbHW} = \sigma_{t\bar{t}} \times 2B(1-B) \tag{5.13}$$

$$t\bar{t} \to b\bar{b}H^+H^- : \quad \sigma_{bbHH} = \sigma_{t\bar{t}} \times B^2. \tag{5.14}$$

As B is assumed to be small, the $t\bar{t} \to b\bar{b}H^+H^-$ process is ignored in the analyses presented here, unless otherwise stated. If an event selection has the acceptance rates ε_W and ε_H for $t\bar{t} \to b\bar{b}W^+W^-$ respectively $t\bar{t} \to b\bar{b}H^\pm W^\mp$ (as determined in the analysis), then the expected number of events m is given by:

$$m = m_W + m_H + m_{other} = m_{t\bar{t}}\left((1-B)^2\varepsilon_W + 2B(1-B)\varepsilon_H\right) + m_{other}, \tag{5.15}$$

where $m_{t\bar{t}}$ is the product of $\sigma_{t\bar{t}}$ and the integrated luminosity, and m_{other} accounts for non-$t\bar{t}$ backgrounds.

Heavy charged Higgs boson

At first order, the presence of a heavy charged Higgs boson does not affect the backgrounds. The parameter of interest is therefore simply the cross section for heavy charged Higgs boson production. This is similar to the case of the Standard Model Higgs boson searches at the LHC, however in that case (see Figure 3.2), μ is typically expressed in units of the cross section predicted by the Standard Model. Here, the focus is on model-independent searches, hence there is no predicted cross section and μ is a dimensionful quantity.

5.4.2 Exclusion limits

If the data appears to be compatible with the background-only hypothesis, the analysis proceeds by rejecting the signal hypothesis for various values of μ. The test statistic used is the one-sided profile likelihood ratio [91],

$$\tilde{q}_\mu \equiv \begin{cases} -2\log\dfrac{\mathscr{L}(\mu,\hat{\hat{\boldsymbol{\theta}}}_\mu)}{\mathscr{L}(0,\hat{\hat{\boldsymbol{\theta}}}_0)} & \hat{\mu}<0, \\ -2\log\dfrac{\mathscr{L}(\mu,\hat{\hat{\boldsymbol{\theta}}}_\mu)}{\mathscr{L}(\hat{\mu},\hat{\boldsymbol{\theta}})} & 0\leq\hat{\mu}\leq\mu, \\ 0 & \hat{\mu}>\mu. \end{cases} \tag{5.16}$$

It is constructed by fitting the model parameters to the data to find the values $\hat{\boldsymbol{\theta}}$ and $\hat{\mu}$ that maximize $\mathscr{L}(\hat{\mu},\hat{\boldsymbol{\theta}})$, as well as the nuisance parameter values $\hat{\hat{\boldsymbol{\theta}}}_\mu$ that maximize $\mathscr{L}(\mu,\hat{\hat{\boldsymbol{\theta}}}_\mu)$ for a given μ. The test statistic is then a function of μ alone and can be seen as a measure of the discrepancy between the data and a given hypothesis about the value of μ: higher $\tilde{q}_\mu$ values correspond to an increasing disagreement. The difference is quantified by calculating the probability, under the given hypothesis, of obtaining a value of $\tilde{q}_\mu$ at least as large as the observed value, $\tilde{q}_\mu^{\text{obs}}$.

If $\text{P}(\tilde{q}_\mu \geq \tilde{q}_\mu^{\text{obs}}|\mu) < \alpha$, then this value of μ could be regarded as excluded at a confidence level of $1-\alpha$. A problem with this approach, however, is that it is susceptible to $\text{P}(\tilde{q}_\mu \geq \tilde{q}_\mu^{\text{obs}}|\mu)$ dropping below α due to a statistical fluctuation of $\tilde{q}_\mu^{\text{obs}}$. This may lead us to exclude a hypothesis to which the experiment is not actually sensitive. In fact, in the limit where the amount of signal is very small compared to the background, the probability for this to happen approaches α. We therefore use the CL_s method [92], which weights the probability of obtaining $\tilde{q}_\mu^{\text{obs}}$ under a given hypothesis about the value of μ with the probability of obtaining q_0^{obs} under the background-only hypothesis, $\mu=0$. The hypothesis is rejected at the confidence level $1-\alpha$ if

$$\text{CL}_\text{s} \equiv \frac{\text{P}(\tilde{q}_\mu \geq \tilde{q}_\mu^{\text{obs}}|\mu)}{\text{P}(\tilde{q}_\mu \geq \tilde{q}_\mu^{\text{obs}}|0)} < \alpha. \tag{5.17}$$

The CL_s method ensures that the signal hypothesis will not be excluded if the data disagrees with both the signal and background-only hypotheses. In particular, if the distributions of the test statistic are very similar for the two hypotheses, then the CL_s quantity always remains large – this means that no exclusion is made if the experiment can not distinguish between the signal and background-only hypotheses. Because the denominator in the definition of CL_s is a probability, it is never larger than one. The CL_s method therefore produces exclusion limits that are more conservative than using $\text{P}(\tilde{q}_\mu \geq \tilde{q}_\mu^{\text{obs}}|\mu)$ directly.

As is the convention[1] at the LHC, α is chosen to be 0.05. The analysis is then carried out by starting from the background-only hypothesis and increasing μ until $\mathrm{CL_s}$ reaches α. Upper limits on μ are thus obtained at the 95% confidence level. Expected limits in the absence of signal are determined by repeating the procedure while using an artificial "Asimov" dataset as input instead of the actual data. The Asimov dataset is an estimate of what the data would look like in the absence of statistical fluctuations, if the background-only hypothesis was true. It is created by profiling the nuisance parameters while fixing $\mu = 0$ and then constructing a representative dataset from the corresponding expected m values. As the fitted values of $\boldsymbol{\theta}$ are obtained while forcing the background-only hypothesis, they are not necessarily close to their true values if there is indeed some signal events present in the data. The expected limits can therefore be seen as somewhat conservative.

Asimov datasets also have another important use. In order to calculate $\mathrm{P}(\tilde{q}_\mu \geq \tilde{q}_\mu^{\mathrm{obs}}|\mu)$, one needs to know the probability density function of $\tilde{q}_\mu$. It can be obtained from numerous Monte Carlo pseudo-experiments, but this can be computationally expensive. We instead make use of the asymptotic approximation that, in the large sample limit, $\tilde{q}_\mu$ always follows a non-central half χ^2-distribution, the median of which can be estimated using an Asimov dataset corresponding to that value of μ [91].

---

[1] In the context of excluding a signal hypothesis. For the purpose of establishing a *discovery* – which means rejecting the background-only hypothesis – a much smaller α, corresponding to five standard deviations, is normally used. The reason for this is that multiple searches (in different mass ranges, for example) are carried out simultaneously, which increases the risk of false positives. When attempting to reject the signal hypothesis, however, increasing the search range only makes it more difficult to exclude the signal everywhere.

6. Searches for $H^+ \to \tau\nu$ in 7 TeV data

In this chapter, three searches for a light charged Higgs boson decaying to $\tau\nu$ *are presented, based on the 7* TeV *dataset collected by ATLAS in 2011. It is assumed that* $\mathscr{B}(H^+ \to \tau\nu) = 100\%$. *In all cases, the signal process is characterized by the additional presence of a top quark that decays to an electron or a muon. This high-*p_{T} *lepton clearly distinguishes these events from most of the multi-jet background, and is used for triggering.*

The cleanest channel is the dilepton final state, where the tau originating from the charged Higgs boson also decays leptonically. The dilepton channel was analyzed with the first 1.03 fb^{-1} *of pp collision data recorded at* $\sqrt{s} = 7$ TeV. *However, only modest sensitivity to a light charged Higgs boson was achieved in this channel and the analysis was not repeated with the full dataset.*

Instead, focus was shifted to events where the tau lepton decays hadronically (τ_{had}*). The hadronic decay modes of the tau have higher branching fractions, and yield events with fewer neutrinos, but come with a challenging background in the form of quark- or gluon-initiated jets that may be misidentified as hadronic tau decays. Because the misidentification probability is not expected to be well-modeled by Monte-Carlo simulations, it is measured in control regions in the data. The* $\mathrm{lepton} + \tau_{\mathrm{had}}$ *channel was analyzed using the full 2011 dataset, corresponding to an integrated luminosity of 4.6* fb^{-1}. *and upper limits on* $\mathscr{B}(t \to bH^+)$ *extracted using the* $E_{\mathrm{T}}^{\mathrm{miss}}$ *distribution. The data was then re-analyzed with a simultaneous treatment of the dilepton and* $\mathrm{lepton} + \tau_{\mathrm{had}}$ *channels. This analysis performed as a test of lepton universality in* $t\bar{t}$ *events, in the form of an event-counting experiment, where the role of the dilepton channel is primarily to constrain the uncertainties on the backgrounds, rather than providing direct sensitivity to the signal. Events where the reconstructed* τ_{had} *has the same sign of charge as the lepton are subtracted from the events where they have opposite charges, which cancels the contributions of gluons and b-jets misidentified as hadronic tau decays. The ratio of* $\mathrm{lepton} + \tau_{\mathrm{had}}$ *and dilepton events is found to be consistent with the Standard Model prediction. Upper limits on* $\mathscr{B}(t \to bH^+)$ *are set in the range 3.2–4.4% for* H^+ *masses within 90–140* GeV. *Combinations of these results with those of other ATLAS searches for charged Higgs bosons, and interpretations in the MSSM* m_h^{max} *scenario were also performed.*

In this chapter, three searches for a light charged Higgs boson decaying to $\tau\nu$ are presented, based on the 7 TeV dataset collected in 2011. Here, it is assumed that $\mathscr{B}(H^+ \to \tau\nu) = 100\%$. In all cases, the signal process is characterized by the additional presence of a top quark that decays to an electron or a muon. This high-p_T lepton clearly distinguishes these events from most of the multi-jet background, and is used for triggering. The cleanest channel (with the least amount of difficult-to-handle backgrounds with misidentified objects) is the dilepton final state, where the tau originating from the charged Higgs boson also decays leptonically. The dilepton channel was analyzed with the first 1.03 fb^{-1} of pp collision data recorded at $\sqrt{s} = 7$ TeV. However, only modest sensitivity to a light charged Higgs boson was achieved in this channel and the analysis was not repeated with the full dataset. Instead, focus was shifted to events where the tau lepton decays hadronically (τ_had). The hadronic decay modes of the tau have higher branching fractions, and yield events with fewer neutrinos, but come with a challenging background in the form of quark- or gluon-initiated jets that may be misidentified as hadronic tau decays. Methods for estimating this background, with decreasing reliance on simulation, were developed. The lepton $+\,\tau_\mathrm{had}$ channel was analyzed using the full 2011 dataset, corresponding to an integrated luminosity of 4.6 fb^{-1}. The data was then re-analyzed with a simultaneous treatment of the dilepton and lepton $+\,\tau_\mathrm{had}$ channels. This analysis is cast as a test of lepton universality in $t\bar{t}$ events, in the form of an event-counting experiment, where the role of the dilepton channel is primarily to constrain the uncertainties on the backgrounds, rather than providing direct sensitivity to the signal.

The analyses presented in this chapter all use single-lepton triggers with a p_T threshold of 20–22 GeV for electrons and at 18 GeV for muons. With these thresholds, electrons with $E_\mathrm{T} > 25$ GeV and muons with $p_\mathrm{T} > 20$ GeV are guaranteed to be in the plateau region of the trigger efficiency curve.

6.1 Dilepton channel

With the first 1.03 fb^{-1} of ATLAS data collected at $\sqrt{s} = 7$ TeV in 2011, a search for light charged Higgs bosons in $t\bar{t}$ events was performed using final states with two charged leptons (electrons or muons). This analysis is also documented in Ref. [93]. Figure 6.1 illustrates the contribution from events involving a charged Higgs boson. If some fraction of top quark decays happen via $t \to bH^+$ and the charged Higgs boson decays solely into $\tau\nu$, a small increase in the number of $t\bar{t}$ events with two charged leptons in the final state is expected, because the tau lepton decays leptonically more often than the W boson does: $\mathscr{B}(H^+ \to \tau\nu \to \ell + 3\nu) = 35\%$ while $\mathscr{B}(W \to \ell + N\nu) = 25\%$, where ℓ denotes either an electron or a muon. However, relying only on the detection of a small excess of such events would give limited sensitivity to the presence of a charged Higgs boson in $t\bar{t}$ decays. Kinematic variables that can further discriminate between events with and without charged Higgs bosons have therefore been identified [94].

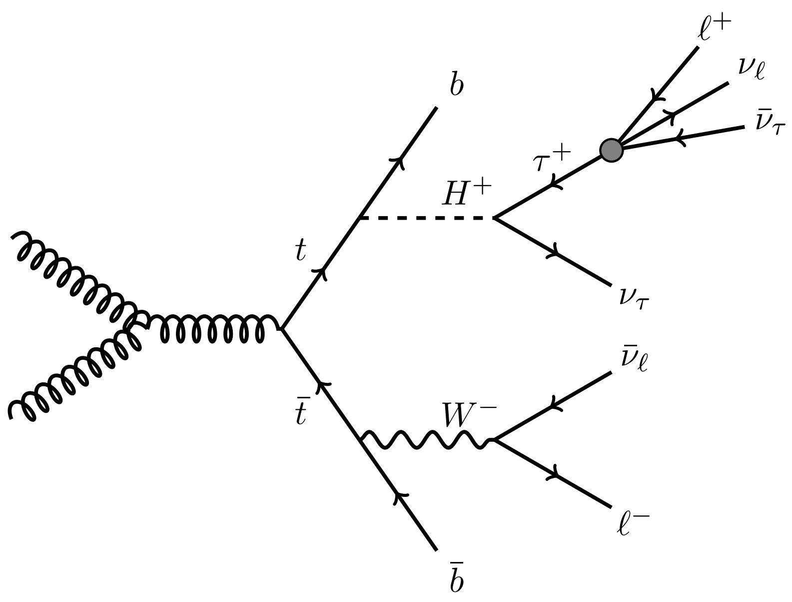

Figure 6.1. Feynman diagram of a $t\bar{t}$ event involving a charged Higgs boson, with two charged leptons $\ell = e, \mu$ in the final state.

Discriminating variables

One useful quantity is the invariant mass $m_{b\ell}$ of the b quark and the lepton coming from the same top quark. It is used here in the form of the variable $\cos\theta^*_\ell$ defined as

$$\cos\theta^*_\ell = \frac{2m^2_{b\ell}}{m^2_t - m^2_W} - 1 \approx \frac{4p^b \cdot p^\ell}{m^2_t - m^2_W} - 1 \tag{6.1}$$

with $p^b \cdot p^\ell = E_b E_\ell (1 - \cos\theta_{b\ell})$, where $p^{b,\ell}$ are the four-momenta of the b quark and the lepton, and $\theta_{b\ell}$ is the angle between them. The approximation in equation (6.1) is valid if the masses of the b quark and the lepton are neglected so that $m^2_{b\ell} = 2p^b \cdot p^\ell$. Equation (6.1) contains only Lorentz invariant products and can be computed in any reference frame. The use of $\cos\theta^*_\ell$ in analyses of top quark decays originates in measurements of W polarization, where θ^*_ℓ is the angle between the lepton momentum and the helicity axis in the W rest frame. Here, the lepton is assumed to appear via the decay of a tau, which dilutes the polarization information. The discriminating power of $\cos\theta^*_\ell$ instead comes from the fact that the lepton in this case receives a lower momentum than if it would come directly from the decay of a W boson. This reduction of the lepton momentum is somewhat counteracted if the charged Higgs boson is heavier than the W, however that instead reduces the momentum available to the b quark. Top quarks decaying via a charged Higgs boson therefore produce $\cos\theta^*_\ell$ values close to -1.

The *generalized charged Higgs boson transverse mass* m^H_{T2} [95] is also used. This is the maximum charged Higgs boson mass allowed in an event, given the known masses of the W boson and the top quark, as well as conservation of momentum in the transverse directions. Following the notation of

Figure 6.1, if one top quark decays into $\bar{b}W^-$ and the other top quark decays into bH^+, then the following set of constraints apply:

$$\begin{aligned}
(p^{H^+}+p^b)^2 &= m_t^2, \\
(p^{\ell^-}+p^{\bar{\nu}_\ell})^2 &= m_W^2, \\
(p^{\ell^-}+p^{\bar{\nu}_\ell}+p^{\bar{b}})^2 &= m_t^2, \\
(p^{\bar{\nu}_\ell})^2 &= 0, \\
\vec{p_\mathrm{T}}^{H^+}-\vec{p_\mathrm{T}}^{\ell^+}+\vec{p_\mathrm{T}}^{\bar{\nu}_\ell} &= \vec{p_\mathrm{T}}^{\mathrm{miss}}.
\end{aligned} \tag{6.2}$$

Here, p^{H^+} and $p^{\bar{\nu}_\ell}$ represent the unknown quantities in the event. With the six constraints of (6.2), there are two degrees of freedom over which the charged Higgs boson mass is maximized to obtain m_{T2}^H. Note that the decay products of the charged Higgs boson are not explicitly included in these equations, as this would not supply any additional constraint on the mass of the charged Higgs boson. The charged Higgs boson can be replaced by a W^+ and the constraints of (6.2) hold even if there is no tau lepton in the event. The m_{T2}^H quantity is therefore always the upper bound on the mass of the boson mediating the top quark decay. By definition, it lies between the true mass of the charged Higgs boson and the mass of the top quark: $m_{H^+} \leq m_{\mathrm{T2}}^H \leq m_t$. This is true even if the top quark radiates a gluon before it decays, as this can only lower the value of m_{T2}^H, which is nevertheless still bounded from below by m_{H^+}.

The variable m_{T2}^H is called the generalized charged Higgs boson transverse mass because of its relation to other transverse mass observables. The widely used W transverse mass m_T^W is defined as

$$\left(m_\mathrm{T}^W\right)^2 = 2p_\mathrm{T}^\ell E_\mathrm{T}^{\mathrm{miss}}(1-\cos\Delta\phi_{\ell,\mathrm{miss}}). \tag{6.3}$$

In an event with a *single* charged lepton ℓ and a single neutrino, m_T^W can be obtained by minimizing the invariant mass of these objects subject to the constraint that the neutrino must be massless,

$$\left(m_\mathrm{T}^W\right)^2 = \min_{\left\{(p^{\mathrm{miss}})^2=0\right\}} \left[\left(p^\ell+p^{\mathrm{miss}}\right)^2\right]. \tag{6.4}$$

If the single charged lepton comes from the decay of a tau lepton, which could in turn be the decay product of a charged Higgs boson, then the constraint $\left(p^{\mathrm{miss}}\right)^2=0$ is not valid as there are three neutrinos in the event. One can instead define the *charged Higgs boson transverse mass* m_T^H by using a constraint on the top quark mass:

$$\left(m_\mathrm{T}^H\right)^2 = \max_{\left\{(p^{\mathrm{miss}}+p^\ell+p^b)^2=m_t^2\right\}} \left[\left(p^\ell+p^{\mathrm{miss}}\right)^2\right]. \tag{6.5}$$

Note that, while m_T^W is obtained as the result of a minimization, m_T^H is the result of a maximization. Finally, in events with *two* charged leptons in the final state, there are neutrinos appearing in the decays of both top quarks. With the set of constraints (6.2), the generalized charged Higgs boson transverse mass m_{T2}^{H} can in turn be written as a maximization of m_{T}^{H},

$$m_{\mathrm{T2}}^{H} = \max_{\{constraints\}} [m_{\mathrm{T}}^{H}(\vec{p_{\mathrm{T}}}^{H^+})]. \tag{6.6}$$

The variable m_{T}^{H} has an analytical expression,

$$\left(m_{\mathrm{T}}^{H}(\vec{p_{\mathrm{T}}}^{H^+})\right)^2 = \left(\sqrt{m_t^2 + (\vec{p_{\mathrm{T}}}^{H^+} + \vec{p_{\mathrm{T}}}^{b})^2} - p_{\mathrm{T}}^{b}\right)^2 - \left(\vec{p_{\mathrm{T}}}^{H^+}\right)^2, \tag{6.7}$$

while the maximization of m_{T2}^{H} over the remaining parameter must be done numerically.

Event selection

In this analysis, events are selected if:

- There are exactly two oppositely charged leptons with $E_{\mathrm{T}} > 15$ GeV (electrons) or $p_{\mathrm{T}} > 15$ GeV (muons).
- At least one of the leptons is matched to the single-lepton trigger object with $E_{\mathrm{T}} > 25$ GeV (electron) or $p_{\mathrm{T}} > 20$ GeV (muon).
- There are at least two jets with $p_{\mathrm{T}} > 20$ GeV.
- Exactly two of the jets are b-tagged.

In order to compute $\cos\theta_\ell^*$ and m_{T2}^{H}, each of the two leptons and the two b-jets must be assigned to either of the two top quarks, one of which is assumed to have decayed via a charged Higgs boson. There is a four-fold ambiguity in this assignment, which is resolved as follows. First, ℓ-b pairings that yield unphysical $\cos\theta_\ell^*$ values (i.e. larger than 1) are assumed to be incorrect and are discarded. If both possible ℓ-b combinations in an event have $\cos\theta_\ell^* < 1$, then the solution which minimizes $\Delta R(\ell,b)_{\mathrm{pair1}} + \Delta R(\ell,b)_{\mathrm{pair2}}$ is chosen. The efficiency of this procedure to find correct ℓ-b pairings is 66% in simulated $t\bar{t}$ events. Then, the ℓ-b pair with the smallest $\cos\theta_\ell^*$ value is assigned to the top quark decay involving the H^+. The efficiency of this second assignment is 62% in simulated $t\bar{t}$ events with a 130 GeV charged Higgs boson.

To further reduce the contribution of non-$t\bar{t}$ backgrounds, the following requirements are also made:

- for $\mu\mu$ events with an azimuthal angle $\Delta\phi_{\mu\mu} > 3.1$, the impact parameters of the muons with respect to the primary vertex must not exceed 0.5 mm in order to rule out the presence of a cosmic muon,
- for ee and $\mu\mu$ events, the dilepton invariant mass $m_{\ell\ell}$ must be larger than 15 GeV and must satisfy $|m_{\ell\ell} - m_Z| > 10$ GeV, together with $E_{\mathrm{T}}^{\mathrm{miss}} > 40$ GeV, to reduce the contribution of $Z \rightarrow \ell\ell$ events,
- for $e\mu$ events, the scalar sum of the transverse energies of the two leptons and all selected jets must satisfy $\sum E_{\mathrm{T}} > 130$ GeV,

- the event kinematics must fit the $t\bar{t}$ hypothesis, i.e. the computation of m_{T2}^{H} must converge.

A signal region is then defined by requiring $\cos\theta_{\ell}^{*} < -0.6$ on the "H^{+} side" of the event while a control region enriched with $t\bar{t} \to b\bar{b}W^{+}W^{-}$ is defined by requiring $\cos\theta_{\ell}^{*} > -0.4$. For the events falling in the signal region, the m_{T2}^{H} distribution is used to set an upper limit on $\mathscr{B}(t \to bH^{+})$.

Background estimation

Contributions from Standard Model $t\bar{t}$, single top quark, $Z+$jets, and diboson processes are estimated using simulated events. Among these, the background from $t\bar{t} \to b\bar{b}W^{+}W^{-}$ events is by far the largest. The Standard Model cross section for this process is 165 pb, however this prediction is not valid in the presence of a charged Higgs boson. For this reason, and in order to reduce the impact of systematic uncertainties, a fiducial cross section σ_{bbWW} is determined using the control region $\cos\theta_{\ell}^{*} > -0.4$, which is mostly free of signal events. The Standard Model $t\bar{t}$ Monte Carlo sample is then normalized to the value of σ_{bbWW}, which is fitted together with the signal cross section. With the $m_{H^{+}} = 130$ GeV signal hypothesis, the best fit value of σ_{bbWW} is 150.4 pb.

$W+$jets and multi-jet events with one or two misidentified leptons constitute a small but non-negligible background. This background is estimated in a data-driven way using the matrix method described in section 5.3. *Loose* leptons are defined with relaxed identification criteria in the case of electrons and relaxed isolation criteria in the case of muons. The lepton identification probabilities p_{r} are measured in $Z \to \ell\ell$ events with a dilepton invariant mass in the range 86–96 GeV. The lepton misidentification probabilities p_{m} are measured in a control region enriched with multi-jet events, obtained by requiring 5 GeV $< E_{\mathrm{T}}^{\mathrm{miss}} <$ 20 GeV. The (mis)identification probabilities p_{m} and p_{r} are parametrized as functions of the type of lepton (electron or muon), its pseudorapidity, p_{T} or E_{T}, and the number of jets and b-jets in the event. These dependencies are treated as uncorrelated and are convoluted using the procedure described in section 5.3.

Systematic uncertainties

Table 6.1 summarizes the systematic uncertainties considered in this analysis. These include uncertainties on the signal and background estimates, which are further discussed below, as well as a 3.7% uncertainty on the measurement of the integrated luminosity [96].

Systematic uncertainties on the detector simulation

A range of systematic uncertainties on the detector simulation are considered. They are related to how well the simulated events reproduce the ATLAS data in terms of trigger, reconstruction, and identification (ID) efficiencies, as well as the energy or momentum scale and resolution of reconstructed objects. The impact of each uncertainty is evaluated by performing the analysis again while shifting the relevant parameter by ±1 standard deviation, as listed in Table 6.1 (the methods used to derive these numbers are discussed in Ref. [93] and references therein). The largest uncertainties are the jet energy scale (up to 14%) and resolution (up to 30%), b-tagging efficiency (up to 16%) and misidentification probability (up to 21%), where all quoted numbers depend on the p_{T} and η of the object in question. All shifts in the energy/momentum scale or resolution of reconstructed objects are propagated to the reconstructed $E_{\mathrm{T}}^{\mathrm{miss}}$.

Systematic uncertainties on the $t\bar{t}$ modeling
When this analysis was performed, no higher-order generator for H^+ events was available. Hence, in order to account for the inaccuracy of a leading-order simulation, the relative acceptance difference between Standard Model $t\bar{t}$ events generated with MC@NLO and the (leading-order) ACERMC generator in the region $\cos\theta_\ell^* < -0.6$ is added as an uncertainty to the leading-order H^+ simulation made with PYTHIA. Uncertainties on the Standard Model $t\bar{t}$ event generation and on the parton shower modeling are estimated by comparing the nominal prediction from MC@NLO interfaced to HERWIG/JIMMY with the prediction from POWHEG interfaced to PYTHIA. Using ACERMC interfaced to PYTHIA, the largest acceptance difference obtained when varying initial- and final-state radiation parameters within a range of values not excluded by data is taken as an uncertainty on initial- and final-state radiation. These uncertainties are all treated as variations of the normalization only.

Systematic uncertainties on the data-driven background estimation
The lepton misidentification probabilities are determined in a control region dominated by gluon-initiated jets, but are used in data events with a higher fraction of quark-initiated jets. This may introduce a bias on the estimate of the background with misidentified leptons, which is evaluated by comparing the misidentification probability in simulated multi-jet and Zbb events. The misidentification probabilities computed with these two samples are found to differ by up to 25%. The measurements of the misidentification probabilities are also affected by the uncertainties on the detector simulation, which enter via the subtraction of simulated events with true leptons. In addition, small variations (1–5%) of the (mis)identification probabilities are observed when varying the Z mass window and $E_{\mathrm{T}}^{\mathrm{miss}}$ requirements used to define the control regions. A total uncertainty of 28% is assigned to the background with misidentified leptons.

Results

Among the selected events, a mostly signal-free control region (CR) is defined as containing the events with $\cos\theta_\ell^* > -0.4$. In contrast, the signal region (SR) is defined as containing the events with $\cos\theta_\ell^* < -0.6$, which includes the bulk of selected events with a charged Higgs boson. For further signal-background discrimination, the distribution of the m_{T2}^H variable within the signal region

Table 6.1. *Main systematic uncertainties considered in the dilepton analysis.*

Source of uncertainty	Treatment in analysis
Electron trigger efficiency	± (0.4–1.0)%, depending on η.
Electron reco. efficiency	± (0.7–1.8)%, depending on η.
Electron ID efficiency	± (2.2–3.8)%, depending on E_T and η.
Electron energy scale	± (0.3–1.8)%, depending on E_T and η.
Electron energy resolution	± (0.5–2.4)%, depending on E_T and η.
Muon trigger efficiency	± (0.5–7.9)%, depending on p_T, η, ϕ, data period.
Muon reco. efficiency	± (0.4–0.8)%, depending on p_T, η, ϕ.
Muon ID efficiency	± 0.4%.
Muon momentum scale	Up to ± 1%, depending on p_T and η.
Muon momentum resolution	Up to ± 1%, depending on p_T and η.
Jet energy resolution (JER)	± (10–30)%, depending on p_T and η.
Jet energy scale (JES)	± (2.5–14)%, depending on p_T and η.
JES (pile-up)	Additional ± (2–7%), depending on p_T and η.
Jet reconstruction efficiency	Randomly drop jets (2%) and symmetrize.
b-tagging efficiency	± (5.7–15.5)%, depending on p_T.
b-tagging mistag rate	± (10–21)%, depending on p_T and η.
b-jet JES uncertainty	Additional ± (1.1–3.2)%, depending on p_T.
$E_\mathrm{T}^\mathrm{miss}$ object dependence	All scale and resolution shifts propagated.
$E_\mathrm{T}^\mathrm{miss}$ (pile-up)	± 10%.
Generator + parton shower	± 6.2 (3.9)% $b\bar{b}W^+W^-$ ($b\bar{b}H^\pm W^\mp$) normalization.
Initial-/final-state radiation	± 7.7% $t\bar{t}$ normalization.
Misid. e/μ	± 28% normalization.
Integrated luminosity	± 3.7%.

is examined. A profile likelihood statistical analysis is performed with the

Table 6.2. *Number of selected events in the dilepton analysis, for simulated processes and 1.03 fb^{-1} of ATLAS data. Here, $\mathscr{B}(t \to bH^+)$ is assumed to be 10% and a fitted value of 150.4 pb is used for σ_{bbWW}.*

$t\bar{t}$ ($bbWW$)	Single top quark	Z+jets	Diboson	Misid. leptons	$\sum$ SM	Data	H^+ 130 GeV
864	18	1.5	0.3	40	924	992	115

branching fraction $B \equiv \mathscr{B}(H^+ \to \tau\nu)$ as the one parameter of interest and the likelihood function given by:

$$\mathscr{L}(B) = \text{Poisson}(n^{\text{CR}}|m^{\text{CR}}) \prod_i \text{Poisson}(n_i|\, m_i) \prod_j \text{p}(\tilde{\theta}_j|\theta_j), \tag{6.8}$$

where m and n indicate respectively the expected and measured number of events in each region, and i indicates the bin of the m_{T2}^H distribution. Nuisance parameters θ_j incorporate the effects of the systematic uncertainties, with each parameter having a nominal estimate $\tilde{\theta}_j$ and a Gaussian constraint $\text{p}(\tilde{\theta}_j|\theta_j)$ as indicated in Table 6.1. The cross section σ_{bbWW} for the process $t\bar{t} \to b\bar{b}W^+W^-$ is included as an additional nuisance parameter that is only constrained by the data. Depending on the signal mass point being studied, the fitted values of σ_{bbWW} are between 0.78 and 1.06 times the Standard Model prediction, with uncertainties of 5–25%. The cross section σ_{bbHW} for the signal process $t\bar{t} \to b\bar{b}H^{\pm}W^{\mp}$ is related to σ_{bbWW} and the branching fraction B via the relation

$$\sigma_{bbHW} = \sigma_{bbWW} \times \frac{2B}{1-B}. \tag{6.9}$$

Table 6.2 shows the number of events in the data that pass the event selection, together with the predictions for Standard Model processes as well as $t\bar{t}$ events with a 130 GeV charged Higgs boson and $\mathscr{B}(t \to bH^+) = 10\%$. The left-hand side plot of Figure 6.2 shows the full $\cos\theta_\ell^*$ distribution of these events, and the right-hand side plot shows the m_{T2}^H distribution of the events in the signal region $\cos\theta_\ell^* < -0.6$. The contribution of $t\bar{t} \to b\bar{b}W^+W^-$ events is shown with a fitted value of 150.4 pb for σ_{bbWW}, as obtained with the $m_{H^+} = 130$ GeV signal hypothesis.

Upper limits on $\mathscr{B}(t \to bH^+)$ are set assuming $\mathscr{B}(H^+ \to \tau\nu) = 100\%$. Figure 6.3 shows the expected and observed exclusion limits at the 95% confidence level as a function of the charged Higgs boson mass. At the highest mass point considered, 160 GeV, the b-jet coming from the decay $t \to bH^+$ usually receives a p_{T} lower than 20 GeV. Such events do not pass the event selection, leading to a severe loss of sensitivity for this mass point.

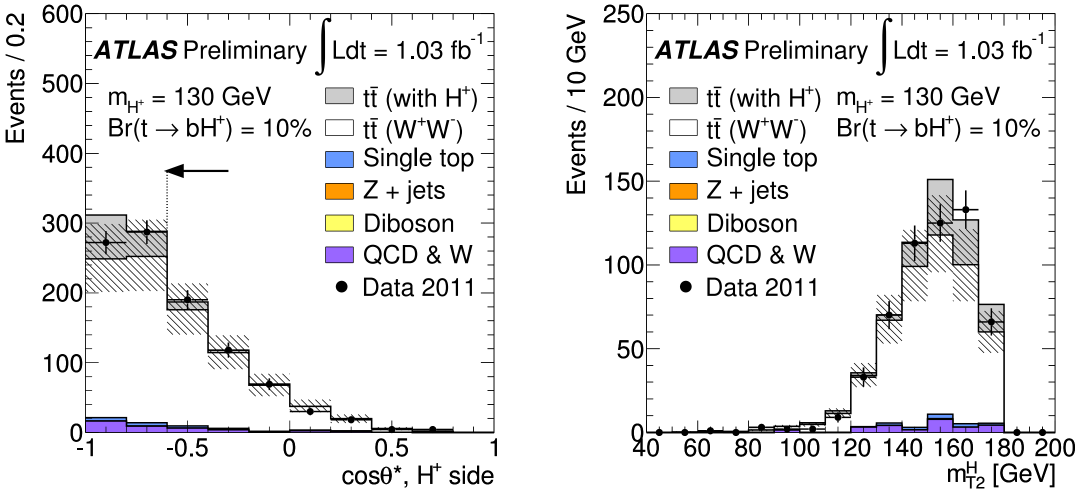

Figure 6.2. The left-hand side plot shows the $\cos\theta_\ell^*$ distribution of the dilepton events. The arrow indicates the signal region $\cos\theta_\ell^* < -0.6$ and the right-hand side plot shows the m_{T2}^H distribution of the events found in this region. The striped area indicates the systematic uncertainties on the backgrounds and the grey histogram shows the contribution of events with a 130 GeV charged Higgs boson with $\mathscr{B}(t \to bH^+) = 10\%$. A fitted value of 150.4 pb is used for σ_{bbWW}.

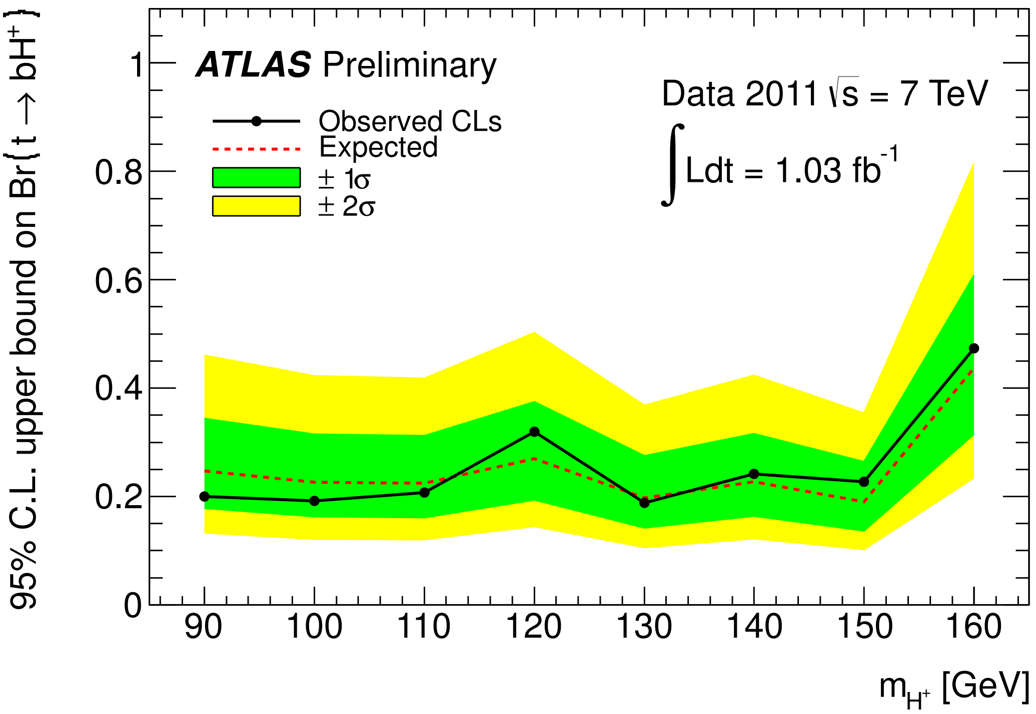

Figure 6.3. 95% confidence level upper limits on $\mathscr{B}(t \to bH^+)$ as a function of the charged Higgs boson mass, obtained in the dilepton analysis. The solid black line indicates the observed limit, while the dashed line indicates the expected limit with the background-only hypothesis. The green and yellow shaded regions indicate the 1σ and 2σ error bands, respectively.

6.2 Lepton+tau channel

This section describes a search for the process $t\bar{t} \to b\bar{b}H^{\pm}W^{\mp} \to b\bar{b}\tau^{\pm}\ell^{\mp}\bar{\nu}\nu$ carried out with the full 2011 dataset, i.e. an integrated luminosity of 4.6 fb^{-1}. Here, the tau lepton decays hadronically, in contrast to the analysis presented in the previous section, which relied on the fully leptonic tau decay modes. The use of a hadronically decaying tau lepton, τ_{had}, introduces more difficult-to-handle backgrounds but allows a higher overall search sensitivity. This analysis, which is also documented in Ref. [97], relies on the theoretical $t\bar{t}$ production cross section $\sigma_{t\bar{t}} = 167^{+17}_{-18}$ pb [69] and uses the $E_{\text{T}}^{\text{miss}}$ distribution to extract upper limits on $\mathscr{B}(t \to bH^{+})$.

Event Selection

Events are selected for further analysis if these requirements are fulfilled:

- The event contains exactly one electron or muon with $E_{\text{T}} > 25$ GeV (electron) or $p_{\text{T}} > 20$ GeV (muon).
- The lepton must be matched to the single-lepton trigger object.
- The event contains exactly one τ_{had} with $p_{\text{T}} > 20$ GeV, $|\eta| < 2.3$, and an electric charge opposite to that of the lepton.
- The event contains at least two jets with $p_{\text{T}} > 20$ GeV.
- At least one of the jets is b-tagged.
- The collection of tracks originating from the primary vertex must satisfy $\Sigma p_{\text{T}}^{\text{track}} > 100$ GeV.

Only τ_{had} objects passing the LLH identification and other criteria listed in section 5.2.4 are considered. Tracks that enter the computation of $\Sigma p_{\text{T}}^{\text{track}}$ must have at least $p_{\text{T}} > 1$ GeV, at least one hit in the pixel detector and at least six hits in the SCT. The requirement on a minimum amount of transverse momentum in the event reduces the amount of multi-jet events otherwise passing the selection. As this quantity is constructed using tracks originating from the primary vertex, it is less sensitive to pile-up than the sum of transverse energy deposits in the calorimeter used in e.g. the dilepton analysis. The efficiency of the full event selection is 23–40% (19–32%) for signal events in the muon (electron) channel, reaching a maximum value at a charged Higgs boson mass around 110 GeV.

Backgrounds with a misidentified lepton

As in the dilepton analysis, misidentified leptons constitute a background that must be estimated in a data-driven way. However, this background is slightly more severe in this case, as each event now contains only a single electron or muon. Similarly to the dilepton analysis, the amount of events with a misidentified lepton passing the event selection is estimated using the matrix method, with lepton identification probabilities measured in $Z \to \ell\ell$ events and misidentification probabilities measured in low-$E_{\text{T}}^{\text{miss}}$ multi-jet events. The (mis)identification probabilities are parametrized as functions of the type of lepton (electron or muon), its pseudorapidity, the distance ΔR to the closest jet, the number of b-tagged jets, the number of τ_{had} objects, the p_{T} of the leading jet, and the data-taking period. The (mis)identification probabilities do vary slightly between data-taking periods as the p_{T} threshold of the trigger changed during the year.

Backgrounds with misidentified hadronic tau decays

Monte Carlo simulations are used to estimate the Standard Model backgrounds with a real lepton. These include events with top quark pairs, single top quarks, W and Z bosons produced in association with jets, and diboson pairs. Only about 44% of the identified τ_{had} objects in the simulated events are matched to a hadronically decaying tau lepton at the generator level. However, the τ_{had} misidentification probability is not expected to be well modeled in the simulation. The simulated events must therefore be corrected based on τ_{had} misidentification probabilities measured in data.

Jets misidentified as hadronic tau decays

The probability for a jet to be misidentified as a τ_{had} is measured in data using a control sample enriched in $W+\text{jets}$ events. These events are required to pass the same lepton selection criteria as used in the main event selection. In addition, events must have a τ_{had} candidate and $E_{\text{T}}^{\text{miss}} > 40$ GeV, but no b-tagged jets. The τ_{had} candidates are not required to pass the LLH identification criteria but must have $p_{\text{T}} > 20$ GeV and $|\eta| < 2.3$, and they must not be within $\Delta R < 0.2$ of an electron or muon. About 0.5% of the selected events contain a true τ_{had}. Simulated events with a true τ_{had} (which are assumed to be well modeled) are subtracted from the data in order to remove this component.

Like the dominant $t\bar{t}$ background, the control sample contains events where high-p_{T} jets mainly originate from quarks instead of gluons. It does, however, contain a much smaller fraction of b-jets. The probability for a b-jet to be misidentified as a τ_{had} is lower than for a jet originating from a light quark, as the track multiplicity in a b-jet is higher. The visible mass measurement used in the τ_{had} identification also offers some discrimination between a b-jet and a τ_{had} object. The difference between the $t\bar{t}$ and $W+\text{jets}$ enriched regions is treated as a systematic uncertainty and is evaluated using simulation.

Having subtracted the events with a true τ_{had}, the jet $\rightarrow \tau_{\text{had}}$ misidentification probability is defined as the number of τ_{had} candidates passing the tau LLH identification criteria divided by the total number of τ_{had} candidates. It is measured as a function of p_{T}, η, and the number of associated tracks. The misidentification probability is found to be on average 7% for 1-prong taus and 2% for 3-prong taus.

In order to construct an estimate of the background with jets misidentified as hadronic tau decays, the measured jet $\rightarrow \tau_{\text{had}}$ misidentification probability is applied as a weight to all τ_{had} candidates in simulated $t\bar{t}$, single top quark, $W+\text{jets}$, $Z/\gamma^{*}+\text{jets}$ and diboson events. The τ_{had} candidate is then treated as

Table 6.3. *Number of events with jets misidentified as hadronic tau decays, as predicted using the misidentification probabilities measured in data, and compared with the result of applying the LLH algorithm to the simulated events. The uncertainties are statistical only, related to the number of data events in the control region and to the limited number of simulated events passing the LLH criterion, respectively.*

Sample	Nominal estimate	Simulation only
$t\bar{t}$	900 ± 15	877 ± 6
$W+$jets	150 ± 3	145 ± 9
Single top quark	81 ± 1	61 ± 2
$Z/\gamma^* +$jets	44 ± 1	69 ± 4
Diboson	6 ± 1	8 ± 1

if it had passed the tau identification, the corresponding jet is removed, and the modified event is passed through the nominal event selection. If it is accepted, it is kept with the weight given by the jet $\rightarrow \tau_{\text{had}}$ misidentification probability measured in data. The corresponding event yields are shown in Table 6.3. Misidentified τ_{had} objects also appear in multi-jet events. To pass the event selection, however, such events must also contain a misidentified lepton and are therefore accounted for in the data-driven estimation of that background.

Electrons misidentified as hadronic tau decays

Electrons misidentified as hadronic tau decays constitute a comparably small background. It is estimated in a similar manner as the jet $\rightarrow \tau_{\text{had}}$ background, using $e \rightarrow \tau_{\text{had}}$ misidentification probabilities measured in $Z \rightarrow ee$ events [98]. The average misidentification probability is 0.2%. In this case, the misidentification probability is the same in $t\bar{t}$ events as it is in the control region.

Backgrounds with real hadronic tau decays

The remaining backgrounds are $t\bar{t}$, single top quark, $W+$jets, $Z/\gamma^* +$jets, and diboson events with a real lepton and a real τ_{had} object. Nominally, these backgrounds are estimated using simulation only.

A data-simulation hybrid *embedding* method is used to cross-check the background simulations. This method consists of selecting events in data that match the nominal event selection, except for having a muon in place of the τ_{had} object. This muon is then replaced with a τ_{had} simulated with TAUOLA. This way, most features of the event, including the underlying event, pile-up effects, jet distributions, and overall normalization, are obtained directly from the data. The *embedding* of the simulated τ_{had} takes place at the detector level, meaning that individual tracks and calorimeter energy deposits of the muon are replaced. The momentum of the tau is rescaled with respect to the muon to take into account its higher mass. When selecting events for the embedding procedure, the p_{T} threshold of the muon is lower than that used for the τ_{had} in the analysis to avoid biasing the event selection. This sample constructed using embedding reproduces both the overall normalization and the shape of the simulated backgrounds within statistical uncertainties, which provides a validation of the Monte Carlo simulation.

Systematic uncertainties

Table 6.4 lists the systematic uncertainties considered in this analysis. Uncertainties related to the simulation of signal and background processes are treated similarly as in the dilepton analysis. The largest uncertainties are the jet energy scale (up to 14%) and resolution (up to 30%). Additional uncertainties are also introduced in this analysis, related to the τ_{had} identification efficiency (up to 7%) and energy scale (up to 5%).

The different jet composition (the fractions of jets initiated by light quarks, b quarks, or gluons) between the $W+$jets dominated region used to measure the jet $\rightarrow \tau_{\mathrm{had}}$ misidentification probability and the $t\bar{t}$ dominated signal region is treated as a systematic uncertainty on the background estimation, and is evaluated using simulation. It is found to affect the estimation of this background by up to 11%. A further 2% uncertainty is contributed by the statistical uncertainty on the control sample. In the case of $e \rightarrow \tau_{\mathrm{had}}$ misidentification, systematic uncertainties arise from the subtraction of electroweak and multi-jet backgrounds and from correlations between tag and probe objects in the determination of the misidentification probability in $Z \rightarrow ee$ events.

Systematic uncertainties on the estimate of misidentified leptons have a larger impact than in the dilepton analysis. They arise mostly from instrumental uncertainties entering via the subtraction of simulated events with true leptons in the computation of the misidentification probability, and from the jet composition (39%, evaluated by comparing the misidentification probability in simulated multi-jet and Zbb events).

Results

The observed number of events in the data after applying the event selection is shown in Table 6.5, together with the predictions under the background-only hypothesis, as well as for an alternative scenario where $\mathscr{B}(t \rightarrow bH^{+}) = 5\%$ and $m_{H^{+}} = 130$ GeV. The backgrounds with real and misidentified hadronic tau decays are scaled to match the change in $\mathscr{B}(t\bar{t} \rightarrow b\bar{b}W^{+}W^{-})$ in the presence of a charged Higgs boson, while the total $t\bar{t}$ cross section is constrained to its theoretical value $\sigma_{t\bar{t}} = 167^{+17}_{-18}$ pb, to which an additional 6% uncertainty is added to account for possible supersymmetric loop corrections [99].

The $E_{\mathrm{T}}^{\mathrm{miss}}$ distributions in the $e+\tau_{\mathrm{had}}$ and $\mu+\tau_{\mathrm{had}}$ channels are shown in Figure 6.4. The data is found to be compatible with the background-only hypothesis. Upper limits on the branching fraction $\mathscr{B}(t \rightarrow bH^{+})$ are therefore extracted with the profile likelihood method, using the $E_{\mathrm{T}}^{\mathrm{miss}}$ distribution (combined from both channels) as a discriminating variable. The expected and observed limits at 95% confidence level according to the $\mathrm{CL_s}$ definition are shown in Figure 6.5.

Table 6.4. *Main systematic uncertainties considered in the lepton* $+\tau_{\text{had}}$ *analysis with* 7 TeV *data. The "shape" uncertainty refers to the relative shift of the mean value of the* $E_{\text{T}}^{\text{miss}}$ *distribution.*

Source of uncertainty	Treatment in analysis
Electron trigger efficiency	Up to ±1.0%, depending on E_{T}, η, data period.
Electron reco. efficiency	± (0.6–1.1)%, depending on η.
Electron ID efficiency	± (2.8–3.5)%, depending on E_{T} and η.
Electron energy scale	± (0.5–2.4)%, depending on E_{T} and η.
Electron energy resolution	Up to ±1%, depending on E_{T} and η.
Muon trigger efficiency	± (0.5–6.0)%, depending on η, ϕ, data period.
Muon reco. efficiency	± (0.4–0.8)%, depending on p_{T}, η, ϕ.
Muon ID efficiency	± (0.3–1.2)%, depending on the data period.
Muon momentum scale	Up to ±1%, depending on p_{T}, η and the charge.
Muon momentum resolution	Up to ±1%, depending on p_{T}, η and the charge.
Jet energy resolution (JER)	± (10–30)%, depending on p_{T} and η.
Jet energy scale (JES)	± (2.5–14)%, depending on p_{T} and η,
JES (pile-up)	Additional ± (2–7)%, depending on p_{T} and η,
Jet reconstruction efficiency	Drop 2% of jets and symmetrize.
b-tagging efficiency	± (5–17)%, depending on p_{T} and η.
b-tagging mistag rate	± (12–21)%, depending on p_{T} and η.
b-jet JES uncertainty	Additional (up to) ± 2.5%, depending on p_{T}.
$E_{\text{T}}^{\text{miss}}$ object dependence	All scale and resolution shifts propagated.
$E_{\text{T}}^{\text{miss}}$ (pile-up)	± 6.6%.
$E_{\text{T}}^{\text{miss}}$ (additional)	<1% from soft jets + ambient.
Tau ID efficiency	± (4–7)%, depending on n_{tracks}.
Tau energy scale	± (2.5–5.0)%, depending on p_{T}, η, n_{tracks}.
jet $\to \tau_{\text{had}}$ (stat.)	±2% normalization.
jet $\to \tau_{\text{had}}$ (jet composition)	±11% normalization.
jet $\to \tau_{\text{had}}$ (detector related)	±23% normalization, ±3% shape.
$e \to \tau_{\text{had}}$	±20% normalization.
Misid. e/μ (p_{r} region)	±5% normalization.
Misid. e/μ (p_{m} region)	±4% normalization.
Misid. e/μ (JES)	±14% normalization.
Misid. e/μ (JER)	±4% normalization.
Misid. e/μ (jet composition)	±39% normalization.
Generator+parton shower	±2% (±5%) $b\bar{b}W^+W^-$ ($b\bar{b}H^{\pm}W^{\mp}$) normalization.
Initial-/final-state radiation	±13% $t\bar{t}$ normalization.
Integrated luminosity	±3.9%.

Table 6.5. *Expected event yields in the $e+\tau_{\text{had}}$ and $\mu+\tau_{\text{had}}$ channels, and comparison with the observed number of events in the data. The numbers in the last two rows are obtained assuming $\mathscr{B}(t \to bH^+) = 5\%$. All other rows correspond to the background-only hypothesis. Statistical and systematic uncertainties are indicated, in this order.*

Sample	Events ($e+\tau_{\text{had}}$)	Events ($\mu+\tau_{\text{had}}$)
Real lepton $+\,\tau_{\text{had}}$	$430 \pm 14 \pm 59$	$570 \pm 15 \pm 75$
Misidentified jet $\to \tau_{\text{had}}$	$510 \pm 23 \pm 86$	$660 \pm 26 \pm 110$
Misidentified $e \to \tau_{\text{had}}$	$33 \pm 4 \pm 5$	$34 \pm 4 \pm 6$
Misidentified leptons	$39 \pm 10 \pm 20$	$90 \pm 10 \pm 34$
Total background	$1010 \pm 30 \pm 110$	$1360 \pm 30 \pm 140$
Data	880	1219
$t \to bH^+$ (130 GeV)	$220 \pm 6 \pm 29$	$310 \pm 7 \pm 39$
Signal+background	$1160 \pm 30 \pm 100$	$1570 \pm 30 \pm 130$

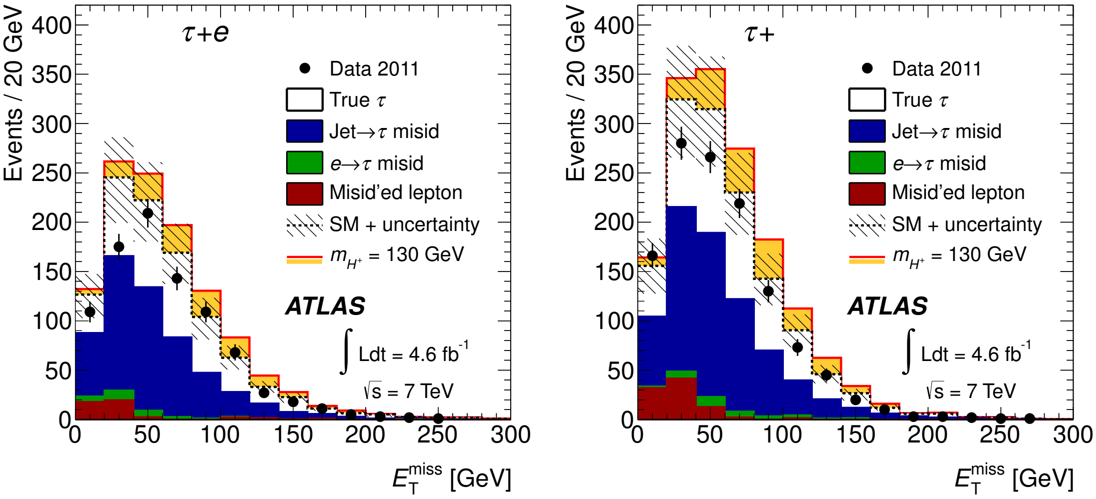

Figure 6.4. $E_{\mathrm{T}}^{\text{miss}}$ distribution in $e+\tau_{\text{had}}$ (left) and $\mu+\tau_{\text{had}}$ events (right). The individual contributions of both the signal and the $t\bar{t}$ background are scaled to match the prediction in the presence of a 130 GeV charged Higgs boson with $\mathscr{B}(t \to bH^+) = 5\%$ and $\mathscr{B}(H^+ \to \tau\nu) = 100\%$. The Standard Model prediction is shown as a dashed line, with the hatched area indicating its total uncertainty.

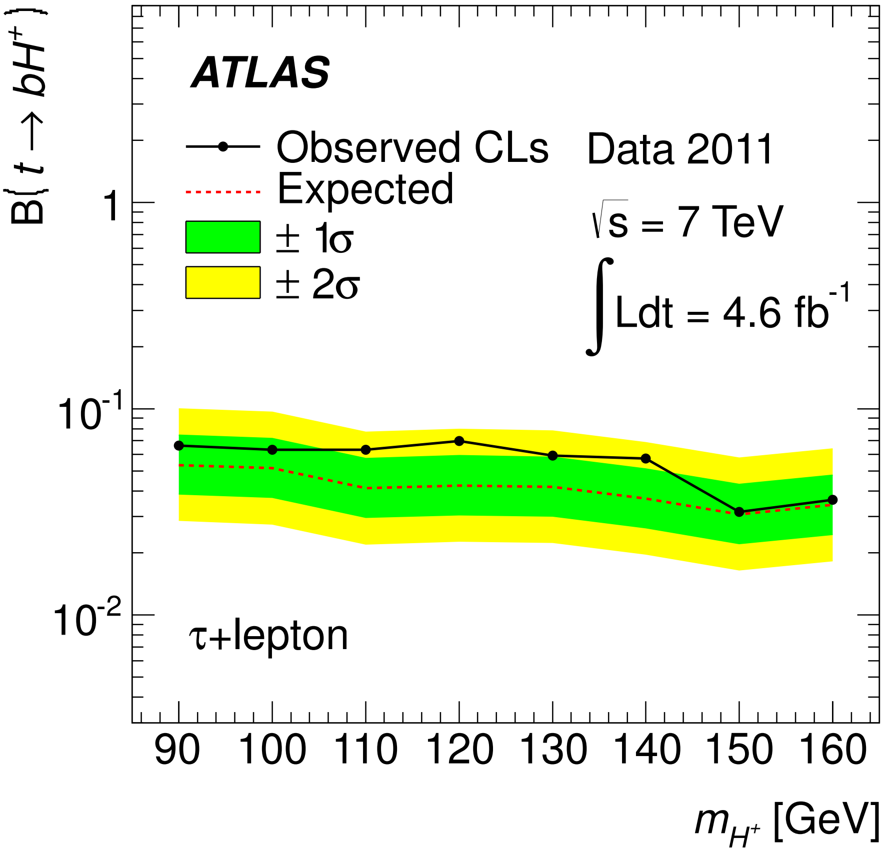

Figure 6.5. Expected and observed 95% confidence level exclusion limits on the branching fraction $\mathscr{B}(t \to bH^+)$ for a range of charged Higgs boson masses between 90 and 160 GeV, and with the assumption $\mathscr{B}(H^+ \to \tau\nu) = 100\%$, as obtained in the analysis of lepton $+\, \tau_{\mathrm{had}}$ events in 7 TeV data.

6.3 Test of lepton universality in $t\bar{t}$ events

The analysis presented here uses an alternative technique for charged Higgs boson searches in $t\bar{t}$ events. As W bosons decay with equal branching fractions to all leptons, whereas charged Higgs bosons decay predominantly to $\tau\nu$, the presence of charged Higgs bosons can be detected by searching for a violation of the lepton universality in top quark decays. This analysis uses the full 2011 dataset of pp collisions at $\sqrt{s} = 7$ TeV, with an integrated luminosity of 4.6 fb^{-1}, and it uses both dilepton events and lepton + τ_{had} events. Lepton universality in $t\bar{t}$ decays is tested by comparing the ratio of the number of lepton + τ_{had} events to the number of dilepton events found in the data to the value of that ratio predicted by the Standard Model. There are two motivations for the use of a ratio. First, while tau leptons decay leptonically more often (35% of the time) than W bosons (25% of the time), their decay products usually have a lower p_{T} than if they would come directly from a W boson and are therefore less likely to be detected. The number of observed dilepton events is therefore expected to decrease in the presence of a charged Higgs boson decaying to $\tau\nu$, while the number of lepton + τ_{had} events is expected to increase. The ratio of the two event yields is therefore more sensitive to the presence of a charged Higgs boson than either of the two channels alone. In addition, many systematic uncertainties affect both channels in the same way and their effects are therefore expected to cancel out when the ratio of event yields is computed. This analysis is also documented in Ref. [100].

Event selection

The following event selection is applied in order to select a sample enriched in $t\bar{t}$ events:

- The event must contain at least one electron or muon, having $E_{\text{T}} > 25$ GeV (electron) or $p_{\text{T}} > 25$ GeV (muon).
- The lepton must be matched to the single-lepton trigger object.
- The event must contain at least two b-tagged jets with $p_{\text{T}} > 20$ GeV.
- The event must have $E_{\text{T}}^{\text{miss}} > 40$ GeV and a solution for $m_{\text{T2}}^{H} > 0$.

In addition, lepton + τ_{had} events must satisfy the following requirements:

- There must be no additional charged lepton in the event.
- The event must have exactly one τ_{had} with $p_{\text{T}} > 25$ GeV and $|\eta| < 2.3$.

Dilepton events are instead selected by requiring:

- There must be exactly one additional charged lepton in the event.
- The second lepton also has $E_{\text{T}} > 25$ GeV ($p_{\text{T}} > 25$ GeV).
- The two leptons have different flavors.

The τ_{had} or non-trigger matched lepton is forced to be on the "H^{+}side" in the calculation of m_{T2}^{H}. Two b-tagged jets are required in order to select a pure $t\bar{t}$ sample. This leads to a lower acceptance for charged Higgs boson masses close to that of the top quark, when one of the b quarks receive very little transverse momentum. However, the aim of this search is mainly to improve the sensitivity in the low end of the considered mass range, i.e. close to the W mass, where the previous searches did not offer a strong discrimination between signal and background events. The selected events are categorized based on whether they fire the single-electron trigger or the single-muon trigger, and each category contains both lepton+τ_{had} and dilepton events. In the following, the lepton appearing first in a final state designation corresponds to the trigger used to select the event. The category of electron-triggered events therefore consists of $e+\tau_{\text{had}}$ and $e+\mu$ events. The category of muon-triggered events consists of $\mu+\tau_{\text{had}}$ and $\mu+e$ events. Dilepton events firing both the electron trigger and the muon trigger are assigned to both categories. This overlap of categories is accounted for when the exclusion limits are computed.

Backgrounds with misidentified objects

Backgrounds with misidentified leptons
The contributions of backgrounds with misidentified leptons are estimated with the matrix method. The same implementation as in section 6.2 is used. Neither the requirement of two b-tagged jets nor the presence of a second lepton is found to have a significant impact on the predictive power of the method. It is validated by comparing the distributions of kinematic variables, including the lepton p_{T} and $E_{\text{T}}^{\text{miss}}$, between the data and the total background prediction in $e+$jets, $\mu+$jets, $e+\mu$, and $\mu+e$ events without τ_{had} or b-jet requirements, and no significant deviations are found.

Backgrounds with misidentified hadronic tau decays
In simulated $t\bar{t}$ events, about 51% of τ_{had} objects passing the lepton $+\,\tau_{\text{had}}$ selections correspond to a true tau lepton at the generator level, and 3% of τ_{had} objects originate from electrons or muons. The contribution of events where an electron or a muon is misidentified as a τ_{had} in data is estimated by applying scale factors to simulated events as described in section 6.2. The remaining 46% of events (according to simulation) contain jets misidentified as τ_{had} objects. This component is also determined by correcting simulated events with scale factors measured in data, as described below.

A new technique to reduce the uncertainty on the jet $\rightarrow \tau_{\text{had}}$ misidentification probability is introduced in this analysis. In the lepton $+\,\tau_{\text{had}}$ analysis presented in section 6.2, the largest contribution to this uncertainty is the difference in jet composition between $W+$jets events, where the misidentification probability is measured, and $t\bar{t}$ events, where it is applied. This comes from the fact that the jet $\rightarrow \tau_{\text{had}}$ misidentification probability depends on which type of parton (light quark, heavy quark, or gluon) originally initiated the jet. However, contributions from jets other than those initiated by light quarks can be effectively eliminated by classifying events based on whether the electric charge of the τ_{had} has the opposite sign (OS) or same sign (SS) compared to that of the lepton. Except for a few rare cases of charge misidentification, real τ_{had} objects in $t\bar{t}$ and signal events all belong to the OS category. Instead of considering only OS events as in section 6.2, however, the SS events are now retained as well, but are assigned a negative weight. The final event yield corresponds to the number of OS events minus the number of SS events (OS-SS). Gluons do not carry electric charge and are therefore equally likely to be misidentified as τ_{had} objects of either charge, and b quarks tend to be produced in pairs (in particular in $t\bar{t}$ events). Both contributions are therefore expected to cancel in the OS-SS procedure. Light-quark initiated jets in $t\bar{t}$ events with leptons are largely dominated by the fully hadronic decay of a top quark and are therefore not charge-symmetric. They contribute more to the OS category and are thus not eliminated. The procedure is demonstrated in Figure 6.6, based on a control region enriched in $W+{>}2$ jets events, selected as follows:

- The event contains exactly one electron or muon, having E_{T} (electron) or p_{T} (muon) larger than 25 GeV.
- The lepton is matched to the single-lepton trigger object.
- The event contains at least one τ_{had} candidate, which is not required to pass the LLH identification.
- There are at least two jets in addition to the τ_{had} candidate.
- No jet is b-tagged.
- The event has $E_{\text{T}}^{\text{miss}} > 40$ GeV and $m_{\text{T}} > 30$ GeV.

The requirement on the W transverse mass m_{T}, defined as in equation (6.3), aims at reducing the contribution of $Z+$jets events with real tau leptons. As in $t\bar{t}$ events, light-quark jets in these events are predominantly produced with an opposite sign of charge compared to the lepton. Figure 6.6 shows that contributions from jets initiated by gluons and b quarks are removed by the OS-SS subtraction, which therefore has two important effects. It reduces the total amount of misidentified hadronic tau decays, and it makes the misidentification probability more uniform between different event selections by only leaving jets initiated by light quarks.

Scale factors used to weight events with jets misidentified as τ_{had} candidates in the simulation are then derived from the $W+>2$jets event selection in data. It can be seen in Figure 6.6, which includes τ_{had} candidates with one or three tracks, that there are more such τ_{had} candidates in the simulated events than in the data. It was found that the track multiplicities of jets misidentified as τ_{had} candidates are not well modeled by the simulation. Track multiplicity scale factors for τ_{had} candidates are therefore computed. For this purpose, the track multiplicity (ranging from 1 to 9) distributions of misidentified τ_{had} candidates in data and in simulation are separately normalized to the same unit area, and scale factors needed to correct the shape of the distribution in the simulated events to that in the data are computed. Only 1-track and 3-track τ_{had} candidates are eventually used in the analysis, the corresponding scale factors are 0.71 ± 0.03 for 1-track τ_{had} candidates and 0.92 ± 0.03 for 3-track τ_{had} candidates, where the uncertainties are statistical in nature.

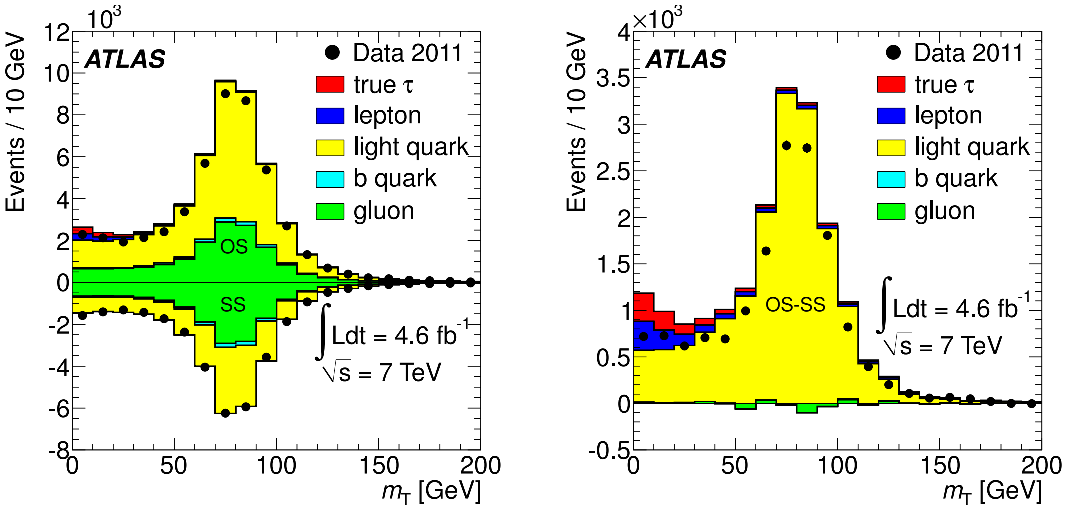

Figure 6.6. Distributions of m_T after applying the $W+>2$jets event selection (the requirement $m_\mathrm{T} > 30$ GeV is not applied in these plots). The colors correspond to the type of highest-energy generator-level particle found within a cone of radius $R = 0.2$ around the τ_had candidate. The left-hand side plot shows OS and SS events with positive respectively negative weights, while the right-hand side plot shows the result of subtracting the SS events from the OS events.

The probability for a light-quark initiated jet to also pass the τ_had identification criteria is then measured in the data, also using the $W+>2$jets event selection. This misidentification probability is binned in p_T and the number of tracks, $\mathrm{N}_\tau^\mathrm{track}$, of the τ_had candidate, as well as in the number of tracks, $\mathrm{N}_\mathrm{iso}^\mathrm{track}$, in the τ_had isolation cone, defined as the volume $0.2 < \Delta R < 0.4$ around the τ_had object. The parametrization of the misidentification probability by $\mathrm{N}_\mathrm{iso}^\mathrm{track}$ is a new feature in this analysis, as it was found that this corrects well for residual differences between $W+$jets events and $t\bar{t}$ events. The misidentification probabilities are shown in Figure 6.7, with two different binnings. A full parametrization in all three variables is used in the analysis. The track multiplicity scale factors and misidentification scale factors are applied to all simulated OS-SS events with τ_had candidates matched to jets. A combined probability of $p_1(1-p_2)+p_2(1-p_1)$ is assigned to events with two τ_had candidates, where p_1 and p_2 are the individual misidentification probabilities.

Systematic uncertainties

The same systematic uncertainties on the detector simulation and the event generators as discussed in section 6.2 are evaluated. However, in most cases, they are expected to have a smaller impact in this analysis, as they largely cancel in the ratio calculation. The distributions of the number $\mathrm{N}_\tau^\mathrm{track}$ of associated τ_had tracks and the number $\mathrm{N}_\mathrm{iso}^\mathrm{track}$ of tracks in the isolation cone of jets misidentified as τ_had candidates in the alternative $t\bar{t}$ samples are reweighted in a correlated way to match those of the nominal $t\bar{t}$ sample before applying the $\mathrm{N}_\tau^\mathrm{track}$ scale factors measured in data, which are found to well reproduce the

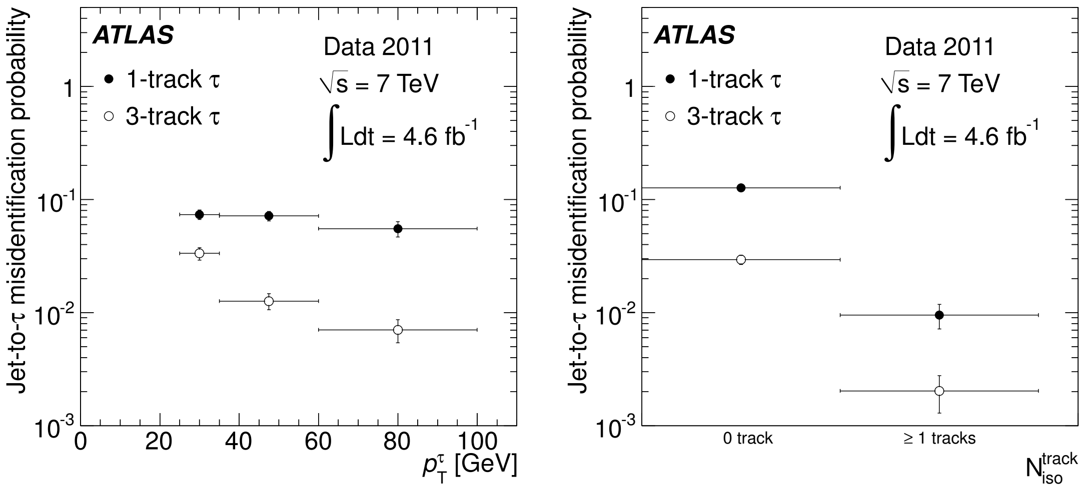

Figure 6.7. Probabilities for a jet initiated by a light quark to be misidentified as a τ_{had} with one or three tracks, measured in OS-SS events in data using the $W+>2$jets event selection, as a function of p_{T} (left) and of the number of tracks $\text{N}_{\text{iso}}^{\text{track}}$ in the isolation cone (right).

track multiplicity distributions in the signal region in the data (simultaneously correcting both $\text{N}_{\tau}^{\text{track}}$ and $\text{N}_{\text{iso}}^{\text{track}}$ in the nominal sample, instead of only $\text{N}_{\text{iso}}^{\text{track}}$, would result in less than a 1% change of the lepton $+\,\tau_{\text{had}}$ event yields). The uncertainty on both the modeling of $t\bar{t}$ events and the parton shower leads to uncertainties on the lepton $+\,\tau_{\text{had}}$ and dilepton event yields of 6–8% and 1–2%, respectively. The uncertainty on initial- and final-state radiation leads to uncertainties on the lepton $+\,\tau_{\text{had}}$ and dilepton event yields of 11%, respectively 8%.

The uncertainties on the track multiplicity scale factors are estimated by varying the requirement on the jet multiplicity, as well as propagating the uncertainties on the number of τ_{had} candidates arising from electrons, muons, or real taus present in the $W+>2$jets selection. They are found to be 7% for 1-track τ_{had} candidates and 11% for 3-track τ_{had} candidates. The jet $\rightarrow \tau_{\text{had}}$ misidentification probability is also sensitive to the amount of τ_{had} candidates arising from electrons, muons, or real taus in the control sample, and is also sensitive to statistical fluctuations in the number of objects passing the τ_{had} identification. In addition, the relative difference between the jet $\rightarrow \tau_{\text{had}}$ misidentification probability obtained in simulation for either the $W+>2$jets region or the $t\bar{t}$ selection is included as an uncertainty on the measured value. Using the already established upper limits on $\mathscr{B}(t \rightarrow bH^+)$, the effect of a possible contamination of the $W+>2$jets region with real hadronic tau decays from signal events is considered and found to change the measured jet $\rightarrow \tau_{\text{had}}$ misidentification probability with less than 1%.

The uncertainty on the estimate of the background due to misidentified leptons is mainly driven by the different jet composition in $t\bar{t}$ events compared to the control region where the lepton misidentification probabilities are derived. In total, the uncertainty on the background with misidentified leptons is 38% for electron-triggered events and 49% for muon-triggered events. As this background is relatively small, however, the effect on the total event yield ratios is only 3.5% and 4.3%, respectively.

Results

The observed OS-SS event yields $\mathscr{N}$ in each of the $e+\tau_{\text{had}}$, $e+\mu$, $\mu+\tau_{\text{had}}$, and $\mu+e$ selections are shown in Table 6.6 together with the predicted values for the background-only hypothesis or in the presence of a 130 GeV charged Higgs boson. The event yields are used to compute the ratios:

$$R_e = \frac{\mathscr{N}(e+\tau_{\text{had}})}{\mathscr{N}(e+\mu)} \quad \text{and} \quad R_\mu = \frac{\mathscr{N}(\mu+\tau_{\text{had}})}{\mathscr{N}(\mu+e)}. \tag{6.10}$$

Figure 6.8 shows the dependence of R_e and R_μ on $\mathscr{B}(t \to bH^+)$ for a H^+ mass of 130 GeV, assuming $\mathscr{B}(H^+ \to \tau\nu) = 100\%$. Electrons and muons produced via $t \to bH^+ \to b\tau\nu \to b\ell\nu\nu\nu$ typically have lower p_{T} than those produced via $t \to bW \to b\ell\nu$. They are therefore less likely to pass the event selection requirements. Despite the fact that the branching fraction of H^+ into electrons and muons via the above mentioned process is higher than that of the W boson, the event yields in the dilepton final states decrease in the presence of a charged Higgs boson, thereby contributing to the increase of R_e and R_μ. For a charged Higgs boson mass of 160 GeV, the rate at which R_e and R_μ change with $\mathscr{B}(t \to bH^+)$ is five times times lower and the analysis is correspondingly less sensitive. At this point, both the lepton+τ_{had} and dilepton event yields decrease with $\mathscr{B}(t \to bH^+)$ because the b-jet coming from $t \to bH^+$ receives a low p_{T}, but the dilepton event yield decreases faster.

Table 6.7 shows the predicted and observed values of R_e and R_μ. The data are found to be compatible with the Standard Model expectation. Note that the relative uncertainties on the expected ratios are smaller than the sum of the uncertainties on the corresponding event yields. This is because many systematic uncertainties are correlated across the lepton$+\tau_{\text{had}}$ and dilepton event selections, leading to R_e and R_μ being largely insensitive to them. Table 6.8 shows the sensitivity of R_e and R_μ to individual uncertainties.

Exclusion limits

Upper limits on the branching fraction $\mathscr{B}(t \to bH^+)$ at 95% confidence level according to the CL$_{\text{s}}$ criterion are determined using the profile likelihood method described in section 5.4, with one important modification. The quantities R_e and R_μ are ratios of two Poisson variables, the probability density function of which is unknown. However, the quantity $\mathscr{N}_{\ell\ell'} + \mathscr{N}_{\ell\tau}$ is also Poisson distributed with a rate $m_{\ell\ell'} + m_{\ell\tau}$, and $0 \leq \mathscr{N}_{\ell\ell'} \leq \mathscr{N}_{\ell\ell'} + \mathscr{N}_{\ell\tau}$. $\mathscr{N}_{\ell\ell'}$ must

Table 6.6. *Expected event yields and comparison with the observed number of events in the data. Combined statistical and systematic uncertainties are shown. The numbers in the last two rows are obtained assuming $\mathscr{B}(t \to bH^+) = 3\%$ with a charged Higgs boson mass of 130* GeV. *All other rows correspond to the background-only hypothesis. Here, V denotes a vector boson.*

Sample	$\mathscr{N}(e+\tau_{\text{had}})$	$\mathscr{N}(e+\mu)$	$\mathscr{N}(\mu+\tau_{\text{had}})$	$\mathscr{N}(\mu+e)$
Misid. leptons	-0.8 ± 3.0	94 ± 37	0.2 ± 1.0	74 ± 37
V+jets, VV	2.1 ± 0.9	0.7 ± 0.4	2.6 ± 1.6	0.7 ± 0.4
Single top	3.3 ± 0.8	24 ± 4	4.6 ± 0.9	18 ± 3
$t\bar{t}$	111 ± 25	980 ± 200	131 ± 28	740 ± 150
Total bkg.	116 ± 25	1100 ± 210	138 ± 29	830 ± 160
Data	144	1247	153	929
$t \to bH^+$	30 ± 4	27 ± 4	35 ± 4	20 ± 3
Signal+bkg.	139 ± 28	1070 ± 200	166 ± 32	810 ± 150

Table 6.7. *Predicted and observed event yield ratios.*

Ratio	R_e	R_μ
Standard Model prediction	0.105 ± 0.012 (stat+syst)	0.166 ± 0.017 (stat+syst)
Measured value	0.115 ± 0.010 (stat)	0.165 ± 0.015 (stat)

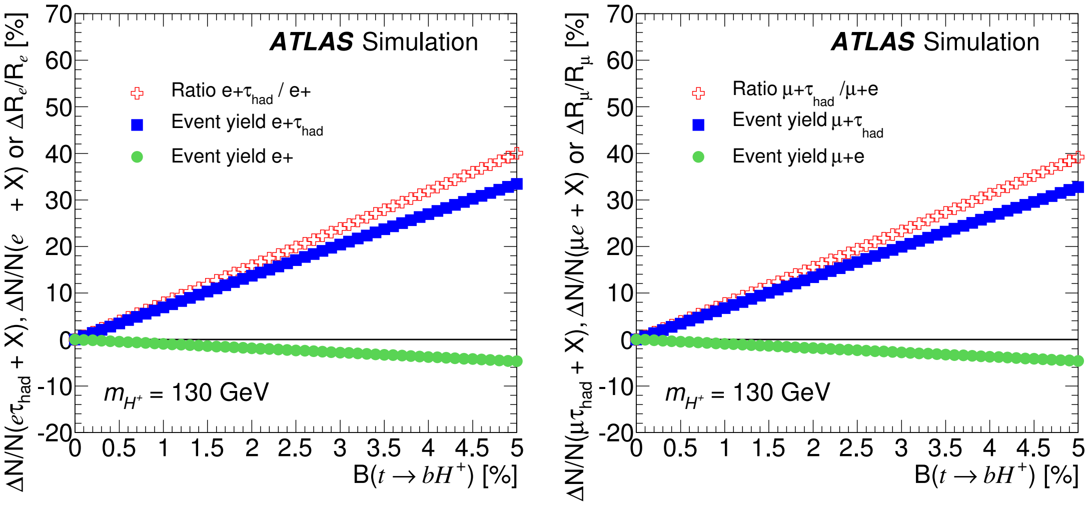

Figure 6.8. The predicted relative change of the event yields $\mathscr{N}(e+\tau_{\text{had}})$ and $\mathscr{N}(e+\mu)$, and of their ratio R_e (left) and the predicted relative change of the event yields $\mathscr{N}(\mu+\tau_{\text{had}})$ and $\mathscr{N}(\mu+e)$, and of their ratio R_μ (right). The plots show the dependence of these variables on the branching fraction $\mathscr{B}(t \to bH^+)$ in the presence of a charged Higgs boson with a mass of 130 GeV.

Table 6.8. *Relative variations of the ratios R_e and R_μ when changing a particular parameter within its uncertainty. When evaluating the ratios, the Standard Model hypothesis is assumed.*

Systematic uncertainty	ΔR_e	ΔR_μ
Electron trigger efficiency	0.1%	N/A
Electron reconstruction and ID efficiencies	0.2%	1.9%
Electron energy resolution	0.1%	<0.1%
Electron energy scale	0.1%	0.3%
Muon trigger efficiency	N/A	0.1%
Muon reconstruction and ID efficiencies	1.0%	0.1%
Muon momentum resolution	<0.1%	<0.1%
Muon momentum scale	0.1%	<0.1%
Tau ID efficiency	3.9%	3.9%
Tau energy scale	2.9%	3.0%
Jet energy scale	0.7%	0.5%
Jet energy resolution	0.4%	<0.1%
Jet reconstruction efficiency	0.1%	0.4%
Jet vertex fraction	0.1%	0.4%
b-tagging	1.9%	2.3%
$E_{\mathrm{T}}^{\mathrm{miss}}$	0.3%	0.1%
Jet → τ_{had} (number of associated tracks)	2.1%	2.1%
Jet → τ_{had} (true τ_{had} contamination)	0.2%	0.2%
Jet → τ_{had} (H^+ signal contamination)	0.6%	0.6%
Jet → τ_{had} (jet composition)	1.3%	1.2%
Jet → τ_{had} (statistical uncertainties)	3.3%	3.2%
$e \to \tau_{\mathrm{had}}$	0.6%	0.3%
Misid. e/μ	3.5%	4.3%
$t\bar{t}$ cross section	0.7%	0.6%
Generator + parton shower	5.7%	4.4%
Initial- and final-state radiation	3.6%	3.7%
Integrated luminosity	0.3%	0.3%
Total (added in quadrature)	10.3%	10.1%

therefore follow a binomial distribution:

$$\mathrm{P}(\mathcal{N}_{\ell\ell'} = k | \mathcal{N}_{\ell\ell'} + \mathcal{N}_{\ell\tau} = n) = \binom{n}{k} p^k (1-p)^{n-k}, \quad p \equiv \frac{m_{\ell\ell'}}{m_{\ell\ell'} + m_{\ell\tau}}. \quad (6.11)$$

The parameter p can also be written as a function of the expected ratio r_ℓ,

$$p(r_\ell) = \frac{1}{1 - r_\ell}. \quad (6.12)$$

Furthermore, the binomial distribution is well approximated by:

$$\text{Gauss}\left(np(r_\ell),\ \sqrt{np(r_\ell)\,[1 - p(r_\ell)]}\right). \quad (6.13)$$

By dividing by n, it follows that the observed quantity $p(R_\ell)$ is also normally distributed with mean $p(r_\ell)$ and standard deviation $\sigma = \sqrt{p(r_\ell)\,[1 - p(r_\ell)]\,/n}$. The likelihood function used to calculate upper limits on $B \equiv \mathcal{B}(t \to bH^+)$ is therefore given by:

$$\mathcal{L}(B, \boldsymbol{\theta}) = \text{Gauss}(p(R_\ell)|p(r_\ell), \sigma(r_\ell, n)) \prod_i \mathrm{p}(\tilde{\theta}_i|\theta_i). \quad (6.14)$$

Limits are set both separately for electron-triggered events and muon-triggered events, and for all events together using the combined ratio:

$$R_{e+\mu} = \frac{\mathcal{N}(e + \tau_{\text{had}}) + \mathcal{N}(\mu + \tau_{\text{had}})}{\mathcal{N}(e + \mu \cup \mu + e)} \quad (6.15)$$

where $\mathcal{N}(e + \mu \cup \mu + e)$ is the number of dilepton events that pass either the $e + \mu$ or $\mu + e$ selections. The fraction of events passing both the $e + \mu$ and $\mu + e$ selections is about 42% and is not counted twice. Figure 6.9 shows the limits derived using R_e and R_μ. Figure 6.10 shows the limits derived using the global event yield ratio $R_{e+\mu}$, with numerical values given in Table 6.9. Using the global ratio, upper limits on $\mathcal{B}(t \to bH^+)$ can be set in the range 3.2–4.4% for H^+ masses within 90–140 GeV. Limits were also extracted using the $m_{\mathrm{T2}}^{\mathrm{H}}$ distribution in $e + \tau_{\text{had}}$ and $\mu + \tau_{\text{had}}$ events and found to be less performant, except in the vicinity of the top quark mass.

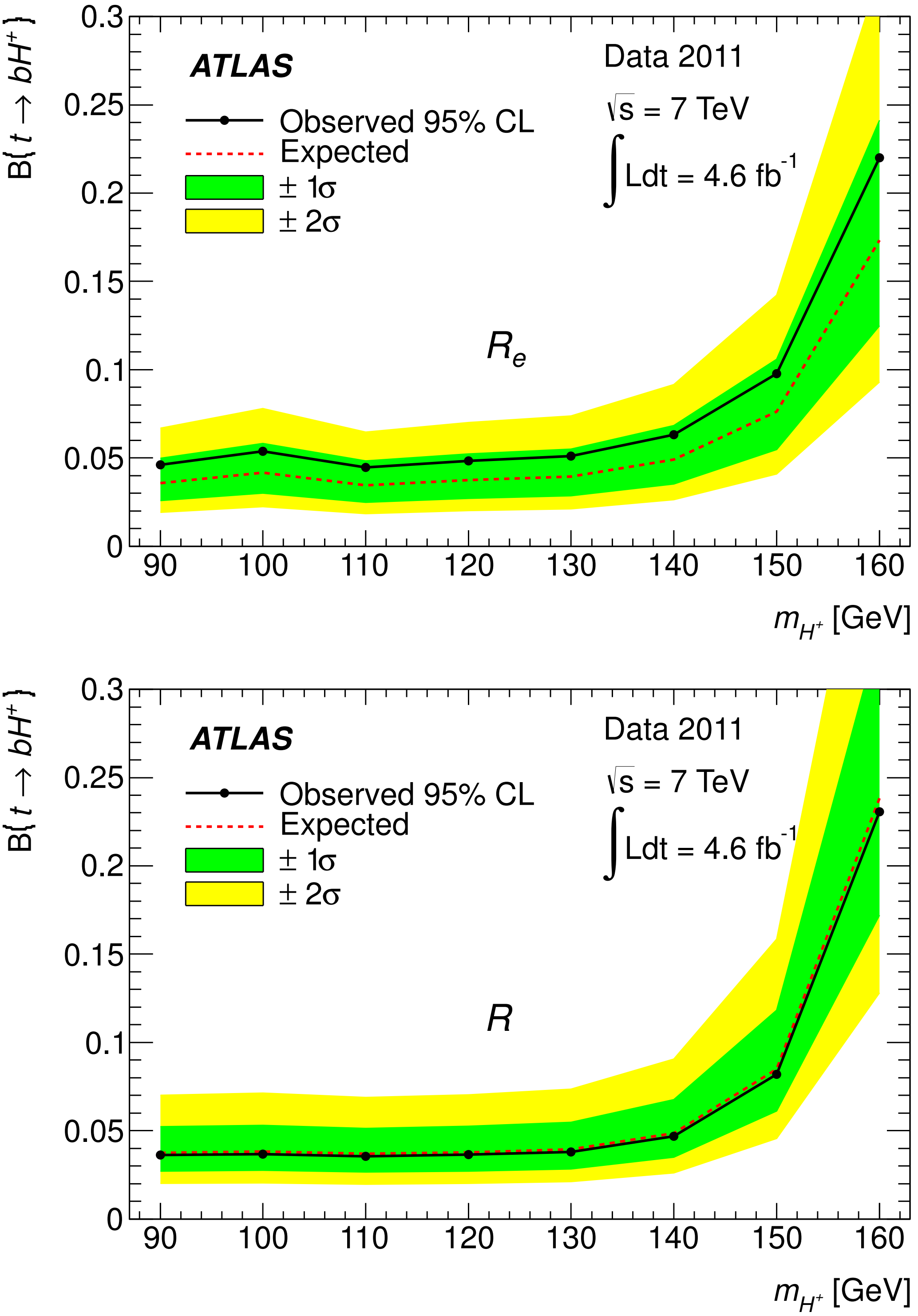

Figure 6.9. Expected and observed 95% confidence level upper limits on $\mathscr{B}(t \to bH^+)$ for H^+ masses between 90 and 160 GeV and assuming $\mathscr{B}(H^+ \to \tau\nu) = 100\%$, using the event yield ratios R_e (top) and R_μ (bottom).

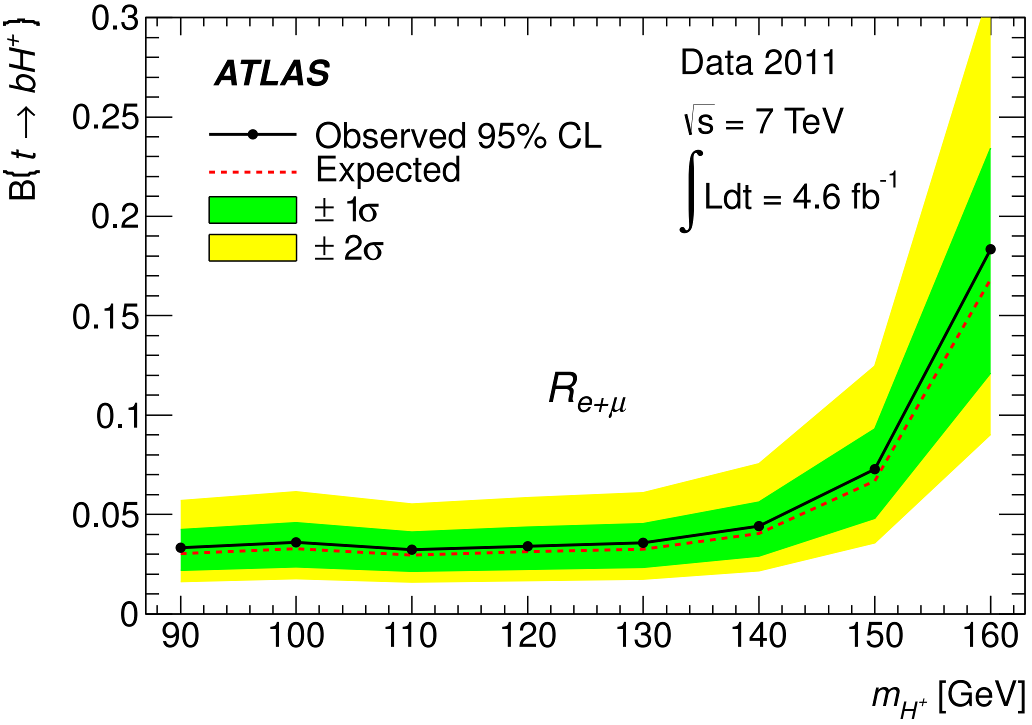

Figure 6.10. Expected and observed 95% confidence level upper limits on $\mathscr{B}(t \to bH^+)$ for H^+ masses between 90 and 160 GeV and assuming $\mathscr{B}(H^+ \to \tau\nu) = 100\%$, using the event yield ratio $R_{e+\mu}$.

Table 6.9. *Observed and expected 95% confidence level upper limits on $\mathscr{B}(t \to bH^+)$ as a function of m_{H^+}, derived from the event yield ratio $R_{e+\mu}$ and assuming that $\mathscr{B}(H^+ \to \tau\nu) = 100\%$.*

m_{H^+} [GeV]	90	100	110	120	130	140	150	160
observed limit	3.3%	3.6%	3.2%	3.4%	3.6%	4.4%	7.3%	18.3%
expected limit	3.1%	3.3%	3.0%	3.1%	3.3%	4.0%	6.7%	16.8%

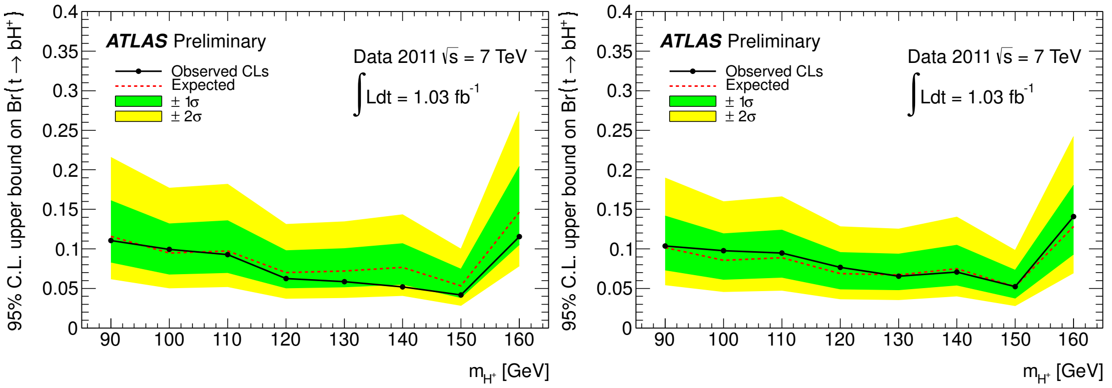

Figure 6.11. 95% confidence level upper limits on $\mathscr{B}(t \rightarrow bH^+)$, with the assumption that $\mathscr{B}(H^+ \rightarrow \tau\nu) = 100\%$, as obtained in the lepton + jets channel [93] (left) and with a combination of the lepton + jets and dilepton channels (right) using early 2011 data.

6.4 Combinations and interpretations

In parallel with the dilepton analysis, another search for charged Higgs bosons in events with a leptonically decaying tau was also performed by ATLAS, using the lepton + jets final state (in this case, the top quark on the "W side" of the event is assumed to decay hadronically). This analysis is also documented in Ref. [93], and the resulting exclusion limits are shown in the left-hand side plot of Figure 6.11. The right-hand side plot shows the result of a combination of the lepton + jets and dilepton (see Figure 6.3) channels. As the dilepton channel contributes very little additional sensitivity, the decision was made to exclude it from future analyses.

The analysis of the lepton + jets channel was however repeated with the full 2011 dataset, together with the lepton + τ_{had} channel (see section 6.2) and the all-hadronic τ_{had} + jets channel [97]. The limits obtained for the lepton + jets and τ_{had} + jets channels are shown in Figure 6.12 (see Figure 6.5 for the lepton + τ_{had} result). The result of a combination of all three channels is shown in Figure 6.13, in the form of model-independent upper limits on $\mathscr{B}(t \rightarrow bH^+)$ as well as their interpretation in the MSSM m_h^{max} scenario.

The individually most sensitive channel is τ_{had} + jets. Figures 6.14 and 6.15 show the result of a combination of the τ_{had} + jets analysis with the test of lepton universality (Figure 6.9). As expected, exclusion limits are particularly improved for low charged Higgs boson masses where the latter has more sensitivity. The direct search in the lepton + τ_{had} channel has comparable sensitivity to the τ_{had} + jets channel for low masses, but can not easily be included in this combination as it is not statistically independent from the test of lepton universality.

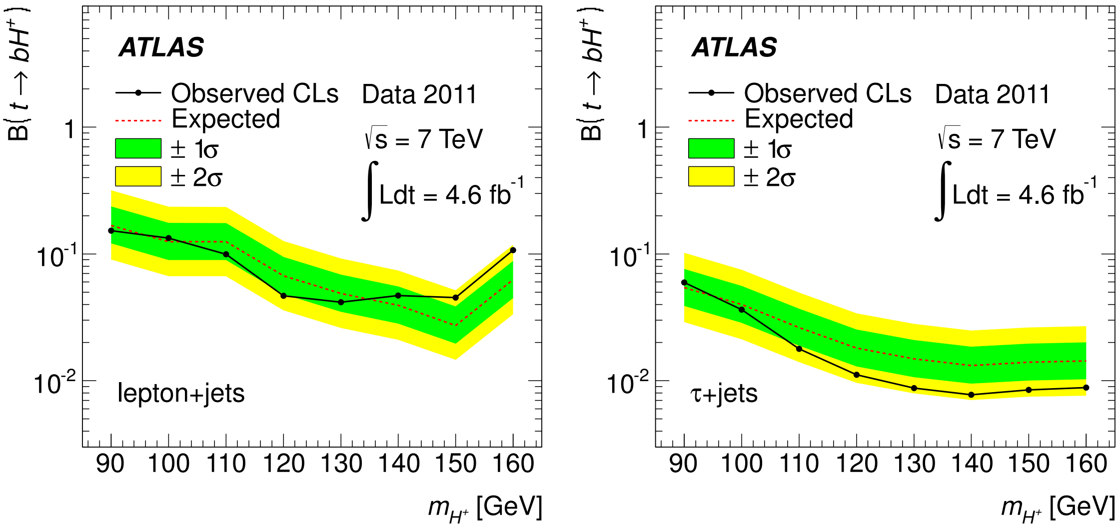

Figure 6.12. 95% confidence level upper limits on $\mathscr{B}(t \to bH^+)$, with the assumption that $\mathscr{B}(H^+ \to \tau\nu) = 100\%$, as obtained in the lepton + jets channel (left) and in the τ_{had} + jets channel (right) [97].

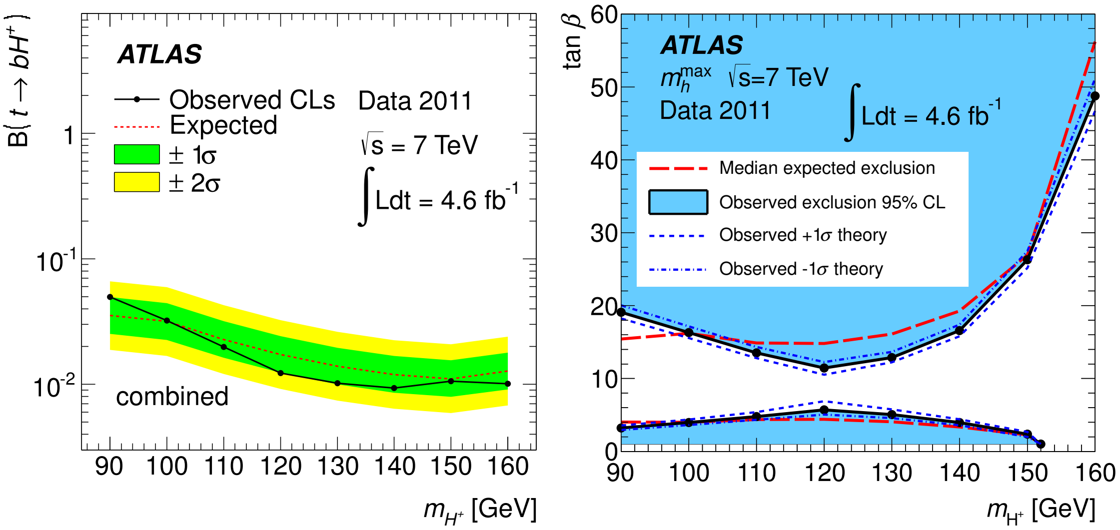

Figure 6.13. 95% confidence level upper limits on $\mathscr{B}(t \to bH^+)$, with the assumption that $\mathscr{B}(H^+ \to \tau\nu) = 100\%$, obtained by combining the lepton + jets, τ_{had} + jets (both from Ref. [97]), and lepton + τ_{had} channels (left), and their interpretation in the MSSM m_h^{max} scenario (right).

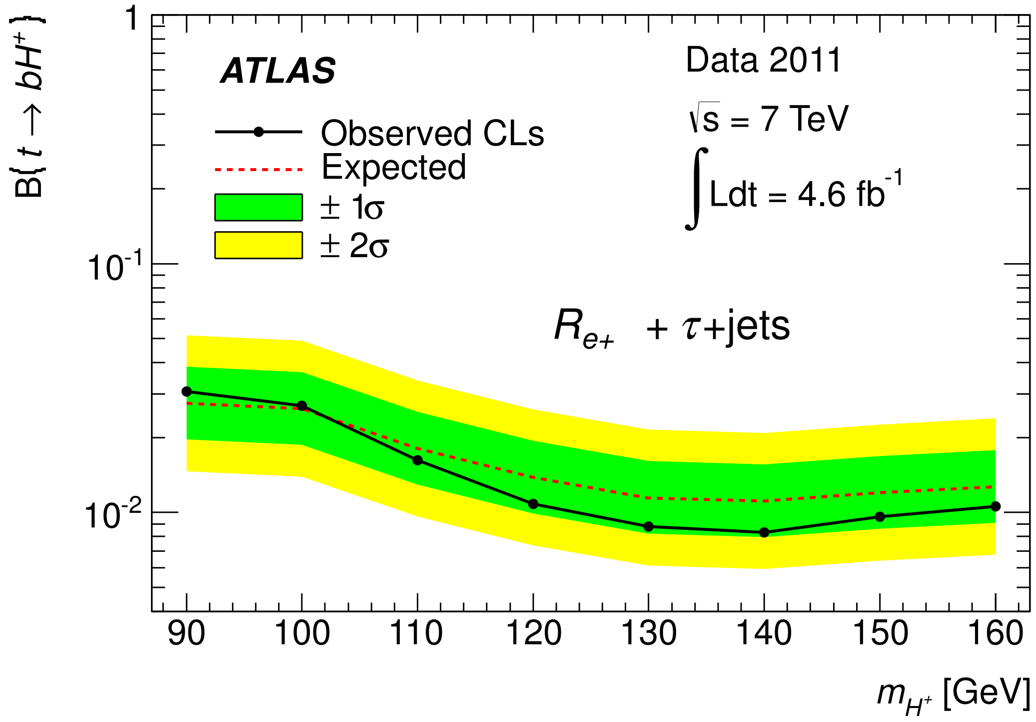

Figure 6.14. 95% confidence level upper limits on $\mathscr{B}(t \to bH^+)$, with the assumption that $\mathscr{B}(H^+ \to \tau\nu) = 100\%$, obtained with a combination of the direct search in the τ_{had} + jets channel and the event yield ratio $R_{e+\mu}$.

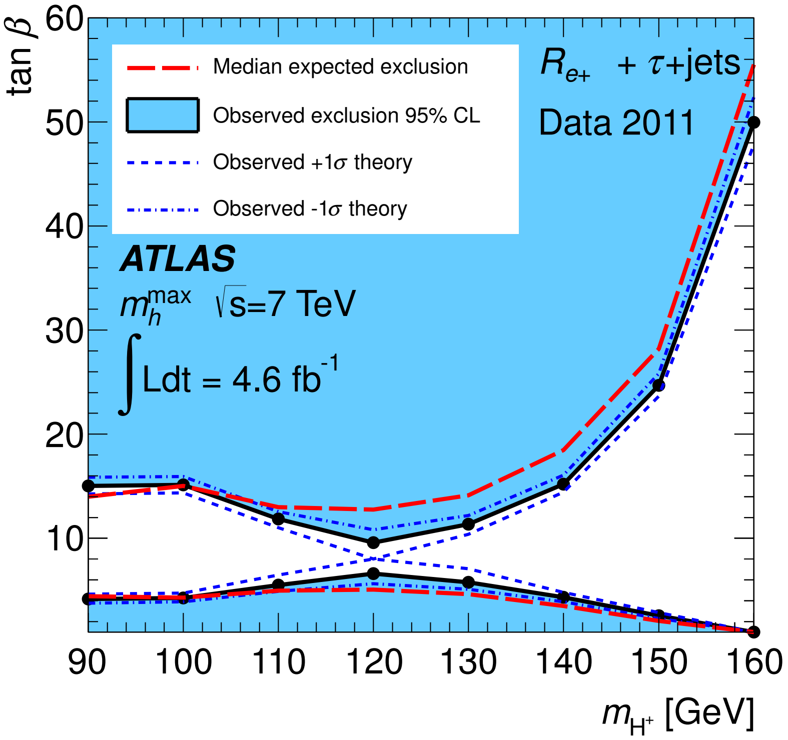

Figure 6.15. 95% confidence level exclusion limits in the parameter space of the MSSM m_h^{max} scenario, as obtained from the combination of the τ_{had} + jets channel and the event yield ratio $R_{e+\mu}$.

7. Searches for $H^+ \to \tau\nu$ in 8 TeV data

With the data collected at $\sqrt{s} = 8$ TeV in 2012, corresponding to an integrated luminosity of 20.3 fb^{-1}, the lepton $+\,\tau_{\mathrm{had}}$ and dilepton channels are analyzed simultaneously. As in the test of lepton universality in $t\bar{t}$ decays presented in section 6.3, this allows for many systematic uncertainties to be constrained by the background-rich dilepton channel. In contrast to the strategy used in the 7 TeV analysis, however, the full distribution of a transverse mass variable is now used to achieve higher sensitivity for charged Higgs boson masses further away from that of the W boson. The search is also extended to consider charged Higgs bosons with masses of up to 1 TeV, i.e. heavy charged Higgs bosons (see section 2.3.2), produced in association with a top quark. The transverse mass variable used to discriminate between signal and background among lepton $+\,\tau_{\mathrm{had}}$ events is

$$m_{\mathrm{T}} = \sqrt{2 p_{\mathrm{T}}^{\tau} E_{\mathrm{T}}^{\mathrm{miss}} (1 - \cos\Delta\phi_{\tau,\mathrm{miss}})}, \tag{7.1}$$

where $\Delta\phi_{\tau,\mathrm{miss}}$ is the azimuthal angle between the τ_{had} and the missing transverse momentum. Note that, here, m_{T} is an effective quantity which in addition to the decay products of the charged Higgs boson also contains a contribution from a neutrino that is produced in association with the electron or muon in the leptonic decay of the associated top quark. Nevertheless, it offers good separation between signal and background, in particular for high masses, as shown in Figure 7.1. Dilepton events are binned in the maximum m_{T} value constructed with either of the leptons in place of the τ_{had} in equation (7.1).

7.1 Event selection

Single-lepton triggers with an E_{T} threshold of 24 GeV or 60 GeV for electrons and a p_{T} threshold of 24 GeV or 36 GeV for muons are used. Events are then selected in the lepton $+\,\tau_{\mathrm{had}}$ channel, labeled as the Signal Region (SR), if they fulfill the following criteria:

- The event must contain exactly one *loose* lepton with $E_{\mathrm{T}} > 25$ GeV (electron) or $p_{\mathrm{T}} > 25$ GeV (muon).
- The lepton must be matched to the single-lepton trigger object.
- The event must also contain exactly one *loose* τ_{had} with $p_{\mathrm{T}} > 25$ GeV and $|\eta| < 2.3$.
- The lepton and the τ_{had} object must have electric charges of opposite signs.

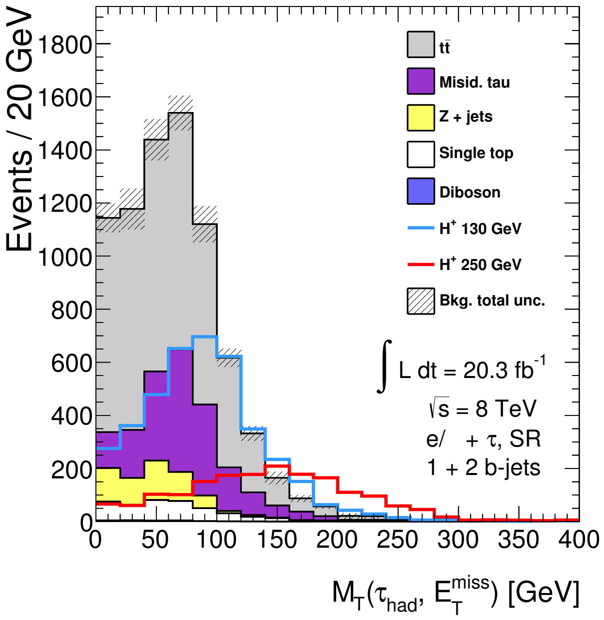

Figure 7.1. Comparison of the m_{T} distribution for the Standard Model backgrounds (stacked histograms) and two signal samples with charged Higgs boson masses of 130 GeV and 250 GeV in the lepton + τ_{had} channel. The normalization of the two signal samples correspond to $\mathscr{B}(t \to bH^+) = 10\%$ or a production cross section of 10 pb, respectively.

- The event must have $E_{\mathrm{T}}^{\mathrm{miss}} > 25$ GeV.
- The event must contain at least one jet with $p_{\mathrm{T}} > 25$ GeV.
- Exactly one or two jets must be b-tagged.
- The lepton and the τ_{had} must also pass the *tight* criteria.

The first steps are performed with loose selection criteria for all leptons and τ_{had} objects. Loose electrons and muons are defined with relaxed identification and isolation criteria, respectively. For the τ_{had} identification, the BDT-based identification is used. Loose τ_{had} objects are defined with a relaxed requirement on the BDT score. Events with a τ_{had} in the region $1.37 < |\eta| < 1.52$, corresponding to the transition regions between the barrel and the end-caps, are discarded. A reliable electron identification is not available in this region and the $e \to \tau_{\mathrm{had}}$ misidentification probability is increased, as such objects are not removed due to overlapping reconstructed electrons.

Dilepton events, labeled as the Control Region (CR), are selected if they fulfill the following criteria:

- The event must contain exactly one loose electron with $E_{\mathrm{T}} > 25$ GeV *and* exactly one loose muon with $p_{\mathrm{T}} > 25$ GeV.
- At least one of the leptons must be matched to a single-lepton trigger object.
- The leptons must have electric charges of opposite signs.
- The event must have $E_{\mathrm{T}}^{\mathrm{miss}} > 25$ GeV.
- The event must contain zero, one, or two b-tagged jets with $p_{\mathrm{T}} > 25$ GeV.
- Both leptons must also pass the tight criteria.

7.2 Backgrounds with misidentified hadronic tau decays

With the tight BDT-based τ_{had} identification, 69% of the τ_{had} objects in simulated $t\bar{t}$ events passing the SR selection are matched to a real hadronic tau decay at the generator level. Meanwhile, 28% of the τ_{had} objects are matched to a quark- or gluon-initiated jet, and the remaining 3% are matched to an electron or a muon. The background with jets misidentified as hadronic tau decays is estimated in a data-driven way with the matrix method. With this method, not only are the misidentification probabilities measured in data, but the distributions of τ_{had} candidates are also taken from the data itself rather than from simulation. The loose and tight τ_{had} selections used to define the (mis)identification probability are here defined with different thresholds on the output of the BDT-based τ_{had} identification. In contrast, in the previously presented analyses, the loose definition included all τ_{had} candidates, i.e. without any requirement on the LLH or BDT identification criteria. It was found that, by retaining some requirement on the BDT score, a large fraction of τ_{had} candidates matched to jets initiated by b quarks and gluons can be eliminated. The misidentification probabilities for the remaining jets initiated by b quarks and gluons are also closer to that of jets initiated by light quarks than if all τ_{had} candidates were included in the loose sample. This strategy therefore ensures a more uniform jet $\to \tau_{\text{had}}$ misidentification probability p_{m} across samples of events with different fractions of jets initiated by light quarks, b quarks, or gluons, hence there is no need for the OS-SS procedure of section 6.3.

The identification probability for real hadronic tau decays, p_{r}, is computed using simulated events of Standard Model processes. The BDT-based τ_{had} identification is designed to give an approximately flat identification probability of real τ_{had} objects with respect to p_{T} and η [90]. A small p_{T}-dependence is nevertheless observed and p_{r} is therefore computed as a function of p_{T}. It is also determined separately for 1-prong and 3-prong τ_{had} objects. In the computation of p_{r}, a small contribution of electrons and muons reconstructed as τ_{had} objects are included. These backgrounds are determined separately, and are therefore not considered as misidentified τ_{had} objects in the context of the matrix method, but are included in the definition of real τ_{had} objects.

The jet $\to \tau_{\text{had}}$ misidentification probability p_{m} is measured in the data, using an event selection enriched in $W+$jets events, where the W boson decays to an electron or a muon. These events are selected as follows:

- The event must contain exactly one loose lepton with $E_{\text{T}} > 25$ GeV (electron) or $p_{\text{T}} > 25$ GeV (muon).
- The lepton must be matched to the trigger object and also pass the tight criteria.
- The event must contain exactly one loose τ_{had} with $p_{\text{T}} > 25$ GeV.
- The lepton and the τ_{had} object must have electric charges of opposite signs.
- The event must not contain any b-tagged jets.
- The event must have $m_{\text{T}}^{W} = \sqrt{2p_{\text{T}}^{\ell}E_{\text{T}}^{\text{miss}}(1-\cos\Delta\phi_{\ell,\text{miss}})} > 50$ GeV.

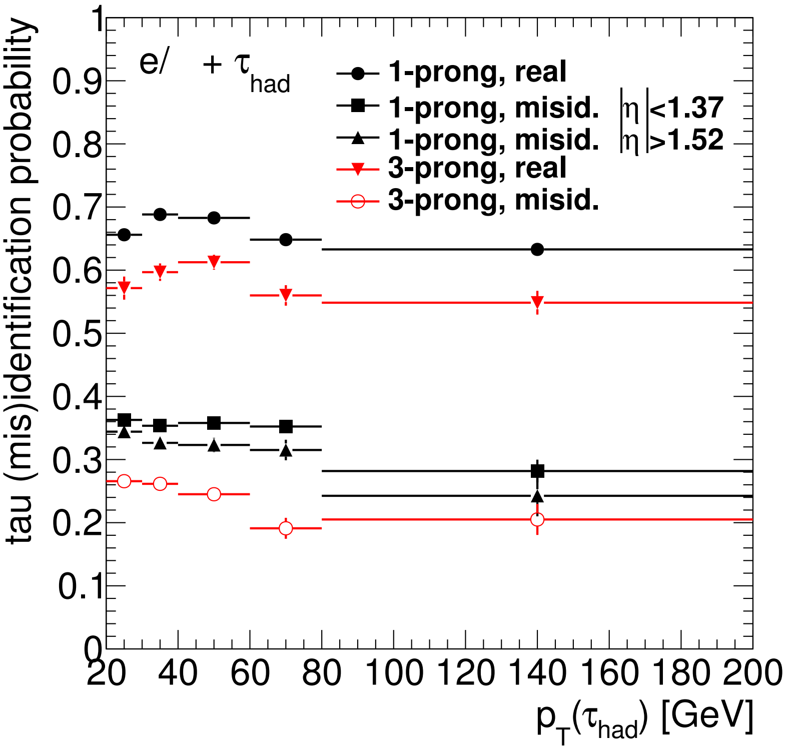

Figure 7.2. The τ_{had} (mis)identification probabilities used in the matrix method.

The contamination arising from events where the τ_{had} originates from a real hadronic tau decay, an electron, or a muon is subtracted using simulated events. The misidentification probability p_{m} is then computed as the rate at which the loose τ_{had} object, assumed to originate from a quark- or gluon-initiated jet, also passes the tight τ_{had} identification. It is measured separately for 1-prong and 3-prong τ_{had} objects, and as a function of p_{T}. For 1-prong τ_{had} objects, p_{m} is also measured separately for the low ($|\eta| < 1.37$) and high ($|\eta| > 1.52$) pseudorapidity regions. Here, the p_{T}- and η-dependencies are not treated as uncorrelated. Instead, a two dimensional binning of p_{m} is used. For 3-prong τ_{had} objects, the difference between the misidentification probabilities in the two regions of $|\eta|$ is found to be small and within the statistical uncertainties. The η-dependence of p_{m} for 3-prong τ_{had} objects is therefore ignored. The distributions of p_{m} and p_{r} used in the matrix method are shown in Figure 7.2. The dependence of p_{m} and p_{r} on other variables, including the flavor of the associated lepton and the number of b-tagged jets, was investigated and found to be negligible.

As in the previously presented analyses, the background with electrons and muons misidentified as hadronic tau decays are estimated using simulated events. In the case of electrons, scale factors are applied to match the misidentification probabilities measured in data.

7.3 Other backgrounds

In the dilepton channel, the matrix method is used in order to estimate the backgrounds with one or two misidentified leptons. For this purpose, the results of Ref. [101] are used directly. For electrons, the (mis)identification probabilities are parametrized as functions of the electron η, the distance ΔR to the closest jet, the p_{T} of the leading jet, the number of b-tagged jets, and the isolation requirement of the trigger. For muons, the (mis)identification probabilities are parametrized as functions of the muon η and p_{T}, the distance ΔR to the closest jet, and the isolation requirement of the trigger.

Very few events with a real τ_{had} and a misidentified lepton are expected, and this is also confirmed by simulation. The estimate of events with misidentified τ_{had} objects therefore also includes the only sizable contribution of misidentified lepton in the lepton $+\,\tau_{\mathrm{had}}$ channel. The nominal analysis therefore does not consider any additional background arising from misidentified leptons in this channel. Hence, no additional background arising from misidentified leptons is considered in this channel. As a cross-check, the matrix method treatment of two potentially misidentified objects was used to confirm that the background component with a real τ_{had} and a misidentified lepton is consistent with zero.

Backgrounds with real leptons and real hadronic tau decays, including $t\bar{t}$, single top quark, $Z/\gamma^{*}+$jets and diboson production, are estimated with Monte Carlo simulations. The POWHEG $t\bar{t}$ sample is reweighted to better match the $t\bar{t}$ p_{T} spectrum in data, as described in section 5.1.2. In addition, the p_{T} spectrum of the $Z/\gamma^{*}+$jets sample is also reweighted, and events with a Z boson produced in association with $b\bar{b}$ or $c\bar{c}$ are initially given a higher weight, in order to match previous measurements by ATLAS [102]. In the final fit, the cross sections for $t\bar{t}$ production, Z boson production in association with light quarks, and Z boson production in association with $b\bar{b}$ or $c\bar{c}$ pairs are left floating and are constrained by the dilepton regions with zero, one, or two b-jets.

7.4 Systematic uncertainties

Systematic uncertainties on the measured luminosity, the simulation of the electron and muon triggers, the reconstruction and identification of electrons, muons, jets, and hadronic tau decays, as well as the energy or momentum scale and resolution of those objects, and of the missing transverse momentum are treated similarly to the previous analyses. Jet-related uncertainties have among the largest impacts on the result and are now given a more detailed treatment: the uncertainties on the jet energy scale and b-tagging are each broken down into 22 different components that are varied separately, compared to only one or two effective components used in the analyses of the 7 TeV data. Tables 7.1 to 7.4 summarize the impact of the detector-related systematic uncertainties on the Standard Model $t\bar{t}$ and signal event yields in the signal region.

The systematic uncertainties arising from both the generation and parton shower model in $t\bar{t}$ events and in signal events are evaluated by comparing the results obtained using POWHEG interfaced to PYTHIA 8 with MC@NLO interfaced to HERWIG. The systematic uncertainties originating from initial- and final-state radiation are evaluated for the $t\bar{t}$ background and low mass signal events using Standard Model $t\bar{t}$ samples generated with ACERMC interfaced to PYTHIA 6, in which parameters controlling the jet production rate are varied. For the high mass signal, this uncertainty is evaluated by varying scale parameters in dedicated signal samples generated with POWHEG interfaced to PYTHIA 8. An additional uncertainty coming from the difference between the calculation of heavy charged Higgs boson production based on 4FS or 5FS is considered and is evaluated with MADGRAPH interfaced to PYTHIA 8. Table 7.5 summarizes the impact of the generator-related systematic uncertainties on the Standard Model $t\bar{t}$ and signal event yields.

All systematic uncertainties are propagated through the matrix method used to estimate the background arising from misidentified hadronic tau decays. As this background is relatively large, this is preferred over the use of an effective uncertainty that would not have the proper correlations with the corresponding variations of the simulated backgrounds. Uncertainties on the simulation affect the measurement of the misidentification probability p_{m} in data via the subtraction of events with real taus, needed to obtain a pure sample of misidentified hadronic tau decays in the data. The uncertainties on the tau identification and electron-veto BDTs also affect the identification probability p_{r}, which is computed using simulated events.

Additional uncertainties on the background with misidentified hadronic tau decays arise from the statistical uncertainties on p_{m} and p_{r}, and from the difference in jet composition between the region used to measure p_{m} and the signal region. The statistical uncertainty on each bin of p_{m} and p_{r} is considered separately. The uncertainty related to the jet composition is evaluated using simulation. The misidentification probability is computed using simulated events passing the same selection as used to measure p_{m} in data, and using simulated events passing the signal selection. The relative difference (computed separately for each bin) is taken as an uncertainty on the values of p_{m} measured in the data. Tables 7.6 and 7.7 summarize the impact of the main systematic uncertainties on the background arising from misidentified hadronic tau decays in the signal region with one or two b-tagged jets.

To simplify the fitting procedure, systematic uncertainties that have negligible effects are pruned from the model and the corresponding nuisance parameters are instead fixed to their nominal values. Normalization uncertainties are removed if the impact on the event yield is less than 0.5%. Uncertainties that affect the shape of the fitted histograms are removed if the relative variation is less than 0.5% in each bin.

Table 7.1. *The effects of systematic uncertainties on the final Standard Model $t\bar{t}$ event yield in the $e+\tau_{\mathrm{had}}$ and $\mu+\tau_{\mathrm{had}}$ channels with 1 b-tagged jet.*

	Event yield shift	
Source of uncertainty	$e+\tau_{\mathrm{had}}$	$\mu+\tau_{\mathrm{had}}$
b-jet (mis)tag efficiency	0.6%	0.7%
Jet energy scale (baseline)	0.3%	0.5%
Jet energy scale (flavor)	$< 0.1\%$	0.3%
Jet energy scale (*b*-jet specific)	0.2%	0.1%
Jet vertex fraction	$< 0.1\%$	0.7%
$E_{\mathrm{T}}^{\mathrm{miss}}$ soft terms resolution	$< 0.1\%$	$< 0.1\%$
$E_{\mathrm{T}}^{\mathrm{miss}}$ soft terms scale	0.1%	0.2%
Tau electron-veto	0.3%	0.2%
Tau energy scale	2.5%	2.6%
Tau identification	1.9%	2.0%
Lepton $E_{\mathrm{T}}/p_{\mathrm{T}}$ scale	0.3%	$< 0.1\%$
Lepton $E_{\mathrm{T}}/p_{\mathrm{T}}$ resolution	0.1%	$< 0.1\%$
Lepton trigger and identification	$< 0.1\%$	1.9%

Table 7.2. *The effects of systematic uncertainties on the final Standard Model $t\bar{t}$ event yield in the $e+\tau_{\mathrm{had}}$ and $\mu+\tau_{\mathrm{had}}$ channels with 2 b-tagged jets.*

	Event yield shift	
Source of uncertainty	$e+\tau_{\mathrm{had}}$	$\mu+\tau_{\mathrm{had}}$
b-jet (mis)tag efficiency	5.1%	5.0%
Jet energy scale (baseline)	1.4%	1.2%
Jet energy scale (flavor)	0.2%	0.3%
Jet energy scale (*b*-jet specific)	0.7%	1.0%
Jet vertex fraction	0.3%	0.2%
$E_{\mathrm{T}}^{\mathrm{miss}}$ soft terms resolution	$< 0.1\%$	0.1%
$E_{\mathrm{T}}^{\mathrm{miss}}$ soft terms scale	0.1%	0.1%
Tau electron-veto	0.2%	0.2%
Tau energy scale	2.7%	2.9%
Tau identification	1.9%	1.9%
Lepton $E_{\mathrm{T}}/p_{\mathrm{T}}$ scale	0.2%	$< 0.1\%$
Lepton $E_{\mathrm{T}}/p_{\mathrm{T}}$ resolution	0.1%	$< 0.1\%$
Lepton trigger and identification	$< 0.1\%$	1.9%

Table 7.3. *The effects of systematic uncertainties on the final signal event yield in the* $e+\tau_{\text{had}}$ *and* $\mu+\tau_{\text{had}}$ *channels with 1 b-tagged jet, assuming a charged Higgs boson mass of 200 GeV.*

	Event yield shift	
Source of uncertainty	$e+\tau_{\text{had}}$	$\mu+\tau_{\text{had}}$
b-jet (mis)tag efficiency	1.9%	2.2%
Jet energy scale (baseline)	1.3%	1.0%
Jet energy scale (flavor)	0.1%	0.2%
Jet energy scale (b-jet specific)	0.8%	0.6%
Jet vertex fraction	0.3%	0.6%
$E_{\text{T}}^{\text{miss}}$ soft terms resolution	0.2%	0.4%
$E_{\text{T}}^{\text{miss}}$ soft terms scale	$< 0.1\%$	0.2%
Tau electron-veto	$< 0.1\%$	$< 0.1\%$
Tau energy scale	0.6%	0.6%
Tau identification	1.8%	1.9%
Lepton $E_{\text{T}}/p_{\text{T}}$ scale	0.3%	0.1%
Lepton $E_{\text{T}}/p_{\text{T}}$ resolution	0.2%	0.3%
Lepton trigger and identification	$< 0.1\%$	1.8%

Table 7.4. *The effects of systematic uncertainties on the final signal event yield in the* $e+\tau_{\text{had}}$ *and* $\mu+\tau_{\text{had}}$ *channels with 2 b-tagged jets, assuming a charged Higgs boson mass of 100 GeV.*

	Event yield shift	
Source of uncertainty	$e+\tau_{\text{had}}$	$\mu+\tau_{\text{had}}$
b-jet (mis)tag efficiency	5.2%	4.9%
Jet energy scale (baseline)	1.4%	2.8%
Jet energy scale (flavor)	0.2%	0.8%
Jet energy scale (b-jet specific)	0.1%	1.7%
Jet vertex fraction	0.2%	0.5%
$E_{\text{T}}^{\text{miss}}$ soft terms resolution	0.6%	0.8%
$E_{\text{T}}^{\text{miss}}$ soft terms scale	0.1%	0.3%
Tau electron-veto	$< 0.1\%$	0.1%
Tau energy scale	2.2%	2.4%
Tau identification	1.9%	2.1%
Lepton $E_{\text{T}}/p_{\text{T}}$ scale	0.7%	0.2%
Lepton $E_{\text{T}}/p_{\text{T}}$ resolution	0.2%	0.3%
Lepton trigger and identification	$< 0.1\%$	1.8%

Table 7.5. *The effects of systematic uncertainties arising from Standard Model (SM) $t\bar{t}$ and signal event modeling on the overall normalization of each sample.*

Source of uncertainty	Total event yield shift
Generator and parton shower (SM and low-mass H^+)	3.2%
Generator and parton shower (high-mass H^+)	5.4%
Initial- and final-state radiation (SM and low-mass H^+)	7.7%
Initial- and final-state radiation (high-mass H^+)	$< 1\%$
High-mass H^+production (4FS vs 5FS)	$< 1\%$

Table 7.6. *The effects of systematic uncertainties on the final event yield predicted by the matrix method used to estimate the jet $\rightarrow \tau_{\text{had}}$ background in the $e + \tau_{\text{had}}$ and $\mu + \tau_{\text{had}}$ channels with 1 b-tagged jet.*

	Event yield shift	
Source of uncertainty	$e + \tau_{\text{had}}$	$\mu + \tau_{\text{had}}$
Jet energy scale (baseline)	1.8%	1.6%
Jet energy scale (flavor composition)	1.9%	1.7%
$E_{\text{T}}^{\text{miss}}$ soft terms	3.8%	3.7%
Tau electron veto	2.2%	2.4%
Tau energy scale	2.6%	2.4%
Jet $\rightarrow \tau_{\text{had}}$ p_{m} (jet composition)	1.7%	1.7%
Jet $\rightarrow \tau_{\text{had}}$ p_{m}, p_{r} (stat)	1.8%	2.0%

Table 7.7. *The effects of systematic uncertainties on the final event yield predicted by the matrix method used to estimate the jet $\rightarrow \tau_{\text{had}}$ background in the $e + \tau_{\text{had}}$ and $\mu + \tau_{\text{had}}$ channels with 2 b-tagged jets.*

	Event yield shift	
Source of uncertainty	$e + \tau_{\text{had}}$	$\mu + \tau_{\text{had}}$
b-jet (mis)tag efficiency	1.0%	1.0%
Jet energy scale (baseline)	1.8%	1.9%
Jet energy scale (flavor composition)	1.8%	1.8%
$E_{\text{T}}^{\text{miss}}$soft terms	3.6%	3.8%
Tau electron veto	2.7%	2.5%
Tau energy scale	2.4%	2.6%
Jet $\rightarrow \tau_{\text{had}}$ p_{m} (jet composition)	1.5%	1.6%
Jet $\rightarrow \tau_{\text{had}}$ p_{m}, p_{r} (stat)	2.6%	2.4%

7.5 Results

The analysis is performed using separate categories of events with zero, one, or two b-tagged jets in the control region, while the signal region is merged to contain events with either one or two b-tagged jets. This is done in order to reduce the uncertainty on the b-jet multiplicity arising from the choice of calculation scheme for the high mass signal process. Figure 7.3 shows the expected and observed distributions of the lepton p_{T}, the p_{T} of the τ_{had} object, and $E_{\mathrm{T}}^{\mathrm{miss}}$ in the signal region. Figure 7.4 shows the expected and observed distributions of the dilepton invariant mass in the control regions. When computing exclusion limits, the electron- and muon-triggered events are merged. The normalization of the background from Standard Model $t\bar{t}$ events with real leptons and hadronic tau decays is allowed to float freely and is constrained by the mostly signal-free dilepton channel. The predicted and observed distributions of (maximum) m_{T} in the signal region and the control regions, used as inputs to the limit computation, are shown in Figure 7.5. The best-fit values of the nuisance parameters under the background-only hypothesis, with their profiled uncertainties, are shown in Figure 7.6. The data favors a $t\bar{t}$ cross section about 11% lower than the theoretical prediction, calculated at NNLO in QCD including resummation of next-to-next-to-leading logarithmic (NNLL) soft gluon terms [70] for a top quark mass of 172.5 ± 1 GeV with PDF and α_s uncertainties determined using the PDF4LHC prescription [103]. The theoretical cross section with its uncertainties is $252.89^{+6.39}_{-8.64}(\mathrm{scale})^{+7.58}_{-7.33}(m_t)^{+11.67}_{-11.67}(\mathrm{PDF}+\alpha_s)$ pb. If the fit is performed under the signal hypothesis, the best-fit value of the signal strength becomes slightly negative – which does not correspond to a physically meaningful scenario – but is consistent with zero within its uncertainty.

The effect of systematic uncertainties is important only for light charged Higgs bosons. For high H^+ masses, the statistical uncertainty is dominant. Figures 7.7 and 7.8 show the pulls on the nuisance parameters for signal masses of 130 GeV and 250 GeV. The $\pm 1\sigma$ error bars indicated in red are the estimated uncertainties on the nominal values of these nuisance parameters as inserted in the fit. An unconditional fit is performed, leaving all nuisance parameters floating. The fit is then repeated for each uncertainty, leaving the parameter of interest floating while all others are fixed to their best-fit values. The black points represent the shift of the best-fit value with respect to the original value of each parameter, in units of the original uncertainty, and the black error bar represents the new uncertainty. If the black error bar is smaller than the red error band, then the computed uncertainty is smaller than the one used as input to the fit, and vice versa. The yellow and hatched blue bands represent the pre-fit and post-fit impact of each nuisance parameter on the fitted value of the signal strength. The nuisance parameters are ranked according to their post-fit impact on the signal strength. Only the most important nuisance parameters are shown. The dominating uncertainties are related to the jet energy scale and to the modeling of $t\bar{t}$ events. The single largest uncertainty is related the effect of the jet composition on the jet energy scale. It is a centrally derived value that is designed to be applicable to any analysis of ATLAS data and therefore assumes completely unknown fractions of quark- and gluon-initiated jets.

The expected and observed limits are shown in Figures 7.9 and 7.10. Upper limits are set on the branching fraction $\mathscr{B}(t \to bH^+) \times \mathscr{B}(H^+ \to \tau\nu)$ in the range 1.1–0.3% for 80 GeV $\leq m_{H^+} \leq$ 160 GeV, and on the signal cross section times $\mathscr{B}(H^+ \to \tau\nu)$ in the range 0.93–0.03 pb for 180 GeV $\leq m_{H^+} \leq$ 1 TeV. Alternative strategies using the OS-SS weighting, the ratio $R_{e+\mu}$, or the m_{T2}^{H} variable for the limit setting were explored but were not found to significantly improve the result. The observed limit presents a downward deviation with respect to the expected limit along the whole mass range. This effect is driven by the electron channel, where the deviation is maximal in the signal mass range 110–250 GeV. It can be traced to a deficit of events in the region 100 GeV $< m_{\mathrm{T}} <$ 200 GeV as well as in the high mass region $m_{\mathrm{T}} >$ 300 GeV. Excluding these problematic bins and recomputing the limits would improve the compatibility between the observed and expected limits to within one standard deviation, while strongly reducing the sensitivity.

7.6 Combination and interpretation

The results presented here are complementary to the search performed with the τ_{had} + jets final state, which has also been updated with the 8 TeV dataset [50]. The lepton + τ_{had} channel is less sensitive than the τ_{had} + jets channel, due to the lower branching fraction, and in the case of a light charged Higgs boson, the presence of an additional neutrino in the event which significantly worsens the resolution of the transverse mass. A combination of the two channels can nevertheless improve upon the τ_{had} + jets result, in particular in the very low mass region $m_{H^+} <$ 100 GeV where the expected exclusion limit is improved by up to 35%. The downward fluctuation observed in the data further improves the observed limits, which are up to 40% lower in the low mass region for the combination than for τ_{had} + jets alone, and up to 20% lower in the high mass region. The combined limits are shown in Figure 7.11. The observed upper limits on the product of branching fractions $\mathscr{B}(t \to bH^+) \times \mathscr{B}(H^+ \to \tau\nu)$ vary in the range 0.6–0.15% for 80 GeV $\leq m_{H^+} \leq$ 160 GeV, while the observed upper limits on the production cross section are in the range 0.43–0.004 pb for 180 GeV $\leq m_{H^+} \leq$ 1 TeV. Figure 7.12 shows an interpretation of this result in the updated m_h^{max}, $m_h^{\mathrm{mod}+}$, and $m_h^{\mathrm{mod}-}$ benchmark scenarios of the MSSM.

Conclusion

This thesis has described searches for charged Higgs bosons decaying to a tau lepton and a neutrino, performed using data recorded by the ATLAS experiment in 2011 and 2012. Final states with two charged leptons, or with one charged lepton and a hadronically decaying tau were used, and charged Higgs boson masses below and above that of the top quark were considered. Simulated backgrounds with real leptons and hadronic tau decays were normalized to data using control regions, and backgrounds with misidentified leptons or hadronic tau decays were estimated from the data itself. With 20.3 fb^{-1} of data collected at a center-of-mass energy of 8 TeV, upper limits at 95% confidence level are placed on the branching fraction $\mathscr{B}(t \to bH^+) \times \mathscr{B}(H^+ \to \tau^+\nu)$ in the range 1.1–0.3% for charged Higgs boson masses between 80 GeV and 160 GeV, and on the top-quark associated charged Higgs boson production cross section in the range 0.93–0.03 pb for charged Higgs boson masses between 180 GeV and 1 TeV. Both the expected and observed limits are the best obtained to date in this search channel. A combination of these results with a search performed using the fully hadronic final state yields corresponding limits of 0.6–0.15% for the low mass range and 0.43–0.004 pb for the high mass range.

During the preparation of this thesis, a Higgs boson was observed for the first time by the ATLAS and CMS collaborations. This proves the existence of at least one scalar field and encourages further searches for additional Higgs bosons. The focus of future searches for charged Higgs bosons will undoubtedly be on the high mass regime. The decay mode of the charged Higgs boson into a tau lepton and a neutrino remains a search channel of high interest due to the relatively clean event signatures and its sizable branching fraction in large parts of the parameter space. The analysis of the lepton $+\,\tau_{\text{had}}$ final state presented in this thesis is less sensitive than the previously published analysis of the $\tau_{\text{had}}+$jets final state, and should be seen as complementary to that search. However, its importance will increase as higher mass ranges are probed, when the relative importance of the missing transverse momentum contributed by the neutrino appearing in the Standard Model leptonic decay of the top quark is reduced. With 20.3 fb^{-1} of 8 TeV data, the sensitivity of the analysis is limited by statistical uncertainties. When more data is collected during Run 2 of the LHC, the sensitivity of this channel can therefore be expected to increase. Interesting prospects for improving the analysis strategy include the use of tau polarization information as the charged Higgs boson and the W boson have a different spin.

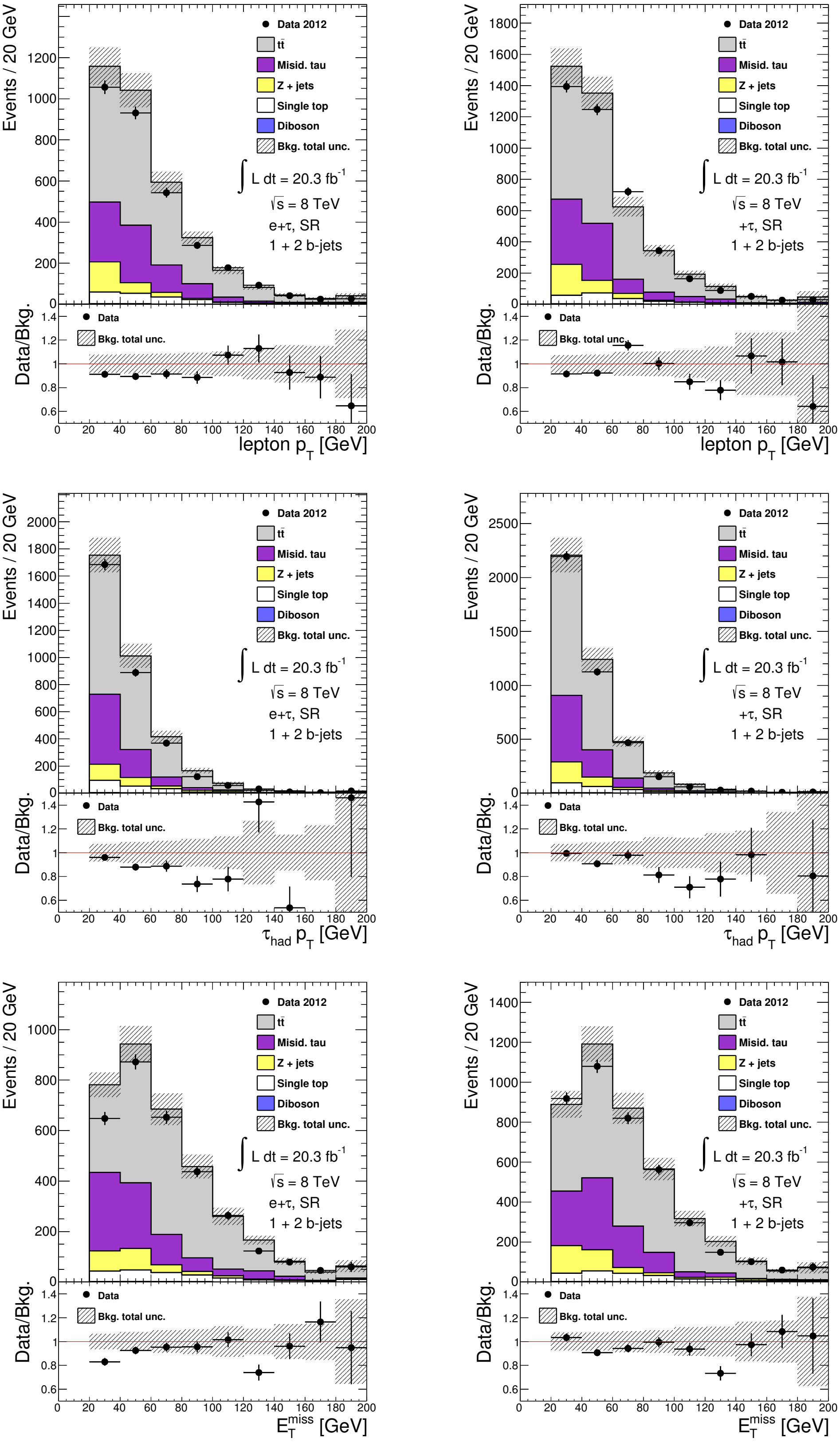

Figure 7.3. The lepton p_{T} (top), the p_{T} of the τ_{had} object (middle), and the $E_{\mathrm{T}}^{\mathrm{miss}}$ (bottom) in $e+\tau_{\mathrm{had}}$ (left) and $\mu+\tau_{\mathrm{had}}$ (right) events passing the SR selection. In all plots, the last bin includes overflow.

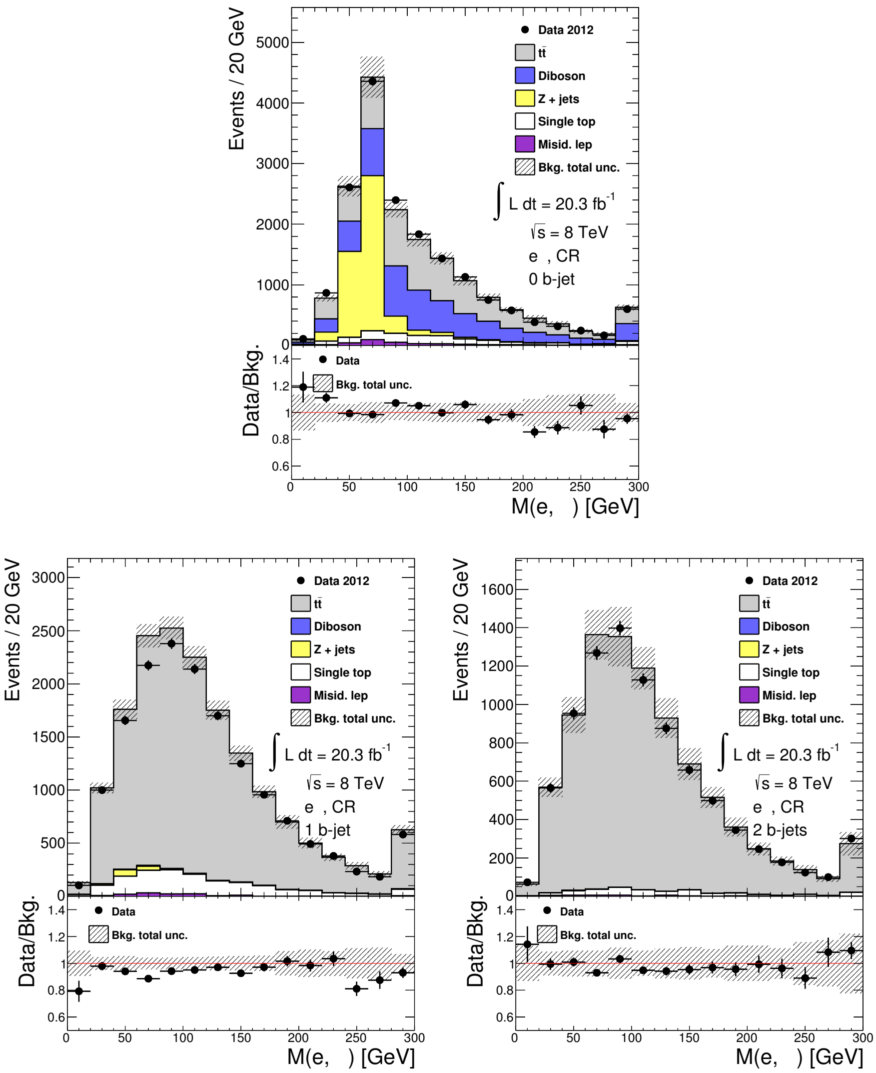

Figure 7.4. The $e\mu$ invariant mass in dilepton events passing the CR selection with 0 b-tagged jets (top), 1 b-tagged jet (bottom left) or 2 b-tagged jets (bottom right). In all plots, the last bin includes overflow.

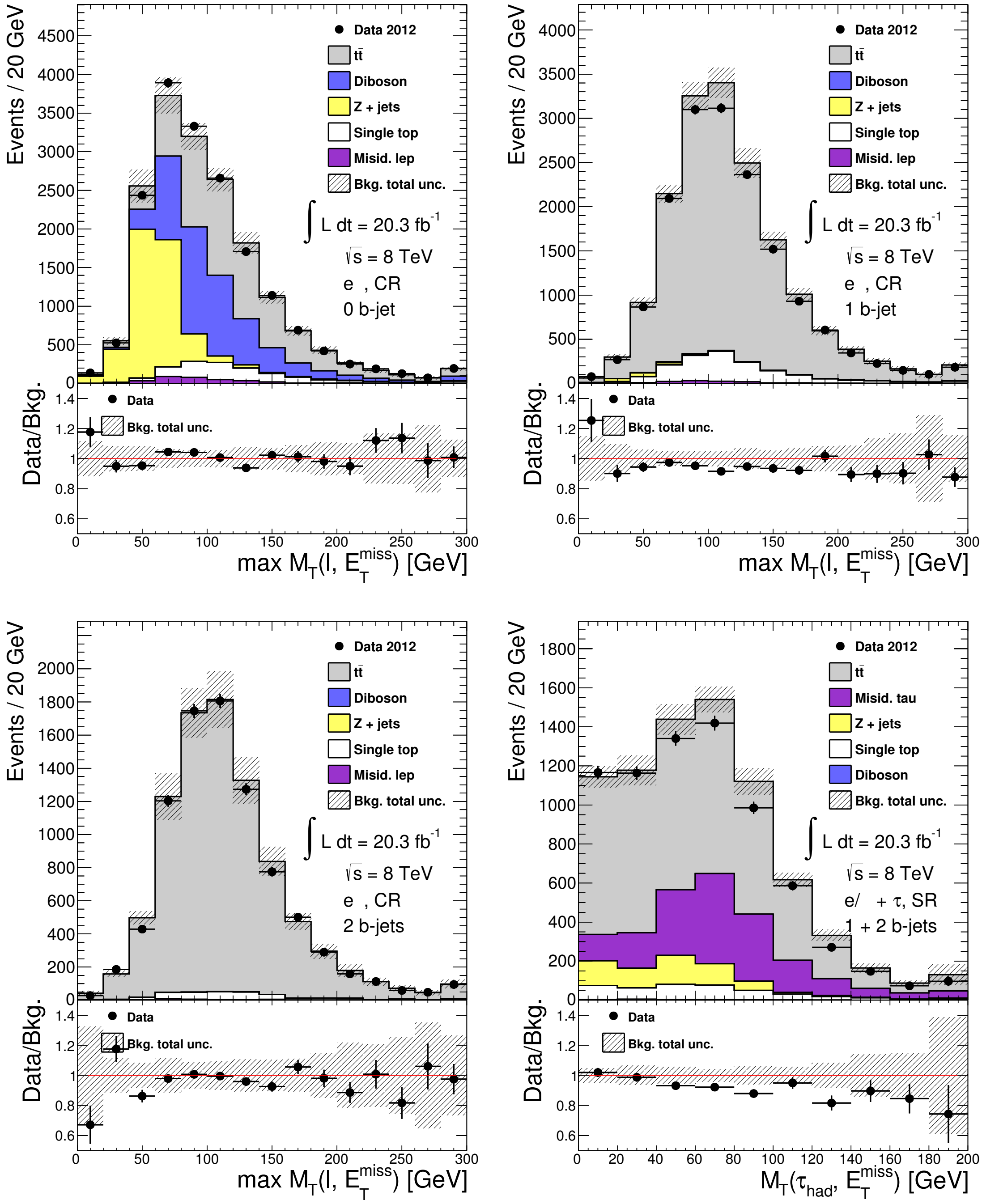

Figure 7.5. The inputs to the fit: the maximum transverse mass of dilepton events passing the CR selection with 0 b-tagged jets (top left), 1 b-tagged jet (top right), and 2 b-tagged jets (bottom left), as well as the transverse mass of lepton + τ_{had} events passing the SR selection with one or two b-tagged jets. In all plots, the last bin includes overflow.

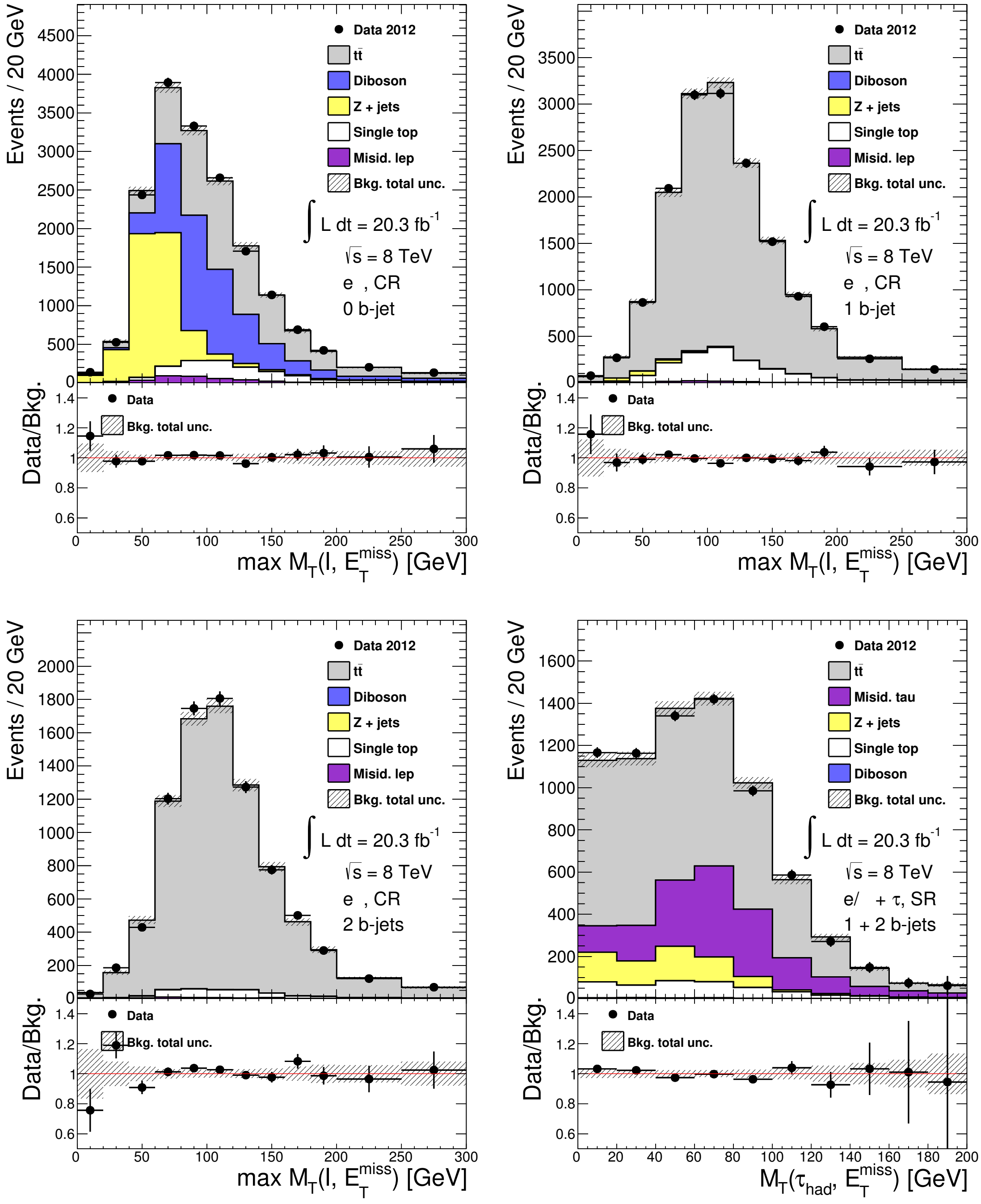

Figure 7.6. Post-fit plots of the maximum transverse mass of dilepton events passing the CR selection with 0 b-tagged jets (top left), 1 b-tagged jet (top right), and 2 b-tagged jets (bottom left), as well as the transverse mass of lepton $+ \tau_{\text{had}}$ events passing the SR selection with one or two b-tagged jets. In these plots, the best-fit values of all nuisance parameters under the background-only hypothesis, and their uncertainties, are shown. The last bin includes overflow.

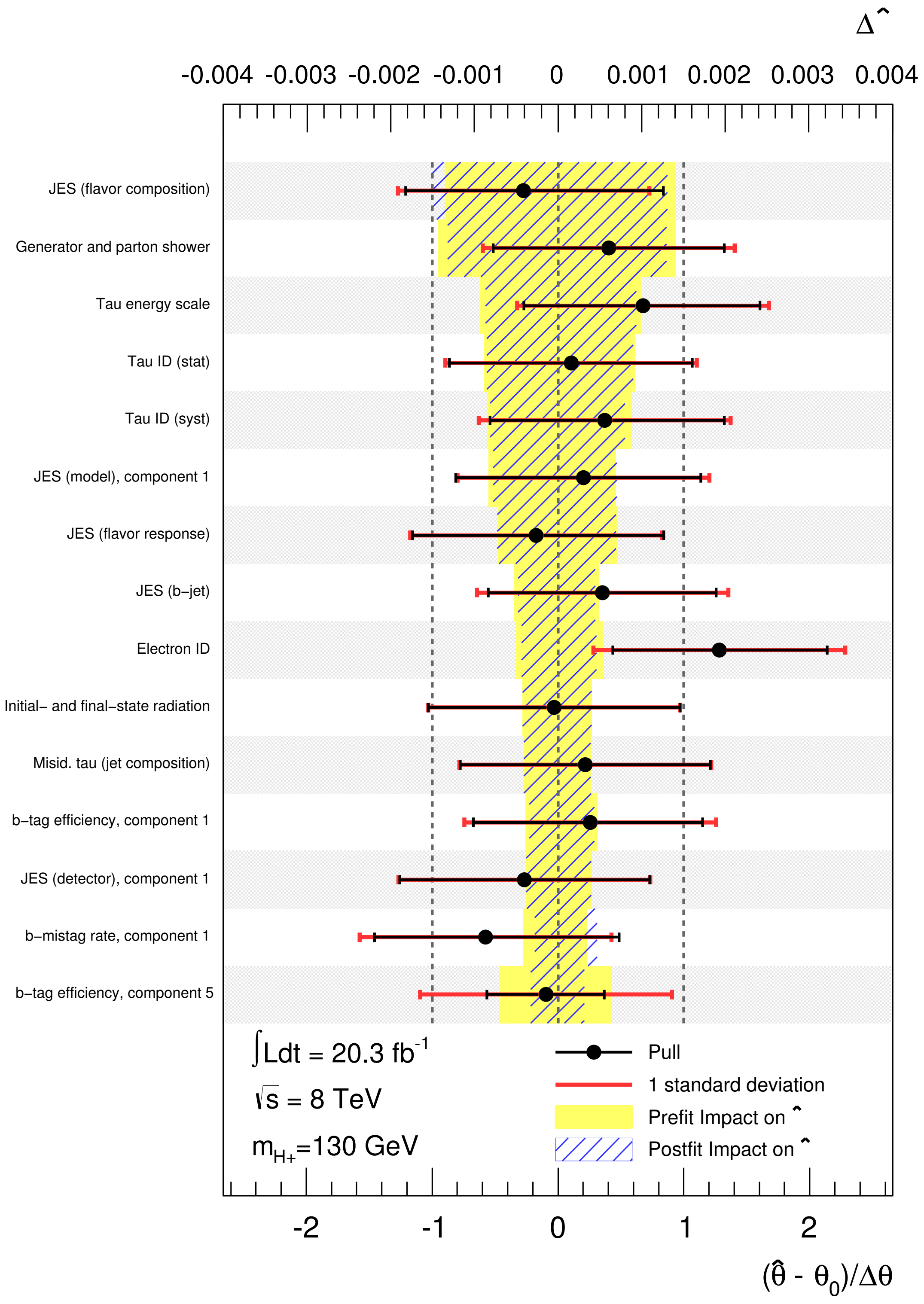

Figure 7.7. Pull distribution for the $m_{H^+} = 130$ GeV hypothesis. The black markers indicate the shift of the best-fit value of each parameter with respect to its nominal value in units of one standard deviation (red) as indicated on the bottom axis, while the yellow and hatched blue bands respectively show the pre- and post-fit impacts on the fitted signal strength as indicated on the top axis. The 15 most important parameters are shown. Some of the uncertainties related to the jet energy scale (JES) or *b*-tagging are split into several effective components.

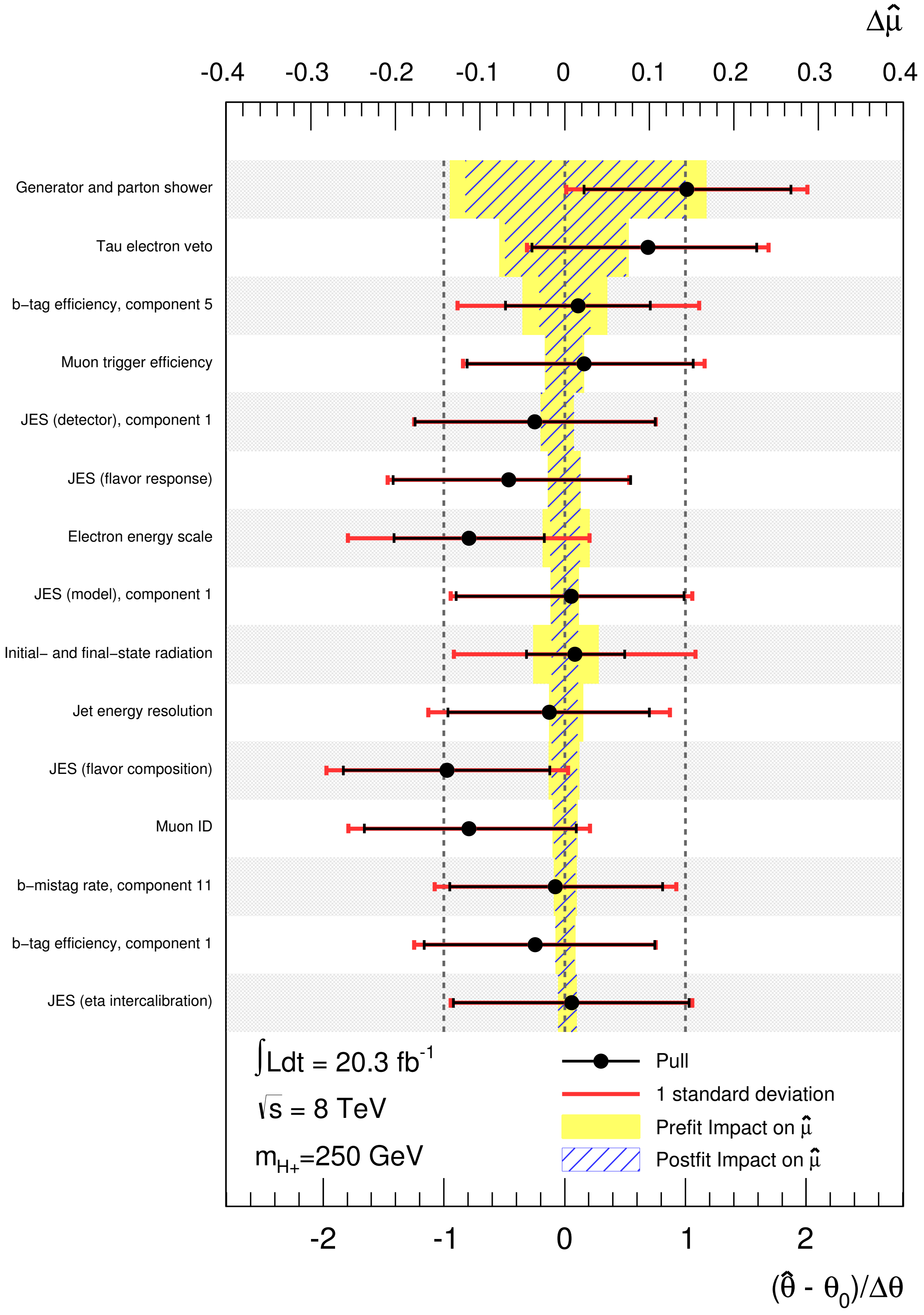

Figure 7.8. Pull distribution for the $m_{H^+} = 250$ GeV hypothesis. The black markers indicate the shift of the best-fit value of each parameter with respect to its nominal value in units of one standard deviation (red) as indicated on the bottom axis, while the yellow and hatched blue bands respectively show the pre- and post-fit impacts on the fitted signal strength as indicated on the top axis. The 15 most important parameters are shown. Some of the uncertainties related to the jet energy scale (JES) or *b*-tagging are split into several effective components.

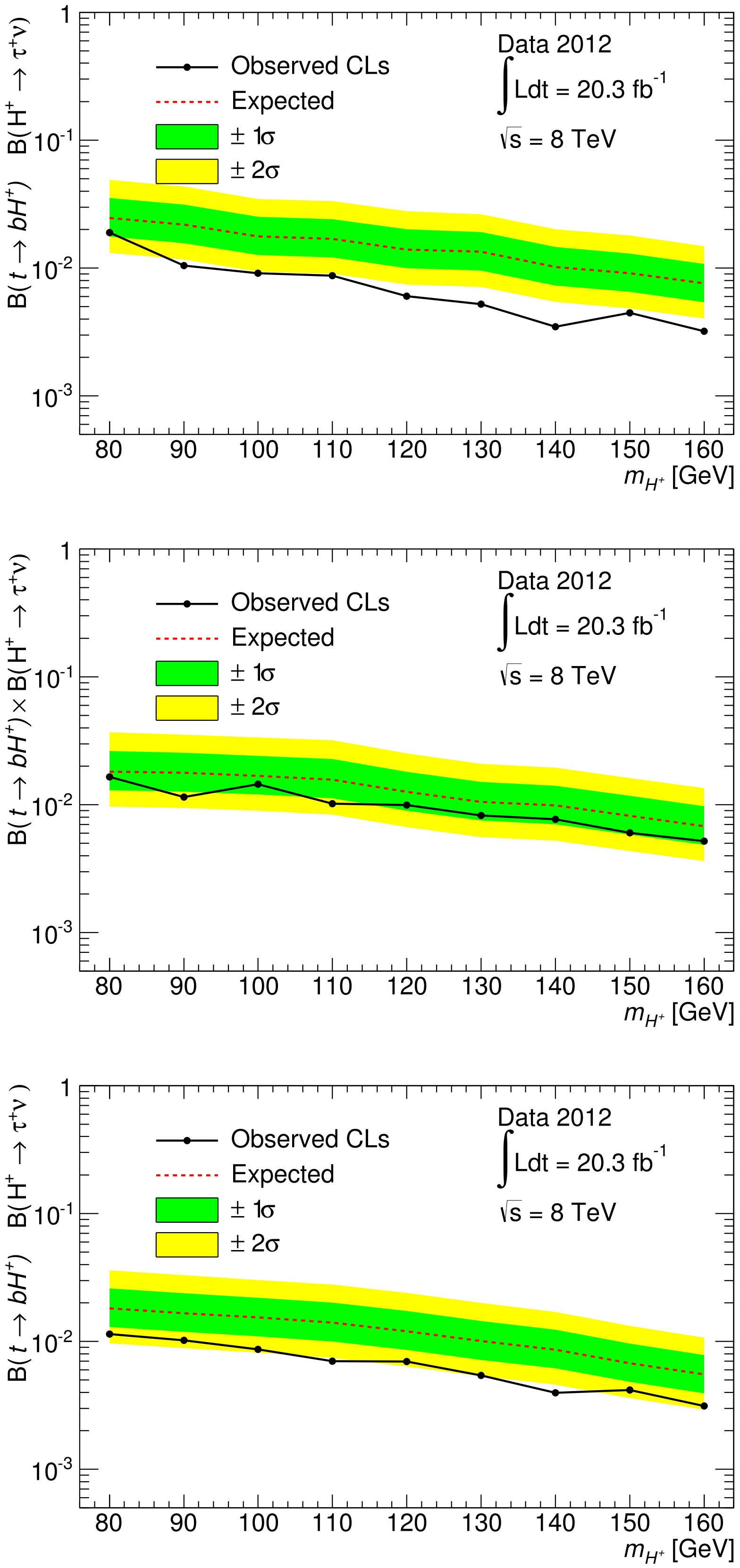

Figure 7.9. Expected and observed 95% confidence level upper limits on light charged Higgs boson production, obtained with electron-triggered events (top), muon-triggered events (middle) and a combination of both (bottom).

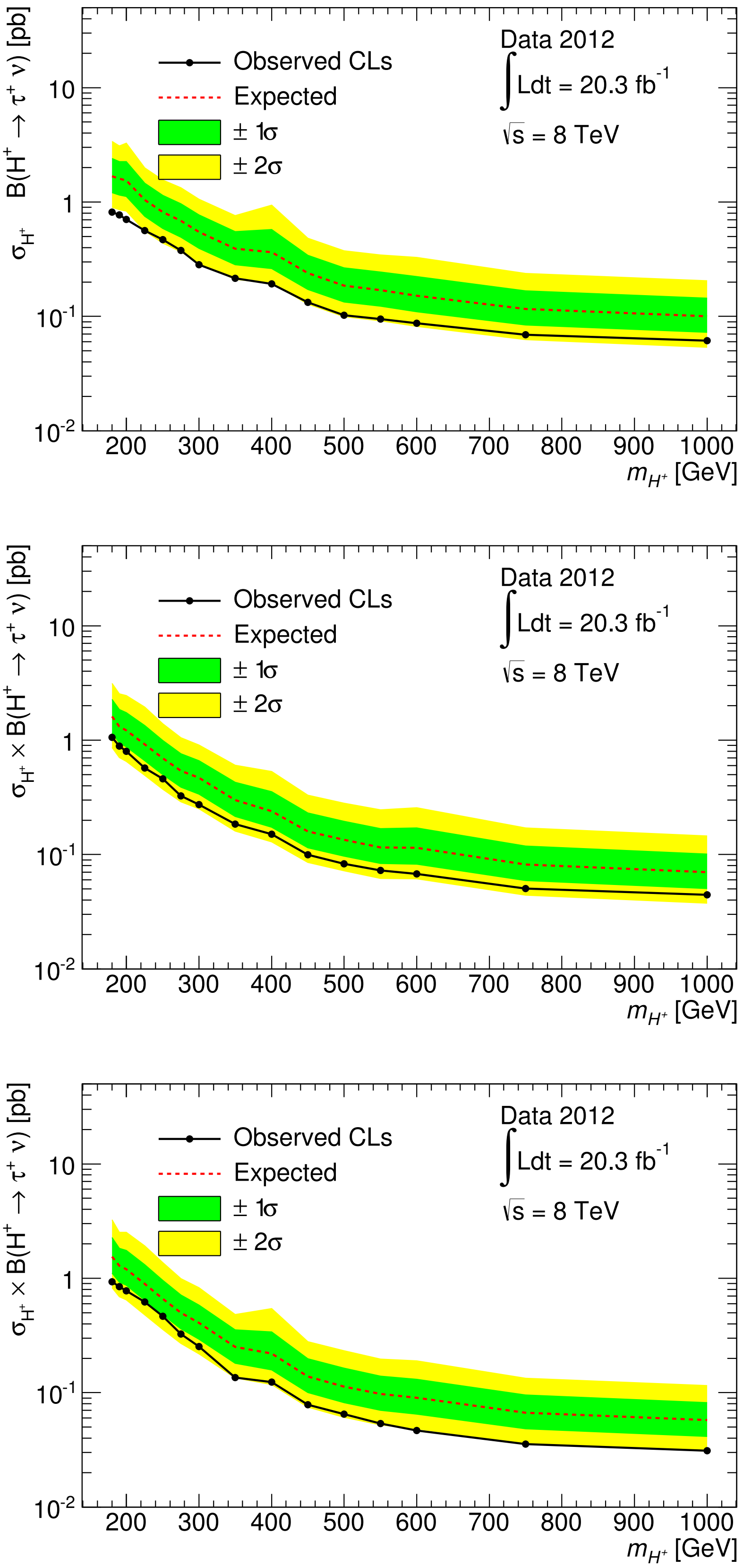

Figure 7.10. Expected and observed 95% confidence level upper limits on heavy charged Higgs boson production, obtained with electron-triggered events (top), muon-triggered events (middle) and a combination of both (bottom).

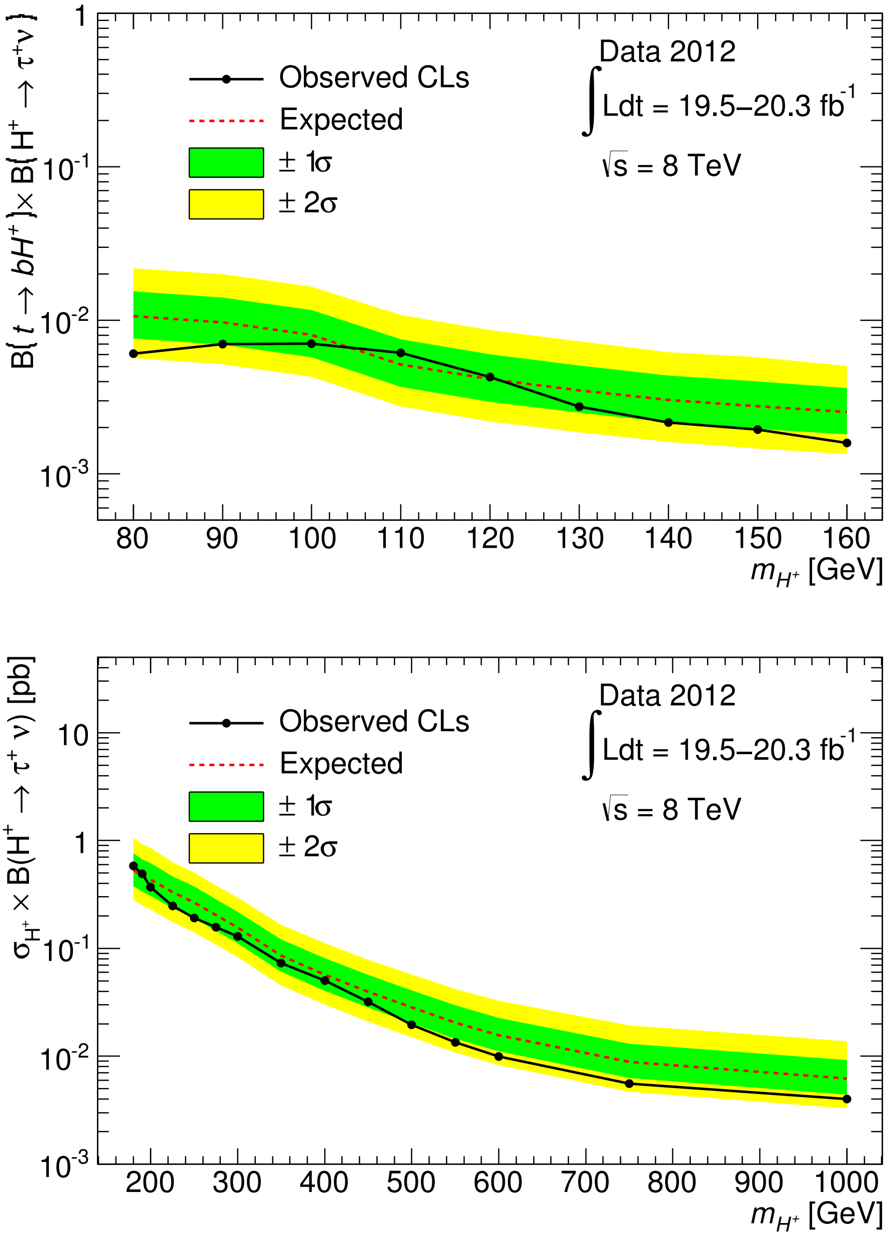

Figure 7.11. Expected and observed 95% confidence level upper limits on charged Higgs boson production in the low (top) and high (bottom) mass range, obtained with a combination of the lepton $+\,\tau_{\mathrm{had}}$ and $\tau_{\mathrm{had}}+$ jets channels.

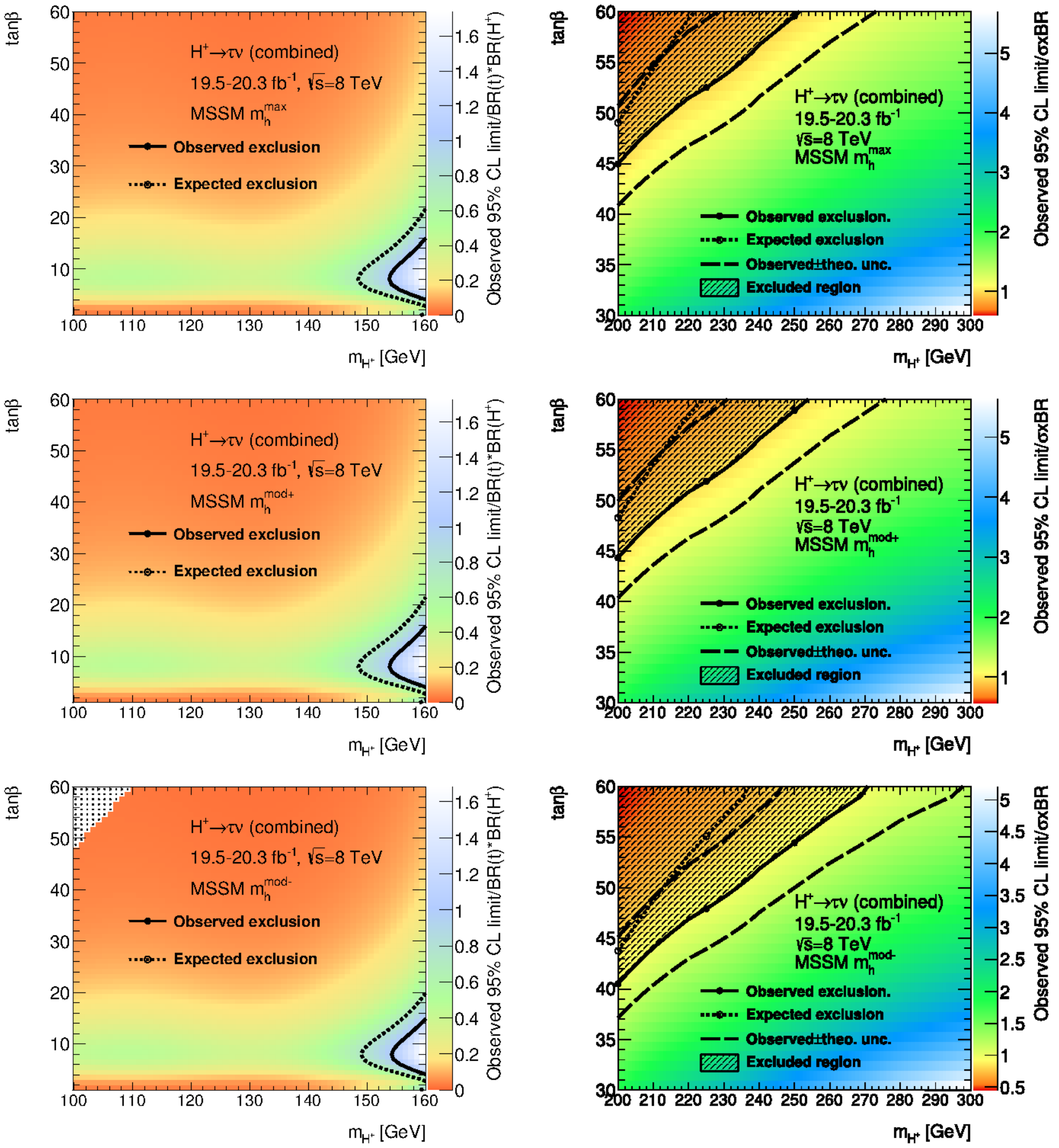

Figure 7.12. Expected and observed 95% confidence level exclusion limits in the $\tan\beta$, m_{H^+} plane for low (left) and high (right) mass ranges in the updated $m_h^{\max}$ (top), $m_h^{\mathrm{mod}+}$ (middle), and $m_h^{\mathrm{mod}-}$ (bottom) MSSM scenarios, obtained by combining the lepton $+\,\tau_{\mathrm{had}}$ and τ_{had} +jets channels. The colors indicate the ratio of the achieved exclusion limit to the predicted signal strength (cross section and/or branching fraction). A large value means that large improvements of the search sensitivity would be needed to exclude that point in the parameter space. Theoretical predictions above $\tan\beta = 60$ are not available.

At the time of writing, the restart of the LHC at $\sqrt{s} = 13$ TeV is imminent. This will mark the beginning of a new chapter of Higgs physics. Up to now, the discovered Higgs boson appears to be consistent with that predicted by the Standard Model. Establishing or disproving this fact will be a key task for the LHC in the years to come. With higher collision energies than ever before, and higher integrated luminosity, we can expect detailed measurements of the discovered Higgs boson, and increased sensitivities in many searches for additional Higgs bosons. This will either validate the last unexplored sector of the Standard Model, or possibly let us discover something completely new.

Résumé en français

1. Le Modèle Standard de la physique des particules

La physique des particules est l'étude des composants microscopiques élémentaires présents dans notre Univers. Toute structure de cet Univers, que ce soit un atome, un grain de poussière ou une galaxie, est formée de particules dites élémentaires. Les atomes, par exemple, qui composent toute la matière terrestre, comportent des électrons qui orbitent autour d'un noyau, qui est lui-même assemblé à partir de protons et de neutrons, lesquels sont formés de quarks up et down. L'électron a deux frères plus lourds: le muon et le tau. Pour chacune de ces particules, il existe un neutrino correspondant. Les neutrinos sont des particules électriquement neutres presque sans masse qui interagissent très faiblement avec toute la matière. Ces particules forment les leptons. Les quarks up et down ont aussi des frères plus lourds: les quarks charmé et top, et les quarks étrange et bottom. Les leptons et les quarks sont tous des fermions de spin $\frac{1}{2}$. Chaque fermion a aussi une anti-particule de charge électrique opposée. Nous ne savons toujours pas si l'anti-neutrino est une particule différente du neutrino. Les fermions interagissent les uns avec les autres en échangeant d'autres particules de spin entier qui sont par conséquent des bosons. À l'échelle microscopique, les forces résultent de ces échanges: la force électromagnétique est transmise par les photons, l'interaction forte provient de l'échange de gluons, et la force faible est convoyée par les bosons $W^{\pm}$ et Z. La force forte, qui agit entre les quarks, forme des systèmes liés appelés hadrons (le proton et le neutron sont des exemples de hadrons).

Le Modèle Standard est une théorie quantique qui décrit toutes les particules élémentaires connues et leurs interactions. L'une des hypothèses sous-jacentes du Modèle Standard est que les lois de la nature doivent être invariantes sous certaines transformations, dites transformations de jauge. Une conséquence de ceci est que les particules élémentaires ne devraient pas avoir de masse. Leur masse apparaît par le biais d'interactions avec un champ de Higgs, qui est un champ scalaire qui possède aujourd'hui une valeur moyenne non nulle dans le vide. Ces interactions produisent également le mélange des états massifs et d'interaction des neutrinos et des quarks. Le champ de Higgs du Modèle Standard donne lieu à une nouvelle particule, le boson de Higgs, qui a été découverte en 2012 au CERN par les collaborations ATLAS et CMS.

Le Modèle Standard est une théorie du monde microscopique dont pratiquement toutes les prédictions ont été confirmées expérimentalement. Pourtant, il est largement admis que ce ne peut être une théorie complète de la nature. En effet, le Modèle Standard est incapable d'expliquer l'asymétrie matière-antimatière de l'univers, la nature microscopique de la matière noire observée par ses effets gravitationnels, et de nombreux autres phénomènes cosmologiques tels l'expansion accéléré de notre Univers. Dans le Modèle Standard, la masse du boson de Higgs est en principe sujette à de grandes corrections quantiques, exigeant du point de vue de la théorie des annulations anormalement fines afin de préserver une valeur finie de l'ordre de 125 GeV. Tous ces points motivent la recherche de nouveaux processus physiques microscopiques allant au-delà du Modèle Standard.

2. Au-delà du Modèle Standard

Le Modèle Standard utilise une forme minimale du mécanisme dites Brout-Englert-Higgs pour atteindre une brisure de symétrie électrofaible. Il n'y a pas de motivation théorique pour cela à part de juste sa simplicité. Or, la réalité peut être plus compliquée. De nombreuses extensions possibles du Modèle Standard ont été proposées, dont certaines comprennent des champs de Higgs supplémentaires. Dans un modèle à deux Higgs-Doublet (2HDM) il ya deux champs scalaires de doublet valeurs complexes, par rapport à un seul dans le Modèle Standard. Le secteur de Higgs du Modèle Standard Supersymétrique Minimum (MSSM), qui peut résoudre un nombre des problèmes évoqués dans le chapitre précédent, est un 2HDM. En tout 2HDM, il ya cinq bosons de Higgs: La CP-même h et H, le CP-odd A et $H^{\pm}$ chargée électriquement. Cette thèse présente des recherches pour les bosons de Higgs chargés.

Dans le MSSM, un boson de Higgs chargé se désintègre principalement par $H^+ \to tb$ ou en particules supersymétriques lorsque cela est permis cinématiquent. La désintegration en quarks de différentes générations est défavorisée et le mode dominant quand tb est interdit cinématiquement n'est pas cb, mais $\tau\nu$. Le mode de désintégration préféré dans quarks légers est la place cs. Pour les modes de désintégration leptoniques, les fractions de branchement relatives sont directement proportionnelles à la masse au carré du lepton chargé. Une désintégration en $\mu\nu$ et $e\nu$ ne sont alors pas possibles par plusieurs ordres de grandeur.

Dans un collideur de hadrons, des bosons de Higgs chargés peuvent être produites dans les désintégrations de quarks top, qui sont produites principalement dans la forme de $t\bar{t}$ paires. Si les bosons de Higgs chargés sont plus lourdes que les quark top, ils seraient plutôt fabriqués en association avec un quark top. Dans le premier cas, le boson de Higgs chargé se désintègre principalement dans un tau et un neutrino, alors que dans le dernier cas, il se désintègre principalement dans un quark top et un quark bottom.

3. Le Grand collisionneur de hadrons

Le Large Hadron Collider (Grand collisionneur de hadrons, LHC), situé au CERN à Genève, en Suisse, est le collisionneur de particules le plus puissant du monde. Le LHC est un accélérateur synchrotron, près de 27 km de circonférence, équipés de plus de 1600 aimants supraconducteurs fonctionnant à 1,9 K et capable de générer des champs magnetique de jusqu'à 8,3 T. Il accélère deux faisceaux tournant en sens inverse de particules de la même charge à l'aide de 400 MHz cavités supraconductrices. Il y a des installations expérimentales où les faisceaux se croisent à quatre points le long de la machine.

Les analyses présentées dans cette thèse utilisent des données recueillies en 2011 et 2012, lorsque le LHC a livré des collisions proton-proton à des énergies de 7 TeV et 8 TeV dans le centre de masse. Une luminosité instantanée de $7,7 \times 10^{33}$ cm^{-2}s^{-1} a été atteint, et des lunminosities intégrés jusqu'à 6 fb^{-1} (23 fb^{-1}) de 7 TeV (8 TeV) ont été delivrés le nombre de collisions à des expériences. Ces données présentent une opportunité pour étudier les processus de physique à des énergies jamais sondé auparavant dans un environnement de laboratoire.

Le résultat le plus important de la première manche du LHC a été la découverte d'un boson de Higgs avec une masse de 125 GeV. Cela confirme l'existence d'au moins un champ de Higgs. Les mesures des accouplements, de spin et la parité de la particule découverte sont compatibles avec les prédictions du modèle standard. Les expériences du LHC ont aussi cherché, entre autres choses, les particules supersymétriques et bosons de Higgs supplémentaires mais ils n'ont pas trouvé une preuve de l'existence de telles particules.

4. L'expérience ATLAS

Le détecteur ATLAS a été conçu pour explorer l'intégralité du potentiel de physique offert par le LHC. Au centre d'ATLAS, se trouve un trajectomètre qui mesure la quantité de mouvement des particules chargées, avec une résolution de $\sigma_{p_\mathrm{T}}/p_\mathrm{T} = 0,05\% p_\mathrm{T} \oplus 1\%$. Du centre vers l'extérieur, cet instrument est subdivisé en un détecteur à pixels de silicium, suivi d'un détecteur à bandes de semi-conducteur (SCT), et d'un détecteur de traces composé de tubes à rayonnement de transition (TRT). Ce trajectomètre est plongé dans un solénoïde supraconducteur développant un champ magnétique axial de 2 T.

Le calorimètre d'ATLAS utilise la technologie à argon liquide dans un rayon de 2 m autour de l'axe du faisceau, et à tuiles scintillantes au-delà. L'énergie des électrons et des photons est mesurée avec une résolution de $\sigma_E/E = 10\%/\sqrt{E} \oplus 0.7\%$. Celle des jets hadroniques est obtenue avec une résolution de $\sigma_E/E = 50\%/\sqrt{E} \oplus 3\%$.

Tout à l'extérieur d'ATLAS, on trouve le spectromètre à muons qui se compose séparément de chambres à dérive de précision et de détecteurs gazeux assurant le déclenchement. Le champ magnétique de déviation est fourni par trois ensembles d'aimants toroïdaux supraconducteurs. Le spectromètre à muons peut mesurer la quantité de mouvement transverse de muons avec une résolution de 10 % à 1 TeV, indépendamment du détecteur interne.

ATLAS est équipé d'un système de déclenchement à trois niveaux qui est utilisé pour réduire le taux d'événements à environ 400 Hz.

Dans le cadre des préparatifs pour la deuxième campagne de prise de données du LHC, l'auteur a contribué à des améliorations du système de contrôle qui maintient la séparation thermique entre le SCT et le TRT . Des mesures de la résistance des modules du SCT sous une polarisation directe ont également été réalisées. Aucune augmentation significative de cette résistance depuis la mise en service d'ATLAS n'a été observée.

Le logiciel d'ATLAS, qui comprend le système de contrôle-commande, d'acquisition de données, les programmes de simulation, de reconstruction et d'analyse des événements, est également décrit dans ce chapitre, en mettant l'accent sur les contributions personnelles de l'auteur.

5. Les techniques d'analyse

Le premier lot de données enregistrées en 2011 par ATLAS à $\sqrt{s} = 7$ TeV correspond à une luminosité intégrée de 4,6 fb^{-1}. Le deuxième lot recueilli en 2012 à $\sqrt{s} = 8$ TeV totalise une luminosité intégrée de 20,3 fb^{-1}.

Les électrons sont reconstruits en faisant correspondre les dépôts d'énergie groupés en amas dans le calorimètre électromagnétique à des traces reconstruites dans le trajectomètre. Les muons induisent des traces observées dans le trajectomètre et dans le spectromètre à muons. Les jets hadroniques sont mesurés dans les calorimètres en utilisant l'algorithme de reconstruction anti-k_t avec un rayon de gerbe de 0,4. Les données mesurées dans le trajectomètre permettent l'identification des jets hadroniques provenant de vertex primaires ainsi que des jets initiés par un quark b. Les désintégrations hadroniques des leptons tau sont reconstruites à partir des jets possédant une ou trois traces associées, et à l'aide d'algorithmes multivariés destinés à éliminer ceux qui parmi eux proviennent de jets initiés par des quarks ou des gluons.

Cette thèse présente la recherche de bosons de Higgs chargés, légers lorsque ceux-ci sont produits dans la désintégration de quarks top, ou lourds lorsqu'ils sont générés en association avec un quark top. Les bruits de fond principaux proviennent alors des processus du Modèle Standard avec production de quarks top, et en particulier du processus $gg \to t\bar{t} \to b\bar{b}W^+W^-$, ainsi que de la production de bosons vecteurs en association avec des jets. La modélisation des événements de signal et des processus de bruit de fond principaux est réalisée par simulation Monte Carlo.

Certains bruits de fond, en particulier ceux qui découlent de faux leptons tau mal identifiés, sont difficiles à simuler correctement et sont donc estimés en utilisant des techniques basées sur les données réelles. La méthode de la matrice est l'une de ces techniques. Elle utilise les probabilités d'identification correcte et erronée mesurées dans les données réelles, sur des événements simulés, ou dans un mélange des deux. Elle peut être utilisée pour évaluer la normalisation et les distributions – fonctions de variables cinématiques – d'événements de bruit de fond avec un ou plusieurs objets mal identifiés.

Tous les résultats des analyses présentées dans cette thèse sont interprétés en testant la compatibilité des données avec tout d'abord l'hypothèse du Modèle Standard uniquement, et ensuite l'hypothèse du Modèle Standard avec un signal de boson de Higgs chargé, le tout en utilisant une méthode fréquentiste de vraisemblance profilée modifiée qui intègre des incertitudes systématiques traitées comme des paramètres de nuisance ajustés aux données. Cette méthode permet de minimiser l'impact des incertitudes systématiques sur la sensibilité de recherche en tirant profit de régions de contrôle dominées par le bruit de fond.

6. Recherche d'un boson de Higgs chargé se désintégrant en un lepton tau et un neutrino tau dans les données prises à 7 TeV

Dans ce chapitre, sont présentées trois recherches d'un boson de Higgs chargé et léger, qui serait généré dans la désintégration de quarks top et qui se désintégrerait en $\tau\nu$. Elles font appel aux données recueillies par ATLAS en 2011 à 7 TeV. Toutes ces analyses partent de l'hypothèse que $\mathscr{B}(H^+ \to \tau\nu) = 100\%$. Dans tous les cas, le signal est caractérisé par la présence additionnelle d'un quark top (produit par paires) qui se désintègre en un électron ou un muon. Ce lepton de haut p_{T} permet de distinguer clairement ces événements de la plupart des fonds multi-jets, et est en conséquence utilisé pour le déclenchement.

En principe, le canal le plus propre est l'état final dilepton, où le tau provenant du boson de Higgs se désintègre d'une manière leptonique. Le canal dilepton a été analysé sur les premières données de collisions pp enregistrées à $\sqrt{s} = 7$ TeV, correspondant à une luminosité intégrée de 1,03 fb^{-1}. Les résultats montrent que cette analyse a une sensibilité modeste à l'observation d'un boson de Higgs chargé et léger. Elle n'a donc pas été répétée sur l'ensemble des données.

Au vu de ce constat, l'accent a été mis sur le canal où le lepton tau se désintègre hadroniquement (τ_{had}). Les modes de désintégration hadronique du lepton tau ont des fractions de branchement plus élevées, et conduisent à des événements qui comportent moins de neutrinos. Cependant, ce canal est entaché d'un bruit fond difficile à estimer, provenant de jets initiés par des quark ou des gluons, qui peuvent être à tort identifiés comme des désintégrations hadroniques de leptons tau. Puisque cette probabilité de confusion est très difficile à modéliser précisément par des simulations Monte-Carlo, elle a été mesurée dans des régions de contrôle sur les données réelles. Le canal lepton $+\,\tau_{\text{had}}$ a été analysé sur l'ensemble complet des données acquises en 2011, correspondant à une luminosité intégrée de 4,6 fb^{-1}. En l'absence de signal observé, des limites supérieures sur le rapport de branchement $\mathscr{B}(t \to bH^+)$ on été extraites en utilisant la distribution $E_{\text{T}}^{\text{miss}}$ de l'énergie transverse manquante.

Par ailleurs, les données ont été réanalysées avec un traitement simultané des canaux dileptonique et lepton $+\,\tau_{\text{had}}$. Cette analyse qui se présente sous la forme d'un comptage d'événements, a été conçue comme un test de l'universalité leptonique dans les événements $t\bar{t}$. Ici le rôle du canal dileptonique consiste principalement à contraindre les incertitudes sur les bruits de fond, plutôt que de fournir une sensibilité directe au signal. Les événements dans lesquels le τ_{had} reconstruit a le même signe de charge que le lepton sont soustraits des événements dans lesquels ils ont des signes de charges opposés, ce qui annule les contributions des jets de gluons et de quarks bottom feignant une désintégration hadronique d'un lepton tau. Le nombre d'événements lepton $+\,\tau_{\text{had}}$ et dileptoniques est finalement mesuré comme étant conforme à la prévision du Modèle Standard. Des limites supérieures sur $\mathscr{B}(t \to bH^+)$ sont alors déduites. Elles vont de 3,2 à 4,4% pour des masses de H^+ allant de 90 à 140 GeV.

La combinaison de ces résultats avec ceux obtenus par d'autres recherches menées au sein d'ATLAS au sujet de bosons de Higgs chargés, ainsi que leur interprétation dans le scénario m_h^{max} du MSSM sont également présentées.

7. Recherches d'un boson de Higgs chargé décroissant en un lepton tau et un neutrino dans les données acquises à 8 TeV

Les données recueillies à $\sqrt{s} = 8$ TeV en 2012, correspondant à une luminosité intégrée de 20,3 fb^{-1}, ont fait l'objet d'une analyse simultanée des canaux lepton $+\,\tau_{\text{had}}$ et dilepton. Comme lors du test de l'universalité leptonique dans la désintégration des quarks top présenté dans le chapitre précédent, l'adjonction du canal dileptonique permet de réduire les incertitudes systématiques du bruit de fond. Cependant, à la différence de ce qui avait été fait à 7 TeV, le test de présence d'un signal est mené sur la distribution d'une variable de masse transverse, laquelle permet d'améliorer la sensibilité d'observation d'un boson de Higgs chargé pour des masses plus grandes que celle du boson W. Cette recherche a été conduite pour une masse du boson de Higgs chargé allant jusqu'à 1 TeV, qui serait produit dans ce cas en association avec un quark top.

Le bruit de fond provenant de l'erreur d'identification de jets hadroniques qui sont parfois confondus avec des désintégrations hadroniques de leptons tau, est estimé par l'usage de la technique dite de la matrice, appliquée sur les données réelles. Cette méthode permet de mesurer les probabilités d'erreurs d'identification directement dans les données réelles, en utilisant de vraies désintégrations hadroniques de leptons tau plutôt que celles fournies par la simulation.

Les principales incertitudes systématiques de cette analyse sont liées à l'étalonnage de l'énergie des jets et à la modélisation des événements $t\bar{t}$. Dans la région de contrôle dileptonique dominée par le bruit de fond, l'analyse est effectuée à l'aide de catégories distinctes d'événements avec zéro, un, ou deux jets étiquetés b, tandis que la région où l'on attend un signal est fusionnée pour contenir les événements avec un ou deux jets étiquetés b, ceci dans le but de réduire l'incertitude sur la multiplicité des jets étiquetés b, découlant du choix du schéma de calcul pour les signaux de masse élevée. Des limites supérieures sont obtenues sur le rapport d'embranchement $\mathscr{B}(t \to bH^+) \times \mathscr{B}(H^+ \to \tau\nu)$ qui varie de 1,1 à 0,3% pour 80 GeV $\leq m_{H^+} \leq$ 160 GeV, et sur la section efficace du signal fois $\mathscr{B}(H^+ \to \tau\nu)$ qui va de 0,93 à 0,03 pb pour 180 GeV $\leq m_{H^+} \leq$ 1 TeV. Ces limites observées sont légèrement plus basses que celles auxquelles on s'attendait.

Ces résultats sont complémentaires avec ceux obtenus par la recherche effectuée dans l'état final $\tau_{\text{had}} + \text{jets}$, qui a également été refaite sur l'ensemble des données acquises à 8 TeV. La combinaison des résultats de ces deux analyses repoussent les limites obtenues par le canal $\tau_{\text{had}} + \text{jets}$ seul, en particulier dans la région de très faible masse $m_{H^+} <$ 100 GeV où l'amélioration de la limite d'exclusion va jusqu'à 35%. La fluctuation négative observée dans les données réelles améliore encore les limites observées: jusqu'à 40% de mieux dans la région de faible masse pour les résultats combinés par rapport à ce qui est obtenu avec le canal $\tau_{\text{had}} + \text{jets}$ seul, et jusqu'à 20% de mieux dans la région de masse élevée. Les limites supérieures observées sur le produit du rapport d'embranchement $\mathscr{B}(t \to bH^+) \times \mathscr{B}(H^+ \to \tau\nu)$ varient de 0,6 à 0,15% pour 80 GeV $\leq m_{H^+} \leq$ 160 GeV, tandis que les limites supérieures observées sur la section efficace de production sont de l'ordre de 0,43 à 0,004 pb pour 180 GeV $\leq m_{H^+} \leq$ 1 TeV. Ces résultats sont également interprétés dans le cadre du MSSM.

Conclusion

Cette thèse a décrit la recherche d'un boson de Higgs chargé se désintégrant en un lepton tau et un neutrino à l'aide des données enregistrées par l'expérience ATLAS en 2011 et 2012. Dans cette étude, nous avons considéré les états finaux comportant soit deux leptons chargés, ou un lepton chargé et une désintégration hadronique d'un lepton tau. Deux cas de figures de production de bosons de Higgs chargés ont été considérés: pour un boson de Higgs chargé dont la masse serait inférieure à celle du quark top, celui-ci serait produit dans la désintégration des quarks top; dans le cas inverse, le boson de Higgs chargé serait produit en association avec un quark top.

Les bruits de fond comportant de vrais leptons et de vraies désintégrations hadroniques de leptons tau ont été simulés, puis ont été normalisés aux données en utilisant des régions de contrôle où le signal attendu est par nature très faible. Les bruits de fond incluant des leptons ou des désintégrations hadroniques de lepton tau mal identifiés ont été estimés à partir des données elles-mêmes. Avec 20,3 fb^{-1} de données enregistrées à une énergie de 8 TeV dans le centre de masse des collisions, des limites supérieures à un niveau de confiance de 95% sont placées sur le rapport d'embranchement $\mathscr{B}(t \to bH^+) \times \mathscr{B}(H^+ \to \tau^+\nu)$. Leurs valeurs vont de 1,1 à 0,3% pour une masse du boson de Higgs chargé allant de 80 GeV à 160 GeV. Pour une masse du boson de Higgs chargé comprise entre 180 GeV et 1 TeV, ces limites concernent la section efficace de production d'un boson de Higgs chargé en association avec un quark top. Leurs valeurs varient de 0,93 à 0,03 pb sur le domaine de masse afférant. Les limites présentées dans cette thèse sont les meilleures obtenues à ce jour dans ce canal de recherche. Une combinaison de ces résultats avec une autre recherche effectuée en exploitant l'état final entièrement hadronique conduit à des limites allant de 0,6 à 0,15 % pour un boson de Higgs chargé léger ($m_{H^+} < m_t$), et de 0,43 à 0,04 pb pour le cas d'un boson de Higgs lourd ($m_{H^+} > m_t$).

Lors de la préparation de cette thèse, un boson de Higgs neutre a été observé pour la première fois par les collaborations ATLAS et CMS. Ceci prouve l'existence d'au-moins un champ scalaire fondamental et nous encourage à poursuivre les recherches de bosons de Higgs supplémentaires. Le future des recherches dans ce domaine résidera sans aucun doute dans le régime de masse élevée: $m_{H^+} > m_t$. Le mode de désintégration du boson de Higgs chargé dans un lepton tau et un neutrino restera un canal de recherche d'un grand intérêt en raison de sa signature expérimentale relativement propre et de son rapport d'embranchement important dans certaines parties de l'espace des paramètres.

L'analyse de l'état final lepton $+ \tau_{\text{had}}$ présentée dans cette thèse est moins sensible que l'analyse précédemment publiée qui exploitait l'état final $\tau_{\text{had}} +$ jets, et doit être considérée comme complémentaire pour ce type de recherche. Néanmoins, son importance augmentera dès lors que des domaines de masse plus élevés seront explorés, puisque l'importance relative de l'impulsion transverse manquante emportée par le neutrino apparaissant dans la désintégration standard du quark top sera réduite. Avec 20,3 fb^{-1} de données recueillies à 8 TeV, la sensibilité de l'analyse est limitée par les incertitudes statistiques. Lorsque plus de données seront enregistrées lors de la deuxième période d'exploitation du LHC, la sensibilité de ce canal pourrait augmenter. Des perspectives intéressantes pour l'amélioration de cette analyse résident dans l'utilisation des informations de polarisation du lepton tau, car le boson de Higgs chargé et le boson W portent des spins différents: 0 et 1.

Au moment de l'écriture de ce document, le redémarrage du LHC à $\sqrt{s} = 13$ TeV est imminent. Cela marquera le début d'un nouveau chapitre de la physique du boson de Higgs. Jusqu'à présent, le boson de Higgs découvert semble être compatible avec celui prédit par le modèle standard. Confirmer ou réfuter ce fait sera la tâche essentielle du LHC pour les années à venir.

Sammanfattning på svenska

Inom partikelfysiken studeras universums minsta byggstenar. Allting, från dammkorn till galaxer, består på en fundamental nivå av elementarpartiklar. Atomer, som bygger upp all materia här på jorden, består till exempel av elektroner som kretsar kring en kärna bestående av neutroner och protoner, som i sin tur består av upp-kvarkar och ned-kvarkar. Elektronen har två tyngre släktingar: myonen och tauonen. För var och en av dessa finns också en neutrino. Neutrinerna är närapå masslösa partiklar som interagerar väldigt svagt med sin omgivning. Upp- och ned-kvarkarna har också tyngre släktingar: charm- och topp-kvarkarna, respektive sär- och botten-kvarkarna. Dessa partiklar utgör tillsammans fermionerna. Varje fermion har också en anti-partikel med motsatt elektrisk laddning. Fermionerna växelverkar med varandra genom att utbyta andra partiklar som kallas för bosoner. På så vis uppstår krafter mellan partiklarna: den elektromagnetiska kraften som förmedlas av fotonen, den starka kraften som förmedlas av gluonerna, och den svaga kraften som förmedlas av $W^{\pm}$- och Z-bosonerna. Den starka kraften, som verkar mellan kvarkarna, binder ihop dessa till sammansatta objekt som kallas hadroner (protonen och neutronen är exempel på hadroner).

Standardmodellen är en kvantfältteori som beskriver alla kända elementarpartiklar och deras växelverkan genom de tre nämnda krafterna. Standardmodellen bygger i stor utsträckning på att fysikens lagar måste vara invarianta under vissa lokala transformationer (så kallade gaugetransformationer) och detta förutsätter att elementarpartiklarna från början är masslösa. De får istället sina massor genom interaktioner med ett Higgsfält. Higgsfältet har den speciella egenskapen att dess styrka inte är noll när dess energi är som lägst. Även i vakuum genomsyras rymden därför av ett starkt Higgsfält och genom kontakt med detta fält får partiklarna sina massor. Higgsfältet ger också upphov till en ny partikel, den så kallade Higgsbosonen. Genom upptäckten av Higgsbosonen vet vi att Higgsfältet existerar och att den teoretiska beskrivningen av hur partiklarna får sina massor verkar stämma med verkligheten.

Det finns vissa problem som inte kan förklaras inom standardmodellen och det står klart att den förr eller senare måste utvidgas till en större teori. I många föreslagna utvidgningar av standardmodellen förekommer mer än ett Higgsfält, och därmed också mer än en Higgsboson. I den enklaste utökningen lägger man helt enkelt till ett extra Higgsfält liknande det som beskrivs av standardmodellen. Då uppstår totalt fem Higgsbosoner, varav tre är elektriskt neutrala och två är elektriskt laddade. Det är jakten på dessa laddade Higgsbosoner som är ämnet för den här avhandlingen.

För att hitta spår av nya partiklar studerar man hur högenergetiska partiklar interagerar med varandra. Den stora hadronkollideraren LHC (Large Hadron Collider) vid forskningslaboratoriet CERN i Genève, Schweiz, är världens kraftfullaste partikelaccelerator. Hadronerna som kollideras är oftast protoner. När två protoner – eller rättare sagt, kvarkar och gluoner inuti protonerna – kolliderar, omvandlas deras rörelseenergi till nya partiklar. Många partiklar är instabila och sönderfaller snabbt till andra partiklar, till exempel elektroner, myoner eller hadroner. Utmaningen är sedan att detektera dessa och försöka återskapa vilka sorts partiklar som från början bildades i kollisionen.

ATLAS är ett stort experiment vid LHC, som bland annat är utrustat med spårdetektorer och kalorimetrar för att mäta olika egenskaper hos olika partiklar. I den här avhandlingen beskriver jag analyser av data från ATLAS i syfte att hitta tecken på existensen av laddade Higgsbosoner. Detta görs genom att studera proton-proton kollisioner där topp-kvarkar bildas. Eftersom topp-kvarken är den tyngsta av alla elementarpartiklar så har den en särskilt stark koppling till Higgsbosonerna. Om de laddade Higgsbosonerna är lättare än topp-kvarken så kan topp-kvarken därför sönderfalla till en laddad Higgsboson och en botten-kvark. Om de laddade Higgsbosonerna däremot är tyngre än topp-kvarken så produceras en laddad Higgsboson vid LHC oftast tillsammans med en topp-kvark. I båda fallen så antas den laddade Higgsbosonen här sönderfalla till en tauon – som är den tyngsta av leptonerna – och en neutrino. Tauonen sönderfaller i sin tur till en eller flera neutriner tillsammans med antingen en elektron, en myon, eller en smal "jet" av hadroner. Analyser som utnyttjar det hadroniska sönderfallet av tauonen har visat sig ha störst känslighet för laddade Higgsbosoner. Hadroniska sönderfall av tauoner är dock svåra att skilja från de andra typer av jets som bildas i stort antal vid proton-proton kollisioner. Det är dessutom svårt att simulera hur ofta andra typer av jets felidentifieras som hadroniska sönderfall av tauoner. Särskilt fokus i detta arbete har därför lagts på att utveckla metoder för att estimera hur stor den här bakgrunden är.

Med antagandet att en laddad Higgsboson alltid sönderfaller till en tauon och en neutrino kan man på 95% konfidensnivå konstatera att om en topp-kvark kan sönderfalla till en botten-kvark och en laddad Higgsboson med en massa[1] mellan 80 och 160 GeV så måste detta ske för mindre än 1% av alla topp-kvarkar, samt att om en laddad Higgsboson med en massa mellan 180 och 1000 GeV produceras tillsammans med en topp-kvark så måste tvärsnittet[2] för den processen vara mindre än 1 pb.

---

[1] Inom partikelfysiken används ett system av enheter där naturkonstanten c, ljusets hastiget i vakuum, har värdet 1 och massa kan uttryckas i Giga-elektronvolt (GeV). En elektronvolt är den energi som krävs för att flytta en elektron över en potentialskillnad på en Volt. Protonen väger 0,94 GeV och topp-kvarken väger ca 173 GeV.

[2] Tvärsnittet är ett mått på hur ofta en viss process inträffar vid en partikelkollision. Med ett tvärsnitt på 1 pico-barn (pb) skulle det finnas ca 20000 händelser med laddade Higgsbosoner i den data som ATLAS samlat in under 2012.

Acknowledgements

During my doctoral studies, I have had the good fortune of being surrounded by incredibly nice, knowledgeable, and helpful people, without whom this thesis would not have been possible. First and foremost, I want to express my deepest gratitude to my supervisors Arnaud Ferrari, Johann Collot, and Mattias Ellert for their support and guidance throughout this work, and not least for their careful reading of many drafts of this document. Arnaud has supervised my work since I was a master's student, and I could not have asked for a better balance between friendship and mentorship, thoughtful direction and freedom to pursue my own interests. Special thanks to Johann for help with all practical matters before, during, and after my stay in Grenoble, and for many insightful discussions. Thanks also to Mattias for patiently answering all my questions about grid-computing

Thanks to Gunnar Ingelman and Tord Ekelöf for getting me interested in particle physics and for arranging the first opportunities for me to enter into the field. Thanks to Richard Brenner for lots of good advice and encouragement.

I owe many thanks to all members of the ATLAS charged Higgs, DCS, and analysis software communities. A few of my closest collaborators deserve special mention: Daniel Pelikan, my good friend and fellow charged Higgs boson hunter since day one; Liron Barak, supplier of inspirational enthusiasm, good advice and delicious treats; Camila Rangel Smith, a fantastic addition to the Uppsala team during the last year; and Max Isacson, resident Viking and plot-maker extraordinaire. Thanks to Silje Hattrem Raddum, Justin Griffiths, and Jana Schaarschmidt for computing the exclusion limits. Thanks to Ewa Stanecka for countless hours of help with the heater pad system. Thanks to Nils Krumnack for guiding me in software development. Thanks to Elin Bergeås Kuutmann for answering my questions about calorimeters.

My sincere thanks go to all other past and present colleagues in Uppsala, Grenoble and at CERN. In particular to my former officemate Mengqing Wu who always brightened my day. And to Inger Ericson and Anic Vey for patient dealings with all practical matters. Thanks to Elias Coniavitis for lots of good advice and shared frustrations over many lunches. Thanks to my colleague and flatmate Dominik Werder, for beautiful music and for overlooking my abuse of common living space during the writing of this thesis.

Thanks also to my family, in particular to my parents Sten and Christina, for all their help and encouragement. Finally, to Angela, the best support in all possible worlds. I love you.

References

[1] Particle Data Group, K.A. Olive et al., *Review of Particle Physics*, Chin. Phys. **C38** (2014) 090001.

[2] P. Higgs, *Broken symmetries, massless particles and gauge fields*, Physics Letters **12** (1964) 132–133.

[3] F. Englert and R. Brout, *Broken Symmetry and the Mass of Gauge Vector Mesons*, Phys. Rev. Lett. **13** (1964) 321–323.

[4] P. W. Higgs, *Broken Symmetries and the Masses of Gauge Bosons*, Phys. Rev. Lett. **13** (1964) 508–509.

[5] G. Guralnik, C. Hagen, and T. Kibble, *Global Conservation Laws and Massless Particles*, Phys. Rev. Lett. **13** (1964) 585–587.

[6] S. Weinberg, *A Model of Leptons*, Phys. Rev. Lett. **19** (1967) 1264–1266.

[7] T. D. Lee, *A Theory of Spontaneous T Violation*, Phys. Rev. **D8** (1973) 1226–1239.

[8] R. D. Peccei and H. R. Quinn, *CP Conservation in the Presence of Pseudoparticles*, Phys. Rev. Lett. **38** (1977) 1440–1443.

[9] J. E. Kim, *Light pseudoscalars, particle physics and cosmology*, Physics Reports **150** (1987) 1–177.

[10] J. Gunion, H. Haber, G. Kane, and S. Dawson, *The Higgs Hunter's Guide*. Frontiers in Physics. Perseus Publishing, 2000.

[11] G. Branco et al., *Theory and phenomenology of two-Higgs-doublet models*, Phys. Rept. **516** (2012) 1–102, `arXiv:1106.0034 [hep-ph]`.

[12] E. A. Paschos, *Diagonal neutral currents*, Phys. Rev. **D15** (1977) 1966–1972.

[13] S. L. Glashow and S. Weinberg, *Natural conservation laws for neutral currents*, Phys. Rev. **D15** (1977) 1958–1965.

[14] R. Haag, J. T. Lopuskanski, and M. Sohnius, *All possible generators of supersymmetries of the S-matrix*, Nuclear Physics **B88** (1975) 257–274.

[15] S. Adler and W. Bardeen, *Absence of higher-order corrections in the anomalous axial-vector divergence equation*, Physical Review **182** (1969) 1517–1536.

[16] S. Treiman, R. Jackiw, and D. Gross, *Lectures on Current Algebra and Its Applications*. Princeton series in physics. Princeton University Press, 1972.

[17] M. S. Carena, S. Heinemeyer, C. Wagner, and G. Weiglein, *Suggestions for improved benchmark scenarios for Higgs boson searches at LEP-2*, `arXiv:hep-ph/9912223 [hep-ph]`.

[18] M. S. Carena, S. Heinemeyer, C. Wagner, and G. Weiglein, *Suggestions for benchmark scenarios for MSSM Higgs boson searches at hadron colliders*, Eur.Phys.J. **C26** (2003) 601–607, `arXiv:hep-ph/0202167 [hep-ph]`.

[19] M. Carena et al., *MSSM Higgs Boson Searches at the LHC: Benchmark Scenarios after the Discovery of a Higgs-like Particle*, Eur. Phys. J. **C73** (2013) 2552, `arXiv:1302.7033 [hep-ph]`.

[20] A. Djouadi, *The Anatomy of electro-weak symmetry breaking Tome II: The Higgs bosons in the minimal supersymmetric model*, Phys. Rept. **459** (2008) 1–241, `arXiv:hep-ph/0503173`.

[21] LHC Higgs Cross Section Working Group, S. Heinemeyer et al., *Handbook of LHC Higgs Cross Sections: 3. Higgs Properties*, CERN-2013-004 (2013), `arXiv:1307.1347 [hep-ph]`.

[22] ALEPH, DELPHI, L3, OPAL, LEP Collaborations, G. Abbiendi et al., *Search for Charged Higgs bosons: Combined Results Using LEP Data*, Eur. Phys. J. **C73** (2013) 2463, `arXiv:1301.6065 [hep-ex]`.

[23] D0 Collaboration, V. Abazov et al., *Search for charged Higgs bosons in top quark decays*, Phys. Lett. **B 682** (2009) 278–286, `arXiv:0908.1811 [hep-ex]`.

[24] CDF Collaboration, T. Aaltonen et al., *Search for charged Higgs bosons in decays of top quarks in p anti-p collisions at $\sqrt{s}$ = 1.96 TeV*, Phys. Rev. Lett. **103** (2009) 101803, `arXiv:0907.1269 [hep-ex]`.

[25] LHC Higgs Cross Section Working Group, S. Dittmaier et al., *Handbook of LHC Higgs Cross Sections: 2. Differential Distributions*, CERN-2012-002 (2012), `arXiv:1201.3084 [hep-ph]`.

[26] R. Harlander, M. Kramer, and M. Schumacher, *Bottom-quark associated Higgs-boson production: reconciling the four- and five-flavour scheme approach*, `arXiv:1112.3478 [hep-ph]`.

[27] M. Flechl et al., *Improved cross-section predictions for heavy charged Higgs boson production at the LHC*, `arXiv:1409.5615 [hep-ph]`.

[28] D0 Collaboration, V. Abazov et al., *Search for charged Higgs bosons decaying to top and bottom quarks in $p\bar{p}$ collisions*, Phys. Rev. Lett. **102** (2009) 191802, `arXiv:0807.0859 [hep-ex]`.

[29] A. Crivellin, *Charged Higgs: Interpretation of B-physics results*, PoS(Charged2014)015 (2014), `arXiv:1412.2512 [hep-ph]`.

[30] T. Hermann, M. Misiak, and M. Steinhauser, *$\bar{B} \to X_s\gamma$ in the Two Higgs Doublet Model up to Next-to-Next-to-Leading Order in QCD*, JHEP **1211** (2012) 036, `arXiv:1208.2788 [hep-ph]`.

[31] BaBar Collaboration, J. Lees et al., *Evidence for an excess of $\bar{B} \to D^{(*)}\tau^-\bar{\nu}_\tau$ decays*, Phys. Rev. Lett. **109** (2012) 101802, `arXiv:1205.5442 [hep-ex]`.

[32] CKMfitter Group, J. Charles et al., *CP violation and the CKM matrix: Assessing the impact of the asymmetric B factories*, Eur. Phys. J. **C41** (2005) 1–131, `arXiv:hep-ph/0406184 [hep-ph]`.

[33] A. Crivellin, A. Kokulu, and C. Greub, *Flavor-phenomenology of two-Higgs-doublet models with generic Yukawa structure*, Phys. Rev. **D87** (2013) 094031, `arXiv:1303.5877 [hep-ph]`.

[34] L. Evans and P. Bryant, *LHC Machine*, JINST **3** (2008) S08001.

[35] ATLAS Collaboration. http://twiki.cern.ch/twiki/bin/view/AtlasPublic/LuminosityPublicResults.

[36] ATLAS Collaboration, *Observation of a new particle in the search for the Standard Model Higgs boson with the ATLAS detector at the LHC*, Phys. Lett. **B 716** (2012) 1–29.

[37] CMS Collaboration, *Observation of a new boson at a mass of 125 GeV with the CMS experiment at the LHC*, Phys. Lett. **B 716** (2012) 30–61.

[38] ATLAS Collaboration, *Measurement of the Higgs boson mass from the $H \to \gamma\gamma$ and $H \to ZZ^* \to 4\ell$ channels in pp collisions at center-of-mass energies of 7 and 8 TeV with the ATLAS detector*, Phys. Rev. **D90** (2014) 052004.

[39] CMS Collaboration, *Precise determination of the mass of the Higgs boson and tests of compatibility of its couplings with the standard model predictions using proton collisions at 7 and 8 TeV*, `arXiv:1412.8662 [hep-ex]`.

[40] ATLAS and CMS Collaborations, *Combined Measurement of the Higgs Boson Mass in pp Collisions at $\sqrt{s} = 7$ and 8 TeV with the ATLAS and CMS Experiments*, ATLAS-HIGG-2014-14, CMS-HIG-14-042 (2015), `arXiv:1503.07589 [hep-ex]`.

[41] The Gfitter Group, M. Baak et al., *The Electroweak Fit of the Standard Model after the Discovery of a New Boson at the LHC*, Eur. Phys. J. **C72** (2012) 2205.

[42] ATLAS Collaboration, *Evidence for the spin-0 nature of the Higgs boson using ATLAS data*, Phys. Lett. **B 726** (2013) 120–144.

[43] CMS Collaboration, *Constraints on the spin-parity and anomalous HVV couplings of the Higgs boson in proton collisions at 7 and 8 TeV*, `arXiv:1411.3441 [hep-ex]`.

[44] ATLAS Collaboration, *Measurements of the Higgs boson production and decay rates and coupling strengths using pp collision data at $\sqrt{s}$ = 7 and 8 TeV in the ATLAS experiment*, ATLAS-CONF-2015-007 (2015), `http://cds.cern.ch/record/2002212`.

[45] ATLAS Collaboration, *Search for neutral Higgs bosons of the minimal supersymmetric standard model in pp collisions at $\sqrt{s}$ = 8 TeV with the ATLAS detector*, JHEP **1411** (2014) 056, `arXiv:1409.6064 [hep-ex]`.

[46] CMS Collaboration, *Search for neutral MSSM Higgs bosons decaying to a pair of tau leptons in pp collisions*, JHEP **1410** (2014) 160, `arXiv:1408.3316 [hep-ex]`.

[47] ATLAS Collaboration, *Search for a CP-odd Higgs boson decaying to Zh in pp collisions at $\sqrt{s} = 8$ TeV with the ATLAS detector*, `arXiv:1502.04478 [hep-ex]`.

[48] CMS Collaboration, *Searches for heavy Higgs bosons in two-Higgs-doublet models and for $t \to ch$ decay using multilepton and diphoton final states in pp collisions at 8 TeV*, Phys. Rev. **D90** (2014) 112013, `arXiv:1410.2751 [hep-ex]`.

[49] CMS Collaboration, *Search for a pseudoscalar boson A decaying into a Z and an h boson in the llbb final state*, CMS-PAS-HIG-14-011 (2014), `http://cds.cern.ch/record/1969698`.

[50] ATLAS Collaboration, *Search for charged Higgs bosons decaying via $H^{\pm} \to \tau^{\pm}\nu$ in fully hadronic final states using pp collision data at $\sqrt{s} = 8$ TeV with the ATLAS detector*, JHEP **1503** (2015) 088, `arXiv:1412.6663 [hep-ex]`.

[51] CMS Collaboration, *Search for charged Higgs bosons with the $H^{+} \to \tau\nu$ decay channel in the fully hadronic final state at $\sqrt{s}$ = 8 TeV*, CMS-PAS-HIG-14-020, CERN (2014), `http://cds.cern.ch/record/1950346`.

[52] ATLAS Collaboration, *Search for a light charged Higgs boson in the decay channel $H^{+} \to c\bar{s}$ in $t\bar{t}$ events using pp collisions at $\sqrt{s}$ = 7 TeV with the ATLAS detector*, Eur. Phys. J. **C73** (2013) 2465, `arXiv:1302.3694 [hep-ex]`.

[53] CMS Collaboration, *Search for H^{+} to $c\bar{s}$ decay*, CMS-PAS-HIG-13-035 (2014), `http://cds.cern.ch/record/1728343`.

[54] CMS Collaboration, *Search for a heavy charged Higgs boson in proton-proton collisions at sqrts=8 TeV with the CMS detector*, CMS-PAS-HIG-13-026 (2014), `http://cds.cern.ch/record/1755203`.

[55] ATLAS Collaboration, *The ATLAS Experiment at the CERN Large Hadron Collider*, JINST **3** (2008) S08003.

[56] A. Barriuso Poy et al., *The detector control system of the ATLAS experiment*, JINST **3** (2008) P05006.

[57] J. Allison et al., *Geant4 developments and applications*, IEEE Trans. Nucl. Sci. **53** (2006) 270–278.

[58] R. Brun and F. Rademakers, *ROOT: An object oriented data analysis framework*, Nucl. Instrum. Meth. **A389** (1997) 81–86.

[59] M. Ballintijn et al., *Parallel interactive data analysis with PROOF*, Nucl. Instrum. Meth. **A559** (2006) 13–16.

[60] T. Sjostrand, S. Mrenna, and P. Z. Skands, *PYTHIA 6.4 Physics and Manual*, JHEP **0605** (2006) 026, `arXiv:hep-ph/0603175 [hep-ph]`.

[61] P. M. Nadolsky et al., *Implications of CTEQ global analysis for collider observables*, Phys. Rev. **D78** (2008) 013004, `arXiv:0802.0007 [hep-ph]`.

[62] S. Frixione, P. Nason, and C. Oleari, *Matching NLO QCD computations with Parton Shower simulations: the POWHEG method*, JHEP **0711** (2007) 070, `arXiv:0709.2092 [hep-ph]`.

[63] H.-L. Lai et al., *New parton distributions for collider physics*, Phys. Rev. **D82** (2010) 074024, `arXiv:1007.2241 [hep-ph]`.

[64] T. Sjostrand, S. Mrenna, and P. Z. Skands, *A Brief Introduction to PYTHIA 8.1*, Comput. Phys. Commun. **178** (2008) 852–867, `arXiv:0710.3820 [hep-ph]`.

[65] S. Frixione and B. R. Webber, *Matching NLO QCD computations and parton shower simulations*, JHEP **0206** (2002) 029, `arXiv:hep-ph/0204244 [hep-ph]`.

[66] B. P. Kersevan and E. Richter-Was, *The Monte Carlo event generator AcerMC versions 2.0 to 3.8 with interfaces to PYTHIA 6.4, HERWIG 6.5 and ARIADNE 4.1*, Comput. Phys. Commun. **184** (2013) 919–985.

[67] G. Corcella et al., *HERWIG 6: An Event generator for hadron emission reactions with interfering gluons (including supersymmetric processes)*, JHEP **0101** (2001) 010, `arXiv:hep-ph/0011363 [hep-ph]`.

[68] J. Butterworth, J. R. Forshaw, and M. Seymour, *Multiparton interactions in photoproduction at HERA*, Z. Phys. **C72** (1996) 637–646, `arXiv:hep-ph/9601371 [hep-ph]`.

[69] M. Aliev et al., *HATHOR: HAdronic Top and Heavy quarks crOss section calculatoR*, Comput. Phys. Commun. **182** (2011) 1034–1046, `arXiv:1007.1327 [hep-ph]`.

[70] M. Czakon and A. Mitov, *Top++: A Program for the Calculation of the Top-Pair Cross-Section at Hadron Colliders*, Comput. Phys. Commun. **185** (2014) 2930, `arXiv:1112.5675 [hep-ph]`.

[71] N. Kidonakis, *NNLL resummation for s-channel single top quark production*, Phys. Rev. **D81** (2010) 054028, `arXiv:1001.5034 [hep-ph]`.

[72] N. Kidonakis, *Next-to-next-to-leading-order collinear and soft gluon corrections for t-channel single top quark production*, Phys. Rev. **D83** (2011) 091503, `arXiv:1103.2792 [hep-ph]`.

[73] N. Kidonakis, *Two-loop soft anomalous dimensions for single top quark associated production with a W^- or H^-*, Phys. Rev. **D82** (2010) 054018, `arXiv:1005.4451 [hep-ph]`.

[74] ATLAS Collaboration, *Measurements of normalized differential cross sections for ttbar production in pp collisions at sqrt(s)=7 TeV using the ATLAS detector*, Phys. Rev. **D90** (2014) 072004, `arXiv:1407.0371 [hep-ex]`.

[75] M. L. Mangano et al., *ALPGEN, a generator for hard multiparton processes in hadronic collisions*, JHEP **0307** (2003) 001, `arXiv:hep-ph/0206293 [hep-ph]`.

[76] J. Alwall et al., *Comparative study of various algorithms for the merging of parton showers and matrix elements in hadronic collisions*, Eur. Phys. J. **C53** (2008) 473–500, `arXiv:0706.2569 [hep-ph]`.

[77] R. Gavin, Y. Li, F. Petriello, and S. Quackenbush, *FEWZ 2.0: A code for hadronic Z production at next-to-next-to-leading order*, Comput. Phys.

Commun. **182** (2011) 2388–2403, `arXiv:1011.3540 [hep-ph]`.

[78] R. Gavin, Y. Li, F. Petriello, and S. Quackenbush, *W Physics at the LHC with FEWZ 2.1*, Comput. Phys. Commun. **184** (2013) 208–214, `arXiv:1201.5896 [hep-ph]`.

[79] J. M. Campbell, R. K. Ellis, and C. Williams, *Vector boson pair production at the LHC*, JHEP **1107** (2011) 018, `arXiv:1105.0020 [hep-ph]`.

[80] ATLAS Collaboration, *New ATLAS event generator tunes to 2010 data*, ATL-PHYS-PUB-2011-008 (2011), `http://http://cds.cern.ch/record/1345343`.

[81] ATLAS Collaboration, *ATLAS tunes of PYTHIA 6 and Pythia 8 for MC11*, ATL-PHYS-PUB-2011-009 (2011), `http://cds.cern.ch/record/1363300`.

[82] P. Z. Skands, *Tuning Monte Carlo Generators: The Perugia Tunes*, Phys. Rev. **D82** (2010) 074018, `arXiv:1005.3457 [hep-ph]`.

[83] Z. Was and P. Golonka, *TAUOLA as tau Monte Carlo for future applications*, Nucl. Phys. Proc. Suppl. **144** (2005) 88–94, `arXiv:hep-ph/0411377 [hep-ph]`.

[84] E. Barberio, B. van Eijk, and Z. Was, *PHOTOS: a universal Monte Carlo for QED radiative corrections in decays*, Comput. Phys. Commun. **66** (1991) 115–128.

[85] M. Cacciari and G. P. Salam, *Dispelling the N^3 myth for the k_t jet-finder*, Phys. Lett. **B641** (2006) 57–61, `arXiv:hep-ph/0512210 [hep-ph]`.

[86] M. Cacciari, G. P. Salam, and G. Soyez, *The Anti-k(t) jet clustering algorithm*, JHEP **0804** (2008) 063, `arXiv:0802.1189 [hep-ph]`.

[87] ATLAS Collaboration, *Jet energy measurement with the ATLAS detector in proton-proton collisions at $\sqrt{s} = 7$ TeV*, Eur. Phys. J. **C73** (2013) 2304, `arXiv:1112.6426 [hep-ex]`.

[88] ATLAS Collaboration, *Pile-up subtraction and suppression for jets in ATLAS*, ATLAS-CONF-2013-083 (2013), `http://cds.cern.ch/record/1570994`.

[89] ATLAS Collaboration, *Performance of the Reconstruction and Identification of Hadronic Tau Decays in ATLAS with 2011 Data*, ATLAS-CONF-2012-142 (2012), `http://cds.cern.ch/record/1485531`.

[90] ATLAS Collaboration, *Identification of the Hadronic Decays of Tau Leptons in 2012 Data with the ATLAS Detector*, ATLAS-CONF-2013-064 (2013), `http://cds.cern.ch/record/1562839`.

[91] G. Cowan, K. Cranmer, E. Gross, and O. Vitells, *Asymptotic formulae for likelihood-based tests of new physics*, Eur. Phys. J. **C71** (2011) 1554, `arXiv:1007.1727 [physics.data-an]`.

[92] A. L. Read, *Presentation of search results: The CL(s) technique*, J. Phys. **G28** (2002) 2693–2704.

[93] ATLAS Collaboration, *Search for a charged Higgs boson decaying via $H^+ \to \tau_{\rm lep} + \nu$ in $t\bar{t}$ events with one or two light leptons in the final state using 1.03 fb^{-1} of pp collision data recorded at $\sqrt{s} = 7$ TeV with the ATLAS detector*, ATLAS-CONF-2011-151 (2011), `http://cds.cern.ch/record/1398187`.

[94] ATLAS Collaboration, *Study of discriminating variables for charged Higgs boson searches in $t\bar{t}$ events with leptons, using 35 pb^{-1} of data from the ATLAS detector*, ATLAS-CONF-2011-018 (2011), `http://cds.cern.ch/record/1336747`.

[95] E. Gross and O. Vitells, *Transverse mass observables for charged Higgs boson searches at hadron colliders*, Phys. Rev. **D81** (2010) 055010, `arXiv:0907.5367 [hep-ph]`.

[96] ATLAS Collaboration, *Luminosity Determination in pp Collisions at $\sqrt{s} = 7$ TeV using the ATLAS Detector in 2011*, ATLAS-CONF-2011-116 (2011), `http://cds.cern.ch/record/1376384`.

[97] ATLAS Collaboration, *Search for charged Higgs bosons decaying via $H^+ \to \tau\nu$ in top quark pair events using pp collision data at $\sqrt{s} = 7$ TeV with the ATLAS detector*, JHEP **1206** (2012) 039, `arXiv:1204.2760 [hep-ex]`.

[98] ATLAS Collaboration, *Performance of the Reconstruction and Identification of Hadronic Tau Decays with ATLAS*, ATLAS-CONF-2011-152 (2011), `http://cds.cern.ch/record/1398195/`.

[99] D. Ross and M. Wiebusch, *MSSM Effects in Top-antitop Production at the LHC*, JHEP **0711** (2007) 041, `arXiv:0707.4402 [hep-ph]`.

[100] ATLAS Collaboration, *Search for charged Higgs bosons through the violation of lepton universality in $t\bar{t}$ events using pp collision data at $\sqrt{s} = 7$ TeV with the ATLAS experiment*, JHEP **1303** (2013) 076, `arXiv:1212.3572 [hep-ex]`.

[101] ATLAS Collaboration, *Estimation of non-prompt and fake lepton backgrounds in final states with top quarks produced in proton-proton collisions at $\sqrt{s} = 8$ TeV with the ATLAS detector*, ATLAS-CONF-2014-058 (2014), `http://cds.cern.ch/record/1951336`.

[102] ATLAS Collaboration, *Measurement of the production cross section of jets in association with a Z boson in pp collisions at $\sqrt{s}$ = 7 TeV with the ATLAS detector*, JHEP **1307** (2013) 032, `arXiv:1304.7098 [hep-ex]`.

[103] M. Botje et al., *The PDF4LHC Working Group Interim Recommendations*, `arXiv:1101.0538 [hep-ph]`.